Time-Resolved Studies of Excited State Molecular Dynamics

by

Lisa Saalbach

Submitted for the Degree of Doctor of Philosophy

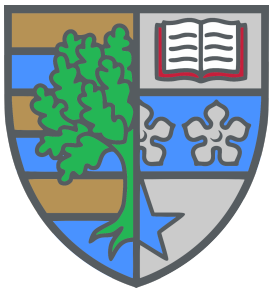

School of Engineering and Physical Sciences
Heriot-Watt University

May, 2020

Abstract

The interaction of light and matter is one that is universal in nature and provides problems to be solved by physicists and chemists alike. This thesis presents a collection of experiments dedicated to understanding the effect of ultraviolet (UV) and vacuum ultraviolet (VUV) radiation on simple model analogues of biologically and environmentally relevant molecules. The energy deposited into the molecular system through this high-energy radiation is typically redistributed by various nonradiative relaxation processes which take place on ultrafast (femtosecond) timescales. What these processes are and whether they can be related to the molecule's structure and function will be explored in this text. In order to do this, the highly-differential time-resolved photoelectron imaging (TRPEI) approach was employed in conjunction with theoretical *ab initio* quantum chemistry calculations. A specific feature that is considered throughout this work is the use of short-wavelength exciting (pump) and ionising (probe) pulses.

Initially, acetylacetone was studied using the TRPEI approach in conjunction with 267 nm pump and 160 nm VUV probe pulses. The femtosecond VUV laser pulses were produced using four-wave difference-frequency mixing in an argon-filled gas cell. These high-energy probe pulses provide a significantly extended view along the reaction-coordinate of interest, through a deep projection into the ionisation continuum. This lab-based approach was able to provide quantitative links between elements of earlier reports on relaxation dynamics in acetylacetone, which sampled smaller subsections of the reaction-coordinate. Four dynamical processes occurring on distinct timescales ranging from <10 fs to over 300 ps were identified, including one signature not previously reported. This work highlights the need for such short-wavelength VUV probes in photoionisation-based investigations of photochemical dynamics. Secondly, the non-adiabatic relaxation dynamics of nitrobenzene and three of its dimethyl-derivatives were investigated using TRPEI and *ab initio* calculations to gain insight into the influence exerted by the nitro-group orientation on the dynamics. Multiphoton ionisation involving two and/or three photons with wavelengths centred at 400 nm achieved a high-energy probe and revealed near-identical dynamical signatures for all four systems, despite the varying effects of steric hindrance on the nitro-group. These could be assigned to dynamical processes occurring on three timescales: sub 30 fs, in the range of 160-190 fs and finally in the range of 90-160 ps, depending on the molecule. Finally, VUV pulses were again employed, this time as the pump in the study of formamide, N,N-dimethylformamide and N,N-dimethylacetamide, which are motifs ubiquitous in nature. Dynamical signatures indicative of rapid relaxation processes were observed on timescales of 10-35 fs and 70-75 fs in all three systems. In addition to the TRPEI results, extensive quantum chemistry calculations revealed different Rydberg-to-valence evolution behaviour in formamide and the two larger amide systems.

To my family

Acknowledgements

I would first and foremost like to thank my supervisor Dr Dave Townsend for his support, not only during my PhD, but throughout my time at Heriot-Watt University. He always took an interest in my work and made time for discussions, where he provided a lot of valuable advice. Secondly, I would like to thank Prof. Martin J. Paterson for his all of his feedback and for his patience with my many questions about performing various computational chemistry calculations. Further thanks goes to Heriot-Watt University and the Engineering and Physical Sciences Research Council for providing me with the funding to pursue this PhD.

Next, I would like to thank Dr Nikoleta Kotsina who played a key role in achieving experimental success for several projects presented in this thesis. I thank her for passing her expertise on to me and for her constant guidance throughout this journey. My thanks also goes to Dr Stuart W. Crane, who taught me about the workings of the lab and was always happy to lend a helping hand if needed. Long days and evenings in the lab were made more enjoyable by Nikoleta and Stuart's companionship and friendship. I will look back on these times fondly. I would also like to thank Chris Sparling for many helpful discussions on various bits of Matlab code and for producing several superb figures, which have been used in this thesis. Life in the lab has definitely been more exciting since he joined the group. I would also like to thank Dr Marco Candelaresi and Dr Magdalena M. Zawadzki for laying the foundations to the vacuum UV experiment. Dr James O. F. Thompson must also be thanked here as he encouraged my enthusiasm for this subject when I was just an undergaduate student, and has remained a good friend ever since. My thanks also goes to Andrew Prentice, Thomas Malcomson, Clement Soulie and Dr Jeremy Coe for all their discussions and input on the computational chemistry side.

Furthermore, I would also like to thank Dr Rachael Tobin, Dr John Tobin, Pete Connolly, Dr Kateryna Kuzmenko, Dr Jack Wildman, Susan Chan and Katya Moncrieff for joining me on this journey. I am grateful that I was able to share this experience with all of you and hope this is a bond that will last a lifetime.

I also thank Nikoleta, Chris, Rachael, Pete and Teodora Grigorova for proof-reading various chapters of this thesis.

Finally, I want to thank my family. I thank my parents Beate and Ralf Saalbach and my brothers, Robert and Philip Saalbach, for supporting me in every way possible. If it was not for you, I would not have come to Scotland and would never have had the opportunity to pursue this path. *Tausend Dank*! And last but not least, I want to thank my partner Dr Niclas K. L. Westerberg for being by my side throughout this experience. I would not have made it this far without your never-ending understanding, support and encouragement. Thank you also for the many

discussions on various aspects of physics (and maybe a tiny bit of chemistry) and for the many hours spent proof-reading this document in its entirety over the course of a few weeks.

To conclude, a quotation by a well-known chemical physicist which expresses the interdisciplinary nature of this work.

"The chemist is a guest at the physicist's table and frequently dines well."[1]

– Richard Bersohn in *Some Pleasures in Chemical Physics*
Annu. Rev. Phys. Chem. **54** (2003)

Research Thesis Submission

Please note this form should be bound into the submitted thesis.

Name:	Lisa Saalbach		
School:	Engineering and Physical Sciences – Institute of Physics and Quantum Sciences		
Version: *(i.e. First, Resubmission, Final)*	Final	Degree Sought:	Doctor of Philosophy in Physics (PhD)

Declaration

In accordance with the appropriate regulations I hereby submit my thesis and I declare that:

1. The thesis embodies the results of my own work and has been composed by myself
2. Where appropriate, I have made acknowledgement of the work of others
3. The thesis is the correct version for submission and is the same version as any electronic versions submitted*.
4. My thesis for the award referred to, deposited in the Heriot-Watt University Library, should be made available for loan or photocopying and be available via the Institutional Repository, subject to such conditions as the Librarian may require
5. I understand that as a student of the University I am required to abide by the Regulations of the University and to conform to its discipline.
6. I confirm that the thesis has been verified against plagiarism via an approved plagiarism detection application e.g. Turnitin.

ONLY for submissions including published works

Please note you are only required to complete the Inclusion of Published Works Form (page 2) if your thesis contains published works)

7. Where the thesis contains published outputs under Regulation 6 (9.1.2) or Regulation 43 (9) these are accompanied by a critical review which accurately describes my contribution to the research and, for multi-author outputs, a signed declaration indicating the contribution of each author (complete)
8. Inclusion of published outputs under Regulation 6 (9.1.2) or Regulation 43 (9) shall not constitute plagiarism.

* *Please note that it is the responsibility of the candidate to ensure that the correct version of the thesis is submitted.*

Signature of Candidate:	Lisa Saalbach	Date:	01/05/2020

Submission

Submitted By *(name in capitals):*	LISA SAALBACH
Signature of Individual Submitting:	Lisa Saalbach
Date Submitted:	01/05/2020

For Completion in the Student Service Centre (SSC)

Limited Access	Requested	Yes		No		Approved	Yes		No	
E-thesis Submitted ***(mandatory for final theses)***										
Received in the SSC by *(name in capitals):*						Date:				

Contents

List of Publications

Publications on which this thesis is based

- M. A. B. Larsen*, T. I. Sølling, R. Forbes*, A. E. Boguslavskiy, V. Makhija, K. Veyrinas, R. Lausten, A. Stolow, M. M. Zawadzki*, **L. Saalbach***, N. Kotsina, M. J. Paterson, D. Townsend, *Vacuum ultraviolet excited state dynamics of small amides*, J. Chem. Phys., **150**, 054301 (2019). - *Joint first author

- N. Kotsina, M. Candelaresi, **L. Saalbach**, M. M. Zawadzki, S. W. Crane, C. Sparling and D. Townsend, *Short-wavelength probes in time-resolved photoelectron spectroscopy: An extended view of the excited state dynamics in acetylacetone*, Phys. Chem. Chem. Phys, **22**, 4647 (2020).

- **L. Saalbach**, N. Kotsina, S. W. Crane, M. J. Paterson and D. Townsend, *Investigating steric effects in the excited state dynamics of methyl substituted nitrobenzene derivatives*, In Preparation.

Other relevant publications

- J. O. F. Thompson, **L. Saalbach**, S. W. Crane, M. J. Paterson and D. Townsend, *Ultraviolet relaxation dynamics of aniline, N,N-dimethylaniline and 3,5-dimethylaniline at 250 nm*, J. Chem. Phys., **142**, 114309 (2015).

- L. B. Klein, J. O. F. Thompson, S. W. Crane, **L. Saalbach**, T. I. Sølling, M. J. Paterson and D. Townsend, *Ultrafast relaxation dynamics of electronically excited piperidine: ionization signatures of Rydberg/valence evolution*, Phys. Chem. Chem. Phys., **18**, 25070 (2016).

- M. M. Zawadzki, M. Candelaresi, **L. Saalbach**, S. W. Crane, M. J. Paterson and D. Townsend, *Observation of multi-channel non-adiabatic dynamics in aniline derivatives using time-resolved photoelectron imaging*, Faraday Discuss., **194**, 185 (2016).

- O. Ghafur, S. W. Crane, M. Ryszka, J. Bockova, A. Rebelo, **L. Saalbach**, S. De Camillis, J. B. Greenwood, S. Eden, D. Townsend, *Ultraviolet relaxation dynamics in uracil: Time-resolved photoion yield studies using a laser-based thermal desorption source*, J. Chem. Phys., **149**, 034301 (2018).

- S. W. Crane, O. Ghafur, **L. Saalbach**, M. J. Paterson, D. Townsend, *The influence of substituent position on the excited state dynamics operating in 4-, 5- and 6-hydroxyindole*, Chem. Phys. Lett., **738**, 136870 (2020).

Chapter 1

Introduction

1.1 Chemistry and Light

Interactions between photons and molecules are ubiquitous and indispensable in nature. Without these processes life on earth would be quite different and likely impossible. Photosynthesis and vision are just two examples of processes in nature that are triggered by the interaction of a molecule with light. To facilitate vision, the visual pigment rhodopsin, consisting of the light-absorbing site (chromophore) retinal bound in the opsin protein, reacts to the absorption of a photon within femtoseconds (10^{-15} seconds). Upon absorption of a photon, the retinal chromophore undergoes isomerisation from an *11-cis*-retinal structure to *all-trans*-retinal [2, 3], as illustrated in Figure 1.1. It has been shown that this isomerisation takes place within 200 femtoseconds [4] and triggers a chain of events which eventually result in the stimulation of the optical nerve. The rapidity of this process is crucial as it has been suggested that, if this step were any slower, it might not occur at all. Instead, competing processes such as energy dissipation to the surroundings [5] would dominate. This fascinating and complex example shows that such ultrafast processes, triggered by the interaction of a molecule with light, are crucial for life as we know it.

There is a well established relationship between the function of a molecule and its structure in biology, but as the example of vision above shows, this relationship is incomplete. Nature is dynamic and therefore such dynamic processes, and

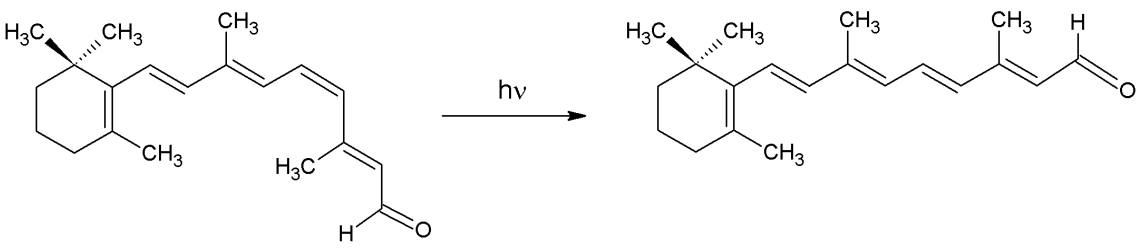

Figure 1.1: The retinal chromophore isomerises from the *cis* structure to *all-trans*-retinal within 200 fs upon interaction with a photon.

the timescales on which they occur, are fundamental in facilitating the function of many systems. A remarkable illustration of this in nature is *photoprotection*, which is observed in biological structures such as the DNA-bases guanine, thymine, adenine and cytosine, as well as pigments in the skin such as melanin. Solar radiation, to which we are all exposed regularly, contains considerable amounts of ultraviolet (UV) light which is known to be harmful and can lead to photodamage [6]. When UV radiation is incident on systems such as the above, however, it is observed that depositing these relatively large amounts of energy only rarely results in mutations or damage to the structure of the molecules [6, 7]. This is because the light absorbing sites in these structures have adapted to dissipate the potentially destructive energy through efficient and rapid decay pathways. Again, the speed of the process is crucial. Slower relaxation dynamics could result in damage to the molecular structure, which would in turn prohibit the molecule from performing its function.

Biological systems are typically large, complex structures with complex dynamics. It is therefore beneficial to start small and consider only the chromophores or common motifs in these light absorbing sites. This has been termed the *bottom-up approach* [7, 8] and is commonly used to break down the complex dynamics by studying *model*-chromophore structures. The findings from studies of the small model systems can then be collated to model and understand the dynamics in larger and more complicated biological molecules. Furthermore, by using the *bottom-up approach*, key coordinates and substructures that play a role in facilitating efficient dissipation of any excess energy, can be determined.

Since the advent of ultrashort, pulsed laser sources, it has become possible to directly probe events taking place on ultrafast timescales. The field of femtochemistry is concerned with the study of such events, including the breaking and formation of chemical bonds and even sub-Ångström motions can be detected using ultrafast laser pulses [9]. Femtochemistry was pioneered by A. Zewail who was honoured with the Nobel Prize in 1999 for his contributions to the research in this area. The limitation of 'traditional', non-time-resolved spectroscopic studies can be illustrated using the "arrow of chemistry" (Figure 1.2). Narrow-linewidth lasers can be used

Figure 1.2: An illustration of the "arrow of chemistry". The reactant and product are known but the dynamics in between take place on a range of timescales.

in frequency-resolved measurements to characterise the initial reactants in a photochemical reaction, as they can provide quantum-state specific information. The final photoproducts can likewise be identified and understood using such methods, but the dynamical processes involved in getting from reactant A (green in Figure 1.2) to product B (blue) remain mostly unobserved (as illustrated by the white, 'unknown' area in the arrow of chemistry). To obtain the complete picture of a photochemical reaction the connecting pathways must be observed, recorded and understood. Time-resolved spectroscopic methods are beginning to be able to achieve this by taking 'snapshots' [9] and creating 'molecular movies' [10].

There are various methods which can discern at least part of the molecular dynamics (see Section 1.3 for examples) but time-resolved photoelectron imaging (TRPEI) [11–16] of gas-phase molecules is the method of choice for the work presented here. It has been used in conjunction with ultraviolet and vacuum ultraviolet light to study various small molecular systems including acetylacetone (Chapter 4), nitrobenzene and its methyl-substituted derivatives (Chapter 5), and small amides (Chapter 6). The value of investigating molecular structures in the gas-phase is related to the idea of the bottom-up approach introduced earlier. The presence of a solvent will modify the dynamics and results in shifted energy levels, which is preferably avoided.

The experimental methods employed in this thesis are outlined in Chapter 2. Furthermore, various computational *ab initio* approaches were used to support the analysis of experimental data presented in Chapters 5 and 6. A background to these theoretical methods is presented in Chapter 3.

Acetylacetone, studied in Chapter 4, is closely related to the chromophore in avobenzone, a molecule used in commercial sunscreens and enters the environment through its use in industrial applications. Understanding the ultrafast molecular relaxation dynamics in such systems can be used to make predictions for new molecules to be used in sunscreens by understanding the process through which they are able to efficiently convert harmful energy from UV radiation, into less damaging forms of energy. Furthermore, it is important to understand the effect of UV light on acetylacetone as this may reveal details of its environmental impact.

Nitrobenzene and its methyl-substituted derivatives are of interest as they have been investigated for their suitability to be used in nitric-oxide (NO) physiology. NO is known to play a vital role in many physiological functions, such as the regulation of blood pressure and muscle relaxation, but also for neurotransmission [17]. Methylated nitrobenzene derivatives can act as photochemically triggered NO-donors, which are pharmaceuticals used to treat various conditions including angina or pulmonary hypertension [17]. The ability of these methylated nitrobenzenes to release NO was linked to the conformation of the nitro-group with respect to the benzene ring [18]. Therefore, this study also provides insight into the effect of the orientation of the NO_2 group on the ultrafast non-adiabatic dynamics and the NO-

release capacity.

Finally, the small amide systems investigated in Chapter 6 were formamide, N,N-dimethylformamide and N,N-dimethylacetamide. These are ideal model systems for the peptide bonds linking amino acids in protein chains [19] and understanding their molecular dynamics on femtosecond timescales will potentially lead towards a deeper understanding of these biological systems. They also provide an opportunity to investigate further the significance of Rydberg-to-valence-state evolution, which has been shown to facilitate radiationless transitions to the ground state in a multitude of other systems [7, 20–23]. In amides low-lying singlet excited states of mixed Rydberg/valence nature are present, making them ideal for extending the investigation from systems such as aliphatic and aromatic amines, where the order (primary, secondary or tertiary systems) and presence of unsaturated bonds have been shown to affect the type of Rydberg state likely to evolve valence character [21–23].

The final Chapter 7 provides the conclusions that can be drawn from the work presented in this thesis as well as an outlook towards future work. The remainder of this current chapter will discuss the background, underlying concepts and experimental methods employed for studying the photo-initiated ultrafast relaxation dynamics in gas-phase molecules.

1.2 Excited State Dynamics

As is well known, the Schrödinger equation (SE) can be used to describe the state of a molecular system and is, in a general form, given by

$$\hat{H}\left|\Psi\right\rangle = E\left|\Psi\right\rangle. \tag{1.1}$$

Here, $\hat{H}$ is the Hamiltonian operator and describes the energy in the system. E is the resultant energy and $|\Psi\rangle$ is the wavefunction. When $\hat{H}$ is constructed and $|\Psi\rangle$ is known, the properties of the molecular system can be deduced. For the study of molecular dynamics, the time-dependence of the wavefunction is essential. The above equation then becomes the time-dependent Schrödinger equation, again in a general form:

$$i\frac{d}{dt}\left|\Psi\right\rangle = \hat{H}\left|\Psi\right\rangle. \tag{1.2}$$

For a single non-relativistic particle the time-dependent SE becomes

$$i\frac{\partial}{\partial t}\Psi(\mathbf{r},t) = \left[\frac{-\hbar^2}{2m}\nabla^2 + V(\mathbf{r},t)\right]\Psi(\mathbf{r},t), \tag{1.3}$$

where, the first right-hand term represents the kinetic energy of as particle with mass m and $V(\mathbf{r},t)$ is a time-dependent potential in position space $\mathbf{r}$. For a molecule, this

SE becomes dependent on a large number of variables as the motions of all electrons and nuclei, as well as their attractive and repulsive potentials, need to be taken into account (discussed in more detail in Chapter 3).

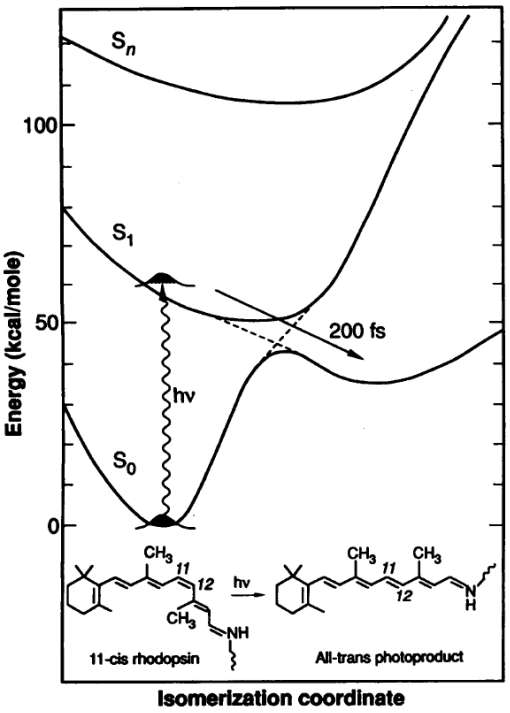

Figure 1.3: Illustration of the potential energy landscape of the isomerisation of retinal. Figure adapted from reference [4].

The Born-Oppenheimer approximation provides a simplification to this complex problem involving many particles. Proposed by Max Born and Robert Oppenheimer in 1927 [24] it states that, due to the large difference in mass between nuclei and electrons, nuclear and electronic motions can be decoupled as they must occur on very different timescales. Electronic motion, for example, occurs on attosecond (10^{-18}) timescales, whereas vibrations typically take place on femtosecond (10^{-15}) timescales. Put in another way, the nuclei can be approximated to be 'frozen' during events that take place on electronic timescales. This approximation leads to the much simplified electronic SE which can be solved for the electrons moving in a stationary potential created by the nuclei (see Chapter 3 for a more in-depth discussion). The general wavefunction solution to the time-dependent SE (when $V(\mathbf{r}, t) \equiv V(\mathbf{r})$) is of the form

$$\Psi(\mathbf{r}, t) = \Psi(\mathbf{r}) e^{-iEt/\hbar}, \tag{1.4}$$

which shows the time-dependence given in the exponential. The SE can then be solved for various different nuclear configurations (geometries) of the molecule, creating potential energy curves in diatomic molecules or surfaces in polyatomic molecules. These express the relationship between the energy of the molecule and

its geometry. An example can be seen in Figure 1.3 which shows potential energy cuts of the electronic ground state S_0 and two singlet excited states along the isomerisation coordinate in the aforementioned rhodopsin. These potential energy surfaces are a crucial tool for identifying the excited state dynamics, as is illustrated by this example showing the pathway for relaxation created between the S_0 and S_1 surfaces in the form of a conical intersection (discussed further below). The dimensionality of these surfaces is dependent on the number of geometric degrees of freedom which is $3N - 6$ for a polyatomic molecule with N atoms. The potential energy surfaces can only be constructed by considering the nuclei as stationary through the Born-Oppenheimer approximation. Since such hyper-dimensional surfaces are difficult to depict, it is typical to show cuts or surfaces along one or two specific internuclear coordinates of interest, as in Figure 1.3.

In regions where two electronic states approach in energy a strong non-adiabatic coupling of the states is usually observed. This is a strong coupling between the nuclear and electronic motions which, from the discussion above, must result in the breakdown of the adiabatic or Born-Oppenheimer approximation. *Non-adiabatic* processes occur in such regions, an example of which is the conical intersection (CI). CIs are observed when two electronic states become degenerate, resulting in an infinite non-adiabatic coupling. They can only occur in polyatomic molecules [25]. This can be demonstrated by considering the electronic part of the SE for a polyatomic molecule, where all but two solutions, ϕ_1 and ϕ_2, have been determined [26]. Additionally, the assumption is made that all solutions form a complete orthonormal set. The states (electronic configurations) which have not yet been determined can then be expressed as a linear combination

$$\Psi = \mathbf{c_1}\phi_1 + \mathbf{c_2}\phi_2. \tag{1.5}$$

Using the fact that the energy E of the (unnormalised) wavefunction Ψ is given by

$$E = \frac{\langle\Psi|\,\hat{H}\,|\Psi\rangle}{\langle\Psi|\Psi\rangle}, \tag{1.6}$$

the secular equations for the system can be determined as

$$\begin{bmatrix} H_{11} - E & H_{12} \\ H_{21} & H_{22} - E \end{bmatrix} \begin{bmatrix} \mathbf{c_1} \\ \mathbf{c_2} \end{bmatrix} = 0. \tag{1.7}$$

Here H_{ij} are Hamiltonian matrix elements $\langle\phi_i|\,\hat{H}\,|\phi_j\rangle$:

$$\begin{aligned} H_{11} &= \langle\phi_1|\,\hat{H}\,|\phi_1\rangle \\ H_{22} &= \langle\phi_2|\,\hat{H}\,|\phi_2\rangle \\ H_{12} &= \langle\phi_1|\,\hat{H}\,|\phi_2\rangle = H_{21}. \end{aligned} \tag{1.8}$$

The energies of the two previously unknown states can now be found using the secular determinant:

$$E_1 = \frac{1}{2}\left[(H_{11} + H_{22}) - \sqrt{(H_{11} - H_{22})^2 + 4H_{12}^2}\right]$$
$$E_2 = \frac{1}{2}\left[(H_{11} + H_{22}) + \sqrt{(H_{11} - H_{22})^2 + 4H_{12}^2}\right]. \tag{1.9}$$

Importantly, in order to obtain degenerate solutions, the discriminant must vanish. This requires the off-diagonal terms to be zero and the diagonal terms to be equal:

$$H_{11} = H_{22}$$
$$H_{12} = H_{21} = 0. \tag{1.10}$$

Therefore, at least two independent nuclear coordinates, that can be varied until these conditions are met, must exist. This can never be the case in a diatomic molecule as there is only one nuclear coordinate - the interatomic distance. Consequently, CIs are only possible in polyatomic molecules (three or more atoms). For diatomic molecules, there exists a non-crossing rule, which dictates that states of the same spin and symmetry cannot cross, and regions where states approach in energy but cannot become degenerate are known as "avoided crossings".

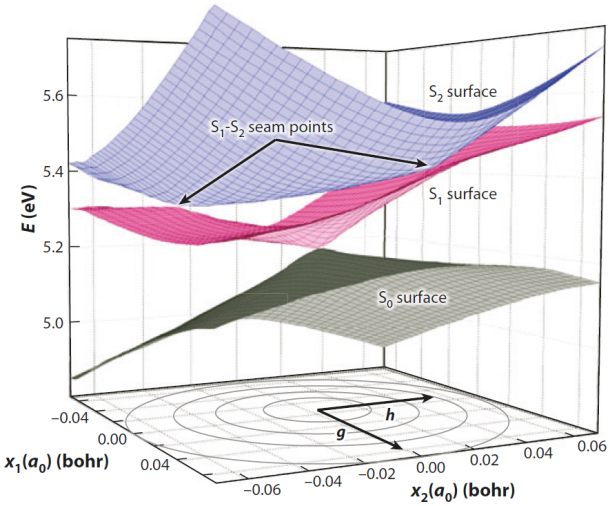

Figure 1.4: Example of potential energy surfaces and conical intersection in cytosine. This figure has been adapted from reference [27].

Conical intersections are often illustrated as a conical funnel, as shown in Figure 1.4. The origin of this funnel geometry can be explained when considering the above expressions (1.7) in a system of two independent coordinates $\mathbf{x}$ and $\mathbf{y}$. These coordinates $\mathbf{x}$ and $\mathbf{y}$ are defined as parallel to the linear coupling H_{12} and the gradient difference in energy respectively: $\mathbf{x} = \boldsymbol{\nabla}(H_{11} - H_{12})$ and $\mathbf{y} = \boldsymbol{\nabla}H_{12}$ [28]. Here $\boldsymbol{\nabla}$ is the gradient with respect to x_1 and x_2 (as used in Figure 1.4). If the point of origin is taken to be a point where the two electronic states are degenerate

($H_{11} = H_{22} = W$ and $H_{12} = 0$), the secular equation becomes

$$\begin{bmatrix} W + (m+k)\mathbf{x} - E & l\mathbf{y} \\ l\mathbf{y} & W + (m+k)\mathbf{x} - E \end{bmatrix} \begin{bmatrix} \mathbf{c_1} \\ \mathbf{c_2} \end{bmatrix} = 0. \tag{1.11}$$

Here, $m = \frac{1}{2}(h_1 + h_2)$ and $k = \frac{1}{2}(h_1 - h_2)$ and h_1 and h_2 denote the change in energy that occurs when moving along coordinate $\mathbf{x}$. From the above secular equation the eigenvalues are found to be

$$E = W + m\mathbf{x} \pm \sqrt{k^2\mathbf{x}^2 + l^2\mathbf{y}^2}. \tag{1.12}$$

This equation is the expression for a double cone, with the tip (vertex) of the cone being the point where the two states are degenerate (the point chosen as the origin). The cone is only circular for $k = 1$ and otherwise elliptical. CIs are often also referred to as "photochemical funnels", a term introduced by Domcke and Stock [29] and provide a pathway for transitions from higher- to lower-lying electronic states through non-adiabatic relaxation processes such as internal conversion. Further discussion of CIs and their relevance for non-adiabatic processes can be found references [28, 30–33].

1.2.1 Wavepacket Dynamics

In a time-resolved spectroscopy experiment, the molecule of interest is first excited using a femtosecond laser pulse and then ionised using a second ultrashort pulse. By introducing a time-delay between the initial excitation and the ionisation, the system can evolve and the molecular dynamics can be observed at different points in time. A schematic of this is shown in Figure 1.5. The initial pulse used to excite the molecule is known as the 'pump' pulse, whereas the 'probe' pulse removes the electron from the excited state, into the ionisation continuum.

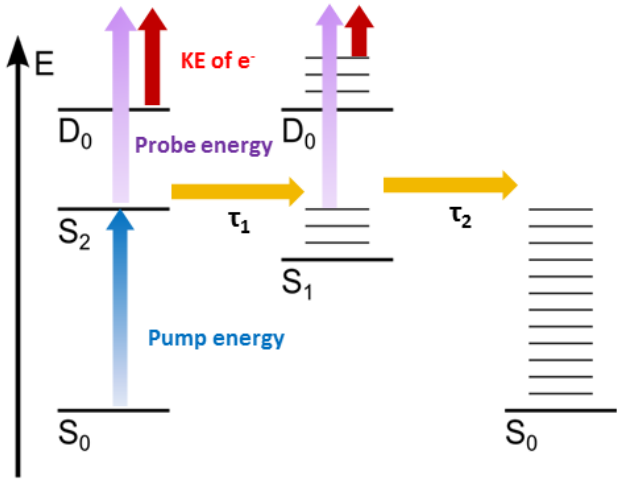

Figure 1.5: Schematic of a pump-probe scheme for time-resolved photoelectron spectroscopy. The ejected electron is detected at different pump-probe time-delays, which provides information about the relaxation dynamics taking place during this time frame. Here, τ_1 and τ_2 indicate timescales on which the two internal conversion processes illustrated take place.

During the initial excitation step more than one molecular eigenstate is typically excited. This is due to the relatively large bandwidth of the femtosecond laser pulses used to excite the molecule (discussed further in Chapter 2). A coherent superposition of molecular eigenstates is created under these conditions [13], also known as a wavepacket $\Psi(t)$:

$$|\Psi(t)\rangle = \sum_N A_N e^{-iE_N t/\hbar} |N\rangle \,. \tag{1.13}$$

Here, $|N\rangle$ are the eigenstates of the system and E_N are the excited state energies. The coefficient A_N is a complex term which contains information on the amplitudes of $|N\rangle$ as well as their initial phases; both properties are set by the pump laser field and the transition dipole moment between the two states. The energy-dependent phase factors $e^{-iE_N t/\hbar}$ describe the evolution of the wavepacket with time and are of the same form as in Equation 1.4. The evolution of the wavepacket is dependent

on the energy difference between these eigenstates, due to the presence of E_N in the phase factor. As this wavepacket evolves, the eigenstates making up the wavepacket may interfere constructively or destructively, altering the nature of the wavepacket.

In order to observe the dynamics, the wavepacket is projected onto the final state by the (second) probe, or ionising, pulse. Doing this at varying delay times after the wavepacket has been initially excited will result in the projection of the wavepacket onto the final state at different stages of its temporal evolution. Using this scheme, the dynamics occurring on ultrafast timescales in molecules can be studied. The final state acts like a 'film' onto which the wavepacket is projected. The time-dependent signal $S_f(\Delta t)$ obtained from a pump-probe measurement, projected onto a single final state, can be expressed as [13]:

$$S_f(t) = |\langle \Psi_f | \hat{\boldsymbol{\mu}} \cdot \boldsymbol{E}_{probe} | \Psi(t) \rangle|^2 = \left| \sum_N B_N^{-iE_N t/\hbar} \right|^2 , \tag{1.14}$$

where $\hat{\boldsymbol{\mu}}$ is the dipole moment operator; the expectation value of which is contained within B_N:

$$B_N = A_N \langle \Psi_f | \hat{\boldsymbol{\mu}} \cdot \boldsymbol{E}_{probe} | N \rangle . \tag{1.15}$$

The resolved differential signal of the final state $S_f(t)$, which is ultimately measured, contains a wealth of information, as will be discussed further below. Furthermore, the above expressions show the importance of the final state in determining the information that can be retrieved using a pump-probe experiment. This will be discussed further in Section 1.3 below.

1.2.2 Relaxation Processes

When a molecule absorbs a photon it is put into an electronically excited state. From there, there are two general pathways for dissipating this energy: via *radiative* relaxation or *radiationless* relaxation mechanisms. Examples of radiative processes are fluorescence and phosphorescence, which were observed as early as the late 16th century and investigated by many well-known scientists in the 19th century, including Sir David Brewster and George Gabriel Stokes (who coined the term fluorescence). The radiationless mechanisms might also be referred to as *non-radiative* or *non-adiabatic* processes. They include processes such as internal conversion and intersystem crossing. The processes discussed here are photophysical rather than photochemical. Photochemical processes include isomerisation (as in the retinal chromophore discussed earlier), dissociation, or H-atom transfer, whereas photophysical processes do not result in any chemical changes but are intramolecular processes [34].

As mentioned above, a conical intersection might facilitate non-adiabatic transitions between electronic states and one of the mechanisms mentioned is internal

conversion (IC). A schematic of an internal conversion process was shown earlier in Figure 1.5. It is a transition between two electronic states of the same spin multiplicity, as indicated by the yellow arrows labelled τ_1 and τ_2. IC processes result in the conversion of electronic energy into vibrational energy, as they mark a transition from a higher lying electronic state to a lower electronic state that is highly vibrationally excited. This ultrafast process takes place on timescales from 10^{-14} to 10^{-11} seconds.

A radiationless relaxation process from one electronic state to another with a different spin multiplictiy is known as intersystem crossing (ISC). It could be illustrated as IC in Figure 1.5 but instead of going from one singlet state to another, the final state would be a triplet state. ISC typically takes place on timescales ranging from 10^{-8} - 10^{-3} seconds, and is thereby a slow process compared to IC, as the transitions are spin-forbidden [35]. Recently however, ultrafast intersystem crossing occurring on the same timescales as internal conversion, has been reported for various systems. Several examples of ultrafast ISC can be found in references [36–41]. One particular system in which rapid ISC has been observed is acetylacetone [42, 43], investigated in Chapter 4 of this thesis. The studies referenced predict that ISC between the S_1 and T_1 states in acetylacetone takes place on a timescale of just over 1 ps, which was also observed in the investigation presented in Chapter 4 and is discussed in more detail there. The rate of ISC processes is in fact dependent upon the nature of the orbitals involved in the process. This notion was coined by M. El-Sayed and is often referred to as El-Sayed's rule [44]. A transition involving a change of orbital type (such as from $^1(\pi\pi^*)$ to $^3(n\pi^*)$) is predicted to be faster than one which does not (such as from $^1(\pi\pi^*)$ to $^3(\pi\pi^*)$), where the slower process is said to be 'forbidden'.

A final non-radiative relaxation process is intramolecular vibrational energy redistribution (IVR) [45, 46]. The exact timescale on which IVR occurs is dependent on the specific molecular system but it is typically rapid and complete within 10^{-14} to 10^{-11} seconds. IVR is the redistribution of energy between various vibrational states of the same energy, due to intramolecular couplings between rovibrational states [47]. Energy is not transferred to the surrounding environment through this process, but merely redistributed among states and no collisions are required for this process to occur. In solution however, vibrational energy can be passed onto the surroundings (i.e. the solvent) which manifests as a heating effect. In the gas-phase studies discussed in this thesis, such surrounding media are of course absent and therefore diffusion of the energy into the surroundings is not possible.

1.2.3 Molecular Orbitals

The electronic structure and mathematical descriptions of molecular orbitals will be discussed in detail in Chapter 3. This section aims to provide an overview of the

qualitative idea of molecular orbitals. Orbitals in both atoms or molecules denote the regions of space where electrons have the highest probability of being located. For hydrogen, the orbitals or wavefunctions are well known and constitute the atomic orbitals. The lowest energy atomic orbital is the 1s orbital which is spherical, whereas the p orbitals are often referred to as *dumbbell* shaped due to a central node. The number of nodes increases in d and f orbitals and so on. For molecules the picture becomes more convoluted as the atomic orbitals of the various nuclei begin to overlap (constructively or destructively) to form new molecular orbitals (MOs). Three main types of molecular orbitals are formed this way: bonding-orbitals, non-bonding orbitals or anti-bonding orbitals. Bonding-orbitals, as implied by their name, promote the stability of the molecule whereas anti-bonding orbitals have the opposite effect. Placing an electron in an anti-bonding orbital (often denoted by a *) will weaken the bond. Non-bonding orbitals contribute neither positively nor negatively to the stability of the system. Molecular orbitals can be grouped into categories of σ- or π-orbitals. These classifications indicate how the MO is formed: σ orbitals are formed by overlapping orbitals along a bond axis, whereas π orbitals display a node along the bond axis or through the nuclei involved in the bond formation. Nitrobenzene is discussed in more detail in Chapter 5, but can be used here as a system for illustrating π bonding and π^* anti-bonding orbitals as shown in Figure 1.6.

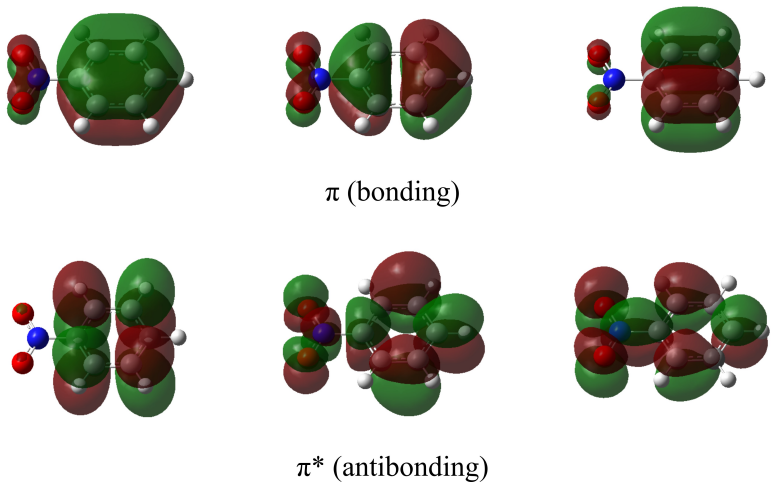

Figure 1.6: Examples of π bonding and π^* anti-bonding orbitals in nitrobenzene, computed using TD-CAM-B3LYP/aug-cc-pVTZ and the Gaussian program [48]. The orbitals located on the benzene ring are good representations of π orbitals. Their interaction with orbitals on the nitro-group is especially visible in the bottom row of this Figure.

Another type of MO that is typically encountered when exploring the excited state dynamics is the Rydberg-type orbital [49]. These are orbitals that are so far removed from the molecule that they strongly resemble atomic orbitals. In photoelectron spectra they are often identified as sharp features, or sharp rings

on velocity map images. Commonly, 3s or 3p Rydberg states have been found to take part in relaxation dynamics [22, 23], which is further discussed in Chapter 6. Additionally, it has been observed that, upon the extension of certain bonds in model chromophore systems, a Rydberg type orbital may evolve valence character, which is accompanied by a lowering in energy and thereby a facilitation of a pathway for radiationless relaxation processes [50, 51]. An illustration of this is given in Figure 1.7, using the example of 4-hydroxyindole. As either the O-H or N-H bonds are extended, the Rydberg-type orbital (3s) shrinks (becoming more valence-type) and acquires anti-bonding character. This lowering of energy can be observed in the potential energy cuts along the relevant internuclear coordinates. Examples of this and further discussion can be found in Chapter 6.

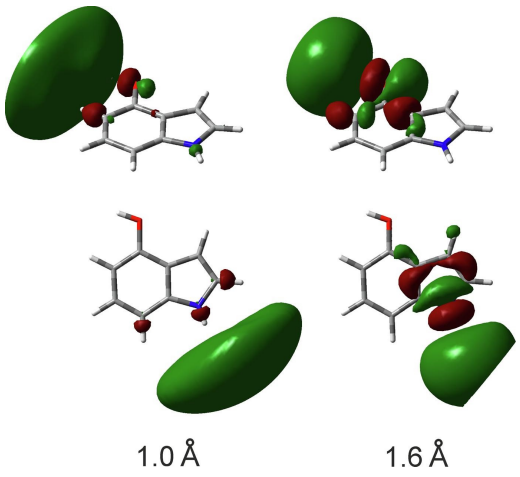

Figure 1.7: Examples of the evolution of orbital character from Rydberg to valence type in 4-hydroxyindole. As the O-H (top) and N-H (bottom) bond distance is increased, the 3s/$\pi\sigma^*$ orbital contracts and acquires anti-bonding character. This figure has been adapted from reference [52].

The role of these mixed Rydberg-valence states in relaxation dynamics has featured heavily in the literature and has been subject of the reviews by Ashfold *et al.* [20] and Roberts *et al.* [7]. They summarise that s-type Rydberg states evolving valence state character along S-X, O-X and N-X bond stretching coordinates have been found to mediate relaxation in small systems. These Rydberg states will evolve either $n\sigma^*$ or $\pi\sigma^*$ character when the bonds are elongated. Focusing on N-X coordinates, examples include basic systems such as ammonia and methylamine. In ammonia, as the N-H bond is extended, the first excited state (3s Rydberg) evolves σ^* character upon separation [53]. A CI is observed between the first excited state (3s/$\pi\sigma^*$) and the electronic ground state when an N-H bond is extended and the molecule evolves a planar structure [20, 54]. The formation of this CI between the potential energy surfaces is illustrated in Figure 1.8. In methylamine, there is now a C-N bond present, and the same evolutionary behaviour from 3s Rydberg to a σ^* orbital upon bond extension is observed here, for both the N-H and C-N stretching

coordinates [20]. Along the N-H coordinate non-adiabatic processes, through a CI between the first excited and the ground states, have been observed by theoretical *ab intio* investigations [55–57]. A similar pathway is accessible at extended C-N bond lengths, however a barrier on this potential energy surface means that this pathway opens up only when the initial excitation is at higher energy (shorter wavelengths) [20, 54]. This barrier, prohibiting relaxation processes and bond dissociation along the C-N bond, is commonly observed for amine systems [20]. This current section provided several brief examples of the importance of these mixed Rydberg-valence states for non-radiative relaxation in model-chromphore systems. Again, this will be discussed further and in more detail in Chapter 6, where three small amide systems are studied using TRPEI.

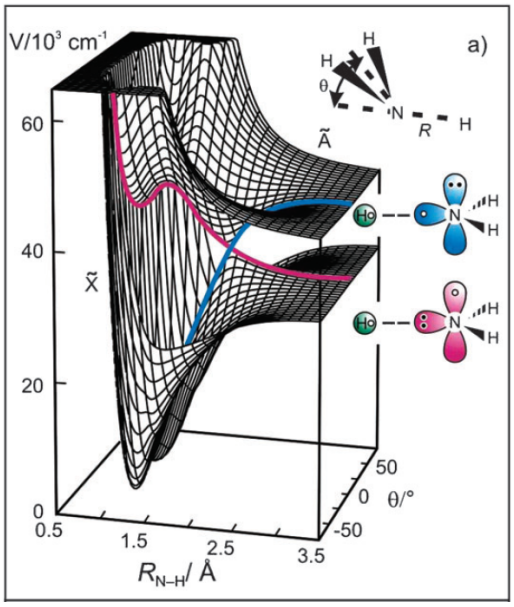

Figure 1.8: The potential energy landscape of the $\tilde{A}(\pi\sigma^*)$ and $\tilde{X}$ states in ammonia. This figure has been adapted from reference [20].

1.2.4 The Franck-Condon Principle

Another crucial concept in spectroscopy is the Franck-Condon (FC) principle [58]. The FC principle can be used to predict the intensity of electronic transitions. First of all, consider a molecule being excited from an initial to an energetically higher lying state by a photon. The change in the electron distribution causes a change in nuclear motion: a vibration. Therefore, electronic transitions are known as *vibronic*, as electronic and vibrational transitions are inherently linked, an effect also known as non-adiabatic coupling. The probability of the vibronic transition taking place is given by

$$P_{i\to f} = |\left\langle \Psi_f^* \right| \hat{\boldsymbol{\mu}} \left| \Psi_i \right\rangle|^2, \tag{1.16}$$

where Ψ_i and Ψ_f are the initial and final state vibronic wavefunctions, respectively and $\hat{\boldsymbol{\mu}}$ is the molecular dipole moment operator given by $\boldsymbol{\mu} = \sum_i q_i \mathbf{r}_i$. Equation (1.16) is the square of the transition dipole moment μ, which gives the intensity of the vibronic transition. The FC principle makes the approximation that the positions of the nuclei (nuclear conformation) only adjust once the electronic transition has taken place [59]. Using this in conjunction with the BO approximation, the vibronic wavefunctions can be separated into electronic Ψ_e and vibrational (nuclear) Ψ_v terms. The transition moment operator is also split into electronic and vibrational terms:

$$\langle \boldsymbol{\mu} \rangle = \langle \Psi_{f,e} \Psi_{f,v} | \, \hat{\boldsymbol{\mu}}_e + \hat{\boldsymbol{\mu}}_v \, | \Psi_{i,e} \Psi_{i,v} \rangle \tag{1.17}$$

where $\Psi_{f,e}$ is the electronic wavefunction of the final state and $\Psi_{i,e}$ is the electronic wavefunction of the initial state (the same holds true for the vibrational part). Since the electronic transition dipole moment is only dependent on the electronic wavefunction and the vibrational one only on the vibrational (nuclear) wavefunction they can be separated:

$$\langle \boldsymbol{\mu} \rangle = \langle \Psi_{f,e} | \, \hat{\boldsymbol{\mu}}_e \, | \Psi_{i,e} \rangle \, \langle \Psi_{f,v} | \Psi_{i,v} \rangle + \langle \Psi_{f,v} | \, \hat{\boldsymbol{\mu}}_v \, | \Psi_{i,v} \rangle \, \langle \Psi_{f,e} | \Psi_{i,e} \rangle \tag{1.18}$$

where the $\langle \Psi_{f,e} | \Psi_{i,e} \rangle$ term is zero due to the orthonormality of the electronic states. Hence, the intensity of an electronic transition is dependent only on the first term in Equation (1.18). The square of the overlap integral between the initial and final vibrational wavefunctions $| \langle \Psi_{f,v} | \Psi_{i,v} \rangle |^2$, often denoted S, is the Franck-Condon factor. This factor determines whether the electronic transition will have any intensity: when the overlap between initial and final vibrational wavefunction is zero, the transition will not be observed.

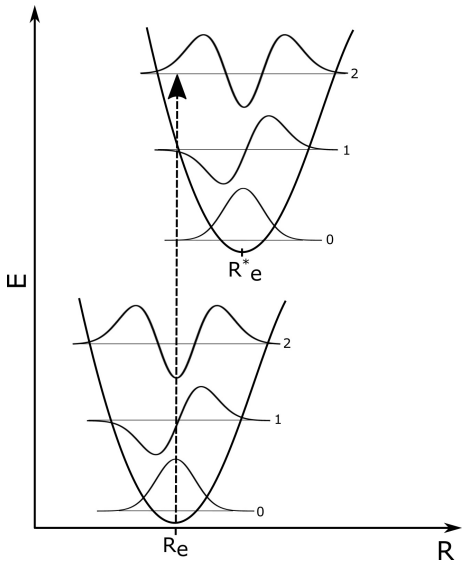

Figure 1.9: An illustration of the basis of the FC principle. E indicates the energy and R is the internuclear coordinate, or bond length in this example.

This is best illustrated using an example of a simple diatomic molecule with internuclear distance R. The potential energy curves of the electronic ground state and one electronic excited state of such a system are shown in Figure 1.9. If an electron is now excited from the ground state (electronic and vibrational), the FC factor S can be used to predict in which vibrational state of the excited electronic state the transition is most likely found after excitation. Since the FC principle states that any changes in the nuclear geometry take place after the electronic transition, R_e must remain constant during it. Thus a vertical line connecting the ground and excited state as shown in Figure 1.9 represents what is known as a *vertical transition*. A non-zero overlap between the vibrational wavefunctions of the initial and final states is obtained when the third vibrational level in the excited state is reached, indicating that this transition is highly probable to occur.

1.3 Spectroscopic Techniques

Photoelectron spectroscopy is based on the interaction of matter with light and provides insight into the electronic structure of the molecule. In photoelectron spectroscopy a sample is ionised using a photon of high-energy and the kinetic energy of the ejected electron is subsequently recorded. The resulting spectrum is a plot of the number of electrons detected against their kinetic energy, and may also be plotted in terms of binding energy. A notable example of this is the work of Turner and Jobory performed in 1962, where the researchers first used photoelectron spectroscopy to determine ionisation potentials in molecules, which could previously only be found using threshold techniques [60]. Photoelectron spectroscopy can be carried out using vacuum ultraviolet and x-ray sources and on solid, liquid or gas-phase samples [61, 62]. This can then be extended to pump-probe methods, where two light pulses are used, one to excite the molecule and the second to ionise it. This principle can be employed in frequency- and time-resolved approaches. An example of a frequency-resolved approach is resonance enhanced multiphoton ionisation (REMPI) [63, 64]. In REMPI, the molecule of interest is initially excited using a stepwise excitation through resonant states. By scanning the wavelength of the laser continuously, while detecting the ions produced, a spectrum of all accessible excited states of the molecule is produced [65]. As mentioned earlier when discussing the concept of the "arrow of chemistry", such methods can provide detailed information on the initial reactants or final photoproducts, but fail to map the pathways linking reactant and product. Information on the dynamics of the redistribution of energy within the molecule is only revealed when time-resolved methods are employed.

Time-resolved photoelectron spectroscopy is the main method of investigation used in this thesis. The very first time-resolved photoelectron spectroscopy (TRPES) [15] studies were carried out in the mid 1980s using pico-second pulses to examine the dynamics of electrons in semiconductor surfaces [66]. In TRPES the molecule is initially excited using one photon (the pump) and subsequently ionised with a second (the probe). The ejected electrons are then detected. The initial pump pulse prepares a wavepacket in the excited state (as discussed earlier) which is then projected onto the final state with the second pulse. Time-resolution is achieved through a variable time delay between the initial exciting and subsequent ionising photons. Since temporal resolution is crucial, femtosecond pulses are used in this technique. These are temporally very short, but due to the time-bandwidth product, they are broad spectrally (see Chapter 2 for more detail) and hence the spectra will not be as well resolved in energy as with a non time-resolved methods where, for example, nanosecond pulses can be used.

The main observable measured in TRPES experiments is the kinetic energy of the ejected electron, which is recorded as a function of pump-probe delay. As was already indicated in Figure 1.5 in Section 1.2.1, the kinetic energy of the ejected

electron will vary with pump-probe delay as the dynamics proceed. The maximum kinetic energy of the photoelectron (pKe) emitted must be equal to the difference between the total energy of both the pump and probe photons and the ionisation potential (IP) of the molecule. Mathematically this can be expressed as

$$pKE = (h\nu_{\text{pump}} + h\nu_{\text{probe}}) - IP, \tag{1.19}$$

where ν_{pump} and ν_{probe} are the frequencies of the pump and probe pulse, respectively.

The wealth of information revealed by photoelectron spectra can be illustrated using the example of all-*trans* 2,4,6,8-decatetraene, as reported by Blanchet *et al.* in 1999 [67]. The authors used time-resolved photoelectron spectroscopy to examine ultrafast internal conversion in the linear polyene which, similar to rhodopsin reviewed at the start of this chapter, displays *cis-trans* photoisomerisation. The S_2 state was excited using a 287 nm femtosecond pulse and a 235 nm pulse was subsequently used to probe the dynamics. From the initially excited S_2 state the population is transferred to S_1 through an ultrafast internal conversion process, which can be observed in the photoelectron spectrum shown in Figure 1.10 (b).

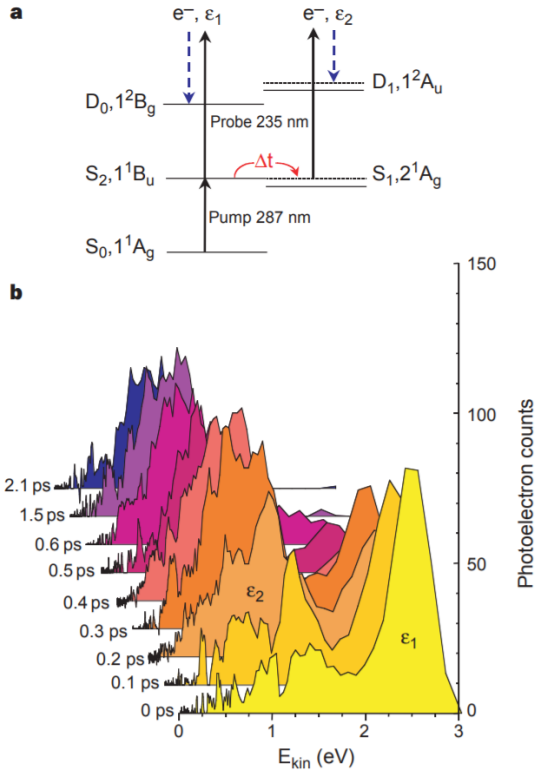

Figure 1.10: A typical photoelectron spectrum from a TRPES experiment along with a schematic outlining the excitation and relaxation processes leading to the observed photoelectron bands. The data shown here is of all-*trans* 2,4,6,8-decatetraene and the figure has been adapted from reference [67].

The spectrum clearly shows the reduction in intensity of band ϵ_1 accompanied by a simultaneous increase in the intensity of the lower-energy band ϵ_2, as the pump-

probe time delay grows. Such a shift in intensity indicates the transfer of population from the higher-lying S_2 to the lower-lying S_1 excited state. There is however, also an evolution of the electronic symmetry taking place. As the schematic in Figure 1.10 (a) shows, the ϵ_1 band originates from the ionisation of the S_2 state into the D_0 state of the cation, whereas the ϵ_2 signature is due to ionisation of S_1 to D_1 in the cation. Both of these processes show a change in symmetry of the electronic states (again, shown in the schematic) and also illustrate the concept of Koopmans' correlations, which will be outlined below. Furthermore, vibrational structure can be observed in the spectrum, indicating that intramolecular vibrational redistribution occurs as part of the relaxation dynamics in this system. A further advantage of time-resolved photoelectron spectrocopy is that even optically dark states can be detected, if the population is transferred to them from the initially excited state. Although, the Franck-Condon principle may limit the states that are observable as will be discussed in Section 1.4.

As was commented on earlier, the observation of population moving between two electronic states, as shown in the example spectrum in Figure 1.10, highlights another important concept in time-resolved photoelectron spectroscopy: *Koopmans' correlations*. The selection rules in photoelectron spectroscopy are not strict: there are no constraints on which molecular state can be ionised, as long as it is energetically achievable. However, the Koopmans' Type I and Type II correlations dictate that certain configurations may be preferentially ionised. Koopmans' picture assumes that there is no instantaneous rearrangement of the core electrons when an independent outer-shell electron is removed. Koopmans' correlations Type I indicate that the probability of photoionisation is related to the type of orbital from which the electron is removed. If, after the outer electron has been removed, the electronic configuration in the neutral molecule matches that of the cation, there is an increased probability for photoionisation to occur, compared to the case where these configurations differ. An illustration of this concept is provided in Figure 1.11. Returning to the study of 2,4,6,8-decatetraene, the correlations allow the change in population from the ϵ_1 band (S_2 state) to the ϵ_2 band (S_1 state) in Figure 1.10 [67] to be observed, as the S_2 and S_1 electronic states in the neutral species correlate to different states in the cation. Koopmans' correlations Type II [68] on the other hand, are related to effects observed when the photoionisation of two different excited electronic states result in the same cation state (illustrated in the right-hand panel of Figure 1.11). Such a process results in two overlapping photoelectron bands and consequently the states cannot be distinguished using the spectrum alone. They might still be discerned, however, if they have different Franck-Condon factors [69] or using photoelectron angular distributions, as will be discussed below. For an extended discussion of the Koopmans' picture see reference [15].

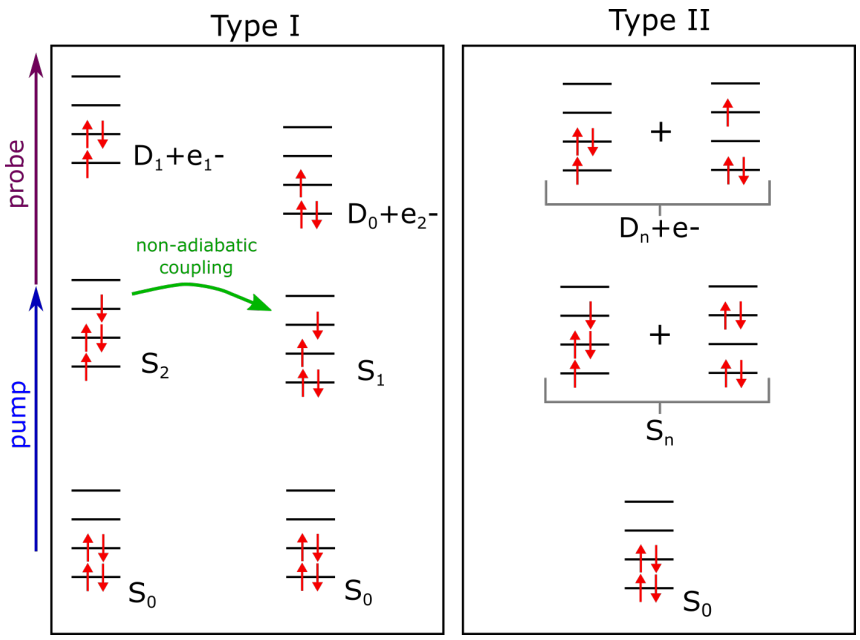

Figure 1.11: Examples of configurations involved in Koopmans' correlations Type I and Type II. The configurations for Type I shown aim to illustrated the process observed in the photoelectron spectrum shown in Figure 1.10.

To add further observables to the TRPES experiment, imaging techniques can be used. An example is the velocity map imaging (VMI) technique, which is discussed in detail in Section 1.3.1. Adding a two-dimensional detection technique advances TRPES to time-resolved photoelectron imaging (TRPEI) [11]. This creates access to an additonal observable: the photoelectron angular distribution (PAD) [11, 70–72]. The PADs reveal the anisotropy of the distribution of the ejected electrons, which provides additional information on the state from which the photoelectrons have been ejected. They rely on the notion that the wavefunction of the photoelectron can be described using a combination of spherical harmonic functions ($Y_{lm}(\theta, \phi)$). The labels l and m represent the orbital angular momentum and lab-frame projection quantum numbers, respectively. These are limited (through vector combinations) to $|l - l'| \leq L \leq l + l'$ and $m + m' = M$, where l' and m' are quantum numbers of the complex conjugate of the wavefunction. Using symmetry arguments [73] the PADs can then be expressed as

$$I(\theta, \phi) \propto \sum_{L=0}^{L_{max}} \sum_{M=-L}^{L} B_{LM} Y_{LM}(\theta, \phi). \tag{1.20}$$

Here, the B_{LM} coefficient is dependent on the order of the photoionisation process and several other factors including the polarisation and energy of the pulse used to ionise the molecule. Another factor is the orbital from which the electron has originated [14, 71, 71, 72]. For states of Rydberg character, the approximation can be made that if the photoelectron was ejected from a state with s-type orbital

character, a distribution of photoelectrons reflecting p-type orbital character would be observed (due to the conservation of angular momentum: $\Delta l = \pm 1$), which is in turn reflected in the *anisotropy parameters*. This is however, only an approximation and low signatures of other partial waves are also observed as demonstrated by Leahy, Reid and Zare in a time-of-flight photoelectron spectroscopy experiment on NO ionised using a REMPI scheme [74].

In 1967, Cooper and Zare [70] outlined the concept of the angular distribution of electrons in a similar manner. They proposed that, for linearly polarised light, the photoelectron differential cross section σ has the following angular distribution:

$$\frac{d\sigma}{d\Omega} = \frac{\sigma_t}{4\pi}[1 + \beta P_2 \cos\theta], \tag{1.21}$$

where P_2 is the second Legendre polynomial, σ_t the total cross section and θ describes the angle between the directions of the polarised light and the ejected electron. The β term was labelled the *asymmetry parameter* (or *anisotropy parameter*) and is related to the angular momentum quantum number, l, which in turn depends on the shape of the orbital from which the electron is ejected. Returning to Equation (1.20), the B_{LM} terms can be converted into the β parameters by normalising the expression using B_{00}, which is integrated over all angles. The above expression and the relation of the β parameters to the photon order of the ionisation processes will be discussed further in Section 2.5.1 of Chapter 2. The temporal and spectral changes of the anisotropy parameters can be extracted and evaluated which will then provide information about the evolution of the observed states. A more detailed discussion of the anisotropy in VMI images, the anisotropy parameters and how they are extracted can also be found in Chapter 2.

Now that the TRPES technique and all its observables have been outlined in detail, the next few paragraphs will provide a brief discussion of selected experimental methods which can offer complimentary information in completing the mapping of the "arrow of chemistry". REMPI was already discussed earlier, as a tool used to characterise the starting and asymptotic end points of a photochemical reaction but there remain parts of the reaction that are unexplored. Information on radiative relaxation processes such as fluorescence and phosphorescence, any active vibrational modes or detailed knowledge of the evolution of the electronic structure of the molecule are not elucidated. Additional techniques including laser-induced fluorescence (LIF) imaging, transient absorption techniques and gas-phase electron diffraction are required to provide further insight, as understanding every aspect of the complete chemical reaction requires a joint effort.

LIF is a very established method, having been developed in the 1960s. It is based on measuring the natural fluorescence of the systems under study and is known to produce very good signal to noise ratios [75]. The systems are initially excited and the relaxation process is studied by monitoring the fluorescence emitted.

Here single-photon counting methods can be used to detect the fluorescence in time-resolved experiments with picosecond resolution [76, 77]. Due to the nature of this method, non-radiative processes can, however, not be observed.

Transient absorption spectroscopy also uses a pump-probe approach [78]. A molecule is initially excited and subsequently a low intensity white-light probe pulse passes through the sample (after a set time-delay). Typically, a difference absorption spectrum is then produced, which is based on the difference between the absorption spectrum of the molecule in the ground state versus that in the excited state. The transient absorption spectroscopy method can be expanded into "two-dimensional" (2D) transient absorption methods. These are more differential as they can provide information on the nature of coupled modes. These may be vibrational coupled modes, interrogated using 2D infrared (IR) methods [79], or electronic coupling (2DES) [80]. The 2D methods employ a configuration of three laser pulses, the time-delays between which are all varied. This method yields a frequency correlation spectrum providing structural but also dynamical information.

Electron diffraction of molecules in the gas-phase can also be carried out in a time-resolved manner [81, 82]. This gives insight into the structural changes a molecule will undergo upon excitation and during the subsequent relaxation processes. The method uses a beam of electrons to probe the structures, much like the early method used on solid samples. These experiments, originally only possible at accelerator facilities, are now also starting to be realised in non-centralised facilities [83].

1.3.1 Velocity Map Imaging (VMI)

Photoelectron imaging techniques provide a new level of information due to the use of a two-dimensional detector, which provide a way of determining the internal energy as well as the velocity of a charged particle simultaneously. Such a simultaneous measurement using a 2D-detector setup was first performed by Chandler and Houston in 1987 on CH_3I [84]. They projected the 3D-spatial distribution (known as a Newton sphere) of methyl photofragments onto a 2D-detector surface using a repeller electrode in combination with a grounded grid. This technique has become known as charged particle imaging and differs from the Wiley and McLaren setup [85] which instead has a pair of grid electrodes (extractor and ground). It is however, limited in resolution as the projection is affected by the birthplace of the charged fragment, washing the signals out and blurring the image. This limitation is addressed by the velocity map imaging (VMI) technique, first conceived by Eppink and Parker in 1997 [86]. It is very much based on the work by Chandler and Houston, but information about the point in space where the charged particle is born is eliminated. The fine metal grids, originally used to create the homogeneous electric fields, were removed and instead two open, annular electrode rings were used

for focusing the charged particles. This test, born out of frustration with the metal grid [87], resulted in a much improved image quality. All particles with equal initial velocity were now being focused onto the same region of the detector, resulting in sharp and defined rings. An example of this is illustrated in Figure 1.12, which shows two ion images of O^+ recorded by Eppink and Parker in 1997. Image (a) is the result obtained using the fine mesh grid, whereas (b) shows the improvement on the image with the electrostatic imaging lens. The image is significantly less blurred and a multitude of sharp, concentric rings are now observable.

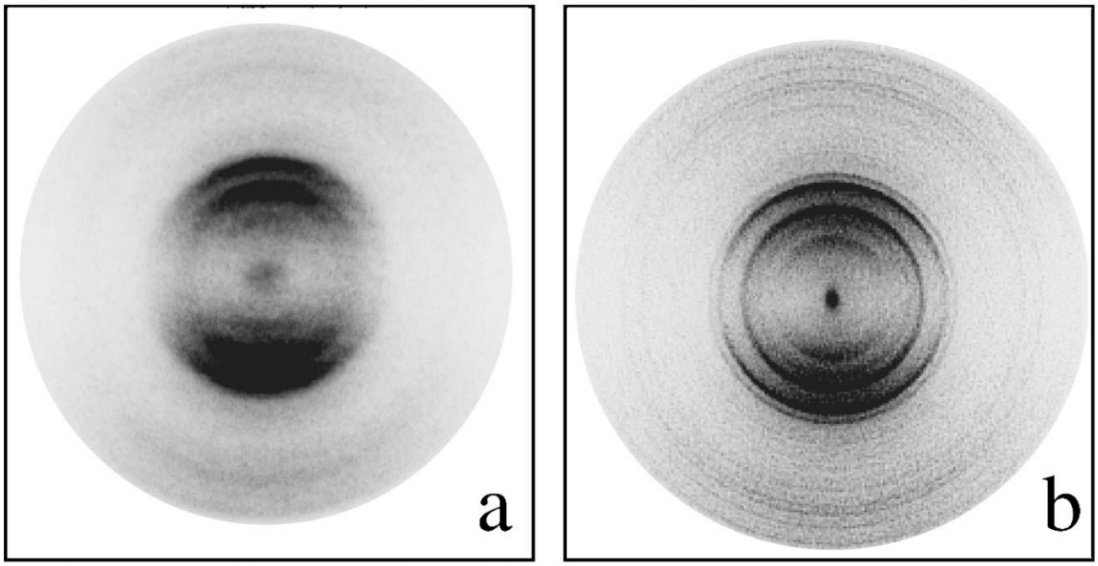

Figure 1.12: Ion images of O^+ excited using 255 nm and focused using (a) a fine mesh grid (b) an imaging lens. This figure has been adapted from reference [86].

An electrostatic lens setup (ion optics) consisting of three electrodes is used in order to map all particles with the same initial velocity onto the same point on the detector. The initial repeller electrode is followed by an extractor electrode and a final grounded plate as illustrated in Figure 1.13. This type of VMI setup is used for the work presented in later chapters of this thesis (see Chapter 2, Section 2.4.1 for detailed description). Such a VMI electrode setup can be used to focus both ions and electrons. The ratio of the voltages between the repeller and lens/extractor electrodes is of importance as it controls the focusing conditions. This basic VMI electrode setup can be extended to perform DC slice imaging [88], which removes the need for image-processing to recover the original 3D distribution. This method is, however, suitable only for ions. For more details on velocity map imaging and related techniques, the reader is referred to a recent review of the development of advanced charged particle imaging methods by Chandler, Houston and Parker [87].

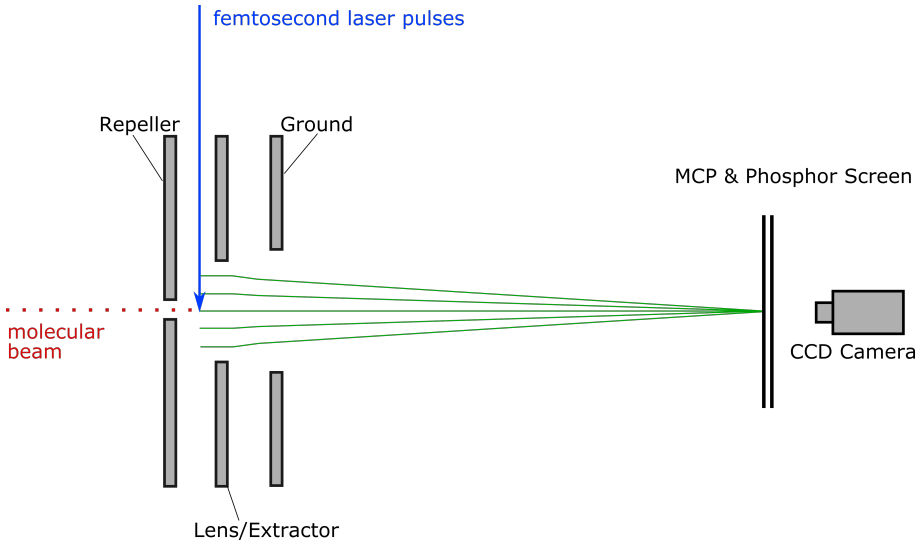

Figure 1.13: A schematic of a typical velocity map imaging setup. Three electrodes are used to accelerate and focus the charged particles in the interaction region onto a detector. Using this method any charged particles with the same initial velocity will be mapped onto the same point on the detector, as indicated by the trajectories (green).

As the 3D distribution is 'flattened' when it is projected onto the detector, it is necessary to extract the 3D information once the image has been acquired. To extract the 3D distribution, it is assumed that the distribution possesses a cylindrical symmetry where the axis of symmetry is parallel to the face of the 2D detector. In order to fulfill this assumption, one must be careful with the polarisations of the laser pulses used, as these must also be parallel to the detector as well as to each other. If the detector lies in the (y, z)-plane (with z being the symmetry axis), the projection of the 3D distribution, $I(x, y, z)$, onto the image plane is given by

$$P(y, z) = \int_{-\infty}^{\infty} I(x, y, z) dx. \tag{1.22}$$

Typical image-processing methods used to recover the 3D distribution are based on using the Abel transform. Strickland and Chandler introduced the use of the Abel transform for reconstruction of these images in 1991 [89]. It is useful to treat the above expression in cylindrical coordinates, in order to compare it to the Abel transform. The radius ρ in cylindrical coordinates can be expressed as $\rho = \sqrt{x^2 + y^2}$ and therefore $dx = \frac{\rho d\rho}{\sqrt{\rho^2 - y^2}}$. Using this the projection of the electron cloud can now be expressed as:

$$P(y, z) = \int_{y}^{\infty} \frac{I(x[y, \rho], y, z) \rho d\rho}{\sqrt{\rho^2 - y^2}}. \tag{1.23}$$

This is now in a form for which an inverse Abel transform can be used in order to recover the initial $I(x, y, z)$ distribution:

$$I(\rho, z) = \frac{1}{4\pi} \int_r^R \frac{\partial_y P(y, z)}{\sqrt{y^2 - \rho^2}} dy. \tag{1.24}$$

Today, routines including Onion-peeling [90], Polar Onion Peeling [91], the BASEX [92] and pBASEX [93] methods as well as a matrix Abel inversion method [94, 95] are all used for reconstruction of the 3D-distribution. An illustration of the distributions recovered using two of these methods is shown in Figure 1.14 and a detailed comparison of the various reconstruction methods is given in reference [96]. The rapid matrix Abel inversion technique used for the work presented in this thesis is discussed further in Chapter 2, Section 2.5.

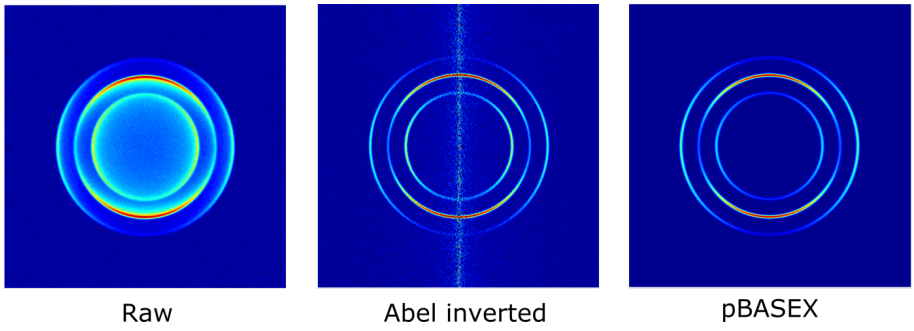

Figure 1.14: The rapid matrix Abel inversion method as well as a pBASEX method have been used here on some simulated data to illustrate the reconstruction of the 3D-particle-distribution from the detected 2D-signal. The images were produced by C. Sparling.

Finally, in order to extract accurate radial information from Abel transformed images, an $(r \sin\theta)$-factor has to be included. This factor weights the signal (S) so that the areas at different radii r become comparable. This is done using the *Jacobian* $(r^2 \sin\theta)$, which describes the area element in spherical coordinates. Using the coordinates as defined in Figure 1.15, the signal can be written as:

$$S(r)dr = \int_0^{\pi} \int_0^{2\pi} I(r, \theta) r^2 \sin\theta d\varphi d\theta dr. \tag{1.25}$$

Integrating over the angle φ (which is symmetric) gives

$$S(r)dr = 2\pi r \int_0^{\pi} I(r, \theta) r \sin\theta d\theta dr. \tag{1.26}$$

The number of pixels on the detector between a radius r and $r + dr$ is proportional to the $2\pi r dr$ factor so the following remains:

$$S(r) = \sum_{r, r+dr} f(r, \theta) r \sin\theta, \tag{1.27}$$

which is discrete as pixels are now being considered. This weighting means that at any radius r the amount of signal is now accurately represented, i.e. the noise along

the centre line, as seen in the Abel inverted image in Figure 1.14, is now removed. It was initially extremely large, as it is associated with the central slice through the spherical particle distribution.

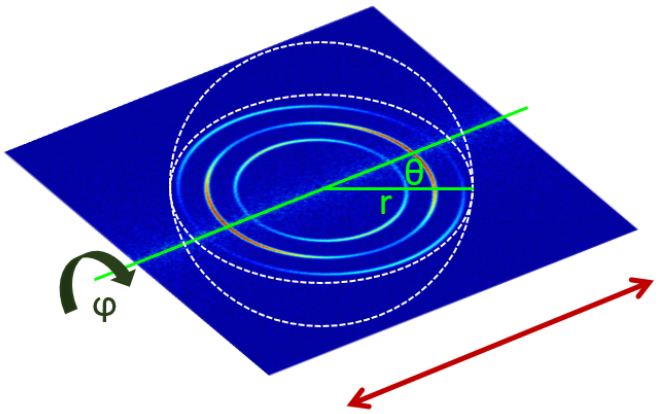

Figure 1.15: Schematic of the coordinates used to illustrate the need for a weighting factor for the radii obtained from an Abel inverted image. The red arrow indicates the laser polarisation direction.

1.3.2 Molecular Beams

In nature biologically relevant molecular systems are typically found in solution. The presence of the solvent will, however, obscure the dynamics of the system of interest and often leads to a much more challenging analysis and interpretation of results. By studying the molecules of interest in the gas-phase, such obscuring signals are removed. Furthermore, much more differential techniques can be used with gas-phase samples, allowing for the deconvolution of various processes and resulting in a deeper understanding of the underlying photochemical processes.

A common method for introducing molecules into the gas phase is the molecular beam [97–99]. A carrier gas (often a noble or other inert gas) is passed over a solid or liquid sample. The resulting mixture of sample and inert carrier gas is then expanded through a narrow orifice (nozzle) into vacuum, during which the mixture is cooled by *supersonic expansion* which results in a beam of internally cool molecules [100]. As the high-pressure region containing the sample is separated by an orifice from a region of very low pressure, the mean free path in the gas is lower than the size of the nozzle. The molecules therefore undergo a multitude of collisions before escaping into the low-pressure region. The translational temperature in the molecular beam after supersonic expansion is given by [101]

$$T = T_0 \left(1 + \frac{\gamma - 1}{2} M^2\right)^{-1}. \tag{1.28}$$

Where, T_0 is the initial temperature or stagnation temperature, which is where the kinetic energy of the molecules is zero but the internal energy is high. The ratio

of the heat capacity at constant volume to that at constant pressure is given by γ. Finally, M is the local Mach number which describes the ratio of free-stream flow to the local speed of sound.

This process cools the sample rapidly to extremely low temperatures of a few tens of kelvin. The result is a beam of very cold, individual molecules of sample and carrier gas. It is important to check for the presence of clusters of molecules, as these are not desirable in the TRPEI experiments presented here. This can be done using the ion mode of the TRPEI spectrometer which, in combination with the time-of-flight tube, can be used as a mass spectrometer. This method is used in the work presented in this thesis, in combination with an Even-Lavie (EL) pulsed valve [102]. The EL valve produces short pulses of molecular beam, the timing of which can be adjusted such that the molecular pulses arrive in the interaction region at the same time as the laser pulses. A further advantage of using an EL valve is the reduction of sample usage which leads to a lowering of the pumping requirements for the vacuum system. The experimental setup is discussed in more detail in Chapter 2.

There are various other methods available for producing samples in the gas-phase. These include electrospray ionisation [103–105], laser desorption techniques and helium nanodroplets [106]. One limitation of the molecular beam is that samples with low vapour pressure (often the case for larger molecules) will not be picked up by the carrier gas. Electrospray ionisation and laser desorption methods both address this issue. Electrospray ionisation disperses the sample into a charged aerosol using a capillary in combination with a charged nozzle. Laser desorption methods on the other hand can provide neutral species, depending on the method employed. The main methods are: direct laser desorption/ionisation [107], matrix-assisted laser desorption/ionisation (MALDI) [108] and laser-induced acoustic desorption (LIAD) [109]. In direct laser desorption the sample is ionised directly using a laser pulse, whereas the MALDI method uses a matrix-crystalline structure into which the sample has been dissolved, making it less likely for the sample to fragment. Finally, LIAD works by placing the sample onto a thin metal foil and irradiating the back of this foil, which results in neutral gas-phase molecules. This method is discussed in detail in the Future Work section of Chapter 7. Finally, nanodroplets can also be used to produce cold molecules. By passing nanodroplets of helium through vapour of sample, the sample is picked up and cooling takes place when the nanodroplets evaporate and leave behind low temperature sample [106].

1.4 Beyond Ultraviolet

In TRPEI experiments, the choice of wavelength for both pump and probe determines the dynamics that can be observed. For the pump pulse to be absorbed, its wavelength must correspond to an optically bright excited state of the system under investigation. Such states can often be determined using absorption spectra, typically in the UV-Visible range. There are however, many smaller molecules, such as ethers, alcohols and small amides, which have a tendency to absorb at shorter wavelengths near or in the vacuum UV (VUV) spectral region (below 200 nm). Therefore, the capability to produce such short wavelengths and subsequently employ them as pump pulses, greatly extends the number of molecular systems that can be studied. One specific example is formamide, studied in Chapter 6, which displays a strong absorption peak centred just above 170 nm.

The probe wavelength on the other hand, determines which cation states can be reached after ionisation, or in other words, how deep it can project into the ionisation continuum. In order to exploit the complete potential of the TRPEI technique a suitable choice of probe-wavelength is vital. Using a high-energy probe in the VUV region extends the observation window along the photochemical reaction coordinate(s). Ideally, the probe should be energetic enough to reveal the whole dynamical process, from initial excitation to the recovery of the ground state or formation of photoproducts. This idea can be illustrated using the example of 1,3-butadiene, the time-resolved photoelectron spectra of which are shown in Figure 1.16.

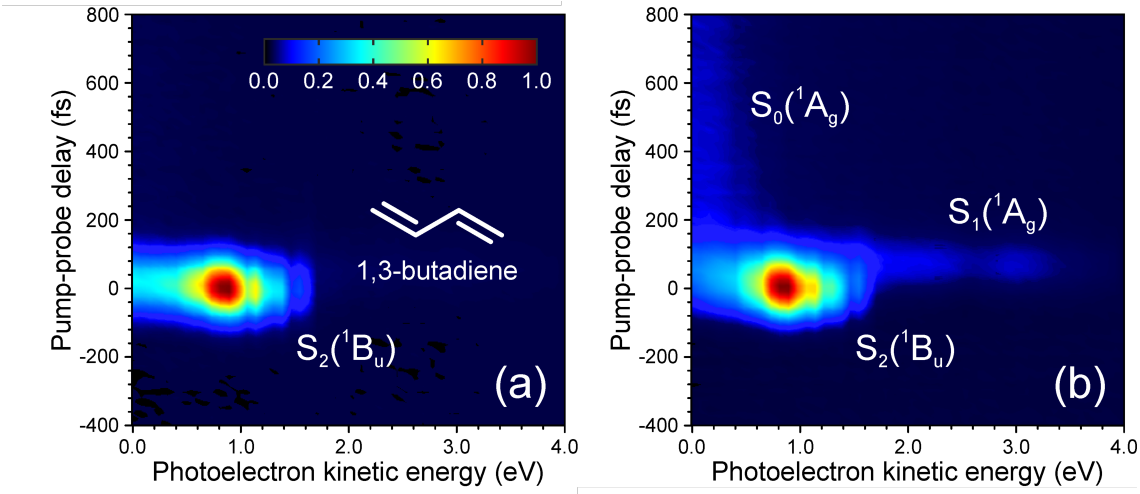

Figure 1.16: Time-resolved photoelectron spectra of 1,3-butadiene recorded using a 267 nm probe at two intensities: (a) 350 nJ and (b) 2.5 μJ. Increasing the intensity alters the process from (1+1′) shown in (a) to a (1+2′) process shown in (b) and more dynamics are revealed.

The TRPES shown are of 1,3-butadiene excited using a pump at wavelength 200 nm and ionised with a 267 nm probe, which was varied in intensity. The photo-

electron spectrum of the initial excitation using a lower probe energy ($\sim$ 305 nJ) is shown in Figure 1.16 (a). It exhibits a very short lived feature ($<$ 100 fs lifetime) which is assigned to the radiationless decay of the initially excited $S_2(^1B_u)$ state. By increasing the energy of the probe pulse from 350 nJ to 2.5 μJ the pump-probe process is altered as there is now a significant contribution from two-photon ionisation (a (1+2′) process). Due to the higher available energy, additional information is revealed, resulting in a more 'complete view' of the relaxation dynamics, as is shown in Figure 1.16 (b). The initial decay of $S_2(^1B_u)$ is still observed, but previously undetected features are now also present. One newly revealed dynamical signature manifests as the extremely short-lived feature between 1.7 eV and 3.4 eV. This can be assigned to the decay of the $S_1(^1A_g)$ state. Furthermore, a longer-lived band at low photoelectron kinetic energies ($<$0.5 eV) is now observed, which can be attributed to ionisation from the vibrationally excited $S_0(^1A_g)$ state. Population is transferred to this state from the rapidly decaying $S_1(^1A_g)$ state.

The (1+1′) process shown in (a) should also be energetically sufficient to ionise the $S_1(^1A_g)$ state. The therefore perhaps surprising absence of any $S_1(^1A_g)$ signature in (a) can be explained using the Koopmans' correlations and Franck-Condon (FC) principle discussed earlier in this Chapter. In the (1+1′) process, the $S_1(^1A_g)$ state can be ionised to the D_0 cation state, however only the lower vibrational levels of this state can be reached where the FC overlap is not sufficient to produce a measurable signal. With the (1+2′) scheme, the cation states can be accessed more efficiently due to a better FC overlap. Additionally there is now the possibility of ionising into the $D_1(^2A_u)$ state. This highlights how short-wavelength probes are able to lift the restrictions imposed by a lack of energy and extend the 'view' of the relaxation dynamics.

Using two photons of a longer wavelength (eg. 400 nm) to achieve a higher energy can, however, be disadvantageous as this can result in signals arising from intermediate resonant states, which will convolute and complicate the photoelectron spectra. Moreover, the signals from the (1+2′) processes shown in Figure 1.16 are very weak as the ionisation cross-section of this process is significantly lower than that of the (1+1′) process. Signals from both the (1+1′) and (1+2′) processes can also not typically be spectrally resolved, although a recent photoelectron-photoion coincidence spectroscopy study has aimed to address this issue [110]. Nevertheless, multiphoton ionisation is a valid option for increasing the probe-energy in order to "see further" along the reaction coordinate. In Chapter 5 of this thesis, both (1+2′) and (1+3′) processes were used to investigate the relaxation dynamics of nitrobenzene and its methyl-substituted derivatives with a 400 nm probe. Care was taken to ensure no resonant intermediate states were present as signal arising from them would lead to the convoluted spectra mentioned above. When such states are successfully avoided, multiphoton ionisation can be used to efficiently extend the observation window. It is however, desirable to employ probes in the VUV region

as they are able to increase the scope and universal utility of ionisation-based time-resolved spectroscopy experiments for a broad assortment of molecular systems. In this thesis, such VUV wavelengths were used as the probe for the investigation of the ultrafast relaxation dynamics in acetylacetone, discussed in Chapter 4 but also as the pump to study small amide systems as outlined in Chapter 6.

A detailed discussion of how the VUV pulses employed in this thesis were achieved, using four-wave difference-frequency mixing (FWDFM), in a noble gas is presented in Chapter 2, Section 2.3.2. Using a commercially available table-top femtosecond infrared (IR) laser system to produce the VUV pulses creates several experimental challenges. Visible and UV wavelengths (400 nm or 267 nm) are routinely produced from the IR output using common birefringent crystals such as β-barium borate (BBO) (again, see Chapter 2 for more details). For the production of VUV pulses however, these are not a viable option as phase-matching restrictions and bandgap absorption prohibit the conversion to such low wavelengths. There are new nonlinear materials such as $KBe_2BO_3F_2$ [111], that do allow for the generation of VUV wavelengths but these are still limited to 150 nm. Noble gases, as used here, can also be employed to produce VUV wavelengths through high-harmonic generation [112–117], which are quite challenging experiments requiring relatively complex experimental infrastructure. Other available options for providing tunable VUV pulses are free electron laser sources at central user facilities [118, 119], which do, however, limit the experimental runtime. Finally, the group of D. Townsend in collaboration with the Laboratory of Ultrafast Optics and Physics (LUPO) led by J. C. Travers at Heriot-Watt University have recently demonstrated the use of hollow-core photonic crystal fibres (HCPCFs) as a source for UV pump-pulses in a TRPEI study on styrene [120]. This method may be improved upon in future to produce VUV pump and probe pulses. A more detailed description can be found in reference [120], and the subject is explored further in the final chapter of this thesis (Conclusions and Future Work, Chapter 7).

Short-wavelength pump and probe pulses have been used by various groups to study ultrafast molecular dynamics. This includes work done by the group of R. S. Minns, who have used a monochromated high-harmonic generation source to produce VUV light (ca. 87 nm, 25 fs) which, in combination with strong-field dissociative ionisation, was used to study vibrationally excited D_2 [121]. They furthermore observed the complete dissociation dynamics in CS_2 using extreme UV (EUV) femtosecond light pulses (57.4 nm) to probe CS_2 in combination with photoelectron spectroscopy [114]. The EUV pulses were also generated using high-harmonic generation (HHG) with a reported cross-correlation of 180 fs for the pump and probe pulses. The above experiments were carried out at the Central Laser Facility.

The group of T. Suzuki has reported studies using short-wavelength light sources, examples being: their investigation of polyatomic molecules using TRPES in combination with vacuum UV pulses produced using HHG [122], or their determination of

the binding energy of solvated electrons [123] achieved using a similar experimental configuration. The group has previously also constructed a source based on a four-wave mixing in neon producing 260 nm pulses which were temporally compressed using a grating-compressor [124]. This work was later extended to a single filamentation cell in which cascaded four-wave mixing occurred in neon, producing deep- and vacuum-UV pulses [125] which were shown to be as short as 17 fs or less [126]. These pulses were then used to study several systems including CS_2 (192-208 nm excitation) [125] and, recently, acetone (ca. 133 nm excitation) [127]. Finally, the group of A. Stolow employed four-wave mixing in a gas-filled cell to produce vacuum UV pulses [128, 129]. Results obtained using the same setup are discussed in Chapter 6 of this thesis, which discusses a collaboration between the Stolow, Sølling and Townsend groups. A detailed description of the experimental configuration will be outlined in that chapter.

1.5 Summary

This chapter has provided an overview of molecular dynamics in the excited state and how these can be studied. Crucial concepts such as the Born-Oppenheimer approximation and Franck-Condon principle were introduced, along with some key radiationless relaxation processes that may be observed. The TRPEI methodology was outlined, along with an explanation of the observables provided by this differential technique. The time-resolved photoelectron imaging method used in this thesis makes use the velocity-map imaging technique, which was discussed in Section 1.3.1, as well as an internally cold molecular beam created by supersonic expansion, outlined in the subsequent section. Finally, it was outlined why there is a need for short-wavelength pump and probe photons in time-resolved photoelectron spectroscopy experiments. The vacuum UV photons can be produced using table top sources, which will be discussed in detail in Chapter 2.

Chapter 2

Experimental Methods

This chapter will give an overview of the experimental methods used in the Ultrafast Dynamics Group at Heriot-Watt University, to obtain the results presented in Chapters 5 and 4 of this thesis. The methods used to record the data in Chapter 6 were similar to that in Chapter 5, but experiments were conducted at the National Research Council Canada in Ottawa (see Chapter 6 for details).

In order to resolve the ultrafast relaxation dynamics of model chromophores, light pulses on the same timescale are required. Therefore, an ultrafast laser system is an essential part of the experimental setup. A brief outline of the basics of ultrafast lasers and the laser setup will be discussed in the first section of this chapter. As already outlined in Chapter 1, the majority of model chromophores absorb light in the ultraviolet (UV) region of the spectrum and the pulses used for ionising the initially excited sample are also required to be in the UV or even the vacuum UV (VUV). Specifically, for the work presented in this thesis, UV wavelengths of 267 nm, 400 nm (Chapter 5) as well as VUV pulses of 160 nm (Chapter 4 and 6) were produced and used as pump and probe pulses. The production of these wavelengths is based on nonlinear optical concepts, which are outlined in Section 2.2. How these wavelengths are then produced in the laboratory from the original infrared (IR) output of the pulsed Ti:Sapphire laser system will be outlined in Sections 2.3.1 and 2.3.2. The velocity map imaging (VMI) spectrometer itself and the ultrahigh vacuum (UHV) setup, as well as sample delivery will be discussed in Section 2.4. Finally, an overview of the software and methods used for data acquisition, data processing and analysis will be presented in the last section of this chapter.

2.1 Femtosecond Laser Pulses

A schematic of the laser setup and optical setup, as used for work presented in this thesis, is shown in Figure 2.1. A modelocked Ti:Sapphire oscillator produces ultrashort (femtosecond, fs) pulses at 800 nm which are then amplified by a regenerative amplifier. This setup will be discussed in further detail in the following subsection. The current section will lay out the underlying ideas required for achieving

the production of ultrashort laser pulses.

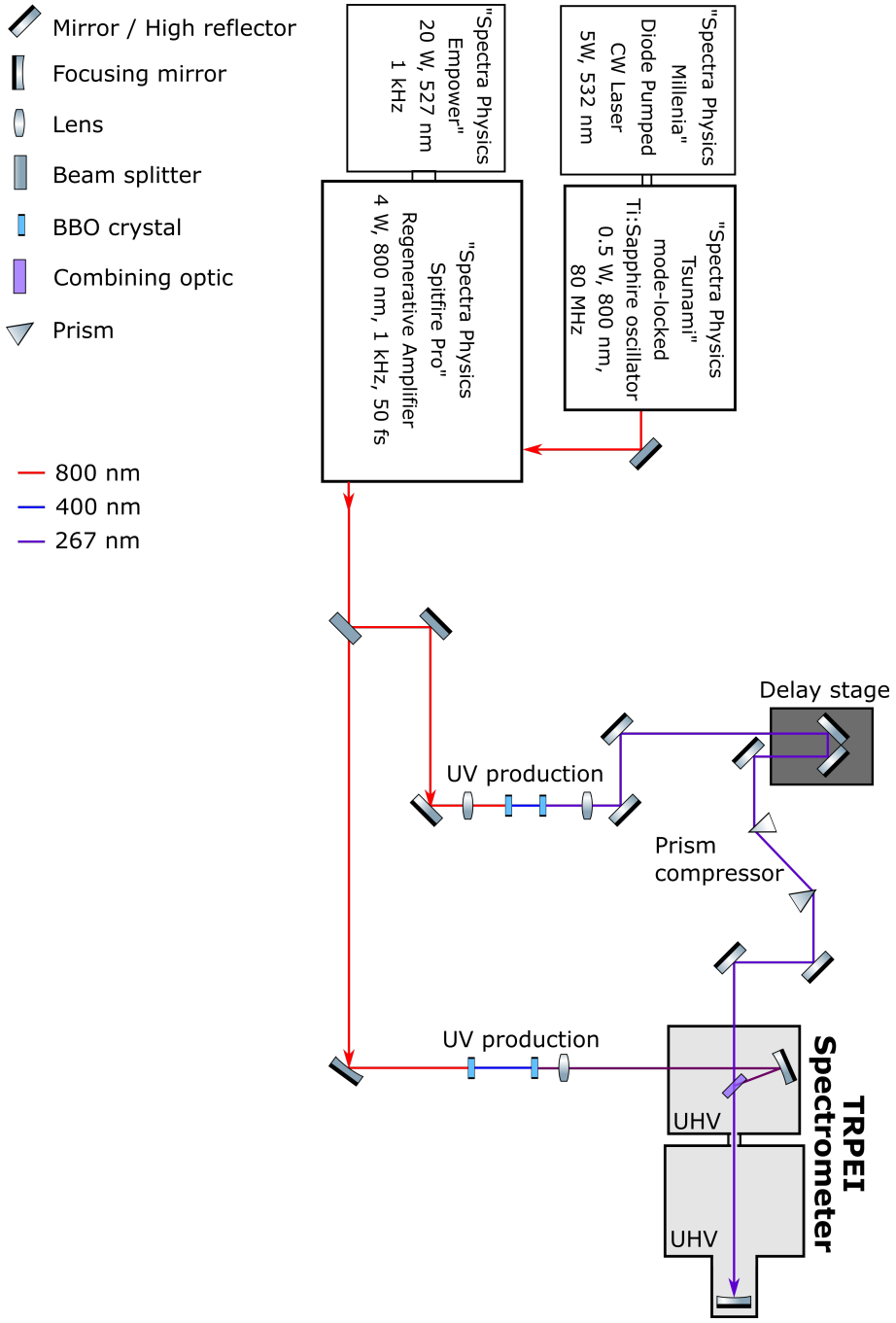

Figure 2.1: A schematic layout of the complete laser setup and a simplified example of a typical optical setup used to produce two different UV wavelengths: 267 nm and 400 nm. In general the 800 nm laser output will be converted to shorter wavelengths using nonlinear optical crystals (more detail in section 2.3). A delay stage, required to introduce the time-delay between the pump and probe lines, and an example prism compressor are also shown.

Ultrashort pulses characteristically display a high peak intensity and broad spectrum [130]. The pulse duration and spectral bandwidth can be related through the

time-bandwidth product, which for a Gaussian pulse is

$$\Delta t \Delta \nu \geq 0.441. \tag{2.1}$$

The pulse is said to be *transform-limited* when this product is exactly equal to 0.441 (for a Gaussian pulse). Such ultrashort pulses can be achieved using the concepts outlined below.

Laser light is produced through an amplification process (stimulated emission) in combination with a feedback loop (oscillator). To provide this feedback a cavity is required. The most basic form of laser cavity consists of two mirrors, with the laser material placed in between. Typically, one cavity end mirror will be 100% reflective whereas the other will be partially reflective, allowing for some light to exit the cavity. As there must be nodes at the cavity end mirrors only longitudinal modes survive inside the cavity. These are the modes which fullfil the relationship

$$\frac{m\lambda}{2} = L, \tag{2.2}$$

where L is the cavity length, λ is the wavelength and m is an integer value. In order to further produce ultrashort pulses, these longitudinal modes have to be locked in phase, a procedure known as modelocking. The pulse duration is dependent on the number of modes oscillating in phase. To produce femtosecond pulses, the number of modes required to be locked in phase is on the order of 10^4 [130, 131].

In general, the techniques used to modelock pulsed laser systems can be divided into two classes: active and passive modelocking techniques. Active modelocking makes use of an external clock source matched to the roundtrip time of the cavity, to generate a signal which modulates the light inside the cavity [131]. In passive modelocking techniques a saturable absorber is used to create the modulation, eliminating the need for an external clock signal as the modulation is, by its own nature, synchronised with the cavity roundtrip time [131–133]. This saturable absorber is commonly a semiconductor saturable absorber mirror (SESAM) [134] but may also be an artificial saturable absorber, an example of which is Kerr-lensing in the gain medium. Kerr-lensing is a third-order nonlinear effect which yields the same result as the saturable absorber. This is the modelocking method used by the Ti:Sapphire oscillator employed at HWU (see Section 2.1.1 for more details). The optical Kerr effect is observed when the refractive index of an optical material becomes dependent on the intensity of the light

$$n = n_0 + n_2 I, \tag{2.3}$$

where I is the intensity and n_0 and n_2 are the refractive index and nonlinear refractive index, respectively. In the cavity the peak intensities are high enough to induce a phase shift (*chirp*) significant enough to result in modelocking through *self-phase modulation* (SPM) or *self-focusing*. SPM is a modulation of the phase of the beam

due to the Kerr effect which leads to a broadening of the spectrum of the pulse. Self-focusing is a nonlinear effect: the intense beam in a nonlinear optical medium will decrease in beam diameter due to varying optical intensities throughout the beam.

These above phenomena of SPM and self-focusing also introduce the concept of chirp. A pulse is said to be chirped when its instantaneous frequency displays a time-dependence. This frequency sweep is caused by a linear effect - dispersion. Dispersion is the temporal broadening of an optical pulse as it travels through a dispersive material, but also refers to the splitting of white light into its component colours when passing through a prism [135]. Dispersion occurs as the refractive index is frequency-dependent which, in turn, varies the phase and group velocities of an optical pulse. The phase velocity v_{phase} represents the speed of the oscillations, whereas the group velocity v_{group} gives the speed of the pulse envelope:

$$v_{\text{phase}} = \frac{\omega}{k} \tag{2.4}$$

and

$$v_{\text{group}} = \frac{d\omega}{dk}, \tag{2.5}$$

where ω is the angular frequency and k the wavevector, and these expressions are true for a propagating wave of the form $\cos(\omega t - kz)$. This is related to the refractive index through k, which can be written as $k = n(\omega)\omega/c$. When the phase velocity varies with frequency (through n) a pulse will exhibit *phase velocity dispersion* (PVD) or *chromatic dispersion*. On the other hand, a frequency-dependent refractive index affects the group velocity, which is known as *group velocity dispersion* (GVD)

$$GVD = \frac{d}{d\omega}\frac{dk}{d\omega} = \frac{d}{d\omega}\frac{1}{v_{group}}. \tag{2.6}$$

This GVD is the cause of the frequency sweep (chirp) of the carrier wave and also leads to a broadening of the pulse envelope. An example of a chirped pulse is shown in Figure 2.2. The instantaneous frequency can be seen to be increasing with time in the pulse illustrated, this is known as an *up-chirp*, whereas a decrease of the frequency with time is known as *down-chirp*.

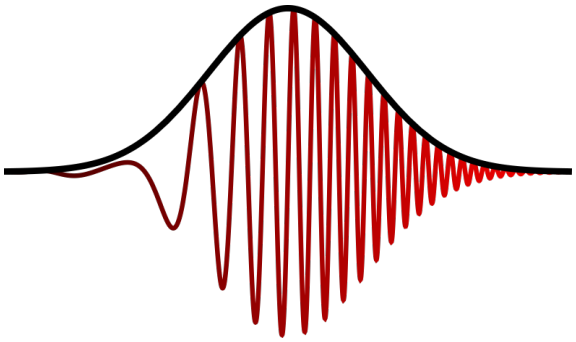

Figure 2.2: Illustration of an *up-chirped* pulse.

A pulse can acquire chirp when it travels through a medium where it experiences chromatic dispersion as just discussed, but also due to nonlinear effects such as SPM described earlier. The Sellmeier equation provides an accurate model of the relationship between the refractive index and the wavelength (or frequency) of an optical material. It is of the form

$$n(\lambda) = \sqrt{1 + \sum_j \frac{A_j \lambda^2}{\lambda^2 - B_j}}, \tag{2.7}$$

where the coefficients A and B are found for each material using nonlinear least squares fitting routines of experimental data. For calcium fluoride (CaF_2) for example, a plot of n vs λ can be used to predict the dispersive properties of CaF_2 at the wavelengths of interest. An example of this is the plot produced by Li [136] shown in Figure 2.3. Similarly, plots of the GVD or the *group time delay dispersion* against wavelength can also be produced. The GVD is related to the second derivative of n with respect to λ and can therefore easily be inferred. This is particularly useful for estimating the most appropriate material to be used for the least GVD at the specific wavelength of choice. As can be seen in Figure 2.3, at wavelengths below 200 nm (in the VUV region), the gradient of the plot steepens rapidly, implying a high GVD.

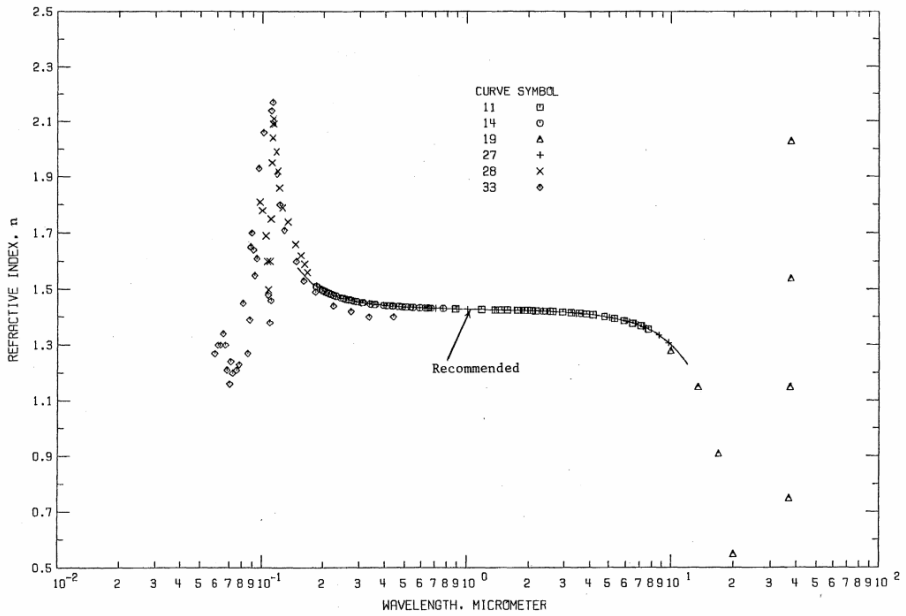

Figure 2.3: A plot of the refractive index vs wavelength for calcium fluoride taken from reference [136]. Different symbols indicate data from other measurements, detailed in reference [136].

The stretching and chirping of the pulse is an unwanted effect as the pulses should be as short as possible to improve the resolution of the time-resolved experiments discussed in this thesis. This is where prism pairs can be used for dispersive compression of optical pulses, reducing the chirp and the pulse duration [137]. Consider Figure 2.4. An input beam is spatially separated when passing through the first prism, the entrance face of which is aligned parallel to the exit face of the second prism. By adjusting the path distance, l, the amount of negative dispersion introduced can be optimised, thereby compensating for any positive dispersion introduced by optical components. In addition to the separation distance of the prisms, the insertion of the prism (its translation perpendicular to the beam path) will also compensate for the positive dispersion by adding more glass into the beam path. This translation of the prisms is often used after adjusting the path distance l to achieve a finer tuning of the prism compressor and to further counteract any positive group delay dispersion. A mirror at the end of this configuration negates the need for two pairs of prisms as the pulses are spatially recombined upon a second pass through the single prism pair.

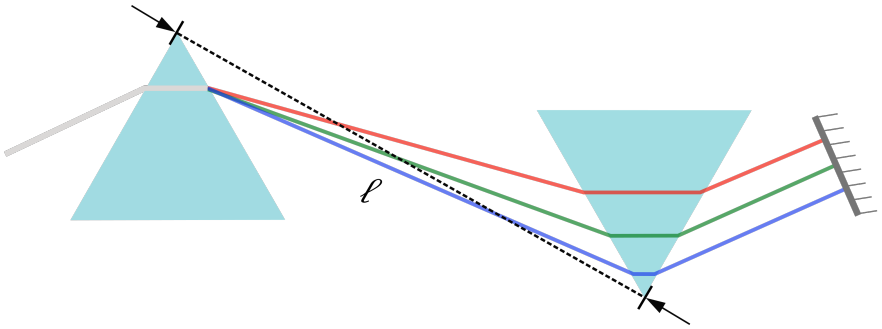

Figure 2.4: A sketch of the effect of a prism pair on the spectral components of ingoing light. The prism compressor shown here is a double-pass setup (due to the mirror), whereas the one employed for work presented here was single-pass, with two prisms.

2.1.1 Femtosecond Laser System

This subsection will outline the laser setup used for the work presented in this thesis (unless stated otherwise). A schematic of the laser system is included in Figure 2.1.

The femtosecond laser pulses are produced by a mode-locked Ti:Sapphire oscillator (Spectra Physics - Tsunami) pumped by a diode-pumped solid-state continuous wave (CW) laser at 532 nm (Spectra Physics - Millennia) with a power of 4 W. The Ti:Sapphire oscillator produces femtosecond pulses centred at 800 nm with a full width at half maximum (FWHM) of 40 nm and at a repetition rate of 80 MHz. The typical output power of this system is 400 mW.

The output from the Ti:Sapphire oscillator acts as a seed input for the regenerative amplifier (Spectra Physics - Spitfire Pro). The pulses are amplified in this system using chirped pulse amplification (CPA)[138], the invention of which has recently been recognised with a Nobel Prize. A schematic of the CPA technique is shown in Figure 2.5. The basic process consists of three steps: initially the ingoing ultrashort pulse is stretched to reduce the peak power; this lower power pulse is then amplified in a laser medium and finally, re-compressed. The result is an ultrashort pulse with increased intensity. The advantage of reducing the peak power of the pulse prior to amplification is that damage to the optical components involved in the amplification process is prevented. Stretching the pulse also introduces chirp, which is compensated for when the pulses are re-compressed. Typically, this stretching and compressing of the pulse is done using grating pairs. This is also true for the Spitfire-Pro amplifier. In the regenerative amplifier the pulsed seed beam is first stretched using a grating pair and then amplified by overlapping it with a high-energy (20 W) pump beam in a Ti:Sapphire crystal. The pump beam is provided by a Q-switched Nd:YLF laser (Spectra Physics - Empower) with a repetition rate of 1 kHz and central wavelength of 527 nm (achieved by frequency-doubling the 1053 nm light emitted by the pumped Nd:YLF rod using a lithium triborate crystal).

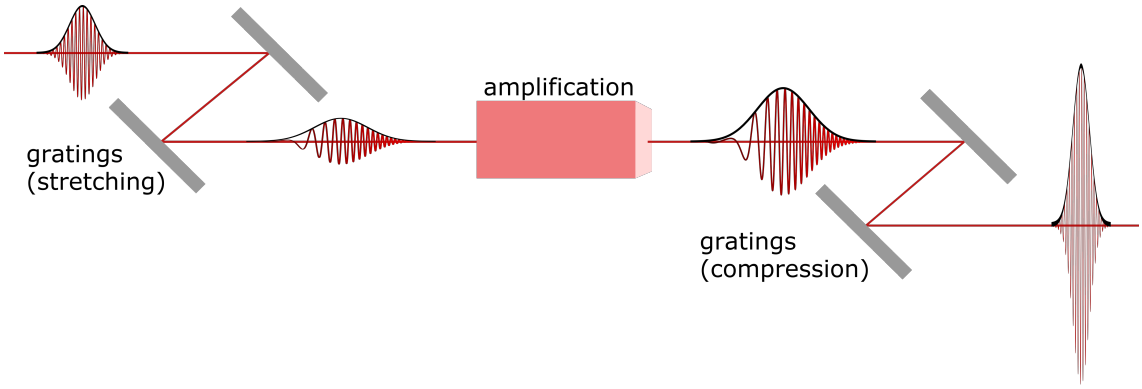

Figure 2.5: A schematic of the chirped pulse amplification process. After being stretched (using a grating pair) the ultrafast pulse has a lower peak-power and is chirped. This chirp is removed when the pulse is compressed again (using a second grating pair).

Two Pockels cells control when light is switched into and out of the cavity. Their timing can be adjusted to determine the number of roundtrips in the cavity which are visualised on an oscilloscope trace, along with the level of amplification. Once amplified a second grating pair is used to re-compress the pulses. The final output of the amplifier are 50 fs pulses centred at 800 nm with a FWHM of 30 nm at a repetition rate of 1 kHz. The average output power is 4 W. Using this output the various wavelengths required to carry out TRPEI experiments can be produced through frequency conversion using nonlinear optical crystals or four-wave mixing in noble gases, which will be outlined in the following section of this chapter.

2.2 Nonlinear Optics

UV and vacuum UV light is required to study the ultrafast relaxation dynamics of the systems of interest discussed in this thesis. The output wavelength provided by the femtosecond laser system employed is, however, in the near-IR. This makes it necessary to shorten the output wavelength, which can be done by making use of various nonlinear optical effects. This section provides a brief overview of the relevant physics.

The study of nonlinear optics is concerned with the phenomena observed when optical properties of a material are altered by intense light (typically laser light) [139]. It is known as *nonlinear* optics as the observed response of the material is nonlinearly dependent on the strength of the optical field applied. When a dielectric material is exposed to a high-power electric field E, the induced polarisation P can be expressed as

$$P(t) = \epsilon_0 \left(\chi^{(1)} E(t) + \chi^{(2)} E^2(t) + \chi^{(3)} E^3(t) + ... \right), \tag{2.8}$$

where χ is known as the optical susceptibility. $\chi^{(2)}$ and $\chi^{(3)}$ are the second- and third-order nonlinear susceptibilities respectively, and the corresponding terms in Equation (2.8) are therefore the second- and third-order nonlinear polarisations. The susceptibilities furthermore consist of a real and imaginary term

$$\chi = \chi' - i\chi'', \tag{2.9}$$

which are responsible for dispersive and dissipative effects, respectively.

The various orders of nonlinear polarisation are responsible for different physical processes. The real first-order term $\chi^{(1)\prime}$, for example, is responsible for birefringence and dispersion in the optical material, whereas its imaginary component describes linear absorption and gain. The $\chi^{(2)\prime}$ term leads to phenomena such as second-harmonic generation and the Pockels effect, whereas processes including four-wave mixing [140] and third-harmonic generation are related to the $\chi^{(3)\prime}$ term. It should be noted here that $\chi^{(2)\prime\prime}$ is zero, implying that no dissipative effects (i.e., heating of medium) occur for second-order processes. Furthermore, the material requirements for second- and third-order nonlinear optical interactions differ. Second-order processes may only take place in noncentrosymmetric crystals, whereas this restriction does not apply to third-order interactions. To illustrate the nature of frequency-mixing in a second order nonlinear optical material the polarisation response, when

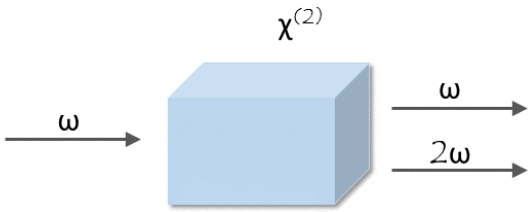

Figure 2.6: A schematic of the concept of the second-harmonic generation (SHG) process in a nonlinear material.

two waves are incident on such a material, can be inspected:

$$\begin{aligned} P = {} & \epsilon_0\chi^{(1)}[E_1\cos(\omega_1 t) + E_2\cos(\omega_2 t)] + \epsilon_0\chi^{(2)}E_1E_2\cos(\omega_1+\omega_2)t \\ & + \epsilon\chi^{(2)}E_1E_2\cos(\omega_1-\omega_2)t + \frac{1}{2}\epsilon_0\chi^{(2)}E_1^2\cos(2\omega_1 t) \\ & + \frac{1}{2}\epsilon\chi^{(2)}E_2^2\cos(2\omega_2 t) + \frac{1}{2}\epsilon_0\chi^{(2)}E_1^2 + \frac{1}{2}\epsilon_0\chi^{(2)}E_2^2. \end{aligned} \tag{2.10}$$

The second and third terms clearly show the origin the of sum (ω_1+ω_2) and difference ($\omega_1 - \omega_2$) frequency mixing processes. The polarisations of the second-harmonic frequencies of the input waves are given by terms five and six. The process of second harmonic generation is also based on this second-order polarisation response of a nonlinear material [141, 142]. A schematic of the process is shown in Figure 2.6. An input pulse incident on a nonlinear material (such as a β-barium borate (BBO) crystal) produces a second wave of twice the frequency of the input, hence the process is often referred to as *frequency doubling*. Some residual of the input wave will also be present after the doubling crystal, travelling in the same direction as the 2ω output. The intensity of the output is proportional to the square of the intensity of the input beam. Under ideal experimental conditions with high intensity, the efficiency of this process can be over 80 % [143]. It is for instance, used to shorten the wavelength of the 800 nm output of the femtosecond laser system described in Section 2.1.1 to 400 nm wavelengths, in order for them to be used as pump or probe beams in the TRPEI experiment. The 267 nm light (used as pump or probe) is produced through a cascaded tripling process, where initially 400 nm is produced by SHG of the fundamental (800 nm) and subsequently sum-frequency generation of both of theses waves produces the desired deep-UV wavelength. For a description of the experimental configuration used to execute this see Section 2.3.1.

In order to produce 160 nm, a third order nonlinear process is used: four-wave mixing (FWM) [140], specifically four-wave difference-frequency mixing (FWDFM). Two waves have to be overlapped in a nonlinear optical medium to produce this effect. The nonlinear medium for this process is typically a noble-gas such as neon

or argon [144]. The configuration to achieve FWM can either be collinear, where the two incident beams propagate in parallel, or non-collinear, where they can be overlapped at an angle, Φ. A non-collinear overlap is advantageous as this helps fulfil the phase-matching condition, as demonstrated by Ghotbi *et al.* [145, 146]. The phase-matching condition for this FWM process in terms of the wavevector **k** is given by

$$\Delta\mathbf{k} = 2\mathbf{k}_{3\omega} - \mathbf{k}_{\omega} - \mathbf{k}_{5\omega} = 0, \tag{2.11}$$

where subscripts ω, 3ω and 5ω denote the fundamental frequency (FF), third-, and fifth-harmonic of the laser output, respectively. Efficient energy exchange between the waves is achieved when the phase-matching condition given in Equation (2.11) is fulfilled. In a non-collinear configuration the angle Φ (Figure 2.7) can be adjusted to optimise the phase-matching and therefore the efficiency of the FWM process (Figure 2.7).

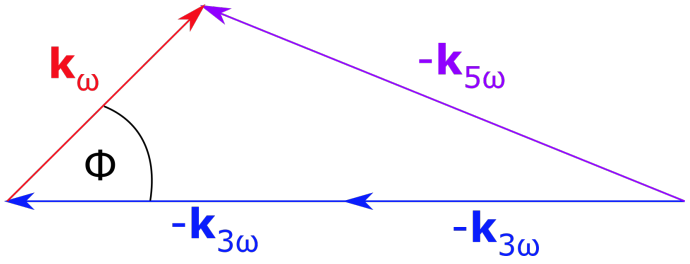

Figure 2.7: The phase-matching condition for four-wave mixing (FWM) visualised. A non-collinear arrangement with angle Φ can optimise the phase-matching.

2.3 Shortening the Wavelength

This section will discuss the optical configurations used to collect the data presented in Chapters 5 and 4 of this thesis. The pump and probe wavelengths employed to study the relaxation dynamics in nitrobenzene and its derivatives (Ch.: 5) are 267 nm for the pump and two photons of 400 nm for the probe. The time-resolved study of acetylacetone (Ch.: 4) also uses a pump wavelength of 267 nm but the probe is in the VUV at 160 nm, in order to project deeper into the ionisation continuum.

2.3.1 Optical Setup: UV + UV

The optical setup used to produce the wavelengths used for the work detailed in Chapter 5 (including typical power readings) is shown in Figure 2.8. The 800 nm output from the regenerative amplifier is split into two beamlines: one to produce the 400 nm probe pulses and one to produce the 267 nm pump pulses. The wavelengths are achieved using SHG in thin BBO crystals. A telescope setup in the 400 nm production line increases the efficiency of the SHG process and ensures the beam diameter is reduced such that the full 400 nm beam will clear the entrance window to the vacuum chamber as well as the aperture of the gate valve (6 mm) separating the *optics* and *main* chambers. A $\frac{\lambda}{2}$ waveplate just before the BBO ensures the correct polarisation (horizontal) of the UV-light is achieved (parallel to the detector in the VMI configuration as discussed in Chapter 1). The third-harmonic (TH) of the 800 nm output (267 nm) is achieved using the *FEMTOKIT* available from EKSMA Optics. The insert in Figure 2.8 shows the effect of each optical component in the *FEMTOKIT*. Initially, the fundamental frequency (FF) is converted to the second-harmonic (SH) by SHG in a thin BBO crystal. The polarisation of the 400 nm light produced is perpendicular to that of the FF at the input. A calcite plate compensates for the group velocity delay introduced during the SHG. This step is followed by a zero-order dual waveplate which rotates the polarisation of the FF so that it is polarised vertically. Furthermore, the FF and SH are now temporally overlapped. The next stage consists of a second BBO crystal where the TH, 267 nm, is produced (via sum-frequency generation) at a horizontal polarisation, ready to be used as a pump-pulse in the TRPEI experiment. A focusing mirror prior to this setup ensures that the 800 nm beam size is reduced so it can pass through the BBO crystals. A telescope after the THG setup re-collimates the beam before it is overlapped with the 400 nm in a combining optic and passes into the spectrometer. Here, the two beams propagate through the interaction region and double-back as they are reflected off a curved aluminium mirror ($f = 10$ cm), which creates a tight focus in the interaction region. This mirror is mounted on an (x,y,z)-translational stage which can be controlled manually from outside of the UHV chamber. This provides the capability of optimising the TRPEI signal centring the foci in the

interaction region.

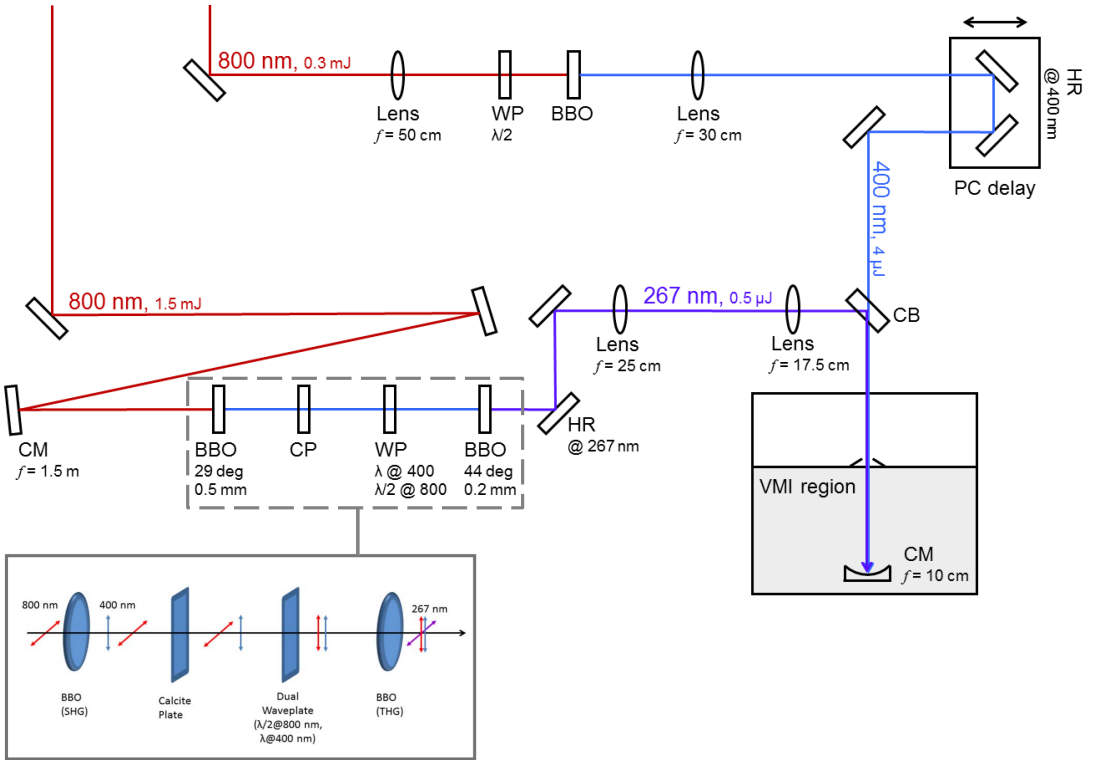

Figure 2.8: Schematic of the optical setup used to produce the 267 nm pump and 400 nm probe pulses for the TRPEI experiment on nitrobenzene and its methyl-derivatives (Chapter 5).

To determine the most suitable energies of the pump and probe pulses for the experiment spectrometer is also used. Using the sample to be studied, the energies of the pump and probe pulses are varied until the best contrast between the combined pump + probe signal and the pump-alone and probe-alone signals are achieved. The spot size of the beams in the focal region and the intensities at the focus, can be estimated based on the spot sizes and pulse energies at the entrance window of the vacuum chamber. The aperture of the gate valve between the *optics* chamber and the *main* chamber is 6 mm and limits the diameters of the ingoing beams. As outlined above the beam diameters were reduced from the laser output (10 mm diameter) to ensure the gate valve aperture is cleared. Based on the Rayleigh criterion and these initial maximum spot sizes, the area of the focal spots for the 267 nm and 400 nm beams can be estimated to be $\sim 90\ \mu m^2$ and $\sim 210\ \mu m^2$, respectively. The resulting intensities (upper bound) at the focus can then be estimated to be $\sim 5\times10^{12}$ Wcm^{-2} and $\sim 2 \times 10^{13}$ Wcm^{-2} for the 267 nm and 400 nm pulses respectively. These intensities are estimated using the pulse energies prior to the vacuum chambers and a maximum beam diameter before focusing and therefore represent an upper bound. The temporal pulse lengths of the 267 nm and 400 nm pulses were obtained

based on the FWHM cross-correlation in combination with a factor of $\sqrt{2}$. High intensities in the 10^{12} Wcm^{-2} are common in TRPEI experiments, where amplified femtosecond laser pulses are employed, even under moderate focusing conditions [12]. The intensity of the 400 nm pulses has to be high as it is used as a multiphoton probe but also just below what is typically considered to be the onset for perturbing high intensity effects, such as the AC stark effect [12, 52].

2.3.2 Optical Setup: UV + VUV

As introduced in Chapter 1 a short-wavelength probe increases how much of the reaction coordinate can be studied, as the probe reaches deeper into the ionisation continuum. For this reason, it is advantageous to produce vacuum UV (VUV) wavelengths and use them as probe pulses. This was done for work presented in Chapter 4. The layout of the complete optical setup used to record the data presented in Chapter 4 is shown in Figure 2.9, including the energies of the beams at various points throughout the optical setup. Three beamlines are used to produce the wavelengths required to carry out this TRPEI experiment. Two of these beamlines are combined in the gas-cell to produce the probe wavelength of 160 nm, whereas the third is used to produce light centred at 267 nm, which acts as the pump. A more detailed schematic of the setup required to produce the VUV (160 nm) light is shown in Figure 2.9. In order to achieve four-wave difference-frequency mixing two beams with a central wavelength of 800 nm and 267 nm, respectively, are focused and overlapped (spatially & temporally) in a gas-cell filled with a noble gas which acts as the nonlinear medium. The noble gas employed here was argon.

As in Section 2.3.1, two thin β - barium borate crystals (BBO) crystals are used to produce the third harmonic (TH) of the 800 nm input (267 nm). A calcite plate and dual waveplate between the crystals again ensure an optimised conversion process by adjusting the polarisation and compensating for the group velocity delay (as detailed in the above section). The 800 nm and the resulting TH beam are combined using a combining optic (Layertec HR/HT 267 nm/400 nm + 800 nm) such that they can then be overlapped in the argon-filled gas-cell. The non-collinear overlap angle is adjusted using the mirror just before the thin focusing lens (f = 60 cm) which focuses the 800 nm in the gas-cell, as well as the combining optic before the gas-cell for the 267 nm. To focus the TH beam in the centre of the gas-cell a focusing mirror (CM f = 1.5 m) is used, which also ensures that the beam diameter is reduced so that it can pass through the BBO setup. Furthermore, the reduction in beam diameter increases the efficiency of the frequency conversion process. The temporal overlap between the IR and TH beams inside the argon-cell is adjusted using a manual linear delay stage in the 800 nm line. The material used for the entrance and exit windows of the gas cell was CaF_2. Their thickness was reduced to 0.3 mm, the minimum required to withstand the pressure gradient

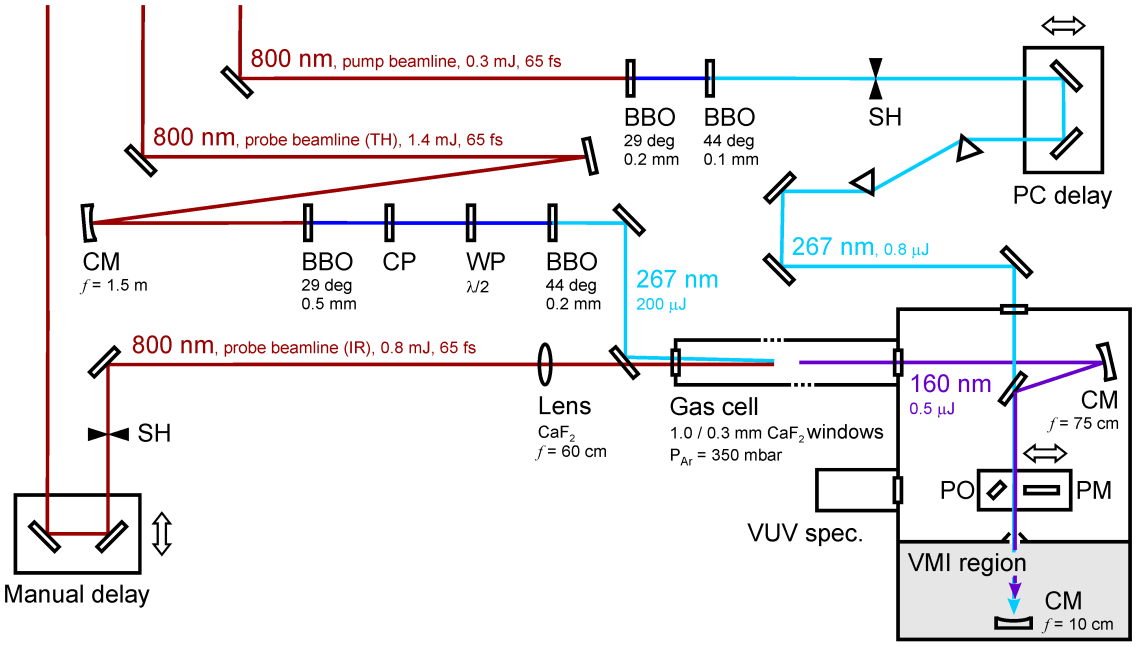

Figure 2.9: Schematic of the optical configuration used to produce the VUV probe and UV pump pulses for the study of acetylacetone (Chapter 4). Abbreviations: BBO (β-barium borate crystal), CP (calcite plate), WP (waveplate), CM (concave mirror), PM (power meter), PO (pick-off optic), SH (shutter to enable one-colour background subtraction).

between the gas-filled cell and atmospheric pressure or the ultrahigh vacuum (UHV) in the TRPEI spectrometer. It is necessary to keep the windows as thin as possible in order to reduce the amount of dispersion and chirp which is introduced when the beam passes through the optical material. The pressure of argon in the 77 cm long static gas-cell is adjusted using a needle valve, and measured using a baratron gauge (Edwards 600AB). Beyond the gas-cell, the beams enter the first UHV chamber (*optics chamber*).

The VUV production is dependent on the pressure of the noble gas in the cell [145, 147]. An example of this for the setup at Heriot-Watt can be seen in Figure 2.10, for one collinear and two non-collinear configurations. This was recorded by M. M. Zawadzki and further details can be found in reference [148]. For the setup used to record the acetylacetone data in Chapter 4 the optimum setup conditions for VUV production used were $\Phi \approx 12$ mrad (non-collinear overlap angle) and an argon pressure of 350 mbar. This resulted in VUV pulses with a maximum energy of 500 nJ. The spectrum of VUV produced using this configuration is shown in Figure 2.11. A cross-correlation (CC) was recorded using xenon (Figure 2.12). The CC was found to be around 150 fs using a Gaussian fit and the 2D-photoelectron spectrum (PES) of xenon shown indicates that the VUV pulse exhibits no significant chirp. This can be deduced since non-resonant 2D-photoelectron spectra are able to provide similar information as that obtained using a frequency-resolved optical gate (FROG) trace [149]. A chirped pulse would result in a distortion or 'bend' in the

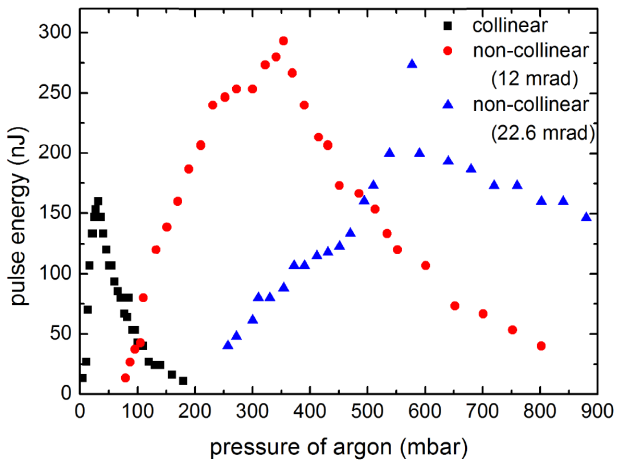

Figure 2.10: The variation of the VUV with pressure in a collinear and two non-collinear setup configurations. This figure is taken from reference [148].

photoelectron spectrum, but the data shown here are highly symmetric and even. This methodology can provide information on the characteristics of the pump and probe pulses due to the employment of a non-resonant or virtual state, a familiar concept in multiphoton ionisation processes or Raman spectroscopy [150, 151]. Instead of exciting a resonant electronic state using the pump photon, a virtual state with no lifetime is considered. This means the signal observed is not convoluted by a lifetime but provides a reflection of the pulses employed. This approach is typically used to provide cross-correlations of pump and probe pulses but can also indicate the presence of chirp [148].

After the VUV light is produced, a spherical concave mirror (Layertec, >90% HRp 145-165 nm at 20° AOI, $f = 75$ cm) coated for high VUV-reflectivity acts as a recollimator. This curved mirror furthermore allows for steering of the 160 nm in the UHV system using an external controller (Newport axis AGILIS AG-UC8). The VUV pulses are overlapped with the 267 nm pump pulses using a second combining optic. The 267 nm pump pulses are produced through two consecutive SHG processes in two thin BBO crystals. The delay stage in this line adjusts the timing between the pump and probe beams. A pair of prisms acts to reduce the chirp of the pulse in this line, on the basis of the principles outlined earlier. It should be noted here that this configuration is single pass, and therefore will result in pulses that have a reduced temporal chirp and pulse duration but are spatially dispersed. It was necessary to adopt this configuration as a double pass setup resulted in losses in intensity too high to perform the TRPEI experiment. Since the temporal pulse duration is one of the crucial parameter for this experiment this configuration is favourable despite its trade-offs with regard to spatial chirp. Both UV and VUV beams are later focused using a curved mirror inside the vacuum chamber chamber where the introduced spatial chip will likely result in a chromatic focal shift in the UV beam. This is typically avoided when using a mirror to focus a beam,

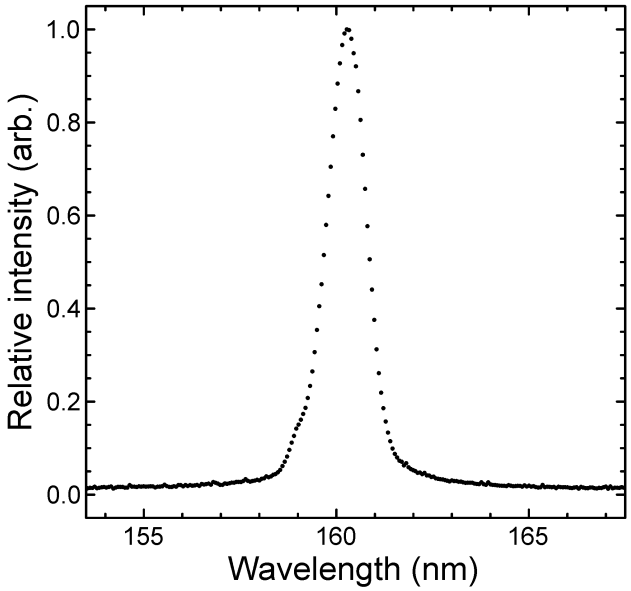

Figure 2.11: The spectrum of the produced VUV light. The data has been intensity normalised and using a Gaussian fit a FWHM of $\sim$ 1.3 nm is extracted.

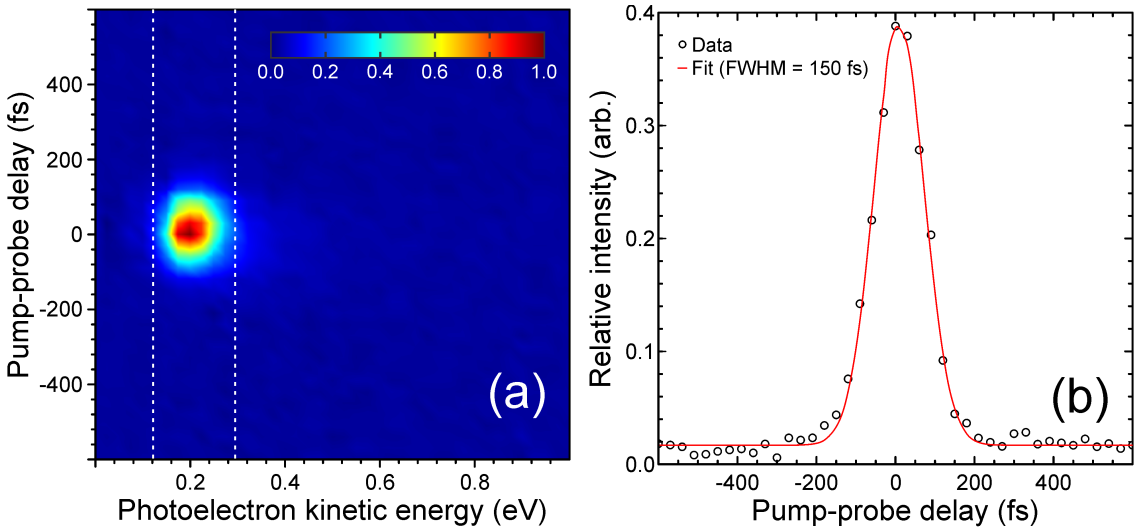

Figure 2.12: The cross-correlation (b) of 160 nm and 267 nm pulses obtained from the photoelectron spectrum of a 1+1′ ionisation using xenon (a). The FWHM has a 1σ uncertainty of $\pm$ 10 fs.

compared to a lens which is known to introduce chromatic aberrations. Focusing lenses have nonetheless been successfully employed previously with this TRPEI spectrometer indicating a certain tolerance for chromatic aberrations for the experiment [94, 152, 153]. A good overlap of the two focussed beams is ensured when initially configuring the TRPEI spectrometer for the experiment. It involves adjusting the velocity mapping conditions such that the focal regions where the pump and probe beams excite sample can be 'viewed' on the CCD. When the focal regions of both beams are successfully overlapped a significant amplification in electron signal is observed. This allows for a precise alignment inside the vacuum chamber and ensures sufficient overlap of the beams, negating concerns of shifted focussing positions. The 267 nm pump beam then enters the first UHV chamber via a window (fused silica) and is overlapped with the 160 nm beam in the combining optic (VUV high-reflectivity coated plane mirror) in the centre of the first chamber. Using two optics coated for VUV-reflectivity after the production stage in the gas cell ensures that any remaining IR and TH light from the FWDFM process are removed. The aforementioned external controller also controls the translation of the stage indicated by dark grey rectangles inside the first vacuum chamber depicted in Figure 2.9. This stage is required for beam diagnostics, where the mirror on the first stage can be moved into the 160 nm beampath, diverting it into a VUV spectrometer (Resonance Ltd VUV mini spectrograph VS7550) mounted on the side of the vacuum chamber. This allows for accurate determination of the central wavelength and spectral bandwidth of the VUV produced. The photodiode (Star Tech Instruments, XR-16-G) mounted on the same translation stage is used to determine the power of the 160 nm light. The second PC-controlled translation stage, with a mirror mounted on top, allows the 267 nm beam to be sent out of the chamber through another window to aid with alignment. Finally, the pump and probe beams were focused in the interaction region between the electrode setup (described below), on a second pass, using a curved mirror which is Al-coated and has a focal length of 10 cm (as above). As done for the UV+UV configuration in the previous section, the area of the focal spots for the 267 nm and 160 nm beams can be estimated to be ~ 90 μm^2 and ~ 30 μm^2, respectively. Using these values an upper bound of the intensities in the focal region can be estimated to be $\sim 8 \times 10^{12}$ Wcm^2 and $\sim 1 \times 10^{13}$ Wcm^2 for the 267 nm and 160 nm beams respectively. The assumptions made previously for the UV+UV setup apply here, except that the energy of the 160 nm pulses are measured inside the vacuum chamber and therefore no losses due to passing through an entrance window are expected. Still, these intensity values represent an upper bound as the maximum possible beam diameter before focusing permitted by the gate valve aperture (6 mm) was used to estimate the focal spot sizes and intensities. A high intensity VUV beam was required for the experiment to be successful.

2.4 Velocity Map Imaging Spectrometer

This section will provide a brief overview of the whole spectrometer setup, followed by a more detailed discussion of the vacuum setup, VMI setup and detection methods and finally sample delivery.

The configuration of the TRPEI spectrometer used for the VUV setup is shown in Figure 2.13. The spectrometer setup consists of three ultrahigh vacuum (UHV) chambers: the *main chamber* in the centre, which is connected via gate valves to the *optics chamber*, and *source chamber*. The optics chamber contains the optical setup required for focusing the pump and probe beams in the interaction region inside the main chamber (as in Figure 2.9). It was designed by M. Candelaresi. The gas cell for VUV production is part of the arm protruding from the optics chamber. It should be noted here that the optical setup inside this chamber is of course dependent on the pump and probe wavelengths used. For the experiment in Chapter 4, where the VUV arm was used, the optical setup is shown in Figure 2.1. The setup for work done in Chapter 5 does not require the VUV arm, instead of which a window was mounted directly onto the optics chamber. The optics chamber and main chamber are connected by a gate valve. This allows for the optics chamber to be opened while the other two chambers remain under UHV conditions. This is particularly useful for realignment purposes but also for the regular cleaning of optics. The source chamber, positioned below the main chamber, is also connected via a gate valve to allow for a fast turnover when refreshing solid samples internally mounted. As indicated by its name, the source chamber's main purpose is for sample delivery. An Even-Lavie molecular beam pulsed valve [102] is mounted here, which allows for the sample to enter the main chamber as a supersonically cooled molecular beam (see Section 2.4.2). Finally, the main chamber contains the ion optics used to focus the electrons or ions onto the detector, consisting of a micro-channel plate (MCP) and phosphor screen (described in more detail below). A window on the top of this chamber allows for an external charge-coupled device (CCD) camera to be mounted and capture images from the detector.

2.4.1 Ion Optics for Velocity Map Imaging and Detection

The concept of VMI was discussed previously and the specific electrode setup (also known as *ion optics*) used for VMI will be outlined here. A detailed schematic of the VMI electrode setup can be seen in Figure 2.14. It consists of five electrodes to which a negative or positive voltage may be applied in order to collect electrons or ions on the detector. The region of interaction between the laser pulses and the sample is located between the repeller (A) and extractor (B) electrodes. The electrons that will be imaged are born here and focused onto the detector, which is found at the top of the flight tube about 260 mm from the interaction region. A voltage ratio

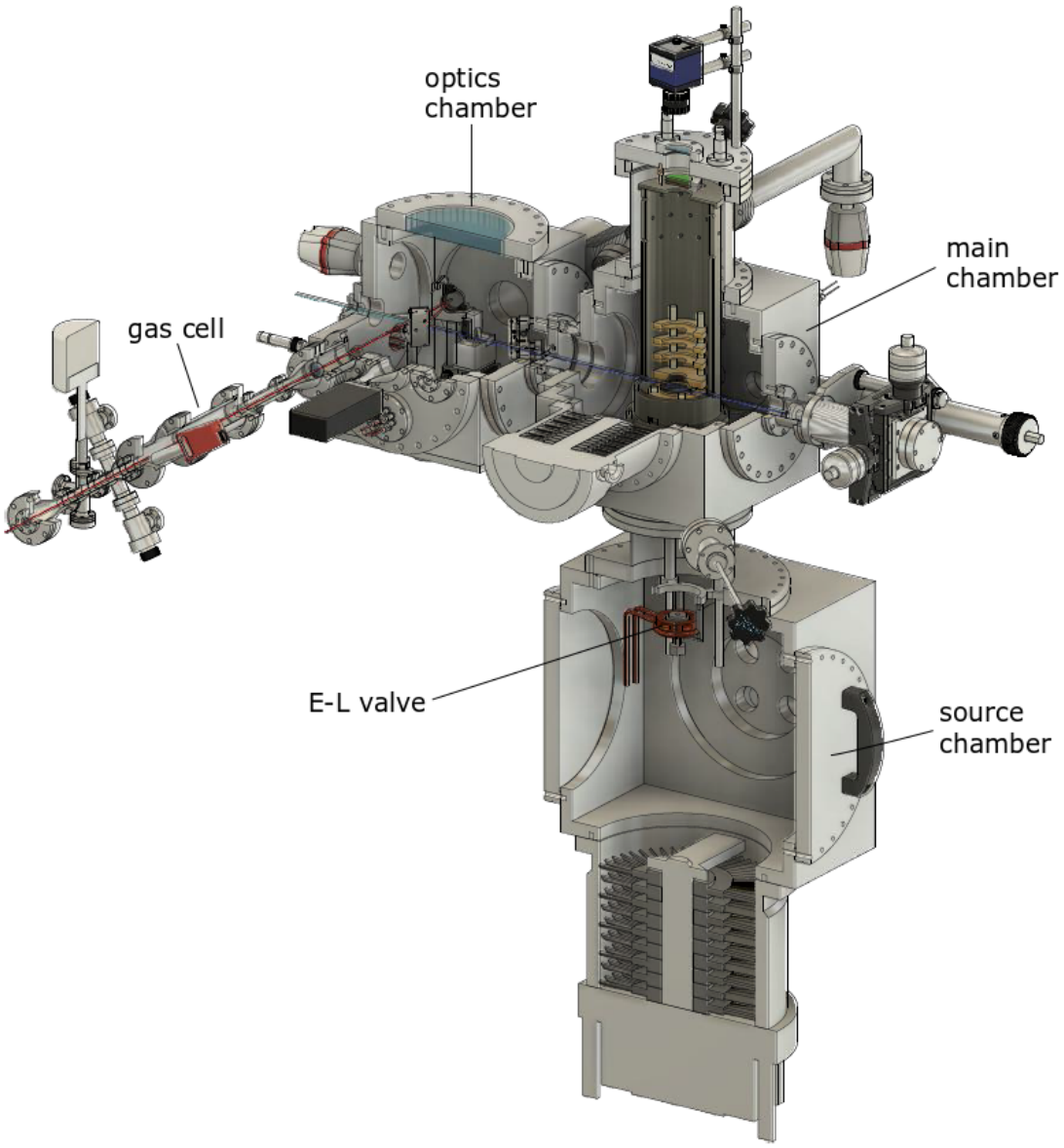

Figure 2.13: The entire vacuum system, including the argon cell (gas cell) arm where the VUV is produced, the optics chamber, and main and source chambers. The spectrometer used to characterise the VUV beam is also shown. Courtesy of Chris Sparling.

of 0.78 between the extractor and repeller electrodes produces the optimal velocity mapping conditions for this setup [94]. The third electrode, C is grounded to achieve a field-free region between C and the detector. The electrodes D and E are also grounded for the purposes of the experiments discussed in this thesis. They provide the optional capability of conducting DC slice-imaging experiments. As shown in Figure 2.13 the electrodes are surrounded by two mu-metal cylinders mounted on a base plate and topped with an end-cap, also made of mu-metal. The nickel-iron alloy shields the electrodes from unwanted, external magnetic fields which could affect the trajectory of the electrons. Rather than blocking the magnetic field lines, the shielding effect is achieved by the high permeability exhibited by the mu-metal,

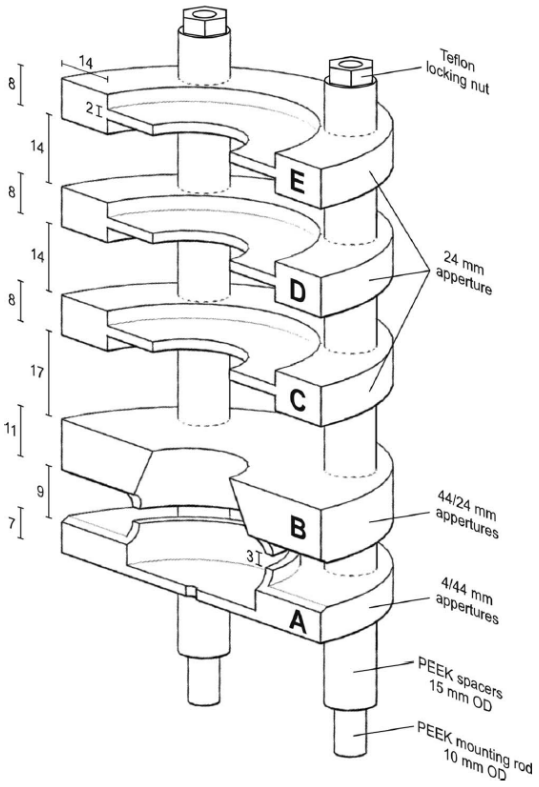

Figure 2.14: A detailed schematic of the ion optics setup at Heriot-Watt, published in [94].

which acts to redirect the magnetic field lines around the area which it is shielding. The electrodes were coated in *Vantablack* (Surrey NanoSystems) material to reduce the increased background scattering signals observed when VUV wavelengths are used (Chapter 4). This coating is crucial when shorter wavelengths are used, as the scattered intensity increases with shorter wavelength, as shown by the well-known relation for Rayleigh scattering [154]

$$I \propto \frac{1}{\lambda^4}. \tag{2.12}$$

As the scattered intensity, I is proportional to the inverse wavelength to the power of four, even a relatively small shortening of the wavelength has a large effect on the scattering intensity. Based on this proportionality relationship, it is evident that reducing the wavelength from 260 nm to 160 nm results in an increase of the scattering intensity by about an order of magnitude. Two main features of this ion optic setup distinguish it from those used by other groups: the first being the conical shape of the extractor electrode, and the second the *lip* on the extractor and repeller electrodes. The former reduces lens aberrations by improving the ability to focus electrons with an initial velocity perpendicular to the time-of-flight axis. The second feature was added to reduce charge-build up on the insulating spacers between the extractor and repeller which may lead to distorted VMI images.

Using the electrode assembly, the electrons/ions are focused onto the detector. This consists of a dual microchannel plate (MCP) which acts as an amplifier of the signal by multiplying the ingoing electron/ions. The resulting electron avalanche is then converted into light when picked up by a P47 phosphor screen which is mounted above the MCP. A monochrome CCD camera (The Imaging Source, DMK 21BF04 - 640 × 480 pixels) is mounted outside the UHV system and images the light from the phosphor screen through a viewport. The timing of the arrival of the pulsed molecular beam and pump/probe pulses in the interaction region is controlled by a delay generator (Stanford DG535). The external trigger is provided by the laser (time delay generator/internal clock) which acts as a reference for the EL valve trigger and the detector. The timing to trigger the EL valve can be adjusted to provide a good temporal overlap of the molecular beam and pump/probe pulses. It can also be used to select ions of a specific mass (flight-time), when the spectrometer is used in ion mode. In order to reduce noise the backplate voltage of the MCP is gated using a high-voltage pulser (DEI PVX-4140).

2.4.2 Sample Delivery

The sample can be introduced into the spectrometer using several methods. Liquid samples are typically placed into a *bubbler*, a sketch of which is shown in Figure 2.15. The sample is placed into a pyrex beaker which in turn is placed into a steel container that can be pressurised. A KF flange with a gas feedthrough allows for a carrier gas, such as helium, to bubble through the liquid, or alternatively flow over a volatile solid sample. The carrier gas is typically at a pressure of 0.5 bar. This puts the sample into the gas phase and the carrier gas and sample mixture can then be directed into the source chamber (and to the E-L valve) using a further feedthrough. Samples with a relatively high vapour pressure are required for this method for a sufficient amount to be put into the gas phase. Samples which are already in the gas phase can also be introduced into the UHV system in this way by connecting the pressurised bottles directly to the feedthrough leading to the source chamber.

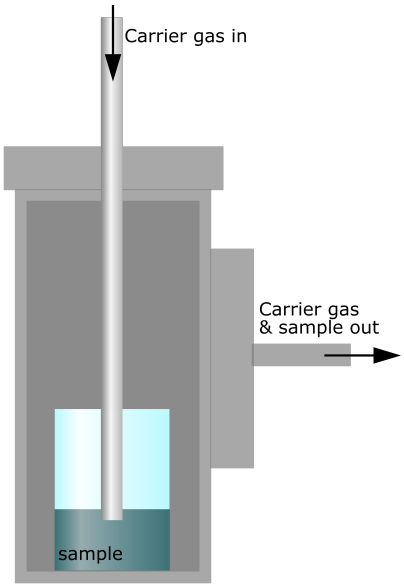

Figure 2.15: A sketch of the bubbler used for sample delivery. A liquid or solid sample is placed in a beaker inside the steel canister. Access to the beaker is provided by a KF40 flange at the top.

Sample mixtures are delivered to a pulsed, molecular Even-Lavie (EL) valve [102] with a conical nozzle of diameter 150 μm. This valve typically operates at the same repetition rate as the laser (1 kHz) producing short (20 - 30 μs) molecular beam pulses. The sample mixture is cooled via supersonic expansion to temperatures under 40 K. A skimmer with a 1 mm diameter orifice is in place between the source and main chambers to pick out the coldest part of this molecular beam before it enters the interaction region. The temperature of the EL valve can be controlled using a chiller (Neslab RTE-110) containing a mixture of ethylene glycol and water. This is to avoid melting of solid samples when loaded directly into a cartridge in the EL valve. The EL valve can also be removed providing an effusive beam setup, as used in Chapter 5. The gate-valve separating the source and main chambers allows for this process to be fairly quick as only the source chamber has to be brought to atmosphere.

2.4.3 Vacuum Setup

The three UHV chambers require two stages of pumping in order to maintain the low pressures required to run the gas-phase TRPEI experiments. A schematic of the vacuum setup can be seen in Figure 2.16. A turbo molecular pump is mounted on each chamber which is in turn connected to a roughing pump via a valve and tubing. Two of these roughing pumps (oil-sealed rotary pumps) are situated in an adjacent room to reduce vibrations and noise, whereas the scroll pump for the optics chamber is positioned next to the UHV chambers. Foreline traps prevent any backstreaming of oil from the roughing pumps (oil-sealed rotary) to the turbo molecular pumps.

The pressure in each chamber is monitored by a wide range gauge (consisting of a Pirani and an inverted magnetron gauge) whereas the pressure in the roughing line can be determined by a separate Pirani gauge. The lowest pressures are found in the "main chamber", which is typically in the low 10^{-7} mbar, provided by a turbo molecular pump with a pumping speed of 440 ls^{-1}. In the adjacent "optics chamber", the pressure is an order of magnitude larger than this (low 10^{-6} mbar) as a pump with a lower pumping speed (61 ls^{-1}) is used for evacuation. Since this chamber contains purely optical components, a low base pressure is not as essential as it is in the main chamber where the interaction of light and sample takes place. Finally, the "source chamber" is also typically in the low 10^{-7} mbar when no sample is injected. When a sample with a carrier gas is injected however, the pressure may rise up to 10^{-4} mbar which is why a large turbo molecular pump (pumping speed: 2200 ls^{-1}) is required for this chamber. As mentioned above, two gate valves connect the three chambers, one between the main and optics chamber, and one between the main and source chamber. This allows for the optics and source chambers to be vented while the electron/ion detector in the main chamber remains under vacuum. This is crucial as the detector may be damaged by prolonged exposure to air.

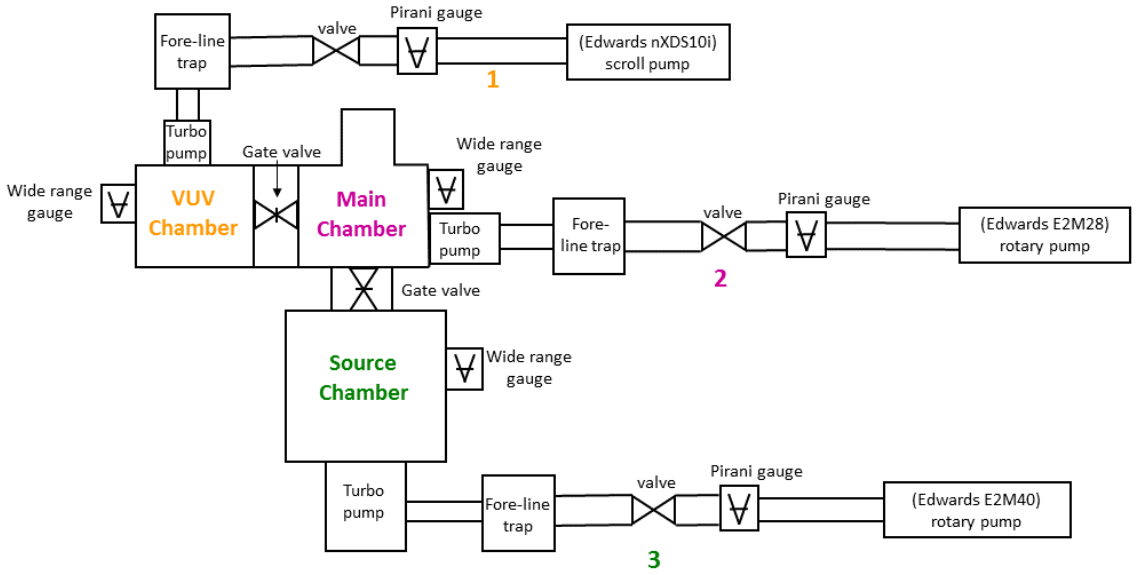

Figure 2.16: A schematic of the vacuum system used, where the numbers 1,2,3 indicate the different lines leading to the roughing pumps for the optics-, main-, and source-chamber respectively.

2.5 Data Acquisition, Handling and Analysis

In order to acquire, process and analyse the data from the TRPEI experiment, the *REPEITS* program is used. It was written by R. Livingstone and is outlined in detail in reference [95]. The program has since been updated to run on the 2015 version of MATLAB but the overall operation of the program is as described in the above reference.

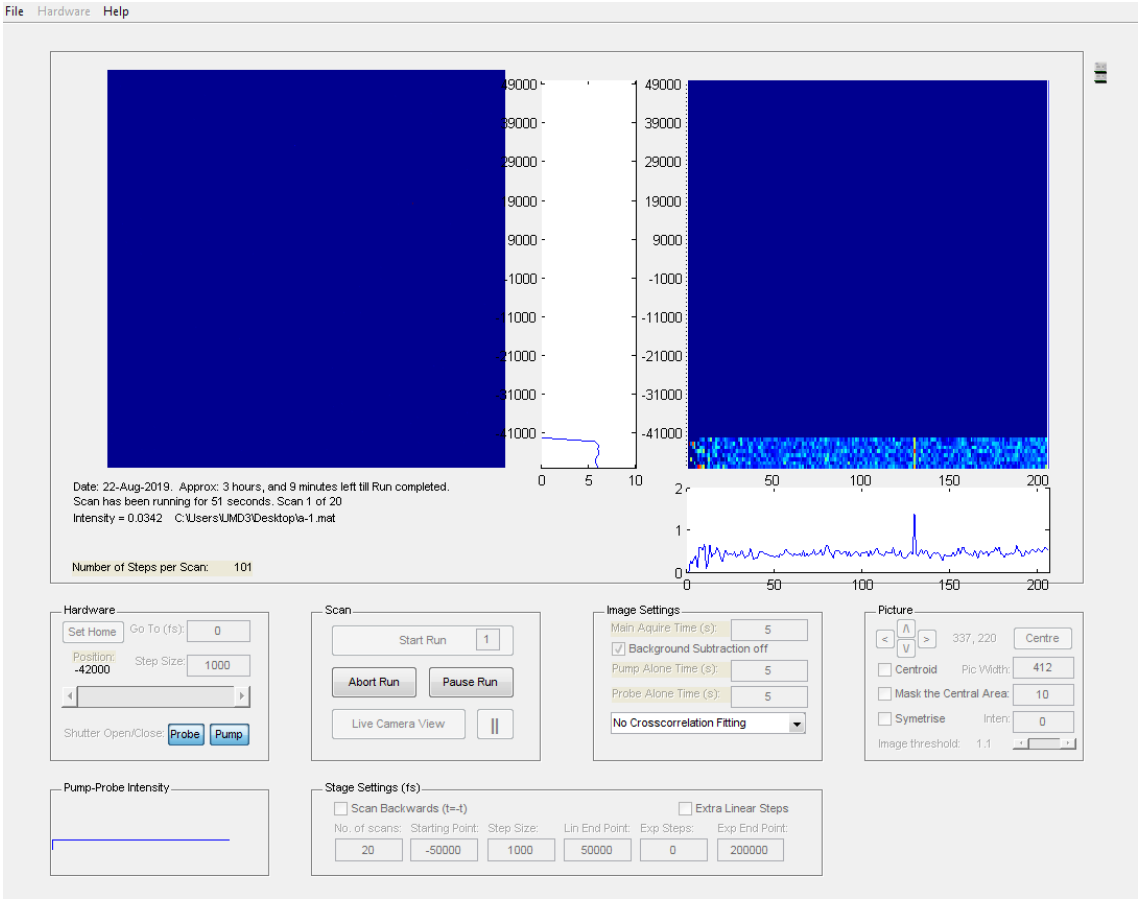

Figure 2.17: A screenshot of the *Acquire* data software. As can be seen all the shutter and translation stage settings can be adjusted as required. There are further options to edit the acquisition time of each VMI image and a graph of the pump-probe intensity gives an indication of the stability of the experiment.

The program is divided into three major parts of code: *Acquire*, *Process* and *Analyse*. The *Acquire* part of the program communicates with the translation stage and controller (Physik Instrumente - M-403.62S/ Mercury Step C-663), the shutters (Thorlabs TSC001) and the monochrome CCD camera. This allows for the VMI images to be collected. A screenshot of the graphic user interface (GUI) of *Acquire* can be seen in Figure 2.17. The acquisition time, time steps and scan direction can be edited using this GUI prior to setting up a scan, which is a complete set of VMI images for all the pump-probe delay times specified by the user. Typically such a scan consists of fine time steps around time-zero (15-30 fs) followed by a region of

longer time steps (60-90 fs) up to a certain point, typically up to 1 ps. Finally, it is possible to define a series of exponential steps to cover the range out to 200 ps pump-probe delay time. The acquisition time can also be set by the user. Individual pump and probe alone times can be set providing the option to acquire pump only or probe only signal in order to perform background subtraction. When a scan is not running, the blue panel on the left-hand side shows a live feed from the camera. Furthermore, a trace at the bottom of the panel shows the overall integrated signal, which is a helpful tool to check for the time-overlap between pump and probe signal. Once a scan is running the blue panel on the right-hand side in Figure 2.17 shows each scan step as it is being acquired in real-time, as well as integrated traces over the delay-time and radial (pxl) axis. It is also possible to use centroiding [155] on the data as it is being acquired, this feature was however, not used in any of the experiments discussed in this thesis.

The VMI images collected are then processed in the *Process* part of the *REPEITS* program. An individual image, scan or collection of scans can be loaded. Typically, a number of scans recorded consecutively will be processed together. The background signal can be subtracted using the "pump" and "probe" subtract options. This is done at every time-delay for the data presented in this thesis. Furthermore, there is an option to symmetrise the VMI image using select quarters.

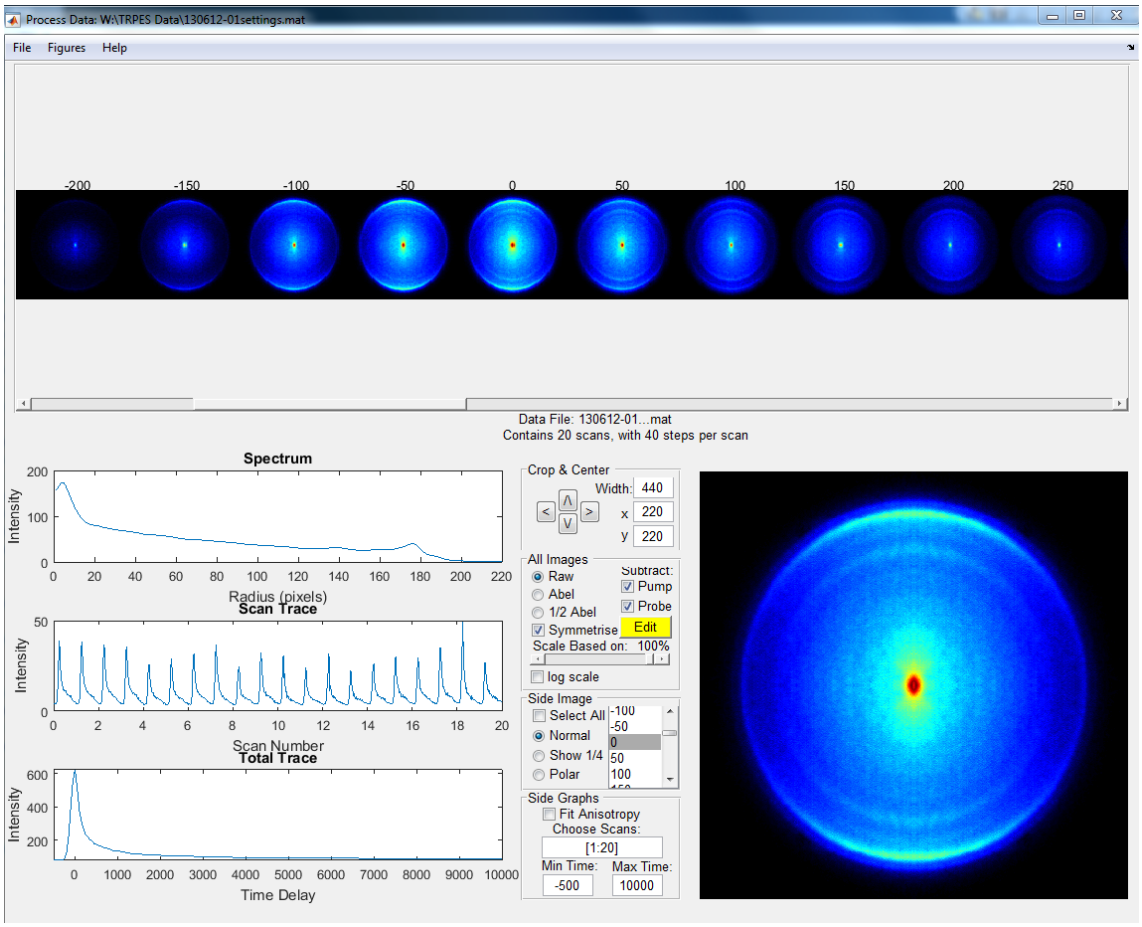

Figure 2.18: A screenshot of the *Process* data software. Along the top of *Process* the VMI image at each time-delay is shown. The VMI images can be viewed as raw, Abel inverted or half raw and half Abel-inverted: a half and half display is shown here. The number of scans and their intensity can be seen in the central white panel labelled "scan trace". The total spectrum and temporal trace are shown in the white panels above and below, respectively. An enlarged version of the VMI image can be viewed on the bottom right of the *Process* GUI. This can be just one VMI image at a specific time-delay or the sum of VMI images over several/all time-delays. The example data shown here is from piperidine TRPEI (see reference [22] for more).

The main processing required is the reconstruction of the 3D velocity distribution of the electrons from the 2D projection onto the detector. When the electron cloud is imaged on the detector, it is unavoidably 'flattened'. The 3D distribution can however, be recovered using several image-processing techniques which were previously discussed in Chapter 1. The technique of choice in the *Process* code is the Abel-transform. This inversion technique works on the assumption that the velocity distribution of the electron cloud possesses cylindrical symmetry (as discussed in Chapter 1). Making use of the Abel-transform is however, a computationally expensive and noise-amplifying method which does not lend itself to real-time or on-the-fly data processing. In order to address these two shortcomings, a matrix inversion method was proposed by Townsend and co-workers [94]. Cho and Na use a similar approach in their work in the area of plasma-diagnostics [156].

As a reminder, the inverse Abel transform (as discussed in Chapter 1 and given in Equation (1.24)) is given by

$$I(\rho, z) = \frac{1}{4\pi} \int_r^R \frac{\partial_y P(y, z)}{\sqrt{y^2 - \rho^2}} dy \tag{2.13}$$

in cylindrical coordinates ($\rho = \sqrt{x^2 + y^2}$) and the detector was assumed to lie in the y, z plane, where z is the symmetry axis.

Now, partitioning the x, y plane into segments of constant ρ and y (Figure 2.19) allows the 3D distribution $I(\rho, z)$ to be described as discrete I_{ij} where i and j are the maximum values of radius ρ and y value, respectively. The area of such a segment is denoted A_{ij}. When $i = j$ the area of the segment is described by

$$\begin{aligned} A_{ii} &= \int_{i-1}^{i} \int_0^{\sqrt{i-y^2}} dxdy \\ &= \int_{i-1}^{i} \sqrt{i^2 - y^2} dy \\ &= -\frac{1}{2} i \sqrt{-1 + 2i} + \frac{1}{2} \sqrt{-1 + 2i} - \frac{1}{2} i^2 \times \arcsin\left(\frac{i-1}{i}\right) + \frac{1}{4} i^2 \pi. \end{aligned} \tag{2.14}$$

The area of all other segments, where $i \neq j$ is given by

$$\begin{aligned} A_{ij} &= \int_{i-1}^{i} \int_{\sqrt{(j-1)-y^2}}^{\sqrt{i-y^2}} dxdy = \int_{i-1}^{i} \sqrt{i^2 - y^2} - \sqrt{(j-1)^2 - y^2} dy \\ &= \left(-\frac{1}{2} j^2 + j - \frac{1}{2}\right) \arcsin\left(\frac{i}{j-1}\right) + \left(\frac{1}{2} j^2 - j + \frac{1}{2}\right) \arcsin\left(\frac{i-1}{j-1}\right) \\ &+ \frac{1}{2} i \sqrt{j^2 - 2j + 2i - i^2} - \frac{1}{2} i \sqrt{j^2 + 2i - 1 - i^2} - \frac{1}{2} \sqrt{j^2 - 2i - 1 - i^2} \\ &+ \frac{1}{2} \sqrt{j^2 + 2i - 1 - i^2} + \frac{1}{2} i \sqrt{j^2 - i^2} \\ &- \frac{1}{2} j^2 \times \arcsin\left(\frac{i-1}{j}\right) + \frac{1}{2} j^2 \arcsin\left(\frac{i}{j}\right) - \frac{1}{2} \sqrt{j^2 - 2j + 1 - i^2}. \end{aligned} \tag{2.15}$$

In terms of the matrices, $\mathbf{A}, \mathbf{I}$ and $\mathbf{P}$ the projection of the initial 3D distribution onto the 2D detector plane can now be expressed as $\mathbf{P} = 2\mathbf{AI}$ and the inverse Abel transform, to recover the 3D distribution is therefore (at large x) given by

$$\mathbf{I} = \frac{1}{2} \mathbf{A}^{-1} \mathbf{P}. \tag{2.16}$$

A number of rapid matrix inversion methods are available to evaluate the above expression, which was implemented in MATLAB by R. Livingstone [94, 95]. This approach was shown to reduce the processing time by about two orders of magnitude compared to other methods [95]. Using standard matrix inversion routines in

MATLAB, one hundred 300 × 300 px images can be inverted in about one second using a standard PC with a 2.67 GHz processor.

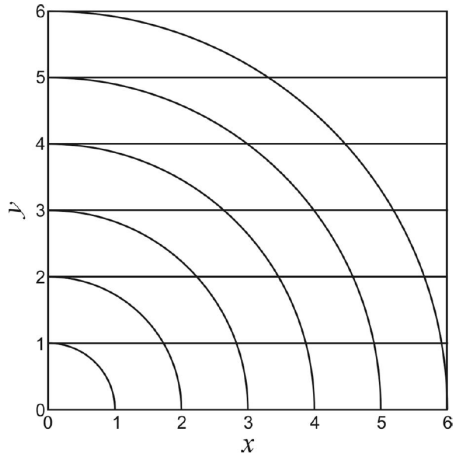

Figure 2.19: Illustration of the partition of the x, y plane into segments of constant values of y and radius, ρ. Figure from reference [94].

The *Analyse* part of the REPEITS program then allows the user to fit the processed data and extract the temporal evolution, decay associated spectra (DAS) as well as β-parameters. Initially the photoelectron data has to be calibrated, in order to convert the radius in pixels to kinetic energy in eV. It is necessary to create a calibration file for each new set of voltage settings for the extractor and repeller electrodes. A sample with a known ionisation potential that produces well-characterised rings in the VMI images is typically chosen to create this calibration file. Atomic species such as xenon fulfil these conditions and are therefore regularly used. Once the data is calibrated it can be cropped in energy or time, energy bin widths can be altered, the lin/log crossover-point can be set as well as the time-zero offset. The $t < 0$ background can also be subtracted to reduce noise. The data can be viewed in 2D mode, top-down as shown in Figure 2.20 or in 3D. Furthermore, the integrated time-trace and spectrum are shown in graphs to the left and below the central 2D/3D photoelectron spectrum. Once this setup has been performed, there are several options for fitting the data using *Analyse*. The "Global Fit" option fits the photoelectron spectrum providing information about the relaxation dynamics. The PES is fitted globally, at every photoelectron energy and pump-probe delay value, using a number of decaying exponentials over the whole spectrum. It is fitted using a Levenberg-Marquardt [157, 158] global fitting routine

$$S(E, \Delta t) = \sum_{i=1}^{n} A_i(E) \cdot P_i(\Delta t) \otimes g(\Delta t), \tag{2.17}$$

where A_i is the decay-associated spectrum (DAS) of data channel i, $P_i(\Delta t)$, the time-dependent population and the experimental cross-correlation, $g(\Delta t)$. The cross-correlation $g(\Delta t)$ is modelled by a Gaussian function, whereas $P_i(\Delta t)$ is modelled

using decaying exponentials

$$P(\Delta t) = e^{-\frac{t}{\tau_i}}, \tag{2.18}$$

with τ_i being the time-constant, which is an indicator of the speed at which the relaxation process takes place. The number of decaying exponentials to be fitted is determined by the user. The DAS shows the amplitude of each exponential decay in each energy bin, which allows for the identification of different processes taking place at different energies. The above expression (2.17) was integrated into the *REPEITS* program to primarily make use of a parallel fit model (although a sequential fit option is available). A parallel fit model is one where all exponential decay functions originate from zero time delay between the pump and probe pulses ($\Delta t = 0$). This type of fit assumes no *a priori* knowledge of the type of dynamical processes present but can identify sequential processes through negative amplitude features, which must mean a rise in signal. This is discussed in more detail in references [14, 159] and will be expanded in the discussions of experimental Chapters 6 and 4.

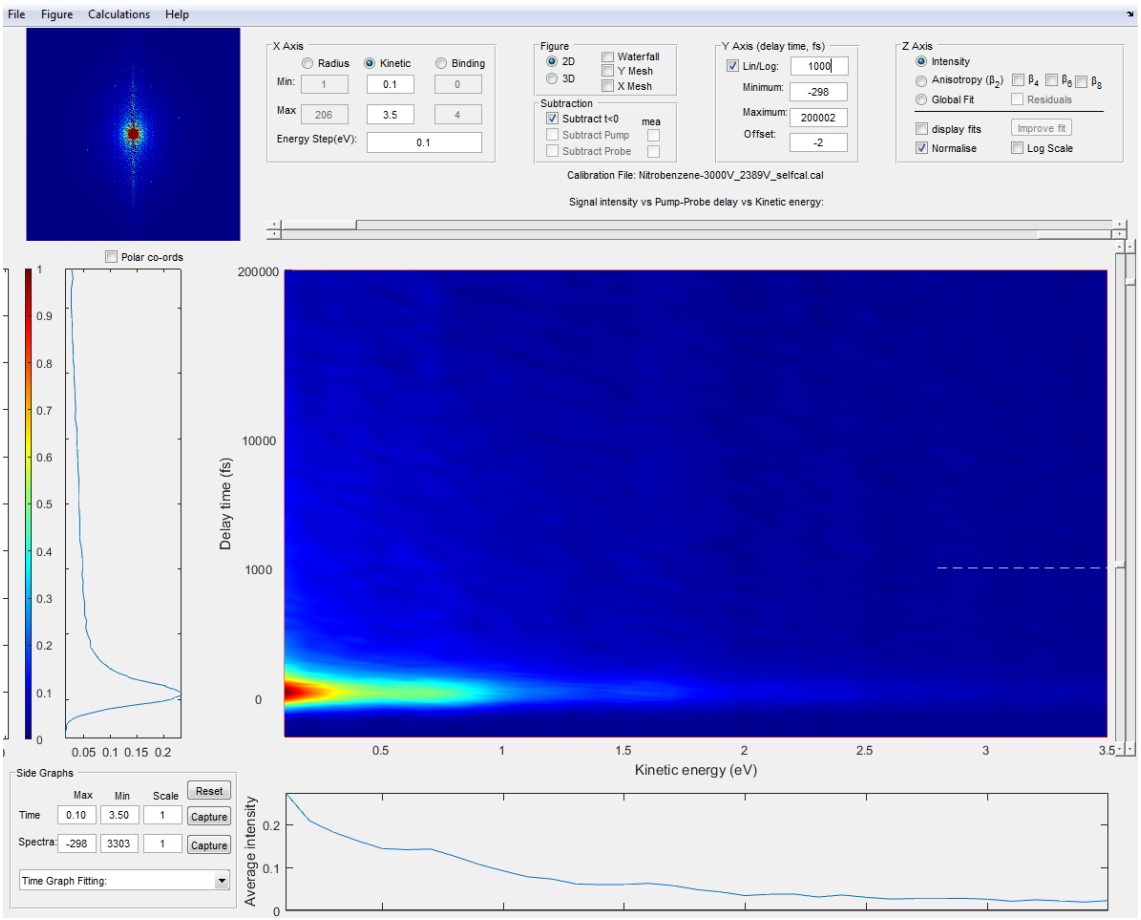

Figure 2.20: The GUI for the *Analyse* part of *REPEITS*. The functionality to fit β_6 and β_8 as shown in the top right hand corner of the GUI was coded by myself (see main text for details). The data shown here is a test on nitrobenzene (see Chapter 5).

2.5.1 Photoelectron Angular Distributions

TRPEI is a highly differential method. So far the extraction of time- and energy-resolved information has been discussed, however angular information can also be extracted and aids in the understanding of the relaxation process. As the surfaces of the Newton spheres created during the photoionisation process [160] are anisotropic, the observed signal is not homogeneous over the surface of the sphere. As discussed in Chapter 1, for photoionisation experiments, the angular distribution provides information about the orbital from which the electron was ejected [11, 14, 71, 72]. This angular distribution, for a two-photon process is given by

$$I(E, \Delta t, \theta) = \frac{\sigma(E, \Delta t)}{4\pi}[1 + \beta_2(E, \Delta t)P_2(\cos\theta) + \beta_4(E, \Delta t)P_4(\cos\theta)], \tag{2.19}$$

where $\sigma(E, \Delta t)$ is the time-dependent electron energy distribution and P_n are the Legendre Polynomials. The β terms describe the degree of anisotropy [71] and vary between $(-1 \leq \beta \leq 2)$. If higher-order photon processes are expected the expression has to be adjusted to

$$I(\theta) \propto \sum_n a_{2n} P_{2n} \cos\theta, \tag{2.20}$$

where n is the photon order. So, as above, if it is a two-photon process $(1 + 1')$ a_4 and P_4 are the maximum terms required. The spectral and temporal evolution of β, extracted by *Analyse*, aids in interpreting the TRPEI data.

The *REPEITS* program was originally capable of only fitting up to β_4. The capability to fit up to and including the β_8 term using *REPEITS* was added by myself in order to fit the data presented in Chapter 5 of this thesis. In this data, multi-photon processes up to the fourth order are observed and therefore the anisotropy fit has to include Legendre polynomial terms up to β_8. The above expression in Equation (2.19) therefore has to be extended to include two further even terms

$$\begin{aligned} I(E, \Delta t, \theta) = \frac{\sigma(E, \Delta t)}{4\pi}[1 + \beta_2(E, \Delta t)P_2(\cos\theta) + \beta_4(E, \Delta t)P_4(\cos\theta) \\ + \beta_6(E, \Delta t)P_6(\cos\theta) + \beta_8(E, \Delta t)P_8(\cos\theta)]. \end{aligned} \tag{2.21}$$

2.6 Conclusion

This chapter has introduced the various components required to perform time-resolved photoelectron imaging experiments. Initially, a brief review of the basic principles of femtosecond lasers and nonlinear optics was presented which was followed by a discussion of the two optical configurations used to perform the UV + UV and UV + VUV experiments, respectively. Subsequently, the TRPEI spectrometer was outlined, including sample delivery methods. The final section of this chapter outlined how the *REPEITS* program is used for data acquisition, processing and analysis.

Chapter 3

Theoretical Methods

It is often beneficial to support the experimental time-resolved photoelectron imaging measurements described in the previous chapter with quantum chemistry calculations. These can be used to determine the states which are initially excited and to identify the molecular states playing a role in the relaxation dynamics. This is crucial to the interpretation of time-resolved studies. Furthermore, in Chapter 5 quantum chemistry calculations are used to determine whether the molecular structures investigated are conformationally locked under experimental conditions. In this chapter a brief introduction to the principles and methods used in computational quantum chemistry, relevant to the work presented in this thesis, will be provided.

Computational chemistry methods have advanced from the first attempts to solve the Schrödinger equation (SE) for hydrogen to modelling larger molecules and even protein folding. Here, it is important to note that there are two approaches: classical and quantum mechanical. Methods based on classical mechanics such as *force-field methods* or *molecular mechanics* can be used for large biological molecules. For much smaller systems, however quantum mechanical methods can be used to provide high-accuracy predictions. The molecular structure, energy and further properties of a molecule can be computed using these methods; bond formation and breaking can also be predicted. Quantum chemical methods can be grouped into two approaches: *semi-empirical* methods and *ab initio* methods. For the purposes of this work *ab initio* (from first principles) methods are relevant; they include wavefunction methods such as the Hartree-Fock (HF) approach but also density functional theory (DFT).

In this chapter, methods for solving the SE will be discussed initially, followed by an introduction to the Hartree-Fock method and an overview of "post-HF" methods. This is followed by a detailed discussion of DFT, and methods to compute excited states such as *time-dependent* DFT (TD-DFT) which was mainly used for the work presented in Chapter 6. The second half of this chapter will look at how these methods are employed and how results are analysed.

3.1 Solving the Schrödinger Equation

Quantum chemistry methods aim to solve the Schrödinger equation in order to obtain the wavefunction, which can then be used to predict a given molecular property. In this context, the only system for which the SE can be solved *exactly* (analytically) is hydrogen (H_2+) or any system containing one electron. For larger atoms or molecules (for any system with more than one electron) approximations are necessary. In operator form the Schrödinger equation is

$$\hat{H}\Psi_i = E_i\Psi_i \tag{3.1}$$

where Ψ_i is the wavefunction of the ith state and E_i its energy. The complete molecular wavefunction is dependent on a total number of $3M+4N$ variables, where M is the number of nuclei and N the number of electrons. This large number of variables contributes to the complexity of the problem. The Hamiltonian is comprised of all the terms making up the energy of a system, so for a molecular system it is given by

$$\hat{H} = \hat{T}_e + \hat{V}_{ee} + \hat{T}_n + \hat{V}_{nn} + \hat{V}_{ne}. \tag{3.2}$$

Here, $\hat{T}$ and $\hat{V}$ are the kinetic and potential energies, respectively. The subscripts n and e denote the nuclei or electron respectively, and combinations of both denote interactions between them. As Equation (3.2) shows, the energy of a molecular system consists of the kinetic energies of the nuclei and electrons as well as the potential energies arising from their attractive and repulsive interactions.

As already noted, the total molecular wavefunction is dependent on a large number of variables. It is therefore desirable to reduce this number to simplify the problem. This can be done using the Born-Oppenheimer approximation introduced in Chapter 1. In the BO approximation the nuclei can be considered as fixed and the SE for only the electrons can be solved in a constant field produced by the nuclei. The SE is simplified to the electronic SE

$$\hat{H}\Psi_e = E_e\Psi_e, \tag{3.3}$$

where Ψ_e is now the electronic wavefunction which can be denoted $\Psi(r_i; R_A)$ where r_i are the electronic coordinates and R_A are the nuclear coordinates which can be treated as parameters, similarly to the electronic charge, for example. Finally, the Hamiltonian is simplified, as the nuclear repulsion and nuclear kinetic energy operator can now be excluded, yielding

$$\hat{H}_e = \hat{T}_e + \hat{V}_{ee} + \hat{V}_{ne}. \tag{3.4}$$

It should be noted here that, to obtain the total energy of the system, the nuclear

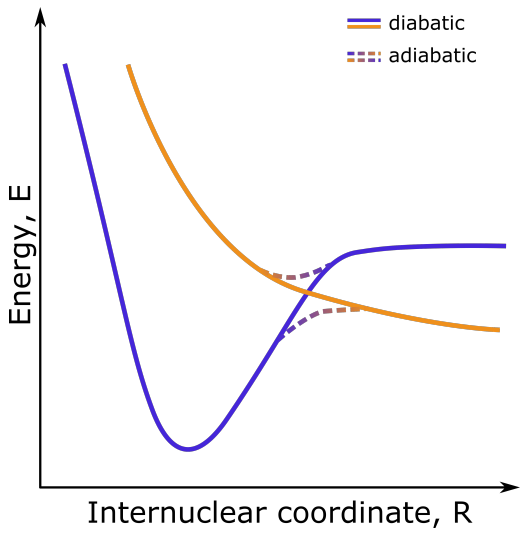

Figure 3.1: A sketch illustrating adiabatic and diabatic curves. The dashed lines indicate what the adiabtic curves would show in a region where the two potential energy curves may be approaching degeneracy. R is a nuclear coordinate of interest.

repulsion does still need to be taken into account

$$E_{tot} = E_e + V_{nn}. \tag{3.5}$$

Fixing the nuclei positions and solving the SE at various nuclear geometries to obtain the electronic energy results in a multidimensional potential energy surface (PES). For molecules (non-linear) the PES has $3M$- 6 dimensions, where M again is the number of nuclei. These complex surfaces may exhibit stationary points including first order saddle points (transition states) and local and global minima. When the electronic states become degenerate, as in Figure 1.4, the BO approximation does, however, break down. It is non-BO terms that are responsible for the coupling of different electronic states. As introduced in Chapter 1, this breakdown of the BO approximation is a crucial concept when studying the relaxation dynamics of molecular systems, as it is observed near conical intersections (CI). Before continuing in the discussion it is necessary to define the terms adiabatic and diabatic, which can be done with the aid of Figure 3.1. Adiabatic surfaces, which are the result of the BO approximation, are indicated by the dashed lines. They do not cross but vary rapidly as a function of the internuclear coordinate in regions of strong non-adiabatic coupling. Crossings are determined by the breakdown of the BO approximation and are therefore diabatic. Importantly, the adiabatic states change along the nuclear coordinate. The "blue" diabatic state 'transforms' into the "orange" diabatic state as the internuclear coordinate, R evolves. This will be important later on in this chapter when the data analysis is discussed. The concept of adiabatic and diabatic states is discussed only briefly here, and a more complete discussion can be found in reference [161].

3.1.1 Basis Sets

Before introducing the methods used to solve the SE, this section will discuss the use of basis sets. The electronic wavefunctions or molecular orbitals (MO) are unknown but can be described using a set of known functions. The set of known functions is referred to as a *basis set* which consists of *basis functions*. If this set is complete, i.e. if there is an infinite number of known functions, the description of the unknown function will be exact. However, an infinite set of functions is not possible numerically, so a finite number has to be chosen. Increasing the size of the basis set will improve the accuracy of the description of the MOs. The issue with this lies in the computational cost which scales as C^4 where C is the number of heavy atoms (not hydrogen) [162]. Therefore, it is important to achieve a good balance between accuracy and feasibility when choosing a basis set. The basis functions are also referred to as *atomic orbitals* (AO) and a linear combination of these can be used to describe the molecular wavefunction/orbital:

$$\phi_i = \sum_{\alpha}^{M} c_{\alpha i} \chi_\alpha, \tag{3.6}$$

where χ_i are the basis functions (or AOs), M is the total number of basis functions in the basis set and the coefficients c_i are the contributions (weights) to the total molecular wavefunction (MO) ϕ_i. There are two common types of functions used to describe AOs; Slater type orbitals (STO) or Gaussian type orbitals (GTO). STOs use spherical harmonics and provide the most accurate description of an AO. The GTOs, however are much simpler to compute and even though the number of GTOs required to obtain a similar accuracy to a Slater type is nearly triple, they are still often favoured [162].

As discussed above, it is desirable to keep the number of basis functions low but the basis set must have sufficient flexibility to describe all MOs required. For example, diffuse basis functions are needed for anions or excited states, in order to take into account electrons further from the core. The typical functions added are only s- and p-wave functions, but higher angular momentum functions can be important for many systems. These are known as *polarisation functions*. By examining the role of different basis functions more closely, the number of basis functions required to produce an accurate description of the system can be reduced. For example, the electrons in the inner orbitals, such as 1s, are critical when predicting the molecular energy. For chemical reactions, however it is the valence electrons that are of interest. Most of the basis functions are typically used to describe the inner shell electrons, thereby neglecting the outer valence region. This means that a lot of computational effort goes into describing the chemically uninteresting and nearly constant part of the system. This is where *contracted* basis sets [162] were introduced. In such basis sets the coefficients of the inner basis functions are fixed, thereby reducing

the amount of parameters that have to be evaluated using the variational method. Examples of this are the Pople style basis sets [163], such as *k-nlmG* basis sets. Here, k represents how many primitive GTOs have been contracted to represent the core orbitals, *nlm* indicates how many functions the valence orbitals have been split into and how many primitive GTOs are used to represent them. Any values after G indicate whether polarisation functions have been included. The largest Pople style basis set is 6-311++G(3df,3pd) where the ++ indicates that diffuse functions have been added, even to hydrogen.

A minimal basis set such as STO-3G contains the lowest number of basis functions required to describe the AOs on every neutral atom in the molecule. So for carbon or nitrogen this would be two s-functions (1s and 2s) and a set of p-functions (2p). The accuracy can be improved by employing more of these functions of varying size, on a neutral atom. This is the purpose of ζ basis sets. A double ζ (DZ) basis set will add double the number of functions, and triple (TZ) or quadruple (QZ) are also possible. This is important when describing the orbitals in molecules where σ and π bonding orbitals are common.

Often used for work presented here is the *aug-cc-pVnZ* basis set, where n has been substituted for *D,T,Q* which stand for double, triple, quadruple. This is the correlation consistent (*cc*) basis set proposed by Dunning and co-workers [164]. The *aug-*, denoting augmented, means that one diffuse basis function is added to every atom and for every angular momentum required (s,p,d etc.). An example of this would be that the *cc-pVTZ* basis set uses s,p,d and f functions on carbon; including *aug-* would then add diffuse subshells to s,p,d and f [165]. Pople basis sets for comparison, use only minimal augmentation [166] unless the + or ++ options are used. An overview of numerous basis sets and their performance, as well as more in depth discussion on the topic can be found in references [167] and [168].

3.1.2 Hartree-Fock Theory

Now that the problem has been set up, a discussion of the basic approach to solving the SE for a molecular system will be presented in this Section. Firstly, the electronic wavefunction has to be constructed. The wavefunction of a single particle can be described as an orbital. A combination of the electron's spatial orbital and spin function - a *spin orbital* - is required to describe the complete electron orbital. The electronic wavefunction can then be written as a linear combination of these spin orbitals for all electrons. This approach is known as the Hartree-product [169]. However, a vital factor is missing in this description: the orbitals must be antisymmetric with respect to particle interchange as dictated by the Pauli principle. So, the original Hartree-product can be improved by including this antisymmetry

condition. This is done in the Slater determinant (SD) [170]

$$\Psi_{SD} = \frac{1}{\sqrt{N}} \begin{vmatrix} \phi_1(1) & \phi_2(1) & \cdots & \phi_N(1) \\ \phi_1(2) & \phi_2(2) & \cdots & \phi_N(2) \\ \vdots & \vdots & \ddots & \vdots \\ \phi_1(N) & \phi_2(N) & \cdots & \phi_N(N) \end{vmatrix}, \quad \langle \phi_i | \phi_j \rangle = \delta_{ij} \tag{3.7}$$

This SD describes a system with N electrons. The terms in the brackets give the positions and spins of the electron. Furthermore, ϕ denotes the one-electron wavefunctions (a wavefunction describing a single electron), which are termed the *molecular orbitals* (MO). Describing the dynamics of a system with several electrons is challenging but can be simplified using independent-particle models. Those are models that disregard some particle interactions. One of these is the Hartree-Fock (HF) [171, 172] method, which treats all particle interactions using a mean-field approach [162]. This average treatment originates from the above Slater determinant as one main assumption is that only a single SD is used to describe the wavefunction. It assumes that each electron moves independently of all the other electrons in the system, which are included by a Coulomb repulsion potential constructed using their average positions.

The Slater determinant describes the best electronic wavefunction, within the approximation that a combination of one-electron wavefunctions can describe a molecular system. In order to determine the best orbitals (one-electron wavefunctions) the variational theorem is applied. The variational theorem states

$$\langle \Psi_{guess} | \hat{H} | \Psi_{guess} \rangle \geq \varepsilon_0 \tag{3.8}$$

where ε_0 is the exact ground state energy and Ψ_{guess} is a trial wavefunction. It implies that the trial wavefunction resulting in the lowest energy is the best guess. So the wavefunction must be minimised in order to solve the problem. It should be noted that this theorem is an aid to solving the problem numerically, as it is analytically impossible for any system bigger than hydrogen. All the above can be combined to construct the Hartree-Fock equations using the Fock operator $\hat{F}$. The Fock operator includes the kinetic energy of the electron, its repulsion from the other electrons in the system and attraction to the nuclei:

$$\hat{F}_i = \hat{h} + \sum_{j}^{N} (\hat{J}_j - \hat{K}_j). \tag{3.9}$$

$\hat{h}$ is the one electron energy operator which describes the motion of electron i in the average field produced by the nuclei. The interaction of the electron with all others (subscript j) in the system is described using the Coulomb and exchange operators, $\hat{J}$ and $\hat{K}$ respectively. The Coulomb operator deals with the repulsion from other

electrons in an average fashion as mentioned above. The Fock operator is not a Hamiltonian however, as it describes the variation of the energy, rather than the total energy itself. The Hartree-Fock equations are given by

$$\hat{F}_i\phi_i = \sum_j^N \lambda_{ij}\phi_j, \tag{3.10}$$

where ϕ are still the MOs. This is obtained by minimising the energy with the constraint that the MOs are mutually orthogonal. The λ_{ij} terms are the Lagrange multipliers used in this process. Here, i denotes the electron being described, while j are the other electrons in the system. Importantly, a set of pseudo-eigenvalue equations can be formed using the canonical MOs ϕ', chosen such that $\lambda_{ij} = 0$ unless $i = j$,

$$\hat{F}_i\phi'_i = \varepsilon_i\phi'_i. \tag{3.11}$$

By expanding the MOs as in Equation 3.6, the HF equations in the atomic orbital basis are obtained, also known as the *Roothaan-Hall* equations [173, 174].

As the Coulomb and exchange operators ($\hat{J}$ and $\hat{K}$) in the Fock operator are dependent on all (occupied) MOs, an iterative method known as the *self consistent field* (SCF) scheme can be used to solve Equation (3.11). In the SCF scheme a basis set of choice is used to construct the initial MOs where a guess is made for the coefficients $c_{i\alpha}$ (from Equation (3.6)). Using this, $\hat{J}$ and $\hat{K}$ can then be computed and $\hat{F}$ is found. The Roothaan-Hall equations can then be solved, yielding new eigenvectors which are a new set of $c_{i\alpha}$ coefficients. Now we have returned to the first step, and the new $c_{i\alpha}$ coefficients can be used to improve the description of the MOs. This continues until the scheme has converged. The procedure is based on the variational theorem: the lower the energy produced using the orbitals, the better they are.

Further approximations can be made to the HF equations, leading to semi-empirical methods for the treatment of large systems. The HF method itself can also be made more accurate by adding ways to take into account the electron correlation that has been treated in an average fashion up until now. This will be discussed below.

3.2 Methods to Include Electron Correlation

The Hartree-Fock method is the foundation of much of electronic structure theory. It averages the electron-electron interaction, or electron correlation (EC), and accounts for 99 % of the energy in the system [162]. The remaining 1 % that is not described however, is related to the electron correlations. These correlations can potentially be crucial when modelling chemical behaviour and therefore many *post*-HF methods have found ways to address this issue and include the electron correlation.

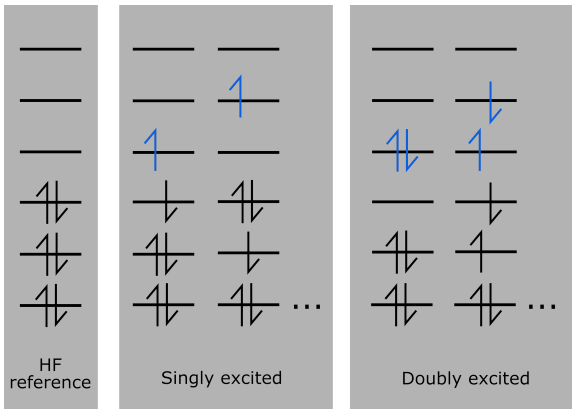

Figure 3.2: An illustration of some excited configurations, from the HF reference configuration. Electrons are moved into virtual orbitals. This creates the additional SDs to include electron correlation. The orbitals unoccupied in the HF reference configuration are virtual orbitals, which can be filled up to achieve more electron configurations.

Examples of such methods are configuration-interaction (CI), Møller-Plesset perturbation theory (MP) [175] or coupled cluster theory [176, 177] (CC). The electron correlation energy for a system describes the difference between the exact ground state energy and the energy calculated using the HF method [178]. This term can also be divided into two subcategories: static and dynamical electron-correlation. The static EC simply describes different electron configurations that may exist in the system, whereas the dynamical EC describes how the motion of one electron is dependent on that of the others in the system (repulsion).

The post-HF methods add corrections to the reference HF wavefunctions, by adding extra SDs to the single HF determinant:

$$\Psi_{EC} = a_0\Psi_{HF} + \sum_{i=1} a_i\Psi_i. \tag{3.12}$$

Here, Ψ_{EC} is the new wavefunction to include electron correlation, Ψ_{HF} is the original HF wavefunction consisting of the single SD and Ψ_i the new additional SDs. The coefficients a_i now need to be determined, and how this is done depends on the type of electron correlation method employed. These additional SDs are constructed by "exciting" an electron from the original HF reference configuration into the virtual orbitals present (unoccupied orbitals that have been produced by the basis functions). Figure 3.2 illustrates this concept of exciting from the HF reference. They are therefore also referred to as *excited* Slater determinants. It can easily be seen how this now takes into account the various electron configurations that exist in a system (static electron correlation). All possible permutations are taken into account and each one is represented by a Slater determinant. The reference configuration may be singly, doubly, triply or quadruply excited and the corresponding Slater determinants are then referred to as *Singles*, *Doubles* etcetera. Again, this

concept is illustrated in Figure 3.2.

3.2.1 Configuration Interaction Method

The configuration interaction (CI) method takes into account the static electron correlation, by linearly adding these excited SDs to the HF reference wavefunction. Similarly to the HF method, CI also uses the variational theorem to evaluate the coefficients of the CI wavefunction. They are varied until a minimum energy is found. A *full* CI (FCI) method, including all possible configurations of electrons, combined with an infinite basis set is very powerful as it would give the *exact* solution to the time-independent SE (not including relativistic effects). Except for very small systems, this is unfortunately impossible. CI methods are therefore often truncated to CI with *Singles* (CIS), CI with *Singles & Doubles* (CISD) and so on. The multi-configuration self-consistent field (MCSCF) field approach is similar to CI. In this scheme not only the coefficients but also the MOs are varied until they are optimised [179]. This is done within the iterative SCF scheme mentioned earlier. Of particular interest here is the *Complete Active Space Self-consistent Field* (CASSCF) method. This is based on MCSCF, but as with CI it is impossible to include all possible configurations for any larger system. In CASSCF the number of configurations included is reduced as the MOs are partitioned into an *active* and an *inactive* space. A select number of MOs chosen by the user is included into the active space and a full CI is then carried out on this reduced space, with all configurations included in the MCSCF optimisation. In this way the number of configurations is greatly decreased in comparison to the full system. The notation for the active space is given by $[n,m]$, with n being the number of electrons in the active space and m the number of orbitals included. Both occupied and virtual orbitals should be chosen to be in the active space, to allow for different configurations/permutations. CASSCF is by no means trivial, as the appropriate active space is dependent on what feature of the system is to be investigated and has to be chosen carefully. However, CASSCF is a very powerful method as conical intersections can be identified using this method.

3.2.2 Møller-Plesset Perturbation Theory

The CI method outlined above can also be expanded by using more than a single determinant as the reference. In fact an MCSCF wavefunction can be used as a reference, and so excitations from all the determinants in the MCSCF wavefunction are included. In this way, a *single-reference* method such as CI, can be evolved to a *multi-reference*(MR) method known as MR-CI. However, the large number of configurations makes this method very computationally expensive. A method of truncating MR-CI, and thereby making it computationally more feasible, is through selecting only configurations that interact with the reference; these are then known

as state selected methods. Perturbation theory can be used to determine such configurations.

Perturbation theory is used in quantum mechanics and is based on the principle that *small* stimulus or change (the perturbation) is added to a known system. The effect of the change on the system can then be studied. In general, in perturbation theory the stimulus to the system manifests in the Hamiltonian as

$$\hat{H} = \hat{H}_0 + \lambda \hat{H}' \tag{3.13}$$

where $\hat{H}_0$ is the known Hamiltonian and λ is the perturbation parameter which determines the strength of the perturbation. The perturbed SE is

$$\hat{H}\Psi = W\Psi. \tag{3.14}$$

In the presence of a perturbation the energy W and new wavefunction Ψ can be expressed as Taylor series. Using this approach the first order correction, as well as higher order corrections, to the known wavefunction and energy can be computed. This approach is used in *Møller-Plesset* perturbation theory (MP) [175]. MP theory adds perturbations to the HF wavefunction to correct for missing electron correlation effects. MP methods may go up to a number of corrections (named MPn) but MP2 is the most common MP method, going up to second order corrections:

$$W = E^{(0)} + E^{(1)} + E^{(2)} = E_{HF} + E^{(2)}. \tag{3.15}$$

$E^{(1)}$ and $E^{(2)}$ are the corrections (first- and second-order) to the unperturbed result. The zeroth order correction is just the HF energy and $E^{(1)}$ is zero. Therefore, it is only at second order correction level that electron correlation is accounted for. MP2 accounts for 80% - 90% of the electron correlation energy [162] and is a relatively computationally inexpensive approach as it scales as M^4 for M basis functions. MP3 and MP4 methods achieve higher accuracies in the accounting for electron correlation but their computational costs increase as M^6 and M^7 respectively. It should be noted that MP2 is not a variational method and therefore can produce results below the true energy. The MP2 method was used to compute the ground state energy curves for nitrobenzene and its methyl derivatives discussed in Chapter 5.

3.2.3 Coupled Cluster Method

Another principal method which includes electron correlation is the Coupled Cluster (CC) approach. The CC wavefunction is given by

$$\Psi_{CC} = e^{\hat{T}}\Phi_0. \tag{3.16}$$

From the above expression we can see that the CC method uses an operator $\hat{T}$ to act on the HF reference wavefunction Φ_0. This operator is known as the *excitation operator*, [162] or *cluster operator*, [180] and is defined as

$$\hat{T} = \hat{T}_1 + \hat{T}_2 + \hat{T}_3 + ... + \hat{T}_N, \tag{3.17}$$

where N is the number of electrons. As before, excited SDs are used but in this CC method they are generated using the cluster operator [180]. The operator $\hat{T}_2$, for example, describes all the double excitations from the mean field; $\hat{T}_3$ all triple excitations from the mean field etcetera. While this operator is also used by the CI method described above, the novelty in the CC method is the fact that the cluster operator is found in the exponent:

$$e^{\hat{T}} = 1 + \hat{T}_1 + \left(\hat{T}_2 + \frac{1}{2}\hat{T}_1^2\right) + \left(\hat{T}_3 + \hat{T}_2\hat{T}_1 + \frac{1}{6}\hat{T}_1^3\right) + ... \tag{3.18}$$

The CC method can therefore take into account the corrections (*S, D, T, Q*) to an infinite order of perturbation and also includes disconnected terms ($\hat{T}_1^2$, or $\hat{T}_2\hat{T}_1$). This provides a significant improvement to the CI approach. Again this method can be truncated, for example to CCSD, the coupled cluster *singles* and *doubles* approach. Even when truncating the method at single and double excitations however, higher order disconnected terms are still included. Due to these disconnected terms the CC method is also considered to be size extensive. It should be noted here that the higher order the correction terms become the less likely it is for these deviations from the mean field to occur, therefore higher order corrections will provide a smaller improvement to the energy.

3.3 Density Functional Theory

A paradigm shift in quantum chemistry was achieved with the introduction of *density functional theory* (DFT). Walter Kohn received part of the Nobel prize for "his development of the density-functional theory" in 1998 [181] (jointly with John A. Pople who received the prize for his work on computational methods in quantum chemistry). DFT was proposed 34 years prior to that by both Kohn and Hohenberg [182], who proved that the electron density ρ can be used to exactly determine the ground-state electronic energy (and all other properties) of a system. This avoids the need to find the wavefunction and solve the SE to obtain the energy. In comparison to the wavefunction which is dependent on $4N$ parameters, where N is the number of electrons in the system, the electron density ρ is dependent only on three spatial parameters.

As already discussed, the ground state energy E_0 is determined by the electronic Hamiltonian, and in fact all the information contained in the Hamiltonian (number

of electrons and nuclei, their charges and positions) can be described using only the electron density, ρ. Since ρ can provide all the information stored in the Hamiltonian it can also provide the ground state energy of the system. This idea was proposed by Hohenberg and Kohn and is known as the first Hohenberg-Kohn theorem. The link between ρ and E_0 is a functional. A functional is a function of which the argument is another function. When this exact Hohenberg-Kohn functional is known it can provide the exact ground state energy using ρ. It assigns a single value E_0 to a given electron density. Since ρ also determines the wavefunction, other ground state properties can also be extracted [183]. In their second theorem Hohenberg and Kohn [182] provided a way of knowing how good a proposed functional is [183]. This is once again, based on the variational principle:

$$E_{HK}[\rho_{guess}] \geq E_{exact}. \tag{3.19}$$

The perfect functional E_{HK} would provide the exact energy. Similarly, if the functional is known ρ_{guess} can be optimised. This perfect functional has not been suggested yet, however new functionals are created at a rapid rate, dealing with the approximations made in the Hohenberg-Kohn (HK) functional and improving results for specific systems.

The energy functional must consist of three parts: the attraction between electrons and nuclei, the kinetic energy and the electron-electron repulsion. It became possible to use DFT for computational chemistry with the introduction of spatial orbitals by Kohn and Sham [184]. Using the Kohn-Sham (KS) approach the electron density is expanded as

$$\rho = \sum_i \left|\Psi_i^{KS}\right|^2, \tag{3.20}$$

where Ψ_i^{KS} are the Kohn-Sham spatial orbitals. Previous models for describing the energy functional were based on the assumption that the system was a non-interacting uniform electron gas (*Thomas-Fermi* model), which is not true for molecular systems and did not allow for the descriptions of chemical bonds. Kohn-Sham theory obtains the energy (kinetic) of the system using the assumption that electrons are non-interacting. So, to account for the electron interaction, an *energy exchange* E_{XC} term has to be added, which includes electron correlation and exchange (spin correlations). This means the DFT energy can be expressed as:

$$E_{DFT}[\rho] = T_S[\rho] + E_{ne}[\rho] + J[\rho] + E_{XC}[\rho], \tag{3.21}$$

where T is the kinetic energy of the system, E_{ne} is the attraction between the electrons and nuclei and J is the Coulomb part of the electron-electron repulsion.

The KS orbitals are obtained from the Kohn-Sham equations:

$$\left(-\frac{1}{2}\nabla_i^2 - \sum_{\text{nuclei A}} \frac{Z_A}{\mathbf{r}_{1A}} + \int \frac{\rho(\mathbf{r_2})}{r_{12}} d\mathbf{r}_2 + \frac{\delta E_{XC}[\rho]}{\delta \rho}(\mathbf{r}_1)\right) \Psi_i^{KS}(\mathbf{r}_1) = \varepsilon_i^{KS} \Psi_i^{KS}(\mathbf{r}_1). \tag{3.22}$$

Similarly to HF theory the Kohn-Sham equations are solved in a self-consistent manner since the KS Hamiltonian is itself dependent on the electron density ρ.

The energy exchange term E_{XC} is what would allow for the exact total energy of a system to be determined using DFT, including electron correlation. DFT can therefore theoretically provide the correlation energy at a relatively low computational effort (the same level as HF). The challenge lies in constructing an exact exchange functional. This is where ideas such as the *Local Density Approximation* (LDA) and *Generalised Gradient Approximations* (GGA) come in. The LDA assumes that the electron density can be treated as a uniform electron gas locally, and has been updated to include spin (*Local Spin Density Approximation* - LSDA), but does not provide very accurate results for the exchange energy. It was improved upon by the GGA which includes the first derivative of the electron density [162]. An example is the B88 correction introduced by Becke [185]. *Meta*-GGA methods include higher order derivatives, again improving accuracy. This can be extended to *hybrid* functionals which use a combination of the exact exchange, LSDA and gradient correction terms. In theory, the functionals can be improved until an exact result is achieved, this concept is illustrated by Jacobs ladder for functionals [186]. A sketch of the concept can be found in Figure 3.3.

An example of a hybrid GGA functional is the B3LYP [187, 188] functional, again proposed by Becke, which is described by

$$E_{XC}^{B3LYP} = (1-a)E_X^{LSDA} + aE_X^{exact} + b\delta E_X^{B88} + (1-c)E_c^{LSDA} + cE_c^{LYP}. \tag{3.23}$$

The B3LYP functional uses the electron exchange energy from a HF calculation in combination with the exchange and correlation energy from a local density approximation (LDA) approach and generalised gradient approach (GDA). The parameters *a, b* and *c* are found by using experimental reference data or can be varied for best results. This gives the B3LYP functional a great amount of flexibility. The B3LYP functional often performs well and is therefore commonly used [189]. An extension to the B3LYP functional, which is particularly well suited to excited state calculations as well as describing Rydberg states, is CAM-B3LYP. Proposed by Yanai, Tew and Handy in 2004, it adds a long-range correction to the B3LYP hybrid. This long-range correction introduces the percentage HF exchange continuously as a function of the interelectronic distance. This is in contrast to the B3LYP functional where there is a distinct point at which this is switched on or off instead. The B3LYP and CAM-B3LYP functionals are employed in Chapters 6 and 5 for the ground state geometry

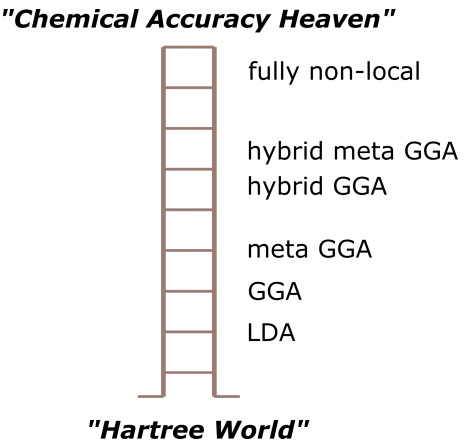

Figure 3.3: Principle of Jacob's ladder of functionals as laid out in reference [186]. The functionals can be improved until, theoretically, the exact total energy can be recovered.

optimisation or excited state calculations using time-dependent DFT. Only the functionals relevant to this thesis have been discussed here, for a discussion of further functionals and details of these the reader is directed to references [162, 183, 189].

3.4 Probing Excited States

The methods described above are for determining ground state properties and energies. For spectroscopy and especially for the study of UV-induced relaxation dynamics it is however, crucial to be able to compute the excited state energies and properties. Methods including *equation of motion coupled cluster* (EOM-CC) theory and *time-dependent* DFT (TD-DFT) can be used to do exactly that.

As the naming of the methods already implies, it is necessary to take into account the time-dependence in order to describe excited states and their properties. As the energy functions are not well defined in time-dependent cases, the perturbation or derivative approaches used for ground state properties cannot describe excited states. Instead, response theory is used to achieve this description of the excited states [190]. The time-dependent version of the perturbed Hamiltonian is given by

$$\hat{H}(t) = \hat{H}_0 + V(t), \tag{3.24}$$

where $V(t)$ is an oscillating electric field and introduces the time-dependence.

In the case of EOM-CC the excited state can be generated by applying the *linear excitation operator* $\hat{\mathscr{R}}$ to the CC ground state wavefunction [191]. The SE is then given by

$$\hat{H}\hat{\mathscr{R}}e^{\hat{T}}\left|\Phi_0\right\rangle = E\hat{\mathscr{R}}\left|\Phi_0\right\rangle, \tag{3.25}$$

where $\hat{T}$ is the coupled cluster operator introduced earlier in Equation 3.17. Both $\hat{T}$ and $\hat{\mathscr{R}}$ are excitation operators. This yields the following effective Hamiltonian

($\hat{H}_{\text{eff}}$)

$$\hat{H}_{\text{eff}} = e^{-\hat{T}} \hat{H} e^{\hat{T}}. \tag{3.26}$$

The energies and eigenstates of this effective Hamiltonian can be obtained as previously. As the Hamiltonian is non-Hermitian, care must be taken when solving for the system properties, since the left and right eigenvectors are no longer Hermitian conjugates [191]. The energies however, can be extracted as for Hermitian systems. An in-depth discussion of this is beyond the scope of this thesis. Furthermore, as in the Coupled-Cluster method for ground state systems described earlier, higher order excitations are included due to the nature of the operator being in the exponent. The EOM-CC including *Singles* and *Doubles* (EOM-CCSD) method is commonly regarded as a highly accurate method for small to medium sized systems, considering its fairly large computational cost [192, 193]. Extensive benchmarking of CC methods for calculating excited states (and oscillator strengths) has been reported in references [194, 195], and citations therein. As an illustration, D. Kánnár *et al.* report that the CCSD method (for excited state energies) shows deviations of 0.3 eV or less when compared to the CC3 method in 104 calculations. Furthermore its standard deviation (with respect to CC3 results), is better than that of the CC2 method also tested.

Response theory is also used to obtain the TD-DFT approach. TD-DFT is based on DFT. Initially, Zangwill and Soven [196] added a time-dependent perturbation (such as a time-varying electric field) to a system in its ground state. They had to make the assumption that the exchange-correlation (xc) potential reacts without memory and instantaneously to a temporal change in charge density, which is now known as the *adiabatic approximation* and is used for almost all TD-DFT applications. Using this approximation the time-dependent Kohn-Sham equation is given by

$$\hat{H}_s[\rho_t]\Psi_p(\boldsymbol{r}, t) = i\frac{\partial \Psi_p(\boldsymbol{r}, t)}{\partial t} \tag{3.27}$$

which can be solved using linear response approaches where the change in electron density is assumed to depend linearly on the time-dependent perturbation. The subscript s denotes the single-particle Kohn-Sham Hamiltonian, Ψ_p are the orthonormal orbitals and $\boldsymbol{r}$=(x,y,z).

Runge and Gross provided the basis for modern TD-DFT with their two theorems. The first Runge-Gross theorem [197] is essentially a time-dependent version of the first Hohenberg-Kohn theorem. It shows that there is a mapping between the time-dependent electron density and a time-dependent external potential. It furthermore states that the initial wavefunction and time-dependent charge density can be mapped to the external potential v_{ext} plus an additive time-dependent function $C(t)$:

$$v_{ext}(\boldsymbol{r}, t) + C(t) \leftarrow (\rho(\boldsymbol{r}, t), \Psi_0). \tag{3.28}$$

The external potential of the system is a functional of the density. The mathematical details of the theoretical background for TD-DFT is beyond the scope of this thesis but a more detailed discussion and review of TD-DFT can be found in reference [198] and others. Furthermore, various publications have provided benchmarking of the TD-DFT method for calculating excited states with an extensive number of functionals a selection of which can be found in references [199–201]. For example, the study by M. R. Silva-Junior *et al.* [199] found the mean absolute deviation for the TD-DFT method in conjunction with the B3LYP functional to be 0.27 eV for singlet excited states when compared to theoretical proposed best estimates of 104 vertical excitation calculations (singlet). The B3LYP functional outperformed both the BP86 and BHLYP functionals also investigated in this study [199].

3.5 Implementations

This section will discuss how the computational results presented as part of this thesis were achieved, as well as some important points about the analysis of the computational output. For the work presented in this thesis the Gaussian computational chemistry program was used. This included three different versions: 03 [202], 09d [203] and 16 [48].

3.5.1 Ground State Geometries

The Gaussian program provides a GaussView [204] graphical user interface (GUI) which can be used to construct the molecules of interest. This method provides the locations of the atoms in Cartesian coordinates but can also be used to describe it in z-matrix notation which makes use of the interatomic properties, such as bond lengths and angles, to define the geometric structure. The ground state geometry has to be initially optimised. The algorithm will compute the ground state energy (using one of the aforementioned methods) of the system at a range of configurations, thereby constructing a potential energy surface. Subsequently the algorithm will search along the potential energy surface using the first and second derivatives ($\partial E/\partial \mathbf{x}$ and $\partial^2 E/\partial \mathbf{x}^2$) of the energy to locate the minimum. The latter is described by the Hessian, which is a matrix of the second order derivatives, and its eigenvalues carry information about the geometry of the surface (maxima, minima, saddle points). The user has to be aware that there are local and global minima, so some chemical intuition is required to test the ground state structure. Different structures may be optimised until the lowest energy one can be found. Here, it can be the case that the difference in energy between two structures is so small that they are both likely to exist in the supersonically cooled beam of the TRPEI experiment. Whether a stationary point on the PES has been found is determined by the first derivative of the energy and the second derivative allows for the identification of the

nature of this stationary point. The stationary point could be a minimum (positive second derivative), maximum (negative second derivative) or saddle point. A first order saddle point identifies a transition state (TS) structure. A frequency calculation (evaluating the vibrational frequencies) will reveal the nature of the stationary point. The number of imaginary frequencies found during a frequency calculation indicates of what order the saddle point is. A number n of imaginary frequency identifies an nth order saddle point [205]. This helps to identify the transition state structures at the top of the barrier as in, for example, Chapter 5, which is important for the determination of an accurate barrier height. The input geometries may also be restricted to a certain symmetry point group, such as in Chapter 5, where nitrobenzene has a high level of symmetry at C_{2v}, for example.

3.5.2 Potential Energy Curves

The ground and excited state potential energy surfaces along a specific coordinate can be produced by using the optimised geometry and for instance stretching a bond or rotating a group of interest with respect to the rest of the molecule. This can be done either in a *rigid* or a *relaxed* fashion. To illustrate this, an example where the coordinate of interest is a bond-specific stretch can be considered. For the relaxed structure, the rest of the molecule is reoptimised with only the bond of interest 'frozen' at a specific bond length. This is done for various different 'frozen' bond lengths. This builds up a relaxed energy surface, as in Chapter 5, where this was done for the ground state of nitrobenzene and its methyl-substituted derivatives. This relaxed ground state surface can then be used as a starting point for excited state calculations. When performing *rigid* calculations, the bond is still stretched, but the molecule is not reoptimised and excited state surfaces are produced from these rigid ground state references. The relaxed picture seems like a more accurate representation of nature. However, it must be considered to what extent this picture still reflects the change of the energy along the specific coordinate of choice as relaxing the structure will invariably alter a range of other coordinates in the molecule.

As already referred to in Section 3.1, in the adiabatic representation the nature of a state may change as the coordinate of relevance evolves. It should be noted here, that the nature of the adiabatic state is determined by the expansion coefficients discussed earlier in this Chapter (Section 3.1.2). Due to this change in character, it is not possible to simply take the output of the excited state calculations at each point along the coordinate and assume that the nature of the state remains the same. This idea is illustrated in Figure 3.4, which is based in Figure 3.1. If the data points shown are two different excited states, the dots need to be 'connected' in the correct order, to produce meaningful diabatic curves. The states are defined at the vertical excitation and 'tracked' from there. They are identified using the specific orbital

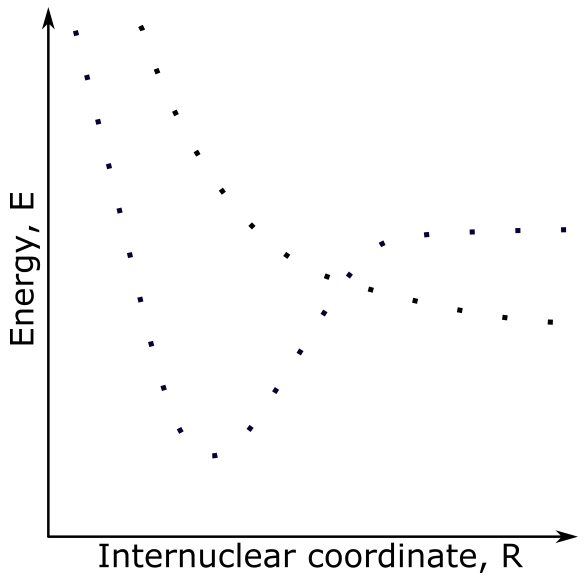

Figure 3.4: An illustration of the necessity to assign a label to each excited state and track this along the reaction coordinate in order to produce the more meaningful diabatic picture. With only two states to track, this seems quite straightforward, however the energetic second state may not correlate to the identified state at each point, so more excited states than required have to be computed, in case the state that is being tracked "moves up" in energy.

excitation components of the response eigenvectors (they will be referred to as *orbital contributions* from here onwards). Each excited state will consist of contributions from various transitions. Typically there is a major contribution which makes up around $> 75\%$ of the state. The state can then be labelled according to the nature of this major contribution (eg.: nπ^*, $\pi\pi^*$ etc.). It should however, be noted that not one excited state consists of exclusively one transition and so the state label is not an exclusive representation of the state. Some excited states may be of a very mixed nature where there are two or more significant contributions. This difficulty can, in many cases, be addressed by performing calculations to determine the *natural transition orbitals* (NTO) [206] which can help identify the major contributions to the states [207]. The NTOs provide a simplified description by identifying the orbital-to-orbital transitions that contribute most significantly to the state.

As the states cannot be ordered purely by energy, the output must be analysed by identifying the major orbital contribution at each point along the reaction coordinate and for each excited state. For molecules with a high symmetry this ordering is made easier as the symmetry label of the transition can be used. The oscillator strength is also useful in 'following' the states along the reaction coordinate. Since, during this analysis, the adiabatic surface is ordered into a diabatic surface, these surfaces may cross, implying a conical intersection might exist. Other molecular properties such as dipole moments can also be used to define diabatic states.

The orbitals themselves can be viewed as part of the output of the excited state calculations. These are crucial for assigning labels to the transitions but might also

give an indication towards the relaxation dynamics themselves. This is particularly evident for any states with Rydberg character. These may evolve more valence character upon a bond stretch for example, which indicates they should lower in energy as they contract. This may indicate the existence of conical intersections where non-radiative relaxation processes can take place.

3.6 Summary

In this chapter a brief overview of computational chemistry concepts and relevant *ab intio* methods was presented. The Hartree-Fock approach was initially discussed followed by an overview of post Hartree-Fock methods. Density functional theory, also used as a tool to obtain the properties of a molecular system, was introduced in Section 3.3. Following this, the EOM-CC and TD-DFT methods used to describe the excited states of a molecular system were introduced. The final section provided insight into some considerations for the analysis of the computational results obtained using the Gaussian software package [48, 202, 203].

Chapter 4

Relaxation Dynamics of Acetylacetone Using a Short-Wavelength Probe

The experimental data presented in this Chapter was collected and analysed by L. Saalbach and N. Kotsina. The initial design and construction of the experimental setup required for the production of the vaccuum UV light (including the vacuum chamber for steering optics and gas-cell arm for four-wave mixing) was carried out by M. Candelaresi and M. M. Zawadzki. This configuration was subsequently refined by N. Kotsina and L. Saalbach.

4.1 Introduction

As already introduced in Chapter 1, short-wavelength probes in time-resolved photoelectron imaging (TRPEI) experiments are desirable as the increased available energy allows us to follow the relaxation dynamics further - potentially all the way to the recovery of the ground state and the appearance of the photoproducts. Therefore, in this Chapter, the highly-differential TRPEI method is used in combination with high-energy probe pulses in the vacuum UV (160 nm) to study the ultrafast relaxation dynamics of acetylacetone (2,4-pentanedione).

Acetylacetone (AcAc), as already briefly introduced in Chapter 1, is part of the UV-absorbing chromphores in several larger molecular systems an example of which is avobenzone found in commercial sunscreens. Understanding how the chromophore is able to efficiently dissipate the energy, obtained through the absorption of a UV photon, is therefore of great interest. Expanded knowledge about the process could support the design of new sunscreens and generally lead to a better understanding of the effect of UV radiation on molecular systems. Furthermore, AcAc is used for various industrial applications, including as a reagent to form chelate compounds and to produce sulfonamide drugs [208]. Due to its use in industrial applications AcAc is found in the atmosphere [208], and studying its photochemistry may contribute

to understanding AcAc's impact on the environment. Finally, it has been found that AcAc, in combination with UV light, may potentially be used in the treatment of waste water to degrade or reduce the toxicity of pharmaceuticals remains and personal care products [209]. A deeper understanding of the mechanisms involved in this purification process may be provided through this investigation into the excited state dynamics of AcAc.

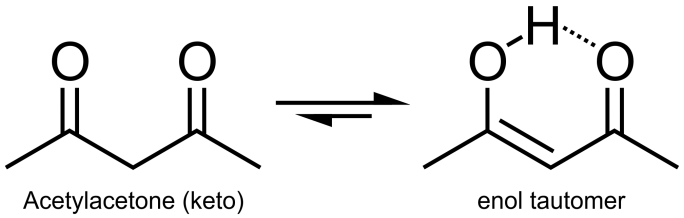

Figure 4.1: Schematic of the keto and enol forms of AcAc

As is illustrated in Figure 4.1, AcAc exists in a keto and an enol form and can undergo tautomerism to switch between both configurations. At room temperature or lower, it has been found to exist primarily in the enol form [210], and therefore this is the form that will be considered throughout this Chapter. The vapour-phase UV-absorption spectrum of AcAc, reported by H. Nakanishi *et al.*, displays a broad and structureless feature centred at 266 nm (4.7 eV). This band was assigned as the $S_2(\pi\pi^*)$ transition [211].

Over the last three decades, the photochemistry of AcAc, when excited to this $S_2(\pi\pi^*)$ state, has been studied by excitation with nanosecond lasers and the subsequent monitoring of photoproducts. A laser induced fluorescence (LIF) study by Yoon *et al.* tracked the production of OH radicals upon excitation of AcAc in the region of 280-310 nm [212, 213]. Using the excitation spectra of OH, the group was able to extract the absorption spectrum of AcAc. This was found to have no structure, which lead Yoon *et al.* to conclude that the S_2 ($\pi\pi^*$) state must be decaying to lower excited states on rapid timescales, resulting in the breaking of the C-O bond and formation of the OH radical. Over a decade later, in 2003, Upadhyaya *et al.* studied this OH radical formation in enolic AcAc again, also using LIF (this time over the 193-266 nm range) [214]. Their study concluded that the production of OH arises primarily from the lowest lying triplet ($\pi\pi^*$) state. This result was however, contradicted by Antonov [215] *et al.* who used a combination of methods to study the photodissociation of AcAc. In their study AcAc was excited at 266 nm and 248 nm, both populating the $S_2(\pi\pi^*)$ state (due to the broad nature of the absorption band) and subsequently investigated using a series of methods: multiplexed photoionisation mass spectrometry, photoelectron-photoion coincidence studies and transient infrared (IR) absorption spectroscopy. Antonov *et al.* observed 15 different primary photoproducts and reported that the tautomerisation from the enol to the di-keto form, as well as non-adiabatic repopulation of the ground electronic state (S_0), must

be key steps on the path to producing these. The $T_1(\pi\pi^*)$ state mentioned above was observed to play a role in the production of some of the photoproducts, but Antonov *et al.* note that five species, including OH as well as CH_3, are observed exclusively when the $S_2(\pi\pi^*)$ state is prepared using multiphoton excitation.

There have also been several time-resolved studies on the dynamics following UV excitation of AcAc. A comparison of the dynamical processes reported by the various gas-phase time-resolved studies introduced here with the results presented in this Chapter is given in Table 4.1 near the end of this Chapter. The first of such studies was an ultrafast electron diffraction experiment carried out by Zewail and co-workers [216] in which the $S_2(\pi\pi^*)$ state was excited using 266 nm. The ultrafast relaxation dynamics of AcAc were observed and Zewail and co-workers, based upon their observations, proposed that initially, the $S_2(\pi\pi^*)$ state undergoes internal conversion to the lower lying S_1 $(n\pi^*)$ state. This rapid first step could not be experimentally resolved. Following this, the $S_1(n\pi^*)$ state was assigned to undergo intersystem crossing (ISC) to the $T_1(\pi\pi^*)$ state, a process which was assigned an exponential time constant of 247 $\pm$ 34 ps. Overall, Zewail's work is in agreement with the above LIF studies, in that the major reaction pathway proceeds via the T_1 state and leads to OH-elimination. A theoretical study by Chen *et al.* furthermore agrees with this general interpretation [217]. Poisson *et al.* reported a femtosecond pump-probe study of AcAc using a 266 nm excitation and multiphoton ionisation with 800 nm pulses [218]. Using their photoelectron imaging data in combination with transient ion signal traces, recorded under various focusing conditions of the 800 nm probe, they extract three exponential decay constants. The shortest time-constant of 70 $\pm$ 10 fs, they assign to the initially excited $S_2(\pi\pi*)$ state departing from the Franck-Condon region, which is correlated with a H-atom transfer between the two oxygen atoms. Internal conversion from the S_2 state to the lower lying $S_1(n\pi^*)$ state was proposed as the second step in the relaxation dynamics and was associated with a 1.4 $\pm$ 0.4 ps decay constant. The final step was observed to be slower, up to 80 ps, and Poisson *et al.* propose this to be ISC to the lower lying triplet states. The timescales reported by Poisson *et al.* for H-atom transfer and IC are close to values reported by solution-phase experiments and nonadiabatic dynamics simulations [219, 220]. In contrast, however, these studies assigned the longer time dynamics to either formation of non-chelated enol conformers, repopulation of the ground state or rotamerisation. In 2018 Bhattacherjee *et al.* aimed at examining the role of the triplet states in the relaxation process of AcAc in more detail [221, 222]. They carried out an ultrafast soft X-ray transient absorption study following the excitation of AcAc at 266 nm. Their experimental results were also supported by a time-dependent density functional theory (TDDFT) study. Bhattacherjee *et al.* report an ISC process from $S_1(n\pi^*)$ to $T_1(\pi\pi^*)$ which takes place on a timescale of 1.5 $\pm$ 0.2 ps, much shorter than what was proposed by any of the previous gas-phase studies. They point out that the initial IC step between $S_2(\pi\pi^*)$ and $S_1(n\pi^*)$

could not be experimentally resolved in this study as there was spectral overlap of core-valence resonances. Still, the authors suggest that the IC should take place in less than 100 fs. This ultrafast ISC process was also suggested by Squibb *et al.* in their recent study which combined time-resolved photoelectron and photofragment ion yield spectroscopy [119]. AcAc was excited using 261 nm and ionised using a high-energy probe with a wavelength of 64.46 nm (19.23 eV), provided by a free electron laser. Detailed quantum chemistry calculations furthermore supported the experimental data. Squibb *et al.* reported extremely short-time dynamics of 50 fs, which was assigned to the IC from the initially excited $S_2(\pi\pi^*)$ state to the S_1 $(n\pi^*)$. From $S_1(n\pi^*)$ the authors have suggested various possible pathways. These include internal conversion to the ground state S_0 resulting in CH_3 elimination and inter-system crossing from S_1 to a $T_2(n\pi^*)$ doorway state, from which population rapidly moves to the lower lying T_1 $(\pi\pi^*)$ state. The second mechanism was proposed to lead to the formation of OH and CH_3 radicals. In the transient data, which extends to 200 ps, various dynamical processes are observed which could potentially provide a complete dynamical picture of the AcAc relaxation dynamics. A full analysis of these results has, however, not yet been published by the authors.

The time-resolved studies discussed above have sampled various sub-sections of the entire dynamical process. Despite these rigorous studies of the ultrafast relaxation dynamics in acetylacetone, a view of the full photochemical dynamics of AcAc upon excitation to the $S_2(\pi\pi^*)$ state is still incomplete. This chapter aims to provide a quantitative link between these previously reported results, creating a more comprehensive picture of the relaxation dynamics. Here, AcAc was studied using time-resolved photoelectron imaging (TRPEI) with a 267 nm pump and 160 nm probe pulse, where the high-energy probe pulse reveals a greatly extended view of the excited state dynamics.

4.2 Experimental Methods

The overall experimental setup as well as details on the production of vacuum ultraviolet (VUV) light have been described in detail in Chapter 2 (Section 2.3.2). Therefore, only a brief description of the experimental setup will be given here. The UV (267 nm) pump beam ($\sim$ 0.8 μJ/pulse) was produced using a pair of thin BBO crystals, which converted the 800 nm femtosecond laser output to the third harmonic. The produced pulses were recompressed in time using a CaF_2 prism pair.

In order to produce the vacuum UV light, which would act as the probe, a 800 nm beam (0.8 mJ/pulse) and a 267 nm beam ($\sim$ 200 μJ/pulse, also produced using a setup of BBO crystals) were overlapped non-collinearly in a gas-cell filled with argon. In argon, they underwent four-wave difference frequency-mixing (FWDFM), a third order nonlinear optical process. A manual delay stage ensured a temporal overlap of the two beams in the gas-cell, maximising VUV production. The overlap

and pressure conditions for this experiment were: a non-collinear overlap angle of approximately 12 mrad and an argon pressure of 350 mbar, yielding 160 nm pulses with an average energy of $\sim$ 500 nJ/pulse.

The UV pump and VUV probe beams were focused in the interaction region on a second pass through the electrode setup. This was achieved using a curved mirror (f = 10 cm). The central wavelength of the VUV pulses was found to be 160 nm and a 150 fs cross-correlation was extracted from a 2D-photoelectron spectrum of xenon (refer back to Chapter 2 for details). The polarisation of both pump and probe beams was parallel with respect to the detector.

A mixture of helium carrier-gas and the sample (acetylacetone 99.95% purity Sigma- Aldrich) entered the interaction region from the source chamber below via an Even-Lavie pulsed valve (operating at 1 kHz) and a skimmer. The electrode setup used for velocity map imaging has been described in detail in Chapter 2 and was, for this experiment, coated in an optically dark (in the VUV region) material (Vantablack, Surrey Nanosystems). The VMI setup ensured that ejected electrons were focused onto the detector setup, consisting of a microchannel plate (MCP) and phosphor screen. The output was imaged using a CCD camera mounted outside the UHV system. Prior to any photoelectron experiments, the VMI spectrometer was used in ion-detection mode to adjust the opening and timing conditions of the Even-Lavie valve such that no clusters were formed.

To obtain the time-resolved spectrum the time delays between pump and probe pulses ranged from -450 fs to +200 ps, where linear steps of 30 fs were taken between -450 fs to +450 fs and larger steps of 90 fs were taken between +450 fs and +990 fs. Beyond +990 fs, 16 exponential steps were taken to reach +200 ps. At every pump-probe delay step pump-only and probe-only images were recorded, which could then be used to provide background subtraction.

4.3 Experimental Results

4.3.1 Photoelectron Spectrum

The photoelectron spectrum (PES) of acetylacetone obtained using 267 nm pump and 160 nm probe pulses is shown in Figure 4.2. A pump-probe delay region from -450 fs to 200 ps was scanned in 53 steps and the resulting VMI images have been combined to produce the photoelectron spectrum shown. The insert shows the four-fold symmetrised VMI image at zero pump-probe delay. As discussed in Chapter 2, individual background pump and probe signals were subtracted at each timestep. The spectrum is shown on a completely logarithmic intensity scale and a mixed linear-logarithmic temporal scale. This has been done in order to highlight the more subtle features in the data. The energetic cut-off of the PES data, observed to be at 3.6 eV, is indicated by the white dashed line. It aligns well with the expected cut-off

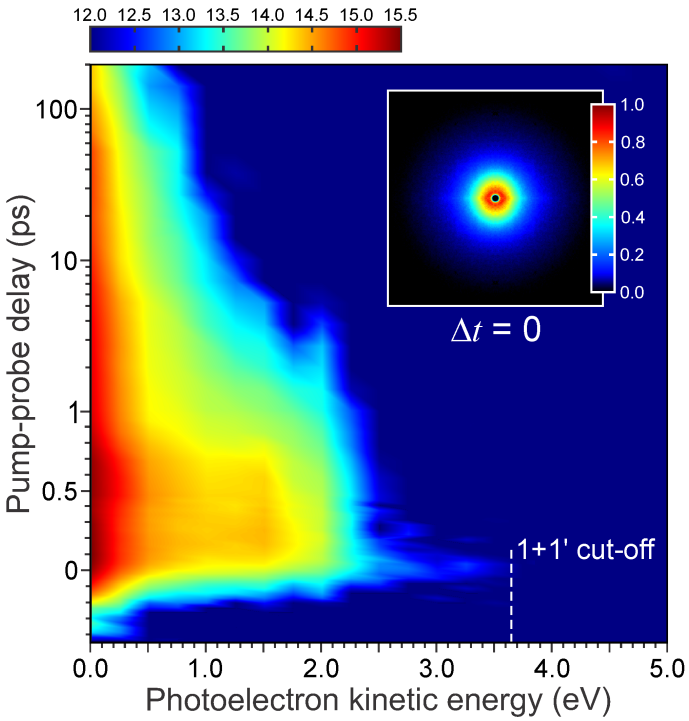

Figure 4.2: The 2D time-resolved photoelectron spectrum of acetylacetone on a logarithmic intensity scale and mixed linear-logarithmic time axis. The lin/log changeover point on the time-axis is at 1 ps and the time axis extends to 200 ps. The white dashed line indicates the energetic cut-off of the (1+1′) process with the 267 nm pump and 160 nm probe (based on the adiabatic ionisation potential of 8.85 eV). The pKE data has been partitioned into 0.1 eV energy bins and the insert on the top-right shows a background-subtracted VMI image of AcAc at zero time delay between the pump and probe pulses. This is represented on a linear scale and the image has furthermore been four-fold symmetrised.

for the (1+1′) process, calculated based on the adiabatic D_0 ionisation potential for AcAc (reported as 8.85 eV [223, 224]) and the pump and probe energies; 4.65 eV and 7.75 eV, respectively.

Three main features are apparent in the photoelectron spectrum recorded. Starting at high energies, the first is a very short-lived feature observed in the region between 2.4 eV and the cut-off at 3.6 eV. Secondly, a longer-lived signature is present between 1.2 eV and 2.4 eV, which extends beyond 1 ps. Finally, below 1.2 eV, the high-energy probe reveals a band spanning the whole recorded temporal region out to 200 ps. Here, the benefit of a high-energy probe pulse becomes very apparent. If a less energetic UV pulse at, for example, 200 nm (6.2 eV) were used instead, any signals currently observed below 1.5 eV in the photoelectron spectrum (Figure 4.2) would not be accessible. This is caused by there being 1.5 eV less energy available to project into the ionisation continuum at 200 nm, than at 160 nm. Furthermore, an additional minor feature is observed below 0.5 eV, evolving towards negative pump-probe delay times. This implies that the signal arises from a process where the 267 nm acts as the probe, and the 160 nm acts as the pump. Such features can

obscure dynamics around the zero pump-probe delay point and complicate the analysis. They are therefore undesirable but often unavoidable when using high-energy probes. Nakanishi *et al.* also report that the absorption cross sections for AcAc at 267 nm and 160 nm are similar [211, 225], making the presence of probe-pump signals likely and not easily avoidable. Their work does however, also indicate that excitation with 160 nm radiation promotes an electron from a different orbital to a higher-lying $\pi\pi^*$ state than the orbital from which an electron is excited to the S_2 ($\pi\pi^*$) state upon absorption of 267 nm radiation. This means that the Koopmans' correlations introduced earlier in Chapter 1 can be applied to distinguish signals from these two transitions. Using Koopmans' Type I correlations it is expected that the S_2 ($\pi\pi^*$) state will exhibit preferential ionisation to the D_0 (π^{-1}) cation state, whereas the $\pi\pi^*$ populated by 160 nm excitation will show a higher propensity for ionisation to a cation state beyond D_2 [226]. Considering the predicted energetics of these transitions in combination with the position of the third photoelectron band in Figure 4.2 it is evident that any photoelectrons originating from probe-pump dynamics are unlikely to be greater than 0.5 eV in the data presented here [224, 226–228]. Therefore, the signatures observed between 0.5-3.6 eV in the photoelectron spectrum are expected to result mainly from pump-probe dynamics and should contain only minimal contributions from probe-pump dynamics.

4.3.2 Decay Associated Spectra (DAS)

The photoelectron spectra were fitted using the global Levenberg-Marquardt routine, discussed earlier in Chapter 2, which provided the decay associated spectra shown in Figure 4.3. Four exponentially decaying functions were required to fit the data satisfactorily. The 1/e-decay lifetimes τ were found to be: $\tau_1 \leq 10$ fs, $\tau_2 = 1.6 \pm 0.2$ ps, $\tau_3 = 20 \pm 4$ ps and $\tau_4 = 330 \pm 40$ ps, where the quoted uncertainties are the respective standard deviation 1σ values. A summary of these timescales (along with further experimental results) is provided in Table 4.1. These lifetimes are in good agreement with values reported in previous studies that sampled more limited parts of the reaction coordinate; except that the τ_3 contribution has not been observed previously. Although the transient signal is quite small, a satisfactory fit of the data could not be achieved without the function described by τ_3. In regard to the first time constant (τ_1) it should be noted that the value extracted by the fit is shorter than the cross-correlation of the two pulses (150 fs). This indicates that fast dynamical processes occur within the cross-correlation timescale and at the very limit of the temporal resolution of this experiment. Again a satisfactory fit could not be achieved without including this near-Gaussian function and the presence of a very short-lived dynamical feature is furthermore confirmed in the DAS signatures discussed below. An exact numerical value cannot be extracted reliably due to the lifetime being shorter than the cross-correlation and only an upper bound of 10 fs

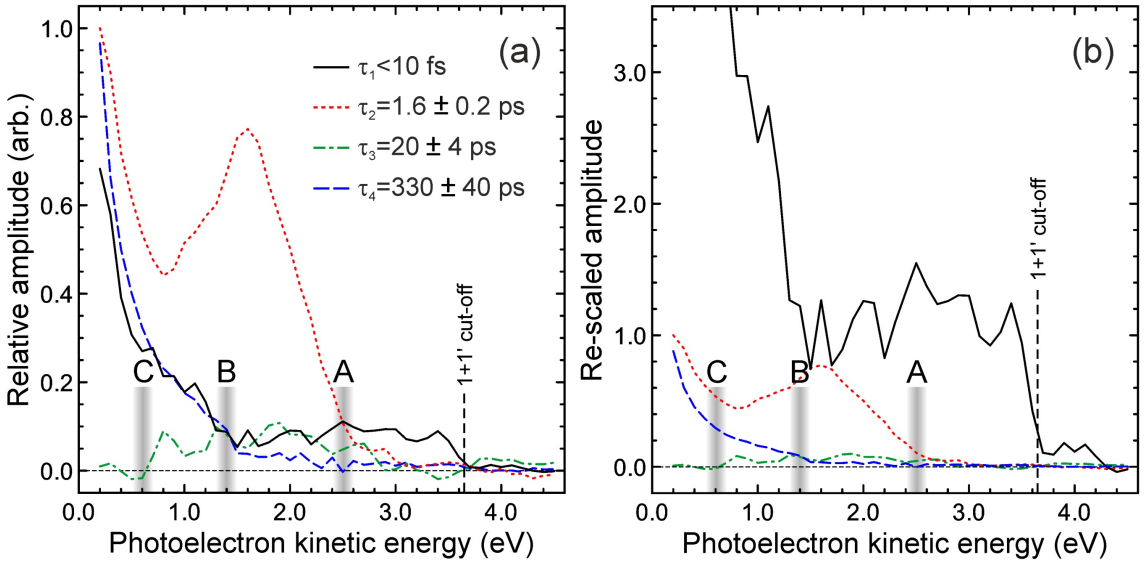

Figure 4.3: Decay associated spectra of acetylacetone (a) and rescaled version of the DAS to account for detection sensitivity as proposed in reference [229] shown in (b). For the scaling an approximate FWHM of 100 fs was used, which resulted in scaling factors of 13.90 : 1.00 : 0.92 : 0.91, for τ_{1-4} respectively and relative to τ_2. The regions shaded in grey indicate approximate positions of several onset thresholds of interest (see main text).

could be attributed using the values produced through fitting to the datasets.

Figure 4.3, clearly shows that signatures of the various dynamical processes can be extracted despite some of their spectrally overlapping contributions. The DAS of the first time-constant τ_1 extends over the whole spectral region up to the $1{+}1'$ cut-off. As the fit indicates, this must be a very fast process with a temporal profile that is close to being Gaussian. The next two time-constants identify dynamics taking place on low picosecond timescales. Their DAS both cut-off at lower energies, about 1 eV below the $(1{+}1')$ ionisation limit (around 2.5 eV). This is indicated as "region A" in Figure 4.3. Finally, the threshold for τ_4 occurs at around 1.4 eV ("region B"). Noting these limits is important as they can be linked to differing Koopmans' correlations and variations in Franck-Condon overlap, which can be used to interpret the results. This will be expanded on in the discussion section below. Both τ_1 and τ_2 also display a steep increase in amplitude at $\sim$ 1.4 eV and 0.6 eV, respectively. These are again indicated by regions B and C in Figure 4.3 (better visualised in (b)).

However, some care must be taken when comparing the magnitudes of these DAS. The DAS for τ_1 exhibits a relatively small amplitude across the spectral range. The associated short-lived feature (in the region of 2.4 eV - 3.6 eV) in the photoelectron spectrum is also quite weak, considering that the intensities are presented on a logarithmic scale. A recent numerical study carried out by N. Kotsina and D. Townsend [229], shows that detection sensitivity effects have to be taken into account for a true representation. The time-constants τ_2 through to τ_4 are at least one

magnitude larger than the cross correlation (150 fs). The feature associated with τ_1 however, arises from the ionisation of a state that is very short-lived in comparison to the temporal pulse width of the pump and probe. Reference [229] discusses the effect of the lifetime of the excited state and the pulse duration of the laser, on the detection efficiency in TRPEI experiments. They concluded that there is under-sampling of states which have a lifetime that is less than the pulse duration. In comparison to states with a significantly longer lifetime than the pulse width, this under-sampling can be of the order of a factor of 10 or larger. The effect was furthermore shown to be independent of factors such as Franck-Condon considerations or the photoionisation cross-section and can therefore be applied to the DAS here, without prior knowledge of such effects. A rescaled version of the DAS is shown in Figure 4.3 (b). The effect on τ_1 is clearly visible as its DAS is significantly increased, whereas the other three DAS remain largely similar to before.

Table 4.1: An overview of the fitted $1/e$ lifetimes extracted from fitting the photoelectron spectrum of AcAc obtained in the experiment presented here, along with the dynamical process which they have been assigned. The errors have been obtained using the standard deviation and are the respective 1σ values. Furthermore recorded in this table are, in chronological order, numerically reported lifetimes as well as their assignments from several previous gas-phase studies of AcAc. All studies included below excited AcAc using the same wavelength (266 nm), except Squibb *et al.* who employed 261 nm pump pulses.

	This work		Xu *et al.* [216]		Poisson *et al.* [218]		Bhattacherjee *et al.* [221]		Squibb *et al.* [119]	
τ_1	< 10 fs	$S_2\ (\pi\pi^*) \rightarrow S_1\ (n\pi^*)$			70 ± 10 fs		< 100 fs	$S_2\ (\pi\pi^*) \rightarrow S_1\ (n\pi^*)$	50 fs	$S_2\ (\pi\pi^*) \rightarrow S_1\ (n\pi^*)$
τ_2	1.6 ± 0.2 ps	$S_1\ (n\pi^*) \rightarrow T_1\ (\pi\pi^*)$			1.4 ± 0.2 ps	$S_2\ (\pi\pi^*) \rightarrow S_1\ (n\pi^*)$	1.5 ± 0.2 ps	$S_1\ (n\pi^*) \rightarrow T_1\ (\pi\pi^*)$		
τ_3	20 ± 4 ps	Relax to $T_1\ (\pi\pi^*)$ min.								
τ_4	330 ± 40 ps	$T_1\ (\pi\pi^*) \rightarrow S_0$	247 ± 34 ps	OH elim. on $T_1\ (\pi\pi^*)$	> 80 ps	$S_1\ (n\pi^*) \rightarrow T_1\ (\pi\pi^*)$				

4.3.3 Photoelectron Angular Distributions (PADs)

The anisotropy parameters were extracted using the appropriate fit to the photoelectron angular distributions (PADs) for (1+1′) processes (up to and including the β_4 term), discussed earlier in Chapter 2 of this thesis. Both β_2 and β_4 are plotted over the whole pump-probe delay timescale in Figure 4.4. They were observed to be essentially invariant with energy and therefore the parameters shown here have been averaged over the 0.2 eV to 2.3 eV spectral region. The β values are very small overall (all lying within -0.1 to 0.1), implying that the anisotropy in the AcAc VMI images is low. Despite this, changes in the anisotropy parameters are still observed at the points where there is a transition from one dynamical process to the next, as indicated by the grey areas in the figure. The information reveals no new dynamical signatures, however it supports the DAS and PES, confirming that there are dynamical processes taking place on three different timescales.

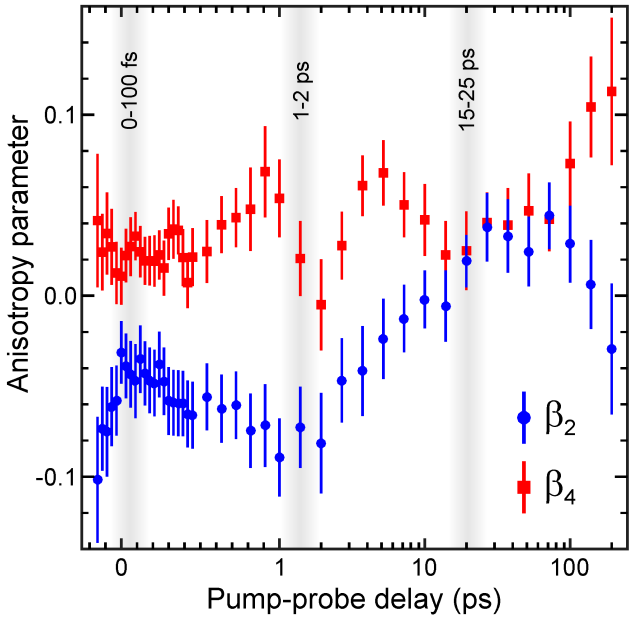

Figure 4.4: Variation of the anisotropy parameters β_2 and β_4 with time in AcAc. These were averaged over the pKe region of 0.2-2.3 eV. The pump-probe delay axis consists of a mixed linear and logarithmic scale, with the lin/log transition point at +1 ps. The error bars indicated are 1σ values. Energy bins of 0.1 eV were used prior to averaging and the fits were performed over angles from $5° \leq \theta \leq 90°$, which removed any distortion from centre-line noise.

4.4 Discussion

Prior to assigning the dynamical processes observed in the experimental data presented above, there is one key caveat that has to be considered in TRPES experiments using vacuum UV probes. This is the fact that the VUV probe may be energetic enough to ionise neutral photofragments, produced when the species un-

der investigation (neutral parent species) is excited. It is therefore possible that some photoelectron signals recorded arise, not only from the parent species that we are interested in, but also from ionisation of a neutral photofragment. Due to the high energy in VUV probes, these fragment-signals may arise from single-photon processes, resulting in strong signatures in the PES. When using UV probes (> 200 nm) in contrast, this is not typically a concern as these do not (in most cases) carry enough energy to induce single-photon ionisation of radical fragments. Such photofragment signals can often be identified by considering the timescale of the rise of the PES signal originating from the fragment. This rise should naturally match the rate of dissociation of the parent species. However, this observation only holds true for primary fragmentation products that do not subsequently undergo further (secondary) dissociation and furthermore, the species must remain in the laser focal volume. The second condition is of no concern for the timescales investigated in this chapter, which are limited to 200 ps. The concerns regarding the energetic accessibility of the fragments can fortunately also be eliminated using the results presented by Antonov *et al.* [215]. The researchers reported the threshold ionisation appearance energies for all photofragments of AcAc to exceed 9.0 eV [215], which is well above the 7.75 eV provided by the VUV probe employed here. We can therefore be positive that the features observed in the PES spectra arise from the ionisation of the excited AcAc parent molecule.

4.4.1 Assignment of Time Constants

This section will consider the assignment of the time constants extracted from the recorded photoelectron spectra shown above. Consider the first time constant τ_1 (< 10 fs). The process described by τ_1 can be seen to originate from $\Delta t = 0$, where pump and probe pulses arrive simultaneously. The pump initially excites the $S_2(\pi\pi^*)$ state and, based on Koopmans' correlations, this would be expected to project preferentially to the D_0 (π^{-1}) cation state [226]. The energetic cut-off observed in the DAS (as indicated in Figure 4.3) furthermore agrees with the expected value for the threshold of the $1+1'$ ionisation process to D_0. These two considerations allow for the dynamical process with a time constant τ_1 to be assigned to the ultrafast internal conversion (IC) from S_2 ($\pi\pi^*$) to S_1 ($n\pi^*$), where the τ_1 DAS can be attributed to ionisation from the S_2 ($\pi\pi^*$) state. This assignment of the very short first lifetime is in agreement with several of the recent studies of AcAc as detailed in the introduction of this chapter [119, 215, 221] .

Another interesting aspect here is the effect of multiphoton excitation on the photochemistry of AcAc. As highlighted earlier, Antonov *et al.* proposed that certain photoproducts such as OH and CH_3 are only produced from the S_2 ($\pi\pi^*$) state upon MPE (at 266 nm and 248 nm excitation wavelengths) [215]. The authors explain that more insight into this observation could be provided by an ultrafast

study using exclusively single-photon excitation. As no signal is observed beyond the 1+1′ process cut-off at 3.6 eV in the PES data presented above, it is reasonable to assume that no MPE is induced by the 267 nm pump used in the TRPEI study of AcAc presented here. Or, put in a different way; the TRPEI data shows no evidence of higher-order (2+1′) processes. Note here that the MPE processes inferred by Antonov *et al.* would result in energies of 9.3 eV and 10.0 eV, respectively. These energies are both greater than the adiabatic ionisation potentials of both D_0 (π^{-1}) and D_1 (n^{-1}) which have been reported as 8.85 eV and 9.53 eV, respectively in reference [224]. There have, however, been reports of "super-excited" bound states which lie energetically higher than the ionisation onset threshold. These have been previously observed in pump-probe studies of various molecules including phenol [230], 1,3-cyclohexadiene [231] and more [232–234].

The $S_1(n\pi^*)$ state, populated via rapid IC from the S_2 ($\pi\pi^*$) state, will, according to the Koopmans' correlations, have a high propensity for ionisation to the D_1 cation state which posesses n^{-1} character. The lower energy cut-off of the τ_2 DAS, with respect to that of τ_1 (shown in Figure 4.3), seems to corroborate this idea. The cut-off is shifted by approximately 1.0 eV which is larger than the energetic gap between D_0 and D_1 in AcAc, which has been assigned values between 0.51 eV and 0.68 eV, by several studies using single-photon ionisation with helium lamp sources [224, 226–228]. In (resonant) multiphoton ionisation studies the size of this gap may be affected by relaxation of the excited state geometry which would result in a change in the Franck-Condon factors. Theoretical work by Squibb *et al.*, for example, predicts that there is an energy difference of 1.27 eV between the transitions: $D_0(\pi^{-1}) \leftarrow S_2(\pi\pi^*)$ and $D_1(n^{-1}) \leftarrow S_1$ ($n\pi^*$) at the S_0 and S_1 ($n\pi^*$) lowest energy geometries, respectively. This is in good agreement with their experimentally observed value of 1.4 eV and slightly larger than the $\sim$ 1.0 eV gap observed here. Based on the above arguments, the τ_2 DAS can be assigned to ionisation originating from the previously populated $S_1(n\pi^*)$ state. Additional sudden rises in amplitude observed in the DAS of τ_1 and τ_2, as seen in Figure 4.3 (bands B and C, respectively), indicate that there are further onset thresholds. These likely result from ionisation into higher-lying cation states. Based on reports by various single-photon ionisation studies [11, 14, 159, 221] such states should be energetically accessible by the total pump + probe energy of 12.35 eV available in this experiment.

Since the relaxation pathway of the population initially placed into the $S_2(\pi\pi^*)$ state has already been followed to the lower lying S_1 ($n\pi^*$) state, it is now of interest to consider what possible pathways for further relaxation are available from $S_1(n\pi^*)$. This is where theoretical work can provide vital guidance. In particular, two theoretical studies by Squibb *et al.* [119] and Chen *et al.* [217] have proposed that in AcAc there exists a triple conical intersection between the $S_1(n\pi^*)$ state and two triplet states which are lower-lying in energy; $T_1(\pi\pi^*)$ and $T_2(n\pi^*)$. This provides the possibility for rapid ISC from $S_1(n\pi^*)$ to one of these triplet states and, in

fact, several recent experimental studies strongly support this as an active pathway occurring on the same timescale as reported here [119, 221, 222]. As discussed in the introductory chapter of this thesis (Chapter 1), ISC usually takes place on relatively long timescales (10^{-8} - 10^{-3} seconds), and therefore the extracted τ_2 lifetime of 1.6 $\pm$ 0.2 ps would conventionally be considered too rapid for an ISC process. However, there have recently been reports of "ultrafast" ISC, including in motifs which are structurally similar to AcAc [42, 235]. Squibb *et al.* [119] explain the rapid nature of the ISC in AcAc by noting that the separation in energy between the three states involved in the triplet CI crossing ($S_1(n\pi^*)$, $T_1(\pi\pi^*)$ and $T_2(n\pi^*)$) is minimal for planar geometries in the vicinity of the $S_1(n\pi^*)$ minimum. Although this extremely fast ISC has been reported by both Squibb *et al.* and Bhattacherjee *et al.* their conclusions as to the states involved in the ISC differ. As it is a triple CI, there are several possible relaxation pathways. The transfer of population from S_1 ($n\pi^*$) to $T_1(\pi\pi^*)$ is favoured by Bhattacherjee *et al.* [221, 222], based on El-Sayed's rules [44] (discussed in Chapter 1). El Sayed's rule states that a transition involving a change in orbital type is predicted to be faster than one that does not, which would make the above pathway favourable. Squibb *et al.*, however, argue that there is an intermediate step involving the $T_2(n\pi^*)$ state. They describe $T_2(n\pi^*)$ as an exceedingly short-lived doorway state [119], where population passes through the state without the total population ever exceeding 10%. Squibb *et al.* predict that subsequently and via this doorway state the $T_1(\pi\pi^*)$ state is reached through almost instantaneous internal conversion (IC).

Region A in Figure 4.3 highlights the onset threshold for the τ_2 DAS which is in close proximity to that of the weaker τ_3 DAS. Considering this, in combination with the fact that both triplet states T_1 ($\pi\pi^*$) and $T_2(n\pi^*)$ should favourably ionise to the $D_0(\pi^{-1})$ and $D_1(n^{-1})$ cation states, respectively, it would seem appropriate to assign the τ_3 DAS as originating from the transition to the $D_1(n^{-1})$ continuum with $T_2(n\pi^*)$ as the origin. The long τ_3 lifetime of 20 $\pm$ 4 ps would, however, be in disagreement with the ultrafast doorway step as proposed by Squibb *et al.* Furthermore, the ionising $D_0(\pi^{-1}) \leftarrow T_1(\pi\pi^*)$ and $D_1(n^{-1}) \leftarrow T_2(n\pi^*)$ transitions (at the S_1 ($n\pi^*$) minimum energy geometry) have been predicted to result in photoelectron energies which lie very close in energy [119]. Also, at the relaxed $T_1(\pi\pi^*)$ minimum energy geometry, the $D_0(\pi^{-1}) \leftarrow T_1(\pi\pi^*)$ transition is expected to result in a photoelectron signature which has been shifted, by approximately 1 eV, to lower energies. Therefore, this would be reflected in the DAS and it indeed corresponds to the difference in energy between regions A and B in Figure 4.3, where region B marks the onset threshold for the τ_4 amplitude. Based on the various arguments above, it is not possible, from the work presented here, to either confirm the direct population of the $T_2(n\pi^*)$ state, nor to rule it out completely. There is, instead, more evidence to support the conclusion that the amplitudes of τ_3 and τ_4 originate from the ionisation of the $T_1(\pi\pi^*)$ state. As the molecular geometry changes from

the S_1 ($n\pi^*$) minimum structure to that of the $T_1(\pi\pi^*)$ state, a change in ionisation efficiency is observed. This is caused by large amplitude motion that accompanies the rather significant change in geometry, where the OH group twists out of the plane in which all other heavy atoms lie [119, 217]. In the data presented here, this change in ionisation efficiency is associated with τ_3. The τ_4 lifetime of 330 ± 40 ps on the other hand describes the general decay of the lower $T_1(\pi\pi^*)$ triplet state. A lifetime on the same timescale (247 ± 34 ps) was identified by Zewail and co-workers [216] who have attributed this to the process of dissociation of OH facilitated by the $T_1(\pi\pi^*)$ state. Although, as discussed above, the recent work by Antonov *et al.* has reported that such fragmentation of OH was only accessible using multi-photon excitation [215]. The TRPEI method employed in this thesis is essentially blind to the formation of photofragments, such as OH, and therefore it is not possible to draw conclusions on the existence or extent of such fragmentation in the relaxation dynamics of AcAc from the results presented here. Furthermore, Antonov *et al.* report that such fragmentation occurs on the S_0 ground state. Here, it is only possible to tentatively suggest a decay of the $T_1(\pi\pi^*)$ state to S_0. To conclude this discussion and in addition to the summary previously provided in Table 4.1, a schematic overview of the proposed relaxation mechanisms for AcAc is given in Figure 4.5.

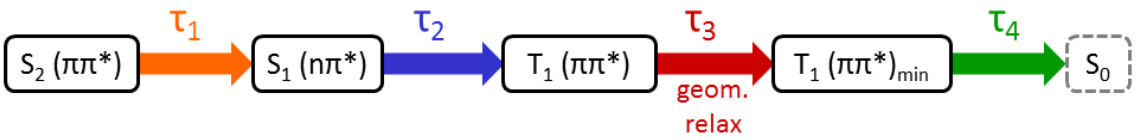

Figure 4.5: Schematic of the proposed relaxation steps in AcAc. The numerical values for the extracted time constants are summarised in Table 4.1.

The VUV probe employed has been able to reveal an extremely extended view of the relaxation dynamics of acetylacetone in this investigation. The repopulation of S_0 may be observed more definitively by using a probe pulse even deeper in the VUV region, however, if the probe energy exceeds 9 eV the possibility of ionising several photoproducts could lead to further congestion of the spectra [215]. Moreover, these photoproducts could originate from either $T_1(\pi\pi^*)$ or S_0 [119, 215]. To resolve the complete map of the dynamics with an even higher-energy probe may therefore, require extremely differential methods such as photoelectron-photoion coincidence measurements.

4.5 Conclusion

A detailed investigation of the ultrafast non-adiabatic relaxation dynamics of the sub-chromophore motif acetylacetone was presented in this chapter. Time-resolved photoelectron imaging in combination with a vacuum-UV probe (160 nm) and UV pump (267 nm) was used to determine the dynamical processes involved. Four different lifetimes could be extracted from the recorded time-resolved photoelectron spectra, which have been assigned as follows: An initial extremely rapid process, complete within < 10 fs, was assigned to an internal conversion process between the initially excited $S_2(\pi\pi^*)$ state and the lower lying $S_1(n\pi^*)$ state. From there, population is transferred to the triplet manifold via a triple conical intersection (which has been theoretically predicted [119]) to the $T_1(\pi\pi^*)$ state. This process takes place on a timescale of 1.6 ± 0.2 ps. A fairly weak but observable signal, revealed in the DAS (τ_3 in Figure 4.3), is assigned to the relaxation from the $S_1(n\pi^*)$ minimum geometry to the $T_1(\pi\pi^*)$ minimum energy geometry. This process occurs on a timescale of 20 ± 4 ps. Finally, the overall lifetime of the triplet state $T_1(\pi\pi^*)$ is 330 ± 40 ps, which may lead to population of the S_0 ground state. This investigation of acetylacetone with a short-wavelength probe in the VUV has been able to provide quantitative links between various elements of several prior studies of the relaxation dynamics in AcAc, which individually sampled subsections of the complete reaction coordinate. Moreover, this work demonstrates that probes in the VUV region, in conjunction with photoionisation-based techniques in time-resolved spectroscopy, provide an extended 'view' of the reaction-coordinate. Finally this study shows that, to fully exploit the capabilities of time-resolved photoionisation-based spectroscopy experiments, short-wavelength probes are crucial and likely to become the norm in future research in this field. Compact and reliable, lab-based short-wavelength sources, such as the one employed here, will be crucial in facilitating a routine use of high-energy probes [236] in photoionisation based techniques in future. This will greatly extend the observable dynamics and provide a more complete understanding of the relaxation mechanism in molecular systems. These short-wavelength sources can be developed further in future to become smaller, more efficient and low-cost, eventually providing easy access to short-wavelength probe pulses. One example of such novel sources is the use of hollow-core photonic crystal fibres, which are discussed in more detail in Chapter 7.

Chapter 5

Steric Effects Influencing Excitation Dynamics in Nitrobenzene Derivatives

The experimental work presented in this Chapter was carried out by N. Kotsina and L. Saalbach. Preliminary data processing was performed by N. Kotsina. Further detailed data analysis was carried out by L. Saalbach. This included the editing of the REPEITS Analyse program to add extended anisotropy fitting capabilities (see Chapter 2). Finally, the *ab intio* calculations presented here were also performed by L. Saalbach.

5.1 Introduction

Nitric oxide (NO) is well-known as a harmful, environmental pollutant which contributes to the formation of smog. In the late 1980s, however, the discovery of NO's role in the relaxation of vascular muscles laid the foundation for broad research into the role of NO in physiology [237]. It is now known that NO performs functions in numerous biological processes such as blood pressure regulation, biodefense, immune stimulation and neurotransmission. Molecules acting as "NO donors" are therefore now being investigated for their use in clinical medicine. These are systems which are able to release NO groups time- and site-specifically in reaction to a specific trigger, such as a photon [238]. In search of such an NO donor T. Suzuki *et al.* studied a series of aromatic nitro-compounds using visible and UV light irradiation [18]. Two of the systems studied are illustrated in Figure 5.1. The compound shown in Figure 5.1 (a) was found to exhibit a good NO-release activity (essential for an NO donor), whereas the system shown in (b) did not. Suzuki *et al.* related this effect to the the conformation of the nitro-group with respect to the aromatic ring [18]. The steric influence exerted by the presence of the two methyl groups on the nitro-group (as in 5.1 (a)), causes the NO_2 group to rotate out of the plane of the benzene ring and the conformation was found to be closely related to the amount of

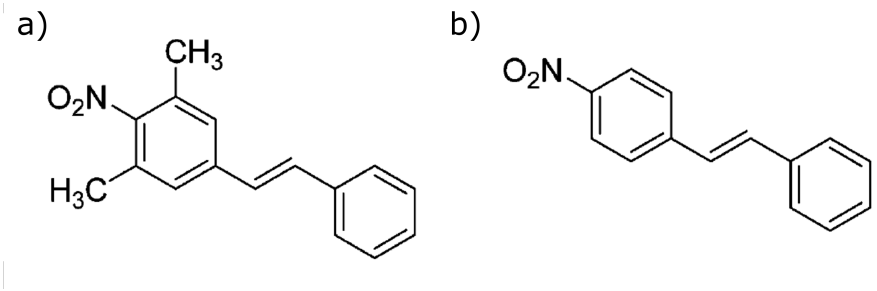

Figure 5.1: Two of the potential photoinduced NO donor systems investigated by Suzuki *et al.* [18].

NO generated [18]. Furthermore, in related systems (nitronapthalenes) the torsional angle has been found to be a key coordinate in facilitating ultrafast relaxation dynamics [239]. The TRPEI study of nitrobenzene and three of its methyl-substituted derivatives presented in this Chapter aims to explore the effect of this conformation of the nitro-group on the non-adiabatic excited state relaxation processes following UV absorption in nitrobenzene (NB) and three methyl-substituted derivatives. The calculated molecular geometries of NB, 2,4-, 2,6- and 3,5-dimethylnitrobenzene (DMNB) are shown in Figure 5.2, illustrating how the conformation of the nitro-group with respect to the benzene ring varies in these four systems, making them ideal candidates for the proposed study.

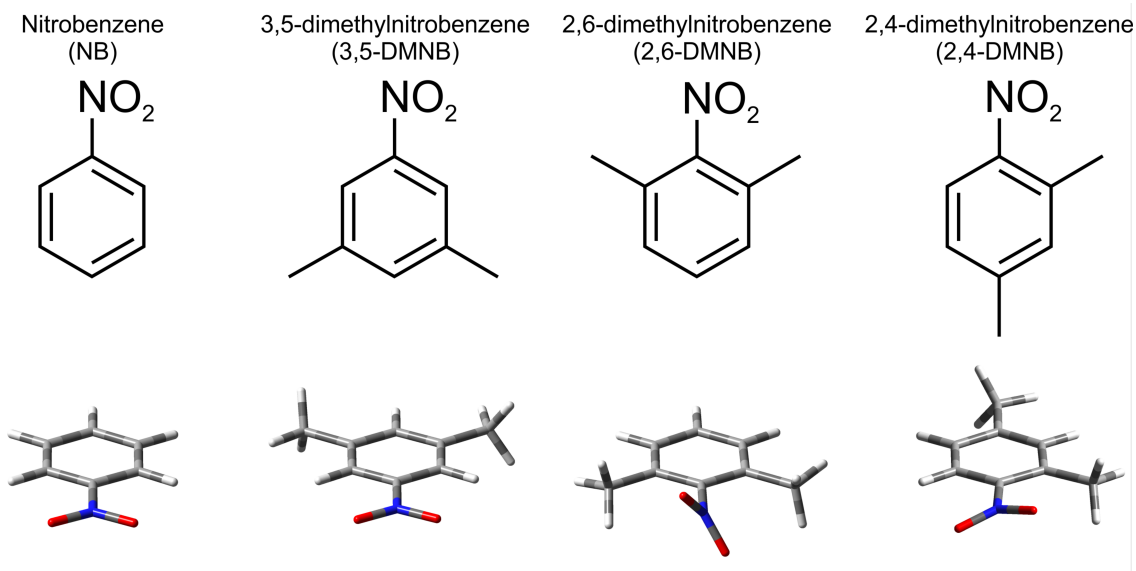

Figure 5.2: Schematic structures of the molecular systems investigated as well as the ground state geometries computed using MP2/aug-cc-pVDZ or MP2/aug-cc-pVTZ in case of nitrobenzene.

The photodissociation dynamics of NB have previously been investigated using various experimental techniques [240–248] and several rigorous theoretical studies have also recently been reported [249–252]. Within the limit of this thesis it is not possible to provide an in-depth review of all these studies, but the following

section aims to summarise the relevant (i.e., mostly gas-phase) literature relating to the observed photodynamics in NB. Little investigation into the photochemical and photophysical processes operating in 2,4-, 2,6- and 3,5-dimethylnitrobenzene has been reported so far and where work has been published it has been focused on the cation species [253]. The review below will therefore concentrate on the relevant literature for NB.

5.1.1 Experimental Studies

Four key photodissociation pathways following UV excitation of NB were identified by Galloway *et al.* in the early 1990s using vacuum-ultraviolet (VUV) photoionisation with molecular-beam mass spectrometry in combination with photolysis wavelengths ranging from 220 - 320 nm [240]. Two dissociation pathways resulting in NO were proposed:

$$C_6H_5NO_2 + h\nu \rightarrow C_6H_5O + NO \tag{5.1}$$

and

$$C_6H_5NO_2 + h\nu \rightarrow C_5H_5 + CO + NO. \tag{5.2}$$

At photolysis wavelengths between 200 nm and 280 nm, NO_2 and atomic oxygen were also observed as photoproducts. The authors suggested the following dissociation mechanisms at these wavelengths:

$$C_6H_5NO_2 + h\nu \rightarrow C_6H_5 + NO_2 \tag{5.3}$$

and

$$C_6H_5NO_2 + h\nu \rightarrow C_6H_5NO + O. \tag{5.4}$$

The production of NO_2 was found to exceed that of NO by nearly 50% at 280 nm and was observed to increase further (up to sixfold) as the photolysis wavelength was shortened to 222 nm [240]. This leads the authors to suggest that a different photolysis mechanism must be active at longer wavelengths, beyond 280 nm. The proposed pathway progresses via the isomerisation of NB to a phenyl nitrite intermediate before producing NO_2 by cleaving the C−ONO bond and producing NO via cleavage of the O−NO bond. Forming the phenyl nitrite intermediate would require breaking of the C−N bond. The NO_2 group itself would remain unchanged during this process, but would have to reorient and form a C−O bond with a member of the benzene ring. The authors suggest that the increased NO_2 signal is observed due to the direct channel dominating below 280 nm [240], whereas the indirect channel via phenyl nitrite is proposed to be more significant at longer wavelengths, increasing the production of NO. A theoretical study linked to this experimental work was published shortly after by Crim and co-workers [252] confirming the possibility of dissociation via a vibrationally excited phenyl nitrite intermediate. A REMPI study

by Marshall *et al.* [254] scanning the wavelength region between 240 - 250 nm also observed fragmentation of nitrobenzene into C_6H_5 and NO_2, as suggested by Galloway *et al.*. Overall, the channel resulting in NO_2 (reaction equation (5.3)) has been determined to be the main relaxation pathway at high energies [255]. A study by Lin *et al.*, however, confirms the importance of the NO product channel (reaction equation (5.1)), as the authors observed a branching ratio of 0.4 for the NO/NO_2 products after 266 nm excitation of NB [246] (discussed in more detail below).

In 1997 Terazima and co-workers carried out the first time-resolved study of NB photodissociation dynamics. NB and nitrotoluene (NT) were investigated in solution using the picosecond time-resolved transient grating method and photoexcitation at 320 nm [241, 242]. Takezaki *et al.* observed two lifetimes for NB: One of ≤ 10 ps was attributed to the relaxation of the vibrationally excited S_1^* to the lowest vibrational level in S_1. A second lifetime of ~ 480 ps was attributed to intersystem crossing (ISC) from T_1 to S_0. Notably, when considering their results for two further systems: ortho-nitrotoluene and ortho-nitrobenzoic acid, the authors speculate that structural changes of the molecule involving the NO_2 group give rise to the short triplet state lifetime, although the authors do not elaborate on this supposition. The same year Terazima and co-workers subsequently published a theoretical study [256] on the same subject followed by a second time-resolved transient grating experiment of NB in ethanol a year later [242]. Drawing on all three studies they conclude that the vibrationally excited state S_1^* relaxes to the S_1 minimum in ≤ 100 fs. From S_1 population then crosses into T_2 and from there to T_1 via internal conversion in 6 ps. The final relaxation from T_1 to S_0 takes place in 480 ps as mentioned above. The theoretical investigation confirmed that the reaction dynamics are driven by out-of-plane NO_2 motions (with respect to the benzene ring) [256].

Zewail and co-workers investigated the structural dynamics of gas-phase NB in 2006 using ultrafast electron diffraction [243]. Their work confirms that NB undergoes structural rearrangement prior to fragmentation into NO and a phenoxyl radical. NO elimination via an intermediate structure (similar to phenyl nitrite but with a pseudo three-membered ring created by an additional N-C bond) was determined as the main reaction pathway following excitation at 266.7 nm. This was confirmed by supporting theoretical calculations which show no direct pathway leading to the phenyl radical and NO_2 products from the T_1 surface, in agreement with the observations made by Galloway *et al.*. Furthermore, only negligible amounts of NO_2 were found to have been produced.

The dissociation pathway via isomerisation to phenyl nitrite, as first suggested by Galloway *et al.*, is also supported by the findings by Li *et al.*, who carried out a one-photon LIF study of gas-phase NB at 266 nm [244]. Kosmidis *et al.* report the absence of the indirect fragmentation channel (via isomerisation to phenyl nitrite) in gaseous NB studied at a longer excitation wavelength of 375 nm, using femtosecond pulses and a time-of-flight spectrometer [245]. This is in disagreement with Gal-

loway's suggestion that the second, indirect fragmentation channel only becomes active above 280 nm. Kosmidis *et al.* further investigated the photofragmentation of NB at various UV wavelengths between 210 - 275 nm [257, 258], observing increased production of phenyl ions below 230 nm and confirming the existence of relaxation pathways as described in Equations (5.1), (5.3) and (5.4).

In 2007 Lin *et al.* conducted a multimass ion imaging study on NB and nitrotoluene (NT) at three UV wavelengths (193 nm, 248 nm and 266 nm) [246]. The authors concluded that dissociation both from (un-rearranged) NB and via phenyl nitrite are direct dissociation processes (occurring on one single potential energy surface). However, dissociation into C_6H_5O and NO after isomerisation to phenyl nitrite is more favourable due to the lower dissociation energy. This implies that NO_2 is mainly produced by direct dissociation of NB (no phenyl nitrite intermediate) which is in disagreement with Galloway *et al.*'s work mentioned above. They furthermore observed a bimodal distribution in the translational energy of the NO product. This was attributed to differing barrier heights of intermediates reached from the ground and triplet states, which is also consistent with the observed dependence of the bimodal distribution on the photolysis wavelength.

The bimodal distribution in the NO product translational energy was also studied by the group of A. Suits using a (1+1) REMPI scheme near 226 nm (excitation and dissociation) combined with state-selected DC slice imaging [247]. The authors concluded that the imaging data, in conjunction with a qualitative theoretical study of the process, suggested that a slow component in the observed bimodal distribution arises due to roaming-mediated isomerisation to phenyl nitrite occurring on the S_0 singlet surface. Their quantum chemistry calculations revealed a roaming-type saddle point on the ground state potential energy landscape which facilitates the structural change to phenyl nitrite. This type of saddle point is formed when the bond distance (between phenyl ring and NO_2 group in this case) becomes very large (greater than 3.2 Å) which results in a "structure" that is near degenerate (1-2 kcal mol^{-}1) to the asymptotic limit corresponding to the detached fragments. The fast component on the other hand is attributed to dissociation on an excited triplet state surface as reported by Lin *et al.*. Suits and co-workers however, argue that a more in-depth study of this pathway is required. Suits and co-workers also predict that internal conversion to the ground state must be taking place, based on the absence of anisotropy in the DC slice images and the observation of only relatively slow NO fragments (implying the energy is mainly deposited into the internal coordinates of the remaining fragments). Furthermore, computed branching ratios indicate a "roaming mediated isomerisation" to phenyl nitrite as the main dissociation pathway, as NO production via a second pathway is abruptly turned off at the energetic threshold for NO_2 production [255].

Finally, a very recent time-resolved photoelectron spectroscopy study of NB and its aldehydes in the gas-phase at 200 nm was carried out by Schalk *et al.* [248].

Two lifetimes of 40 fs and 480 fs were observed in the photoelectron spectra of NB. The shorter time constant was attributed to ultrafast decay from an initially excited charge transfer (CT) state to S_1, whereas the long lifetime corresponds to either the release of NO_2 or the relaxation via internal conversion directly to the ground state (without passing through any triplet states). Furthermore, the theoretical part of this publication predicts the total energy required to reach unimolecular dissociation into benzene and NO_2 to be 4.1 eV (302 nm). This prediction offers an explanation for the previously observed dependence of NO_2 production on photolysis wavelength.

5.1.2 Theoretical Studies

The first, fully dedicated theoretical study of NB to be discussed here is that by Quenneville *et al.* from 2011 [251]. The authors employed TD-DFT and MRCI methods as well as CASSCF to study the relaxation pathways in NB and other nitroarenes. The authors suggest that pyramidalisation and rotation of the NO_2 group, the ONO angle and NO bond stretches are involved in creating a conical intersection (CI) between S_1 and S_0 (and possibly T_0, but this triple CI is not confirmed in their study). Based on computed spin-orbit coupling (SOC) values the authors confirm that their work supports the findings of Terazima and co-workers (discussed earlier) in that the population from the S_1 state predominantly moves to T_2 via ISC. The singlet to triplet transition fulfils the criterion set by El-Sayed's rule as a change in state character is involved since S_1 has $n\pi*$ and T_2 has $\pi\pi^*$ character.

Following this, in 2014, Dreuw and co-workers employed a variety of different levels and types of quantum chemistry approaches to examine the non-radiative relaxation of NB [250]. TD-DFT was observed to underestimate the energies of the charge transfer states in NB, which Quenneville *et al.* had previously accounted for by using a long-range corrected functional [251]. Dreuw and co-workers conclude that NB initially undergoes internal conversion facilitated by an asymmetric NO stretch. A scissoring motion of the oxygen atoms in the nitro-group then provides the possibility of intersystem crossing onto the triplet manifold. Finally, intersystem crossing to the ground state from the lowest triplet state is predicted to be mediated by a bend of the NO_2 group which aligns it out of the plane of the benzene ring. Relaxation directly to the ground state from the excited S_1 state via internal conversion is also predicted to be energetically accessible (through more ONO bending), but only 20% of the population follows this pathway according to Dreuw and co-workers [250].

The most recent theoretical treatment of the photodissociation dynamics of NB was carried out by Giussani and Worth [249] using a photochemical reaction path approach which allows for the relaxation of all degrees of freedom in the molecule. The authors have investigated the decay paths from the singlet $S_4(\pi\pi^*)$ (5.01 eV) state and the lower-lying singlet $S_2(n_a\pi^*)$ (3.32 eV). The $S_4(\pi\pi^*)$ state has a non-

zero oscillator strength and is accessible at UV wavelengths around 245 nm, but is believed to lie out of reach in the study presented here which uses a 267 nm pump. According to the authors, the majority of the decay path from $S_4(\pi\pi^*)$ takes place on the singlet surface, although some of the population may cross from S_1 onto the triplet manifold instead of relaxing to the ground state directly. By considering the geometries of NB at the minima, CI and singlet-triplet crossing regions, the molecular coordinates facilitating relaxation can be deduced. All molecular coordinates vary during the optimisation, however the NO stretch and ONO bond angle were shown to be evolving noticeably during the relaxation on the singlet surface. For the triplet pathway it is the ONO bend that is significant and the conical intersection between the lowest excited singlet state and the ground state is characterised by the shortening of the C-N bond, which is in agreement with the work by Dreuw and co-workers. The out-of-plane distortion of the nitro group (distortion of NO_2 with respect to the plane of the benzene ring) found at the conical intersection to the ground state by Quenneville *et al.* [251] lies 0.5 eV higher in energy than the structure characterised by Giussani and Worth [249]. For the relaxation from the triplet structures to the ground state, both Dreuw and Quenneville found that there is an involvement of the nitro-group bending out of the plane. Giussani and Worth conclude that the out-of-plane distortion of the nitro-group with respect to the benzene ring (nitro-group torsion and pyramidalisation) may not be as crucial as predicted by the other two theoretical studies.

Finally, Giussani and Worth related their results to the experimental data by Takezaki *et al.* in two different interpretations. The first attributes the 100 fs lifetime to the decay from the first singlet state back to the ground state, the 6 ps component to the population moving from the singlet to the triplet manifold and the final 480 ps component to the relaxation from the lowest lying triplet state to the ground state. The second proposed relaxation pathway is inspired by the photophysics of 1-Nitronaphthalene which displays a spin-multiplicity change on a timescale of only 100 fs [259, 260]. NB could behave the same way, the authors argue, meaning that 100 fs would be attributed to the transfer onto the triplet manifold and the 6 ps component to the relaxation from the lowest single state to the ground state, with the 480 ps component describing the decay from the triplet to the ground state. The isomerisation to phenyl nitrite was also investigated by the authors, identifying two possible mechanisms and concluding that if relaxation takes place via the triplet manifold, then isomerisation to phenyl nitrite is not required. The authors also support the idea of a roaming mechanism proposed by Suits and co-workers [255].

Overall, it is evident that despite many recent experimental and theoretical efforts, the photodissociation of NB and the molecular coordinates involved in the processes are not yet fully explored and understood. The following report of an experimental TRPEI study of NB and its methyl-substituted derivatives in con-

junction with supporting *ab initio* quantum chemistry calculations aims to reveal the ultrafast molecular relaxation dynamics exhibited by NB upon the absorption of 267 nm UV light. Comparing the non-adiabatic dynamics in NB with those in the methylated derivatives (2,4-, 2,6- and 3,5-dimethylnitrobenzene (DMNB)) will elucidate the role of the NO_2 group configuration and ring-deformations in the efficient energy dissipation process. The computed ground state structures of all four systems investigated are shown in Figure 5.2. The NO_2 group conformation with respect to the aromatic ring is clearly altered upon methylation of the benzene ring in 2,4- and 2,6-DMNB whereas the "weighing down" of the benzene ring in 3,5-DMNB will reveal the effect of ring-deformations on the relaxation dynamics. Such ring-deformations have previously been found to play a role in the relaxation dynamics of other systems such as aniline and its derivatives [23, 261]. In this chapter, the conformation of the nitro-group will be defined by the angle between the plane of the NO_2 group (planar) and the plane in which the benzene ring lies. For example, when the angle is 0°, all atoms lie in the same plane, whereas an angle of 90° denotes a conformation where the planar nitro-group is perpendicular to the benzene ring. This will also be referred to as the dihedral angle throughout the chapter.

5.2 Experimental Methods

The experimental setup has been described in detail in Chapter 2 with the optical configuration set out in Section 2.3.1. Briefly, NB (Fisher Scientific, 99.5% purity) as well as 3,5-, 2,6- and 2,4-DMNB (Sigma-Aldrich, $>$ 98 % purity) were brought into the gas-phase by flowing He (0.25 bar) over the sample contained in the external bubbler. The Even-Lavie valve (with 150 μm aperture) was not used in a pulsed mode in this setup and therefore the resulting molecular beam was continuous. The effusive beam entered the molecular chamber via a skimmer, where it was intersected perpendicularly by the co-propagating pump (267 nm, 0.5 μJ) and probe (400 nm, 4 μJ) femtosecond laser pulses. The pump and probe pulses were produced by frequency conversion of the 800 nm output from our 1 kHz regeneratively amplified Ti:Sapphire laser system (Spectra-Physics, Spitfire Pro/Empower and Spectra Physics, Tsunami/Millennia Pro). The non-linear optical medium used to achieve the second and third harmonic (probe and pump, respectively) of the laser output through frequency doubling were thin β-barium borate crystals. The precise temporal delay between pump and probe was introduced using a PC-controlled linear translation stage and the two pulses were overlapped in a combining optic prior to the main vacuum chamber. The light pulses initially passed straight through the VMI set-up and were focused on the second pass through the interaction region using a curved Al mirror (f = 10 cm) inside the chamber. As detailed previously in Chapter 2 the intensities of the 267 nm and 400 nm beams in the focal region are estimated to be $\sim 5 \times 10^{12}$ Wcm^{-2} and $\sim 2 \times 10^{13}$ Wcm^{-2}, respectively. These

values represent an upper bound (refer to Chapter 2 for further details). The pulses intersected the molecular beam in the centre of the ion optics set-up where multiphoton ionisation takes place. Ejected electrons were focused onto an MCP and phosphor screen and the resulting VMI images were collected on a CCD camera. To rule out the presence of clusters, a time-of-flight (TOF) spectrum was recorded for each sample using the above setup but with positive charges on the ion optics. The pump-probe delay steps used were 30 fs in the region of -300 fs to + 300 fs and increase to 90 fs in the region from + 300 fs to 1 ps. Beyond 1 ps exponential steps were taken up to 200 ps. A typical data set contains 10 of these scans. A pump- and probe-alone background signal was recorded at each time delay to allow for an accurate background subtraction during data processing. A cross-correlation (CC) of the 267 nm and 400 nm pulses was determined using ionisation of xenon which was also used to calibrate the VMI images. The CC was found to be 140 fs.

As indicated above, the experimental configuration did not use the EL-valve in pulsed mode (as previously done for the acetylacetone measurements in Chapter 4). Regarding the sample density, general values in pulsed molecular beams have been reported to typically range between $10^{13} - 10^{14}$ particles cm^{-3} [262–264]. The calibration of the density of a molecular beam is however, known to be a non-trivial problem and error prone [265]. In their 2012 publication Parker, Eppink and co-workers estimate the sample density in a pulsed molecular beam through considering the change in pressure in the chamber. Applying this method to the experiment in this chapter gives an estimated gas load of $\sim 4 \times 10^{-4}$ bar L s^{-1} which corresponds to $\sim 9 \times 10^{18}$ particles s^{-1} in the chamber (carrier gas + sample). Since the beam employed here is not pulsed however, a value per shot as calculated by the authors does not apply. Another way in which the amount of sample present can be estimated is using the count-rate of electrons detected as done by McKay *et al.* [266]: countrate $= \sigma N l F$. Here, σ represents the photoionisation cross-section ($\sim 2.6 \times 10^{-17}$ cm^2 for nitrobenzene [267]), l is the interaction length (estimated to be 1 mm, based on the Rayleigh range for the 400 nm light) and F is the photon flux ($\sim 8 \times 10^{12}$ photons per pulse of 400 nm light, but two photons will be required for ionisation). Photoelectron acquisition rates for the TRPEI spectrometer employed here are estimated to be 5-10 per laser shot [94], yielding a number density of $\sim 480 - 960$ NB molecules mm^{-3}.

5.3 Computational Methods

The Gaussian software package was used to carry out all *ab initio* calculations presented here. The Gaussian 03 version [202] was used for ground state geometries and scans, whereas for the excited states Gaussian 16 [48] was used as its improved handling of TD-DFT calculations is beneficial. The ground state structures of all systems were computed using MP2 theory with the aug-cc-pVDZ basis set, except for NB where the aug-cc-pVTZ basis set was feasible (see Chapter 3 for more details). The optimised geometries are shown in Figure 5.2. Nitrobenzene is highly symmetric (C_{2v}) whereas the other three structures posses lower symmetry. In 3,5-DMNB, for example, C_{2v} symmetry might be initially expected, however, the methyl groups preferentially stagger, breaking this symmetry. The structure consisting of the staggered methyl groups in 3,5-DMNB was found to be about 18 cm^{-1} lower in energy than the eclipsed (higher symmetry) geometry. This difference in energy is low enough that both geometries would be present in the molecular beam under the experimental conditions described here (methyl groups are free to rotate). Such a staggering effect seems to be mitigated by the presence of the nitro-group in 2,6-DMNB as it retains a C_2 symmetry. For 2,4-DMNB the most energetically favourable dihedral angle (the angle between the plane of the benzene ring and the plane of the nitro-group) was not trivial to locate. Initial optimisations using DFT(B3LYP)/aug-cc-pVTZ (not shown here) indicated the minimum to be at ~ 21 degrees, but using the computationally more expensive MP2 method it was found to be at 35.2 degrees. The influence of various benzene ring substituents on the torsional angle of the NO_2 group in aromatic nitro systems was also investigated computationally by two earlier studies [268, 269].

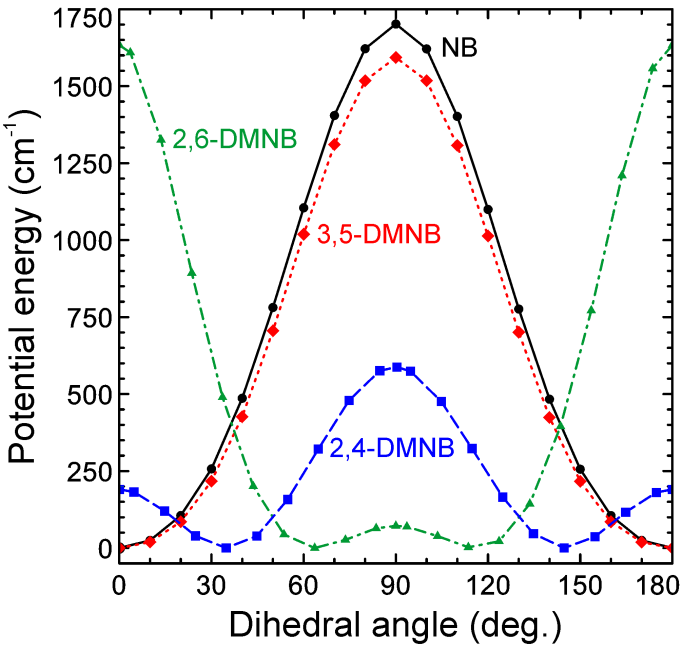

Figure 5.3: Ground state potential energy cuts of NB, 2,4-, 3,5- and 2,6-DMNB produced using MP2/aug-cc-pVTZ for NB and MP2/aug-cc-pVDZ for the other systems.

Relaxed ground state cuts computed about the NO_2 group torsion coordinate (dihedral angle) are shown in Figure 5.3 and aid in determining whether the structures are conformationally locked in the ground state. Again, the MP2 method in conjunction with the aug-cc-pVTZ basis set was used to produce these relaxed cuts for NB, and the aug-cc-pVDZ basis set was instead employed for the larger methylated systems. Transition state structures were optimised using the same methods and basis sets, and confirm the exact location of the maxima shown. The points have been computed in steps of 10 degrees from the structure at the optimised angle and the symmetry of the rotation can be used to plot all results within a range from zero to 180 degrees. Since the NO_2 group is symmetric, the first 180 degrees (or in fact 90°) of the rotation can be thought to be representative of the complete 360 degrees.

Nitrobenzene is predicted to be planar with a high barrier to rotation of 1702 cm^{-1}. The value compares favourable with the 1590 cm^{-1} value reported by Borisenko *et al.* from their electron diffraction study [270]. A further electron diffraction study reported a value of 1427 ± 336 cm^{-1} [271] and slightly lower values are reported by one microwave spectroscopy (1329 cm^{-1}) [272] and one Raman spectroscopy (1140 cm^{-1}) [273] study. Theoretical investigations using DFT methods in combination with a B3 based functional report extremely high values around 2200 cm^{-1} [243, 274]. Considering the experimental values reported, the computationally expensive MP2 method employed here performs well. As would be predicted, the barrier for 3,5-DMNB (1593 cm^{-1}) is very similar to that of NB and in 2,6-DMNB

Table 5.1: Energies (in eV) and oscillator strengths of four singlet excited states in NB and the methyl derivatives. The values were obtained using the ground state geometries computed using MP2 (as discussed in the main text), in combination with TDDFT and the CAM-B3LYP functional. The basis set used were aug-cc-pVTZ for NB, 3,5-DMNB and 2,4-DMNB. For 2,6-DMNB aug-cc-pVDZ was used. The results from an EOM-CCSD/aug-cc-pVTZ calculation for NB are also included. Symmetry labels reported correspond to NB transitions only. Orbital notation corresponds to that used by Dreuw and co-workers [250].

		TD-CAM-B3LYP				EOM-CCSD
		NB	3,5-DMNB	2,4-DMNB	2,6-DMNB	NB
S_1	$n-\pi^*$ $^1A_2$	3.91 (0.0000)	3.80 (0.0000)	3.79 (0.0224)	4.98 (0.0358)	4.02 (0.0000)
S_2	$n'-\pi^*$ $^1B_1$	4.38 (0.0004)	4.29 (0.0003)	4.32 (0.0005)	4.27 (0.0002)	4.53 (0.0005)
S_3	$\pi-\pi^*$ $^1B_2$	4.76 (0.0187)	4.31 (0.0263)	4.61 (0.0446)	4.59 (0.0177)	4.89 (0.0087)
S_4	$\pi'-\pi^*$ $^1A_1$	5.08 (0.2198)	4.80 (0.1969)	4.94 (0.1618)	3.67 (0.0108)	5.58 (0.2348)

the barrier is also comparable at 1633 cm^{-1}. The lowest barrier preventing free rotation of the NO_2 group is found in 2,4-DMNB (588 cm^{-1}), which is still believed to be insurmountable under the molecular beam conditions used here.

The relaxed and optimised ground state geometries computed at the various dihedral angles have been used to calculate the first few excited states in NB and 2,6-DMNB, at the same dihedral angles. These were computed using time-dependent DFT (TD-DFT) and the long-range corrected CAM-B3LYP functional. Again the aug-cc-pVTZ basis set is used, except in 2,6-DMNB where aug-cc-pVDZ was employed. Excited state energies and oscillator strengths obtained in the FC region are collated in Table 5.1. The diabatic cuts for NB and 2,6-DMNB are shown in Figure 5.4. Significant barriers to rotation of the NO_2 group are observed in the S_3 states for both molecules (7985 cm^{-1} and 2662 cm^{-1} for NB and 2,6-DMNB, respectively), although the S_2 and S_1 cuts show maxima at differing angles (90° and 0° respectively). These shallower barriers still range between 1387 cm^{-1} and 2331 cm^{-1}. More detailed references to this plot will be made in the discussion section of this chapter.

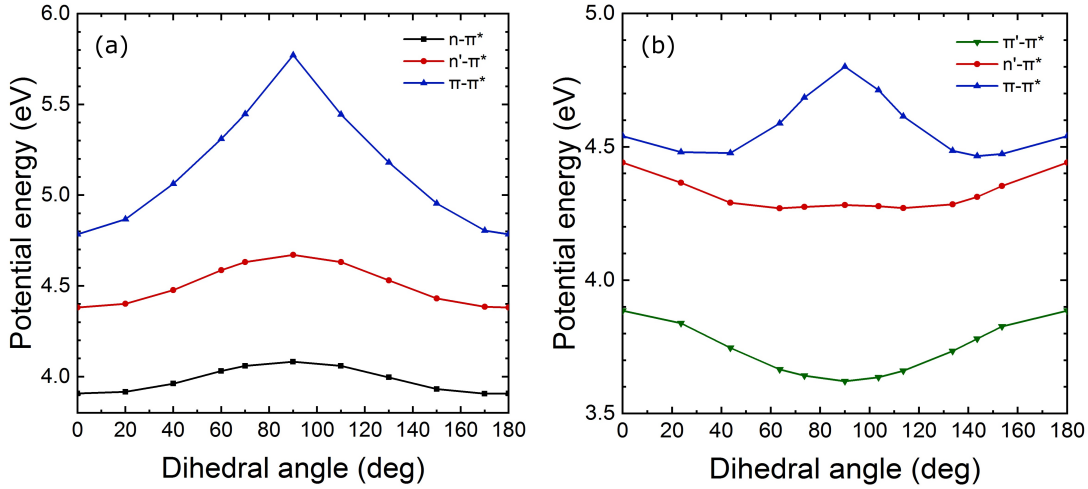

Figure 5.4: The first three excited state potential energy cuts for the rotation of the nitro-group in NB (a) and 2,6-DMNB (b), computed using TD-CAM-B3LYP/aug-cc-pVTZ and TD-CAM-B3LYP/aug-cc-pVDZ respectively. The relaxed MP2 ground state geometries were used as starting points.

The notation used to identify the orbital character should briefly be outlined. In the first column of Table 5.1, the character of the transitions is identified using n and π labels. In this ordering the labelling refers to the transitions in NB and is consistent with that suggested by Dreuw *et al.* [250], who also provide illustrations of the relevant molecular orbitals in NB. Here, the n and n$'$ labels describe the HOMO-2 and HOMO-4 orbitals respectively. Both are mainly located on the nitro-group but also extend onto the benzene ring. The π and π' labels identify the HOMO and HOMO-1 orbitals which have previously been illustrated in Chapter 1, Figure 1.6 (top row right and middle, respectively.). The relevant π^* orbital (HOMO+1) is also shown in this illustration (bottom row, far right) and is delocalised over both the nitro-group and benzene ring. For the methyl-substituted systems the orbitals change slightly, but the overall character remains the same and therefore the labels still apply.

5.4 Results

5.4.1 UV-Vis Spectra

Prior to the time-resolved study, an absorption spectrum in the ultraviolet to visible (UV-Vis) region was recorded for all four systems (shown in Figure 5.5) using a commercial UV-Vis spectrometer (Shimadzu UV-2550). The vapour pressure of all four molecules was sufficient to record the gas-phase UV-Vis spectra. A significant absorption peak centred at around 240 nm is present for NB, with two shoulders to the right of it. In 3,5- and 2,4-DMNB similar peaks can be observed, both red-shifted to longer wavelengths. For 2,6-DMNB a strong peak is not visible above 220 nm, however a shoulder is visible between 230-250 nm and there is a low but non-zero absorption signal extending out to 410 nm. At 410 nm all signals are observed to cut-off.

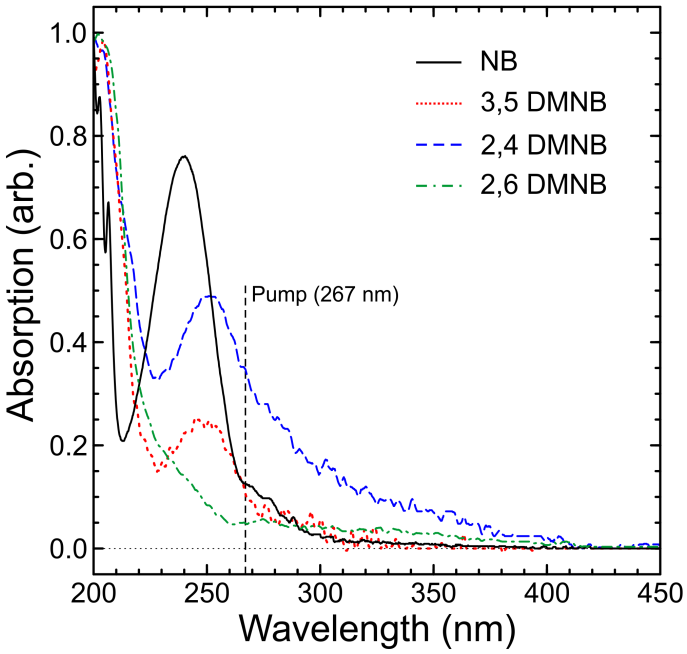

Figure 5.5: The normalised UV-Vis spectra recorded of all four systems in the gas-phase. The pump wavelength is indicated by the vertical dashed line.

In NB the excited state energies presented earlier (Table 5.1) predict a bright $\pi' - \pi^*(^1A_1)$ transition near 244 nm (5.08 eV) which is in good agreement with the strong absorption peak seen in Figure 5.5, centred at $\sim$ 240 nm. This band was also observed by Marshall *et al.* [254] and the assignment of the band made here is in agreement with the work by Lin *et al.* [246]. The shoulder located at the longer wavelength edge of the strong peak centred at 240 nm actually exhibits four weak features [275]. The feature centred at 280 nm has previously been assigned to the S_1 state by Abbot *et al.* [276] and Nagakura *et al.* [277]. Recently Lin *et al.* however argued that this band is more likely a combination of the S_2 ($^1B_1$) and S_3 ($^1B_2$)

states. The computationally obtained energy of the $S_2(n'\pi^*)$ state (also with a non-zero oscillator strength f) predicts a peak at 283 nm and we can therefore assign this feature to the $S_2(n'\pi^*)$ state in NB. As Table 5.1 indicates, the $S_3(\pi\pi^*)$ transition is expected to lie at $\sim$ 260 nm. This region describes the strong $S_4(\pi'\pi^*)$ absorption peak rather than the weak 280 nm feature. It is, however, possible that the energy of this state may be underestimated by the TD-DFT method as it has been shown to have charge-transfer character [250, 278] (known to often be treated unsatisfactorily by TD-DFT [279]). In comparison to the EOM-CCSD results, the output produced using the TD-DFT approach is only $\sim$ 0.1 eV lower in energy, implying that it has performed reasonably well. This indicates that the strong peak centred at 240 nm is likely to be a combination of $S_3(\pi\pi^*)$ and $S_4(\pi'\pi^*)$. The $S_2(n'\pi^*)$ and $S_1(n\pi^*)$ states can be assigned to the very weak bands at 280 nm and 350 nm (detailed by Marshall *et al.* [254]).

Similar assignments can be made for 2,4- and 2,6-DMNB, although the S_1 state in the latter is predicted to exhibit $\pi'\pi^*$ character, rather than $n\pi^*$ as in the other three systems under consideration. The shoulder at $\sim$ 240 nm in 2,6-DMNB can be assigned to the bright $S_4(n\pi^*)$ state, and the broad intensity feature at longer wavelengths is a combination of $S_3(\pi\pi^*)$ at 270 nm (non-zero f), $S_2(n'\pi^*)$ at 290 nm (negligible f) and $S_1(\pi'\pi^*)$ at 337 nm (non-zero f). The not-insignificant oscillator strength predicted in the $S_1(n\pi^*)$ state of 2,4-DMNB is in agreement with the pronounced "tail" observed between 330-410 nm and the $S_2(n'\pi^*)$ and $S_3(\pi\pi^*)$ states are merged with the high f feature centred at $\sim$ 260 nm, which is assigned to the $S_4(\pi'\pi^*)$ state.

The $S_1(n\pi^*)$ state in 3,5-DMNB and NB is predicted to have zero oscillator strength, matching the earlier cut-off of absorption signal observed in these two systems (at around 330 nm). The second and third excited singlet states are predicted to lie very close in energy in 3,5-DMNB, although $S_2(n'\pi^*)$ again has negligible oscillator strength and the weak signal between 280-290 nm can therefore be assigned to a combination of S_2 and $S_3(\pi\pi^*)$. The strong peak centred at $\sim$ 250 nm is signal arising from the red-shifted $S_4(\pi'\pi^*)$ state.

5.4.2 Photoelectron Spectra

All four systems, NB, 2,6-, 2,4- and 3,5-DMNB were excited using femtosecond laser pulses centred at 267 nm and probed using multiphoton ionisation at 400 nm. The VMI images recorded for NB at selected time delays are shown in Figure 5.6. The data shows a broad anisotropic ring decaying as the pump-probe delay increases. The absence of sharp rings in the VMI data indicates that no resonant Rydberg states have been ionised by the first 400 nm probe photon (via a $1+1'+1'$ process), which might obscure the dynamics. The VMI images of NB are representative for all the systems under study as the relaxation dynamics observed for all four systems

are very similar (which will be illustrated below). The strip of photoelectron images already reveals some of the dynamics: the strong signal observed at Δt=0 begins to reduce in intensity after about 300 fs and at large time delays, even at 200 ps, a weaker constant signal at smaller radius (lower energy) is still observed.

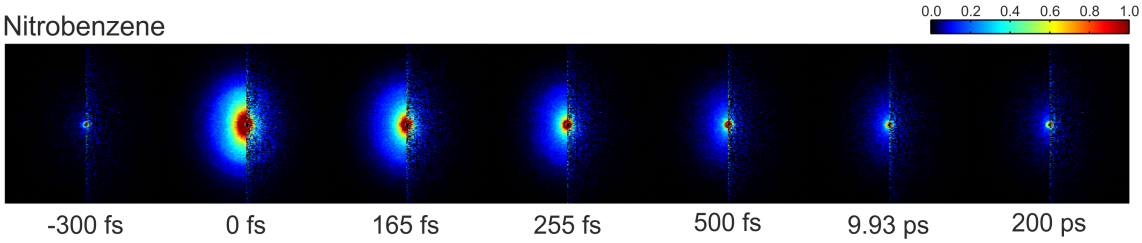

Figure 5.6: VMI images of NB at several pump-probe time-delays. The pump and probe alone signal recorded at each time-delay and has been subtracted in the images shown. The laser polarization of both the pump and probe beams is vertical with respect to the image.

This behaviour can be seen more clearly in the 2D-Photoelectron spectra of all four systems shown in Figure 5.7. The (1+2′) process cut-offs are indicated by the vertical white dashed lines in the spectra. The cut-offs were calculated using the ionisation potentials (IP) reported for NB (9.94 eV [280]), 2,4-DMNB (9.36 [281]) and 2,6-DMNB (9.17 [281]). For 3,5-DMNB the IP is not known. The signal-to-noise levels of the 2D-photoelectron spectra shown here are lower than those obtained for acetylacetone in the previous chapter as a fewer number of total scans were collected due to time-constraints. The signal-to-noise ratio for 3,5-DMNB is noticeably worse than that of the other systems as it is the only solid sample and therefore more difficult to introduce into the gas-phase.

The dynamics observed for all systems under study are near identical. Each system displays a distinct short-lived feature and a lower intensity signal is observed to run out up to the limit of the experiment at 200 ps. This is particularly clear at low photoelectron kinetic energies. Using the Levenberg-Marquardt global fitting routine (introduced in Chapter 2) a total of three time constants are required to fit each of the 2D-photoelectron spectra satisfactorily. The distinct short-lived feature is characterised by a near-Gaussian time-constant which is indicative of a rapid initial relaxation process. As the experimental cross-correlation was 140 fs, a reliable lifetime could not be extracted from this extremely short-lived feature and only an upper bound of 30 fs can be assigned. Two longer time constants are required to satisfactorily describe the longer-lived feature observed in all four spectra. In NB the two longer lifetimes extracted are a τ_2 of 0.18 ps and a τ_3 of 90 ps. Similar time constants are obtained when fitting the data of 2,4-, 2,6- and 3,5-DMNB, which are summarised in Table 5.2.

From the photoelectron spectra it is evident that there are signals extending beyond the (1+2′) cut-off. These likely arise from a (1+3′) multiphoton ionisation

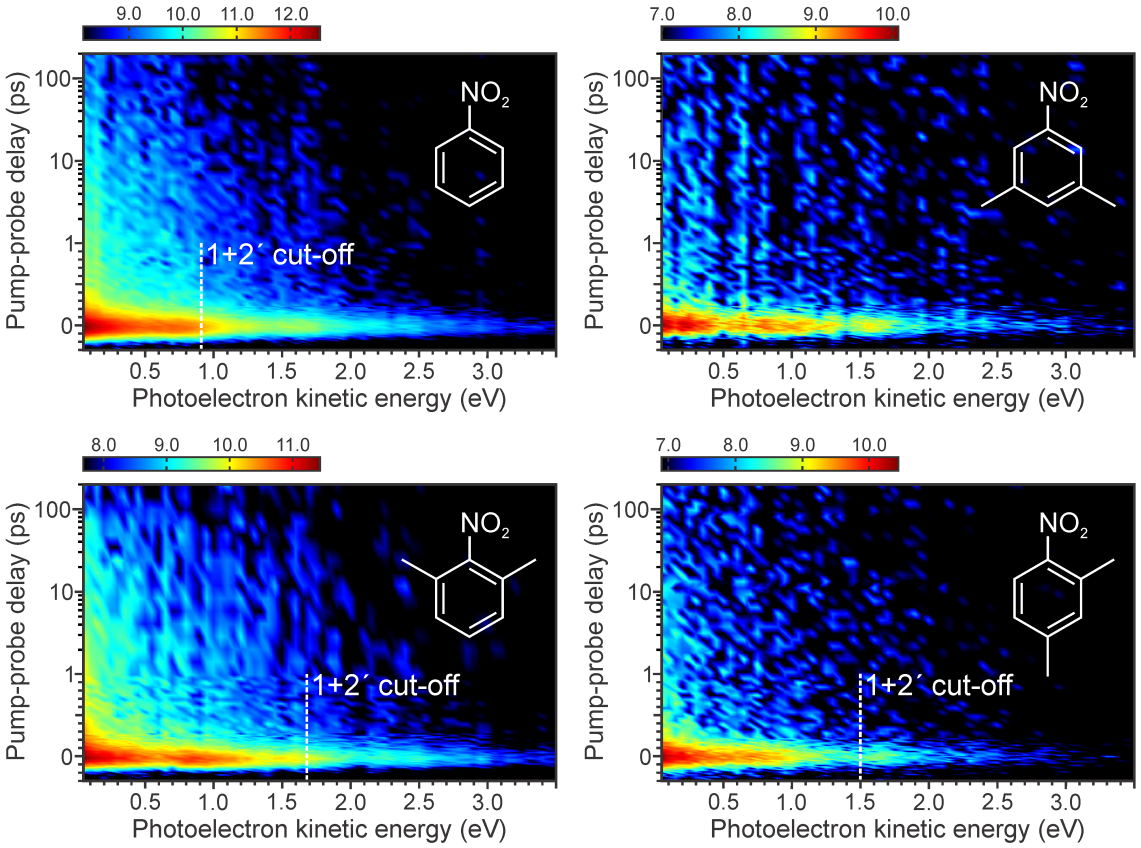

Figure 5.7: The 2D time-resolved photoelectron spectra of NB, 3,5-DMNB, 2,6-DMNB and 2,4-DMNB (left to right). The intensity colour map is presented on a natural logarithmic scale based on the output directly obtained from the imaging CCD camera.

Table 5.2: A summary of the time constants extracted using the Levenberg-Marquardt global fitting routine, for NB and its three methyl-substituted derivatives following 267 nm excitation.

	NB	3,5-DMNB	2,4-DMNB	2,6-DMNB
τ_1	<30 fs	<30 fs	<30 fs	<30 fs
τ_2	0.18 ± 0.02 ps	0.16 ± 0.04 ps	0.19 ± 0.04 ps	0.16 ± 0.03 ps
τ_3	90 ± 10 ps	160 ± 35 ps	120 ± 25 ps	90 ± 20 ps

process and will be considered in more detail in the discussion section below, which includes a further figure (Figure 5.10) in which the signal intensities below and above the (1+2′) cut-off are compared.

5.4.3 Decay Associated Spectra and Photoelectron Angular Distributions

The decay associated spectra (DAS) for all four systems studied are shown in Figure 5.8. Vertical dashed lines again indicate the energetic cut-off of the (1+2′) process, where known. Three exponentials are required to fit the time evolution of each of the systems with each exponential fit originating at zero time-delay. The bulk of the signal is described by a time constant between 160 fs and 190 fs, depending on the system (yellow-dashed line) and the very long-lived feature manifests as a low signal running through all of the spectra (blue dashed-and-dotted line).

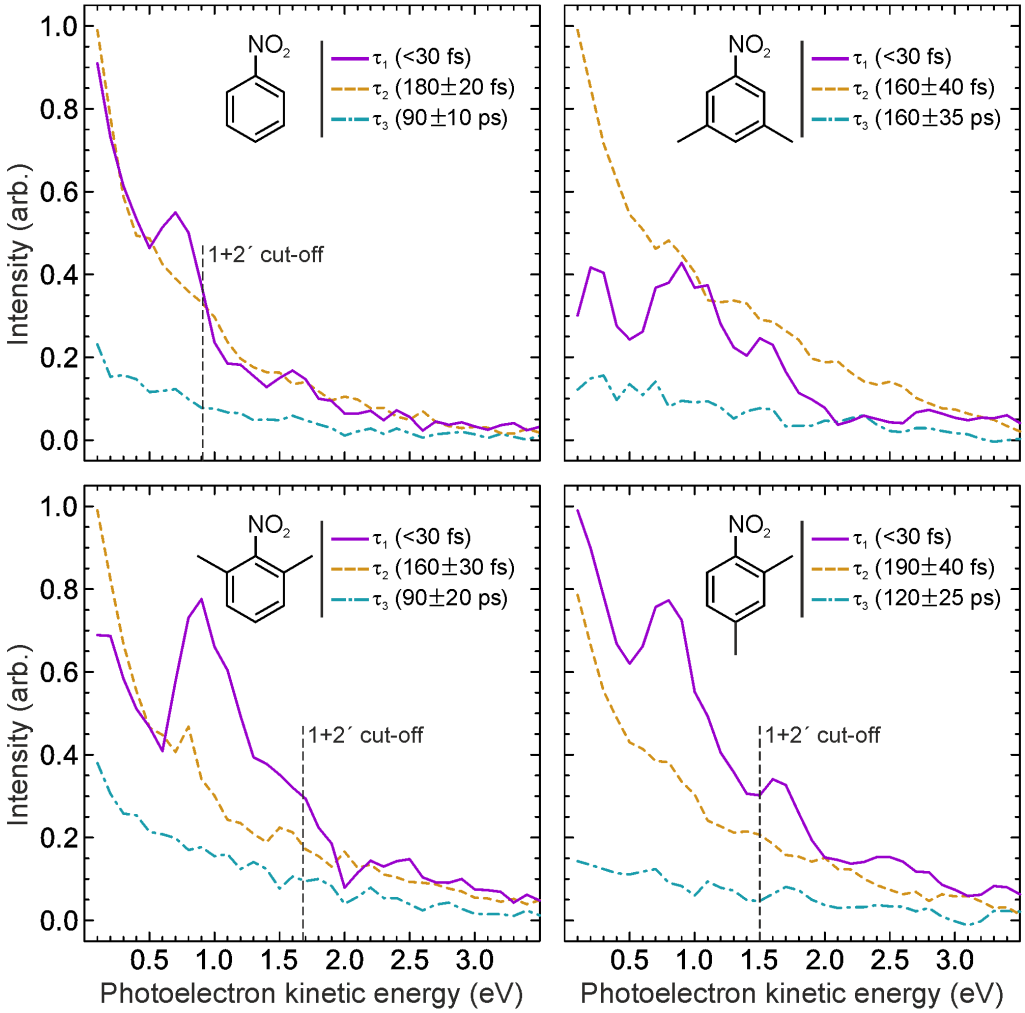

Figure 5.8: Decay associated spectra of all four systems under investigation.

Interestingly though, the DAS also highlight peaks that are otherwise easily missed in the 2D-photoelectron spectra. These peaks, centred at around 0.7 eV in

NB, 0.8 eV in 2,4-DMNB and 0.9 eV in 3,5-DMNB and 2,6-DMNB are described by the shortest time constant (<30 fs) in each system. It is interesting to note that in 2,4-DMNB a second feature (also very short-lived) is visible beyond the (1+2′) cut-off between 1.6 eV and 1.7 eV. In 2,6-DMNB a shoulder is visible at around 1.5 eV, extending beyond the (1+2′) cut-off. Finally, in 3,5-DMNB it appears that there are three peaks present in the DAS of the τ_1 time-constant. However, this data has the lowest-signal to noise ratio and therefore caution has to be exercised when examining subtle features. It is most likely that only the central feature at 0.9 eV is a true signal not arising from noise.

In the previous chapter on acetylacetone, the onset of the DAS could be matched to the most probable transitions using Koopmans' correlations. Here, this task becomes more challenging as the (1+3′) contributions obscure such cut-offs. Indeed in the τ_2 and τ_3 DAS no clear onsets are observed for any of the four systems. According to the assignments by Kobayashi and Nagakura [281, 282] the D_0 and D_1 states in NB both possess π^{-1} character, and D_2 shows n^{-1} character. Detailed correlations between excited and cation states have been reported by the authors [281]. The π character observed in D_0 matches that in $S_3(\pi\pi^*)$, whereas D_1 possesses a different kind of π character (π'). Therefore the $S_3(\pi\pi^*)$ is expected to ionise preferentially to $D_0(\pi^{-1})$ but not $D_1(\pi'^{-1})$. The favoured $D_0 \leftarrow S_3$ transition matching the (1+2′) cut-off is observed in the τ_1 DAS. A similar restriction applies for the $S_1(n\pi^*)$ state which will show a higher propensity for ionising into the $D_2(n^{-1})$ state, but $S_2(n'\pi^*)$ on the other hand will not. The state with matching n′ character (correlating to the S_2 excited state) is not identified by Kobayashi and Nagakura who have assigned characters up to D_3 only [281]. S_2 is therefore likely to favourably ionise to a state beyond D_3. Energetically this means that the preferential transition from the first excited state to D_2, and that of the second excited singlet state to its corresponding cation state, is only observable with the (1+3′) process (not with (1+2′) ionisation). The excess energy from these transitions would place signals arising from these processes in the high-energy half of the pKE spectrum, where little DAS signal is observed. The Koopmans' correlations will be discussed further in Section 5.5 below. Kobayashi and Nagakura also studied the photoelectron spectra of 2,4- and 2,6-DMNB but have only partially assigned the characters of their first four ionised states [282], hindering assignments of the DAS signatures based on Koopmans' model. Cation state energies of 3,5-DMNB have not been reported. One final stipulation is related to the altered ordering of the excited states in 2,6-DMNB. In contrast to NB and 2,4- and 3,5-DMNB, the lowest lying excited state in 2,6-DMNB has $\pi - \pi^*$ character, which would affect the Koopmans' correlations. This could be reflected in the DAS, perhaps explaining the larger τ_3 contribution compared to the other systems.

In Chapter 2, the relationship between the order of the photoionisation process and the number of β-parameters (Legendre polynomials) was introduced (Equation

2.19). A (1+1′) process requires the first two anisotropy parameters (β_2 and β_4) to describe the anisotropy of the particle distribution. The (1+2′) and (1+3′) processes used for the study of NB and its methyl-substituted derivatives require two further terms β_6 and β_8 to fully describe the distribution (Equation 2.21). The REPEITS *Analyse* code was edited by myself to extend the fit to extract and plot the additional two anisotropy parameters. Figure 5.9 shows 2-dimensional plots, in photoelectron kinetic energy and pump-probe delay time, of the four relevant anisotropy parameters in NB. NB here is representative for all four systems. As evident from Figure 5.9, there is a positive β_2 parameter which extends out to the 200 ps limit of the experiment, whereas β_4, β_6 and β_8 are negligible throughout. Furthermore, the noise increases as the order of the anisotropy parameter increases, due to the reduced contribution of the higher order parameters. No significant temporal variation is observed in the map of β_2, which leads to the conclusion that the anisotropy parameters are unlikely to reveal additional dynamical information in this instance.

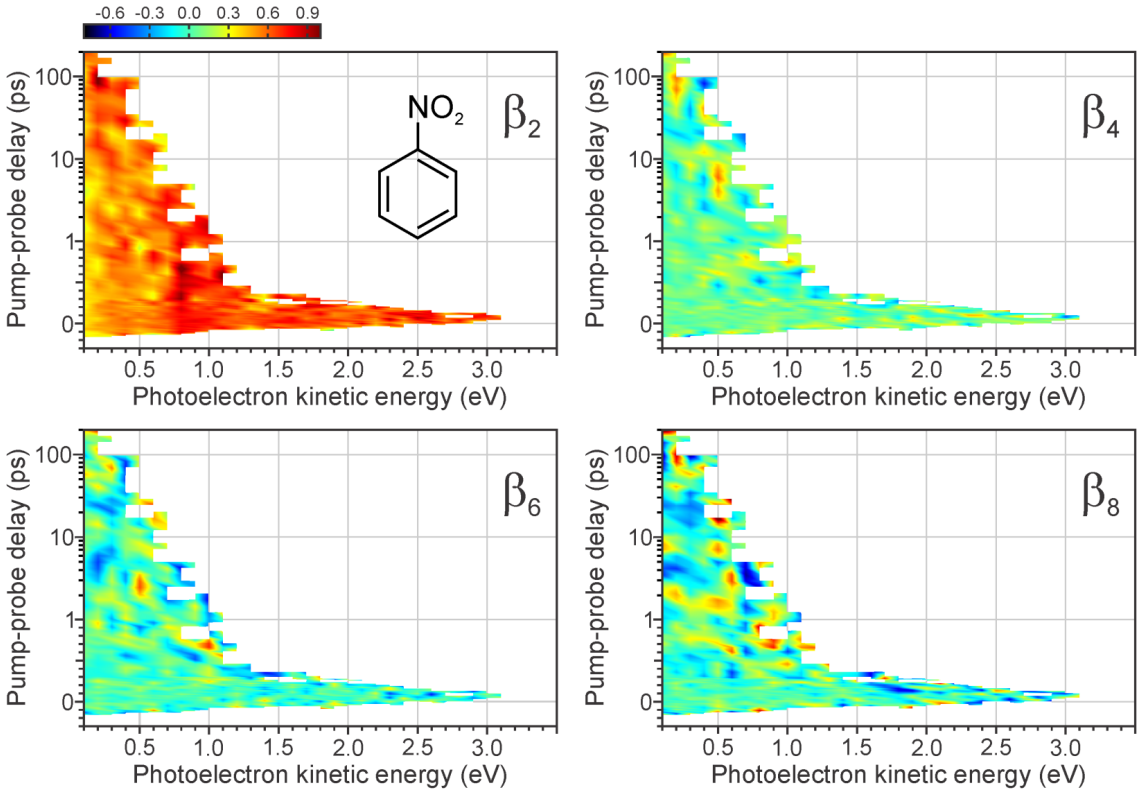

Figure 5.9: 2D maps of the four anisotropy β parameters fitted for nitrobenzene. These are plotted on the intensity scale indicated in the top left corner of the figure.

5.5 Discussion

As indicated by the excited state energies presented earlier in Table 5.1, the 267 nm pump employed here excites mainly the S_3 state in NB and the methylated systems, although some direct optical population of S_2 is also likely, especially in

3,5-DMNB where the states are predicted to be almost degenerate (by our TD-DFT calculations). The excited state plots for NB and 2,6-DMNB shown in Figure 5.4 confirm that in the initially excited S_3 states there is still a significant barrier to rotation which cannot be overcome by the 267 nm excitation. Therefore, the 'locking' of the nitro-group conformation is a valid assumption, even in the excited state.

As was observed in the photoelectron spectra, signals arising from (1+3′) multiphoton ionisation are present beyond the (1+2′) cut-off. To inspect the similarity of the spectra below and beyond this cut-off, a plot of the time-evolution of the photoelectron spectra integrated over either energy region (below and above (1+2′) cut-off) is shown in Figure 5.10. These plots may be used to partially disentangle the overlapping (1+2′) and (1+3′) signals by identifying any changes in the integrated signals above the (1+2′) cut-off. For 3,5-DMNB the IP is not known but was estimated to be the same as that in 2,6-DMNB. The comparison of the dynamical signatures in these two regions shows that no previously unobserved signals arise above the (1+2′) photoionisation limit and that the relative heights of the traces also remain the same. Three photons of 400 nm equate to a probe energy of $\sim$ 9.3 eV, which should provide sufficient energy to ionise photofragments including phenyl C_6H_5 (IP: 8.67 [283]), phenoxyl C_6H_5O (IP: 8.56 eV [284]) or NO. The NO_2 fragment cannot be observed due to its high IP (9.6 eV [285]) and the probability of observing signals arising from the ionisation of the NO photoproduct is low due to a combination of factors. Firstly, its IP has been reported as 9.26 eV [286, 287], which is at the energetic limit of the probe and secondly the resulting NO fragment is found in the $v = 0$ vibrational state after dissociation [240, 255, 288]. The justification for the absence of dynamical features due to the ionisation of the phenyl or phenoxyl photofragments on the other hand is not initially apparent. Electrons resulting from the ionisation of these fragments would posses excess kinetic energies in the range of 0.7-1.0 eV, lying within the low kinetic energy region (blue data points) shown in Figure 5.10. As such, their dynamical signatures may be obscured by the strong signals at early pump-probe delay times, but as the fragments are likely produced at later times a rising signal at long delay-times where there is only a low constant signal, may be expected. The consideration of lifetime is key here. Zewail and co-workers determine that the NO product is released within 8.8 ps [243] whereas Y. T. Lee and co-workers report that the experimentally observed dissociation of NB occurs on a timescale of $\sim$ 59 ns [246, 289] (both using 266 nm excitation). Theoretical work by Lin *et al.* also predicts the formation of fragments to occur on timescales outside our observation window [246]. The delayed formation of the photoproducts would explain the absence of any rising signals due to photofragments within the 200 ps observation window of this current experiment. Using the above observations in combination with the results from this TRPEI study it can be argued that fragmentation occurs on the S_0 ground state and on extremely

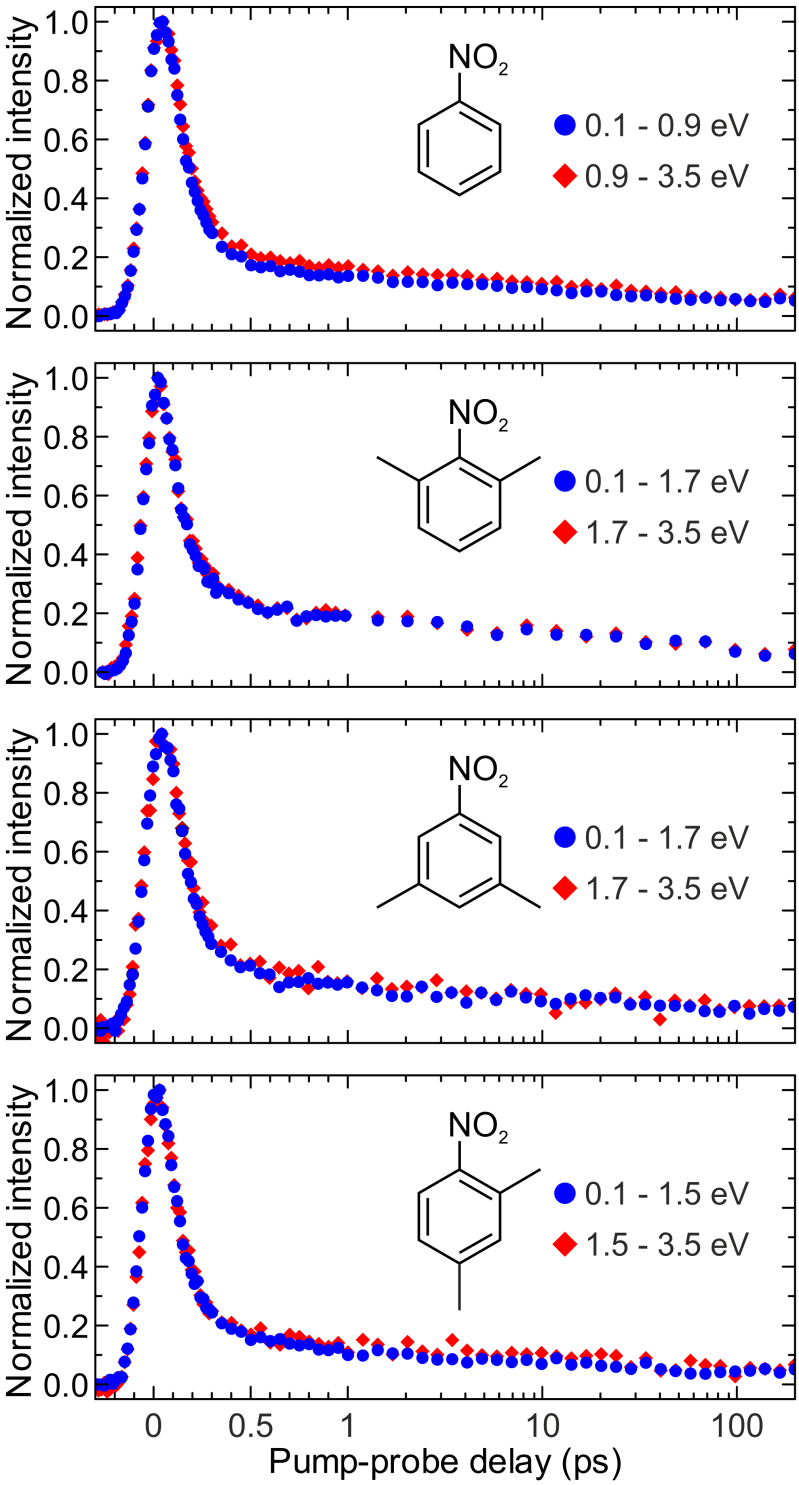

Figure 5.10: The variation in intensity of the signal over the whole range of time delays is shown for all four systems here. The blue (dots) markers indicate the photoelectron signal integrated over the regions leading up to the (1+2′) energetic cut-off, whereas the red (diamond) markers are signals integrated from the cut-off out to 3.5 eV.

extended timescales. It cannot be ruled out that a slowly rising contribution may be obscured by the decaying signal at long pump-probe time delays as the plots in Figure 5.10 do not show a complete decay to zero, but a remaining low-level signal present even at 200 ps. As previously in the study of acetylacetone (Chapter 4), the assumption that the fragments will not leave the focal volume within the time of the experiment can be made. The second assumption ruling out any secondary dissociation of the photoproducts is less trivial to confirm in this case. Galloway *et al.* observed the fragmentation of phenoxyl into several products within their experimental timeframe of 50 ns (240 nm photolysis wavelength) [240] and such secondary fragmentation is also mentioned by Suits and co-workers [247]. These smaller secondary fragments are likely to have a higher IP and may therefore not be observed, even with the 9.3 eV available in this experiment. Since the precise timing of secondary fragmentation is not known, it can only be speculated that it might occur on very short timescales, a further factor prohibiting the observation of photofragment signal in the photoelectron spectra reported here.

The theoretical studies by Giussani *et al.*, Dreuw and co-workers, as well as Quenneville *et al.* all predict a conical intersection between the S_1 state in NB and a member of the triplet manifold [249–251]. A three-state degeneracy is observed between S_1, S_0 and a member of the triplet family by Quenneville *et al.* and by Dreuw and co-workers, which is accessed by an out-of plane bend of the nitro-group. As discussed in the introduction section of this chapter, various experimental studies also predict fragmentation to occur from the triplet surface. Takezaki *et al.* assign their 6 ps lifetime observed to an ISC process and the 480 ps lifetime as the relaxation from a triplet state to the ground state [241, 242]. The energy provided by the (1+2′) process in this current study is not sufficient to observe any signals from these low-lying triplet states, but three photons of 400 nm in the (1+3′) process are. Features from dynamics on the triplet surface are, however, not observed in the data presented here. There is the possibility that the triplet state dynamics are rapid, and occur much faster than the rate-limiting step of the dynamics observed. This would result in little to no population build up in these states making them not observable. This notion is comparable to the concept of the 'steady state' behaviour that is well-known in basic chemical kinetics. The TRPEI study conducted by Schalk *et al.* (using a 200 nm pump) also observed only very little evidence of dynamics taking place on the triplet manifold and used theoretical calculations to argue that the manifold is avoided [248].

Now that various aspects of the photoelectron spectra have been discussed the extracted lifetimes can be assigned to dynamical events. The first lifetime observed in all four systems ($\tau_1 < 30$ fs) indicates the presence of a rapid dynamical process. Based on the excited state calculations presented here, as well as the study by Giussani and Worth [249], it is predicted that 267 nm excites the $S_3(\pi\pi^*)$ state in NB, slightly above the state origin. A relaxation to the S_3 minimum is therefore likely

to be described by this ultrafast dynamical signature. The excited state potential energy cuts along the dihedral angle coordinate (Figure 5.4) indicate that NB (and 2,6-DMNB) are excited into the S_3 state already very close to the minimum, however, since these plots only show the potential energy landscape along one specific coordinate, it is likely that what is observed here is a local minimum. The calculations reported by Giussani *et al.* indicate that reaching the global minimum of the third excited state involves a shortening of the N-O bonds as well as a reduction of the O-N-O angle [249]. The onset in the τ_1 DAS in NB discussed earlier also indicates ionisation into the D_0 state from $S_3(\pi\pi^*)$, confirming the involvement of this state in the initial observed step of the relaxation dynamics. As the τ_1 time constants extracted are only an upper limit, it is possible that the processes in the other three systems differ, but the overall similarity of the photoelectron spectra strongly suggest that the same process occurs in all four systems.

Returning to NB, the next two steps characterised by τ_2 (180 fs) and τ_3 (90 ps) likely follow directly from the relaxation to the S_3 minimum. The step described by 180 fs is assigned to an IC process from the S_3 surface to S_2, followed by a second IC step to S_1 and subsequent decay of this state, complete within 90 ps. Again this is in agreement with the relaxation pathway stipulated by Giussani and Worth and the extremely similar timescales observed in the methyl-substituted systems imply that the same dynamics operate in all four systems. A further approach that can be used to disentangle the signals arising from the two different mulitphoton processes is to make use of the energetics in conjunction with the Koopmans' correlations and the DAS. The earlier discussion of the predicted Koopmans' correlations concluded that both S_1 and S_2 must preferentially ionise to a higher cation states (above D_1), which cannot be achieved with the (1+2′) ionisation. Therefore, a difference in the (1+2′) process and (1+3′) process signals would be expected, but this is not observed (Figure 5.10). The absence of novel dynamical signatures in the high-energy region of the photoelectron spectrum confirms that both the S_1 and S_2 excited states are observed with (1+2′) mutliphoton ionisation. The discrepancy between this observation and the predictions made using the Koopmans' correlations (based on assignments made by Kobayashi and Nagakura [281]) could be explained by strongly mixed characters in the cation states, which would alter the Koopmans' correlations. Further theoretical investigation of the cation states may be required to explain this discrepancy between the observed and predicted results.

Theoretical work by Quenneville *et al.* supports the here proposed relaxation pathway via internal conversion processes on the singlet surface. The group has computed the singlet surfaces as a function of the S_1 reaction coordinate and their plots indicate that population transfer from $S_4 \rightarrow S_3 \rightarrow S_2 \rightarrow S_1$ in NB does not require or involve a torsion of the nitro-group [251]. As such, non-adiabatic relaxation between these singlet states through IC is consistent with the observation of near-identical relaxation dynamics between the systems with varying, locked nitro-group

conformations. Efficient IC processes for any state above S_1 are also predicted by Zewail and co-workers [243], and Suits and co-workers suggest that the dissociation is slow and due to internal conversion to the ground state S_0 as they observe a large amount of internal energy in the phenoxyl product [247]. Energetically the recovery of the ground state signal should be possible to observe with the (1+3′) process, but a conclusive signal is not observed. Since there is a non-zero dynamical signature present beyond the experimental delay-time limit of 200 ps, it is likely that S_0 signal is slowly growing in, producing this 'levelling-off' of the long-time signal. This would be consistent with the earlier discussion regarding the production of photofragments on extended (nanosecond) timescales, which are in all likelihood formed on the electronic ground state. These observations are in agreement with the roaming-mediated isomerisation to phenyl nitrite suggested by Suits *et al.* [247] as this mechanism is predicted to proceed via the singlet surface and result in product formation on S_0.

To conclude the discussion, the time-resolved photoelectron imaging study of NB and its methyl derivatives has revealed no significant deviations between the dynamics of the four systems studied: NB, 2,4-, 2,6- and 3,5-DMNB. This strongly implies that the nitro-group torsion does not facilitate the ultrafast non-adiabatic relaxation dynamics in the aromatic nitro compounds studied. Torsional motions have been associated with dynamics crossing from the singlet to the triplet manifold which are therefore not likely to be major contributing pathways at 267 nm excitation. The results obtained here support the theoretical pathways predicted by Giussani and Worth, which involve motions localised on the NO_2 group [249]. The conclusions drawn from the results of this study agree with the initial predictions made by Galloway *et al.* that internal conversion to the ground state is followed by fragmentation on the S_0 surface [240, 288]. The mediation of the ultrafast relaxation dynamics through motions localised on a specific part of the molecule has been considered previously by the group of A. Stolow, who coined the term 'dynamophore' [290]. From what has been observed here it can be concluded that the NO_2 group acts as the dynamophore in NB and its methyl-substituted derivatives studied. This is a perhaps surprising result, given the observations made in the study by Suzuki *et al.* discussed earlier, where the NO-release activity in a series of aromatic nitro-compounds was found to be dependent on the orientation of the NO_2 group [18]. Since the nitro-group orientation does not mediate the ultrafast dynamics in these systems, however, it can be speculated that steric effects related to the methyl groups may hinder the isomerisation to phenyl nitrite on the S_0 surface. This may in turn affect the fragmentation process which is predicted to occur at long-lifetimes on the S_0 surface.

5.6 Conclusion

This Chapter outlined an investigation into the ultrafast relaxation dynamics in NB, 2,4-, 3,5- and 2,6-DMNB following UV excitation. The choice of molecular systems provided scrutiny of the role of the nitro-group configuration in the excited state molecular dynamics of the four systems. Computational *ab initio* calculations confirmed that the nitro-group was not able to freely rotate under the experimental conditions employed, in the ground and relevant excited states. The four systems were found to exhibit near identical relaxation dynamics, which consist of an extremely rapid process (sub 30 fs) and two longer dynamical signatures ranging between 160-190 fs and 90-160 ps respectively. The sub 30 fs lifetime was assigned to the population leaving the Franck-Condon region, and relaxing to the minimum on the S_3 surface. The internal conversion from S_3 to the next lower-lying singlet state was determined to be complete within 200 fs, whereas the final relaxation step observed describes the decay of the S_1 state. It is predicted that fragmentation occurs on the S_0 ground state surface, likely via a roaming-mediated isomerisation to phenyl nitrite suggested by Suits and co-workers [247]. The timescale of the production of the photoproducts is believed to extend well beyond the observation window of this experiment (200 ps), as observed and predicted by Y. T. Lee and co-workers [246]. No dynamical processes occurring on the triplet surface were observed, which is in agreement with theoretical predictions made which conclude that the crossing to the triplet manifold must involve a torsion of the nitro-group [250, 251] - a motion clearly not accessed here. The non-adiabatic dynamics are most likely facilitated by localised motions on the nitro-group, as predicted by theoretical work [249].

Chapter 6

Excited State Dynamics of Small Amides

This chapter will discuss work published in reference [291], which appeared as a *Feature article* in The Journal of Chemical Physics. The work presented is a collaboration between the groups of A. Stolow at the National Research Council (NRC) Canada and the University of Ottawa, T. I. Sølling at the University of Copenhagen and D. Townsend at Heriot-Watt University. The experimental results were collected at the University of Ottawa by R. Forbes and M. M. Zawadzki, and analysed by M. A. B. Larsen at the University of Copenhagen. All *ab initio* calculations and analysis of these, as well as a minor amount of experimental data analysis (improved $t \leq 0$ background subtraction) were carried out by L. Saalbach.

6.1 Introduction - Amine and Amide Motifs

In nature, the amine and amide groups are ubiquitous; they are found in peptides, amino acids, the DNA bases and neurotransmitters. This might be explained by the fact that these groups display biologically favourable qualities such as superior resistance to damage upon exposure to ultraviolet (UV) radiation, which is a key requirement for a biological chromophore. Furthermore, formamide and its methyl-derivatives specifically, are excellent models for the peptide bonds, linking amino acids in protein chains [19]. An understanding of the role played by these subunits can be gained by studying how excess energy is redistributed in the molecule using time-resolved techniques. This is of great interest as it may infer how the larger biological structures (amino acids, DNA bases etc.) are affected by the properties of their constituents.

Another interesting feature in amines and amides is the presence of low-lying singlet excited states of mixed Rydberg/valence nature. These are often 3s type Rydberg orbitals in the Franck-Condon region which develop σ^* valence character upon bond extension. These types of orbitals have been shown to facilitate radiationless transitions to the S_0 ground state as they lower in energy [20–23, 292] when

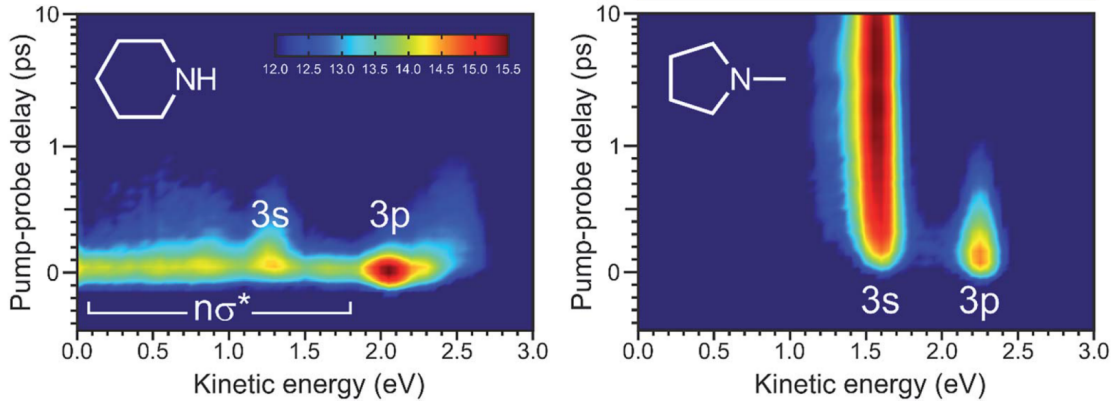

Figure 6.1: 2D photoelectron spectra of piperidine and N-methylpyrrolidine, adapted from reference [23].

the Rydberg state acquires more valence character. This can promote the formation of conical intersections as low-lying excited states approach S_0 or form crossings with each other, providing opportunities for nonadiabatic relaxation mechanisms to occur. Such Rydberg-to-valence evolution is typically found in small hetero-atomic systems along N-H, O-H or S-H bonds. The significance of states with σ^* valence character with respect to photodynamics has been investigated broadly, as is summarised in the reviews by Ashfold *et al.* [20] and Roberts and Stavros [292].

Aliphatic amines, for example, exhibit this 3s Rydberg state which has the potential to develop σ^* character when a N-H bond in these systems is elongated. In several TRPEI studies from 2016 it was found that in primary (1°) and secondary (2°) aliphatic amines, valence character evolution does take place, and sub-picosecond dynamical signatures have been attributed to this behaviour [21, 22, 293]. For tertiary (3°) aliphatic amine systems, however, very long excited state lifetimes (>10 ps) have been reported [21] and it was concluded that these are in fact due to the 3s Rydberg state avoiding the expected evolution of valence σ^* character. This behaviour can be compared for two specific examples: the secondary aliphatic amine piperidine [22]; and the tertiary species N-methylpyrrolidine [21]. Their photoelectron spectra are shown in Figure 6.1. An excitation at 200 nm in both of these systems populates a member of the 3p Rydberg manifold, which rapidly relaxes to a 3s Rydberg state via internal conversion in <400 fs. Beyond this step the dynamics are less similar with piperidine exhibiting another rapid decay in 180 fs in contrast to the slow decay of 160 ps observed in N-methylpyrrolidine. Computational *ab initio* calculations provide some insight into these differing behaviours; when N-C bonds are extended it is not the 3s but the 3p Rydberg states that appear to show evolution of σ^* valence state character in primary, secondary and tertiary amine systems. This leads to lowering in energy of these states which facilitates the rapid initial relaxation from a 3p Rydberg state to a 3s Rydberg state via internal conversion. The 3s states only evolve the anticipated σ^* character upon N-H bond extension, which

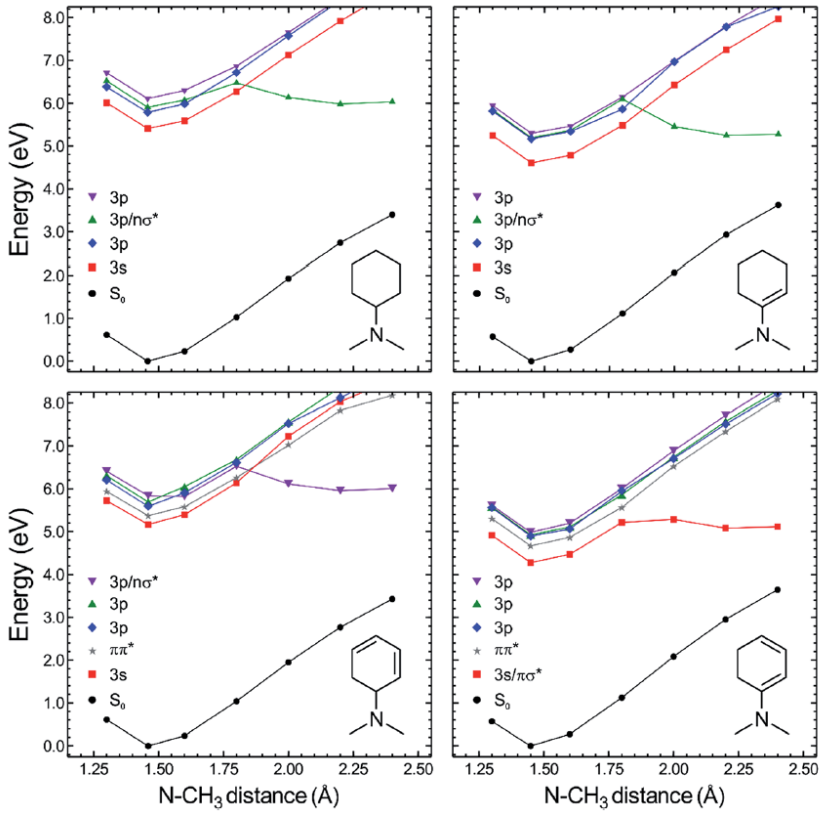

Figure 6.2: Potential energy cuts along the N-CH_3 coordinate (produced using EOM-CCSD/aug-cc-pVDZ) in several model aromatic amine systems, where conjugation was introduced at different positions around the aromatic ring. This figure has been adapted from [23].

is of course not possible in tertiary systems as only N-C coordinates are present.

The trends displayed in *aromatic* amine species differ from what has been established for the aliphatic systems outlined above. The tendency for 3s Rydberg states to evolve valence σ^* character seems to hold along both N-H and N-CH_3 coordinates in aromatic systems of any order ($1°, 2°, 3°$). An example of this is provided by two recent TRPEI studies comparing the relaxation dynamics of aniline ($1°$) [261], N,N-dimethylaniline (N,N-DMA - $3°$) and 3,5-dimethylaniline (3,5-DMA - $1°$) [23, 261]. The first study used a pump of 250 nm [261] whereas a 240 nm pump was used in the second study [23]. The systems display fast relaxation dynamics of about 100 fs which have been linked to the Rydberg-valence evolution of the 3s Rydberg state. It was observed that along both N-H (and N-CH_3 where present) coordinates the S_2 3s-Rydberg state develops valence character in all three systems.

The latter study contains an *ab initio* investigation into the role of unsaturated chemical functionality on relaxation dynamics. This theoretical work was produced by myself during my MPhys final year project [294], forming a relevant connection to the study on amide systems outlined here. As illustrated in Figure 6.2, carbon double bonds (C=C) were introduced at different positions around the ring in model aromatic amine systems in this theoretical investigation, published in [23].

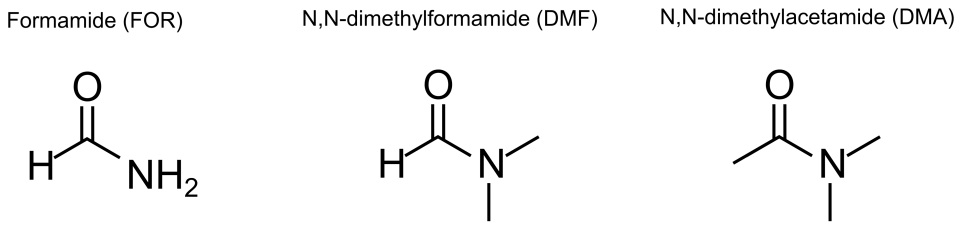

Figure 6.3: Illustrations of the three amide systems under investigation. Only the keto tautomers shown are expected to be present under the experimental conditions used in this study (see reference [309]).

The potential energy cuts along the N-CH_3 stretch show the effect of the C=C bond location on the states facilitating a route for radiationless relaxation processes. The proximity of an unsaturated carbon bond to the N atom with its lone pair, appears to influence which Rydberg state evolves valence character. This should be observable in the relaxation dynamics, although experimental investigation of this behaviour has not yet been carried out. Such proximity effects were also investigated in a study of acrylonitrile and its methyl-substituted derivatives [295]. Overall, the introduction of conjugation and the presence of π-bonding in aromatic systems appear to play a role in determining the nature of the character of the states along nuclear coordinates of interest.

This chapter will present an investigation into the influence of the proximity of the carbonyl (C=O) group to either the NH_2 or $N(CH_3)_2$ groups on the relaxation dynamics in formamide (FOR), N,N-dimethylformamide (DMF) and dimethylacetamide (DMA), illustrated in Figure 6.3. The three systems are studied using time-resolved photoelectron imaging in conjunction with vacuum UV (VUV) pump pulses, with a central wavelength of 159.4 nm (7.78 eV). As reported by several spectroscopic [296–300] and theoretical investigations [301–307], this wavelength excites a member of the 3p Rydberg manifold as well as a $\pi\pi^*$ valence state in FOR, which is associated with the carbonyl group. The reported absorption bands are redshifted for DMF and DMA [296–298] making members of the 3d Rydberg manifold energetically accessible [305, 308].

6.2 Experimental Methods

The experimental setup used to record the TRPEI data in Ottawa has been described previously in references [128] and [129]. The methods used to generate vacuum UV light are very similar to the ones outlined in Chapter 2. The laser system employed (Coherent Legend Elite Duo) produces output pulses of 35 fs (FWHM) and a central wavelength of 800 nm with a repetition rate of 1 kHz. The pulse energy is 7.0 mJ.

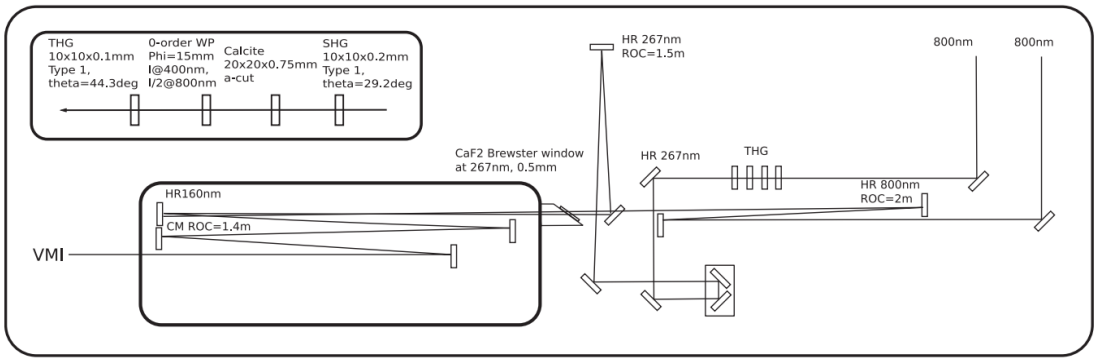

Figure 6.4: A schematic of the experimental setup used for the production of the fifth harmonic (VUV) at Univeristy of Ottawa/NRC. This figure has been adapted from reference [128]. Note that the input energies given in this figure have been adjusted for the experiment described here.

This output was split and 0.75 mJ/pulse was used to produce the 267 nm probe pulses through frequency conversion. Two BBO crystals tripled the frequency of the fundamental, resulting in pulses of the third harmonic (267 nm) with an energy of 2.5 μJ/pulse. The vacuum UV (VUV) probe pulses were produced using 2.75 mJ of the 800 nm laser output. As detailed in Chapter 2, a TH beam of the 800 nm output needs to be overlapped with the fundamental in a noble gas in order to produce VUV via four-wave mixing. This was done here by splitting the fundamental beam into two further beamlines; one with a power of 1.75 mJ/pulse to produce 130 μJ/pulse of 267 nm via frequency tripling using two BBO crystals, a calcite plate and zero-order waveplate. Once again, this is very similar to the method described in Section 2.3.2 of Chapter 2. The TH output of this process was non-collinearly overlapped with a beam of the fundamental (1 mJ/pulse) in argon. The pressure of Ar in the cell was kept at 40 mbar using a needle-valve to control the inflow of new gas.

A schematic of the described optical setup can be seen in Figure 6.4 which is taken from reference [128]. The input energies have been adjusted here, but the optical layout is accurate. VUV is produced through the four-wave difference-frequency (FWDFM) scheme discussed previously in Chapter 2. The fifth harmonic produced is centred at a wavelength of 159.4 nm with an estimated energy of $\sim$ 0.5 μJ/pulse. Several dichroic mirrors with high-reflectivity at 160 nm are used to remove any residual 267 nm and 800 nm. Two curved aluminium mirrors focus the final UV pump and VUV probe pulses prior to overlapping them in a collinear geometry using a dichroic mirror. In contrast to the setup for VUV production at Heriot-Watt (see Chapter 2), all of the steering and beam separation as well as the overlap of the final UV and VUV beams takes place inside the Ar cell. This requires electrical and optomechanical hardware to be vacuum compatible to minimise outgassing. The Ar cell is connected to the TRPEI spectrometer by a 0.5 mm CaF_2 window, as this has a good transmission at 160 nm ($\sim$ 94 %). The time-delay between the pump and

probe beams is introduced using an automated delay stage in the probe beamline. The spectrometer itself consists of two chambers, one source chamber where the molecular beam is prepared and a chamber where the velocity-map imaging (VMI) setup and interaction region are situated. These chambers are both differentially pumped. Filter paper was soaked in the samples (FOR, DMA or DMF) which were obtained from Sigma-Aldrich (purity of 99.5 % or greater). This was then placed in a cartridge behind the molecular pulsed valve (Even-Lavie, 1 kHz) and subsequently 1.3 bar of helium carrier gas was passed over this sample soaked paper, producing the desired mixture of sample and carrier gas. The pulsed valve itself was kept at 60°C. After leaving the valve the mixture passed through a skimmer (1.0 mm orifice) and entered the interaction region located between the repeller and extractor electrodes of a VMI electrode setup (similar to the one described in Chapter 2). The photoelectrons produced upon ionisation of the sample are accelerated along a flight tube using the VMI optics and then detected on a microchannel plate (MCP) detector (40 mm diameter) and phosphor screen (P47). Achromatic relay optics imaged the output from the detector setup on a CCD camera.

The acquired images underwent several processing procedures. Initially, the background signal was subtracted. This consists of removing the pump and probe alone signals which is done by averaging the signals recorded at negative time delays and subtracting these from the data. A second correction was then applied in order to remove signals resulting from the ionisation of any residual background gas in the interaction chamber. These were removed by subtracting signal measured when the laser pulses and molecular beam timings were desynchronised. This was carried out at every pump and probe delay step. The background subtracted images were then Abel-inverted using the rapid matrix inversion method discussed in Chapter 2 Section 2.5 and also in reference [94]. Representative background subtracted and Abel-inverted VMI images of FOR, DMF and DMA around the $\Delta t = 0$ pump-probe delay are shown in Figure 6.6. Nonresonant $(1 + 1')$ ionisation of xenon was used to determine the cross-correlation, which ranged from 83-97 fs at FWHM. The Xe measurements also provided calibration to convert the scale of the VMI images from pixels to photoelectron kinetic energy. To determine the ideal temperature and timing of the Even-Lavie valve as well as the He backing pressure setting which avoids the formation of clusters, the ion mode of the spectrometer was used before setting out to collect TREPI measurements.

The analysis of the data is much as described in Chapter 2. The Levenberg-Marquardt routine discussed earlier is used to fit the photoelectron spectra and their time-dependence, which is then used to extract the lifetimes for the dynamical processes observed. The angular information is extracted by fitting the required β-parameters for this process: β_2 and β_4. This was also discussed in detail in Chapter 2.

6.3 Computational Methods

The supporting *ab initio* calculations for this work were carried out by me using the Gaussian09 software package [203]. The ground state geometries for FOR, DMF and DMA were optimised using density functional theory with the B3LYP [188, 310] functional and the aug-cc-pVTZ basis set. Analytical Hessian calculations confirmed that the optimised structures obtained were minima. Excited state energies for the singlet states in the vertical region were calculated using two methods: the equation-of-motion coupled cluster method with single and double excitations (EOM-CCSD) and the aug-cc-pVTZ basis set [190], as well as time-dependent DFT (TD-DFT) in conjunction with the CAM-B3LYP [311] functional and aug-cc-pVTZ basis set. For details on the computational methods and basis sets refer back to Chapter 3. These results and further theoretical (as well as experimental) data are summarised in Tables 6.1 and 6.2. The state labelling was assigned using the largest individual orbital character in the vertical Franck-Condon region (see Chapter 3, Section 3.5 for more information on this). In all three systems the orbital contributions were observed to be heavily mixed, but the contributions used for assignment were typically $> 50\%$.

Both the EOM-CCSD and TD-DFT methods were used in FOR to produce potential energy cuts along the N-H bond stretching coordinate. The results are compared in the first two panels ((a) and (b)) of Figure 6.5. As indicated, it was the hydrogen atom furthest from the amide C=O group that was displaced to produce the cuts shown. The cuts are in very good agreement qualitatively but vary slightly energetically, as would be expected using the two methods. Since the TD-DFT approach has a lower computational cost and the qualitative agreement between the two approaches is very good along the N-H coordinate, the TD-DFT method was then also used to compute the stretches along the N-CO bond in FOR (again indicated in Figure 6.5, panel (c)) and also along the N-CH_3 coordinate in DMF. The same basis set (aug-cc-pVTZ) and functional (CAM-B3LYP) as above were used throughout. The stretches shown are rigid, i.e. the molecular geometry was not relaxed as the bond was stretched (see Chapter 3, Section 3.5.2 for an expanded discussion on this). As mentioned above, the orbital contributions are heavily mixed. As the bonds are stretched, this mixing becomes more pronounced in some cases, complicating the state assignments. This was especially true along the N-CO coordinate shown in panel (c) of Figure 6.5. Computing the natural transition orbitals (NTOs) [206] can help to identify the dominant contributions by simplifying the description of the electronic transition. This was done at particularly convoluted points as well as other key points along the reaction coordinate, using the same computational method (TD-CAM-B3LYP/aug-cc-pVTZ).

It is worth noting some key observations from the potential energy cuts. The first is the apparent dissociative nature of the $\pi\pi^*$ state along the N-CO stretch in FOR. These states are typically bound. This unusual behaviour may in part be due

Table 6.1: The computed vertical excitation energies in eV and oscillator strengths (in parenthesis) for FOR. Further theoretical data from previous studies as well as experimental values are presented for comparison. The assignment of x, y and z labels for the p states are based on standard Gaussian09 molecular orientation conventions and are for guidance only, as orbitals are not always directed entirely along these axes.

	This Work		Previous Work					
FOR	EOM-CCSD/ aug-cc-pVTZ	TD-CAM-B3LYP/ aug-cc-pVTZ	TD-SOAP/ et-pVQZ [301]	MR-CISD + Q/ d0-aug-cc-pVDZ [304]	EOM-CCSD/ PBS [305]	CASSCF/MR-CI/ 6-31+G** [307]	CASSCF/CASPT2/ ANO-TZP [306]	VUV abs. data [300]
$n \rightarrow \pi^*$	5.72(0.001)	5.62(0.001)	5.71(0.001)	5.78(0.001)	5.71(0.000)	5.86(0.000)	5.61(0.001)	5.82
$\pi \rightarrow 3s$	6.91(0.021)	6.72(0.017)	7.32(0.021)	6.77(0.021)	6.73(0.021)	6.14(0.022)	6.52(0.024)	6.35
$n \rightarrow 3s$	7.00(0.001)	6.75(0.004)	6.64(0.009)	6.78(0.006)	6.81(0.002)	6.49(0.000)	6.59(0.003)	...
$n \rightarrow 3p_y$	7.56(0.136)	7.28(0.066)	7.42(0.085)	7.47(0.058)	7.38(0.072)	7.16(0.060)	7.31(0.065)	7.40
$\pi \rightarrow 3p_y$	7.76(0.001)	7.49(0.001)	8.07(0.016)	7.62(0.000)	7.59(0.001)	7.01(0.001)	7.04(0.000)	...
$\pi \rightarrow \pi^*$	7.79(0.232)	7.81(0.211)	7.77(0.282)	7.71(0.338)	7.66(0.211)	7.94(0.149)	7.41(0.371)	7.36
$n \rightarrow 3p_x$	8.06(0.060)	7.64(0.093)	8.25(0.008)	7.84(0.017)	7.88(0.064)	7.50(0.041)	7.73(0.022)	7.72
$\pi \rightarrow 3p_x$	8.34(0.006)	8.09(0.008)	8.95(0.005)	8.03(0.001)	8.17(0.008)	7.57(0.005)	7.97(0.007)	8.02
$n \rightarrow 3p_z$	8.39(0.006)	8.11(0.004)	9.01(0.026)	8.08(0.013)	8.20(0.006)	7.47(0.005)	7.81(0.005)	7.83
$\pi \rightarrow 3p_z$	8.68(0.007)	8.51(0.009)	9.60(0.009)	8.28(0.033)	8.52(0.006)	7.40(0.136)	7.72(0.101)	8.22

Table 6.2: A summary of the computed vertical excitation energies in eV and oscillator strengths (given in parentheses) for DMF and DMA. As in Table 6.1, x, y and z contribution follow standard Gaussian09 orientation conventions and are for guidance only.

	This Work		Previous Work				This Work	
DMF	EOM-CCSD/ aug-cc-pVTZ	TD-CAM-B3LYP/ aug-cc-pVTZ	TD-B3LYP/ aug-cc-pVTZ [308]	CASSCF/CASPT2/ ANO-TZP [306]	VUV abs. data [308]	DMA	EOM-CCSD/ aug-cc-pVTZ	TD-CAM-B3LYP/ aug-cc-pVTZ
$n \rightarrow \pi^*$	5.81(0.001)	5.69(0.001)	5.59(0.000)	5.64(0.001)	5.57	$n \rightarrow \pi^*$	5.85(0.001)	5.74(0.001)
$\pi \rightarrow 3s$	6.21(0.016)	6.13(0.022)	5.62(0.021)	5.92(0.005)	5.96	$\pi \rightarrow 3s$	5.99(0.017)	5.96(0.023)
$\pi \rightarrow \pi^*$	6.69(0.184)	6.64(0.127)	6.32(0.108)	6.50(0.365)	6.24	$n \rightarrow 3s$	6.69(0.022)	6.51(0.018)
$\pi \rightarrow 3p_y$	6.99(0.005)	6.89(0.005)	6.28(0.004)	6.77(0.001)	6.54	$\pi \rightarrow 3p_x$	6.81(0.005)	6.72(0.005)
$n \rightarrow 3s$	7.05(0.021)	6.83(0.051)	5.99(0.009)	6.48(0.002)	6.12	$\pi \rightarrow 3p_z$	6.81(0.085)	6.78(0.127)
$\pi \rightarrow 3p_x$	7.14(0.001)	7.06(0.001)	6.49(0.000)	6.63(0.002)	6.74	$\pi \rightarrow 3p_y$	6.88(0.001)	6.85(0.002)
$\pi \rightarrow 3p_z$	7.40(0.078)	7.38(0.054)	7.00(0.068)	6.55(0.004)	6.90	$\pi \rightarrow \pi^*$	6.92(0.204)	6.92(0.115)
$\pi \rightarrow 3d_{z^2}$	7.51(0.001)	7.42(0.001)	6.91(0.000)	7.24(0.000)	...	$\pi \rightarrow 3d_{xy}$	7.31(0.001)	7.25(0.000)
$n \rightarrow 3p_y$	7.71(0.028)	7.41(0.026)	6.59(0.017)	7.09(0.010)	6.97	$n \rightarrow 3p_x$	7.47(0.006)	7.22(0.005)

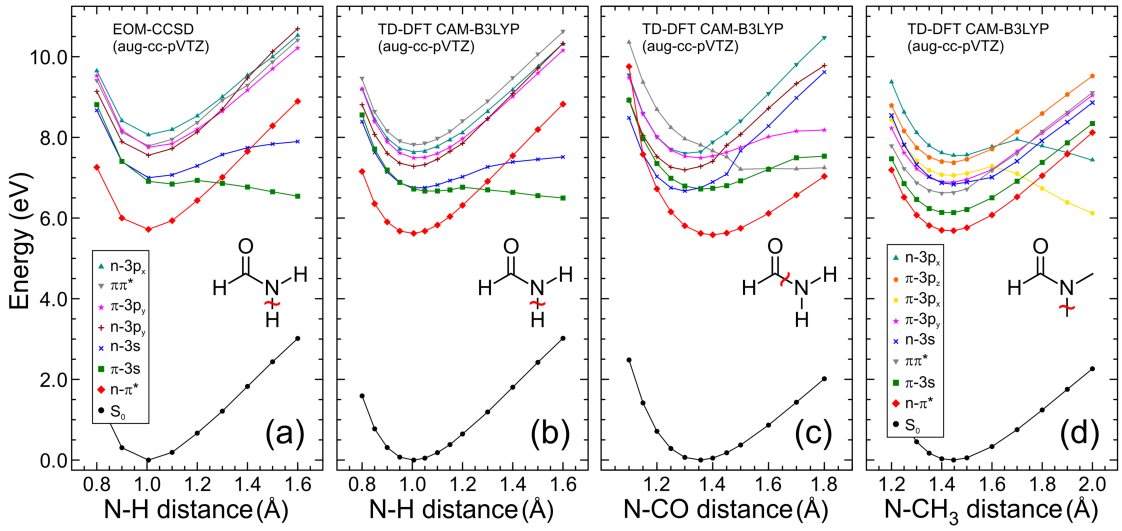

Figure 6.5: Diabatic potential energy cuts along N-H ((a) and (b)) and N-CO (c) in FOR as well as the N-CH_3 bond in DMF, (d). Panels (a) and (b) show the cuts along the same N-H bond but produced using different computational methods EOM-CCSD/aug-cc-pVTZ and TD-DFT/aug-cc-pVTZ, respectively. The legend given in (a) also applies to panels (b) and (c). This figure has been adapted from reference [291].

to the fact that the N-CO bond, which was stretched, being located at the centre of the molecule. The elongation of the bond eventually resulted in a localisation of the orbitals onto the two molecular fragments, which caused a distortion of the orbital character. This became very obvious when comparing the visualised orbitals to other cuts where "peripheral" bonds were elongated. Panel (c) is furthermore a good example of the TD-DFT's inability to describe points of degeneracy and regions where the Born-Oppenheimer approximations break down (see Chapter 3). In close proximity to these points the orbital descriptions of states become more significantly mixed and the sharply varying curves are observed due to the diabatic sorting.

Further key observations are the Rydberg-to-valence character evolutions observed for FOR and DMF. In FOR the 3s state evolves σ^* valence character whereas for DMF it is the 3p Rydbgerg state that exhibits this behaviour along the N-CH_3 stretch. This implies that the Rydberg-to-valence evolution observed in primary and tertiary amides is similar to that in aliphatic amines. The extensive mixing of the states does however, mean that this interpretation, based on only the three systems under investigation here, is somewhat challenging. Furthermore the assignments are not trivial, as shown by the differences in state assignment between this work and that by Shastri *et al.* [308] or Lipciuc *et al.* [312]. The use of natural transition orbitals to support the assignment presented does, however, reinforce the confidence in the results reported here, with relevance to the Rydberg-to-valence evolutions for the N-H and N-CH_3 stretches in FOR and DMF.

The photodissociation of DMF upon excitation at 193.3 nm (6.41 eV) has been observed experimentally, with evidence of fragmentation along both N-CO and N-CH_3 coordinates [312]. This implies that the computational methods employed here overestimate the absolute energies along these coordinates but also at the vertical. In Tables 6.1 and 6.2 the vertical values can be compared to experimental work, which again shows that both the EOM-CCSD and TD-DFT methods employed tend to overestimate the energy values. For FOR the EOM-CCSD method overestimates the energies by an average of 0.30 eV and TD-DFT by 0.13 eV. In DMF it is 0.50 eV and 0.37 eV, respectively. This overestimation is also true for many of the other methods given in the table for FOR, whereas performance for DMF generally seems better.

6.4 Experimental Results

6.4.1 Photoelectron Spectra

The time-resolved photoelectron spectra (PES) obtained for FOR, DMF and DMA are shown in Figure 6.7. The adiabatic D_0 ionisation potentials (IP) for FOR and DMF have been reported ([313] and references therein) as 10.22 eV and 9.05 eV, respectively. Using this and the total 12.43 eV of energy put in by the (1+1′) ionisation process (7.78 eV + 4.65 eV), the photoelectron kinetic energetic cut-offs for FOR and DMF are 2.21 eV and 3.38 eV, respectively. These cut-offs correspond to the cationic ground state in both systems. For DMA the adiabatic IP has not been reported but similar vertical IP values for both DMF (9.14-9.25 eV) and DMA (9.09-9.20 eV) have been determined. This suggests that the adiabatic IP in DMA is also likely similar to that of DMF. The high similarity of the PES of DMF and DMA in Figure 6.7 furthermore seem to support this notion [314–318]. Minor signals are observed beyond the cut-off and are due to (1+2′) process taking place. In the systems under investigation, the difference in energy between the first and second cation states D_0 and D_1 is fairly small (<0.5 eV) [299, 313–315, 319]. This means that excitation to the D_1 state is also a channel that is energetically accessible. The first two cation states possess n^{-1} and π^{-1} character in FOR, whereas in DMF and DMA it is the the D_0 state that possesses π^{-1} character and the D_1 state is of n^{-1} character [314–316]. This will become relevant in the discussion of the experimental results where Koopmans' correlations have to be taken into account when interpreting the data presented here.

A sharp feature is present centred around 2.1 eV in the time-resolved photoelectron spectrum of FOR shown in Figure 6.7. At energies below 1.8 eV a much broader band with little structure is observed. The fact that the feature centred at 2.1 eV is quite narrow implies that it arises from Rydberg state ionisation. A narrow feature is an indicator for a significant amount of $\Delta\nu = 0$ transitions (for a

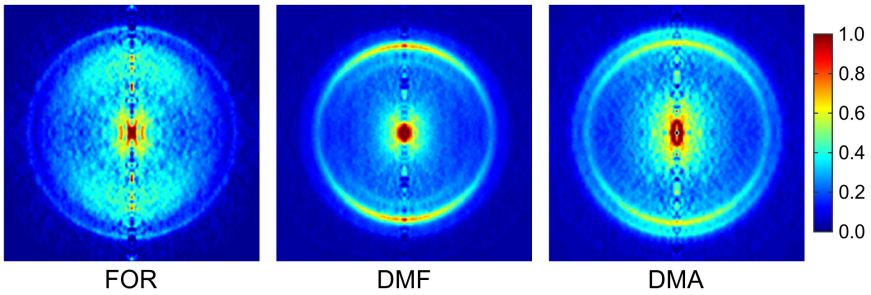

Figure 6.6: The Abel-inverted VMI images for FOR, DMF and DMA at around $\Delta t = 0$ pump-probe delay. The images are background subtracted and symmetrised. For reference, the polarisation (linear) direction of the pump and probe is vertical with respect to the images in this figure. This figure has been published in reference [291].

non-mode specific quantum number ν) [320], and Rydberg states are state selective. The broad width of the feature at 1.8 eV on the other hand indicates that it is due to ionisation from a valence state. There are however, indications of two narrow peaks on the broad signature at 1.4 eV and 1.1 eV, which can be made out more clearly on the time-slices presented in Figure 6.7. In the time-resolved photoelectron spectrum of DMF three narrow features are present at 1.5 eV, 2.1 eV and 2.9 eV as well as evidence of a weaker broad band at lower energies. These sharp bands are again indicative of ionisation from a Rydberg state. The photoelectron spectrum of DMA is similar to that of DMF, with two sharp peaks at higher energies (2.3 eV and 2.9 eV) as well as two shoulders, one at higher energy (3.3 eV) and one at 1.6 eV - best observed in the time-slices. Again the narrow width of the shoulders and distinct sharp bands suggest that they are due to Rydberg state ionisation.

From the experimental values given in Table 6.1 and previous work [299, 300], it is evident that the 159.4 nm (7.78 eV) pump employed in the current study will excite a 3p Rydberg state in FOR, specifically the n-3p$_x$ transition. Furthermore, the broad underlying feature in the FOR photoelectron spectrum is likely to be due to the $\pi\pi^*$ valence transition, which lies within that spectral region (Table 6.1). The narrow peaks at 1.1 eV and 1.4 eV, on top of the broader background, could be indications of either vibrational structure or the presence of lower-lying Rydberg states. A lower-lying Rydberg state which would be a potential candidate is the n-3s transition. This lies energetically $\sim$ 1 eV below the n-3p$_x$ transition (Table 6.1), putting it at 1.1 eV, exactly where one of the narrow peaks is observed. The second peak might then be expected to arise from the π-3s transition but in order to conform with Koopmans' correlations, this would preferentially ionise to the D_1 (π^{-1}) cation state, meaning that instead of lying very close to the n-3s transition it would actually be expected at around 0.4 eV. No peaks are discernible in that region of the photoelectron spectrum of FOR presented. Using the fact that, according to the EOM-CCSD results, it lies 0.3 eV below the initially excited transition, another

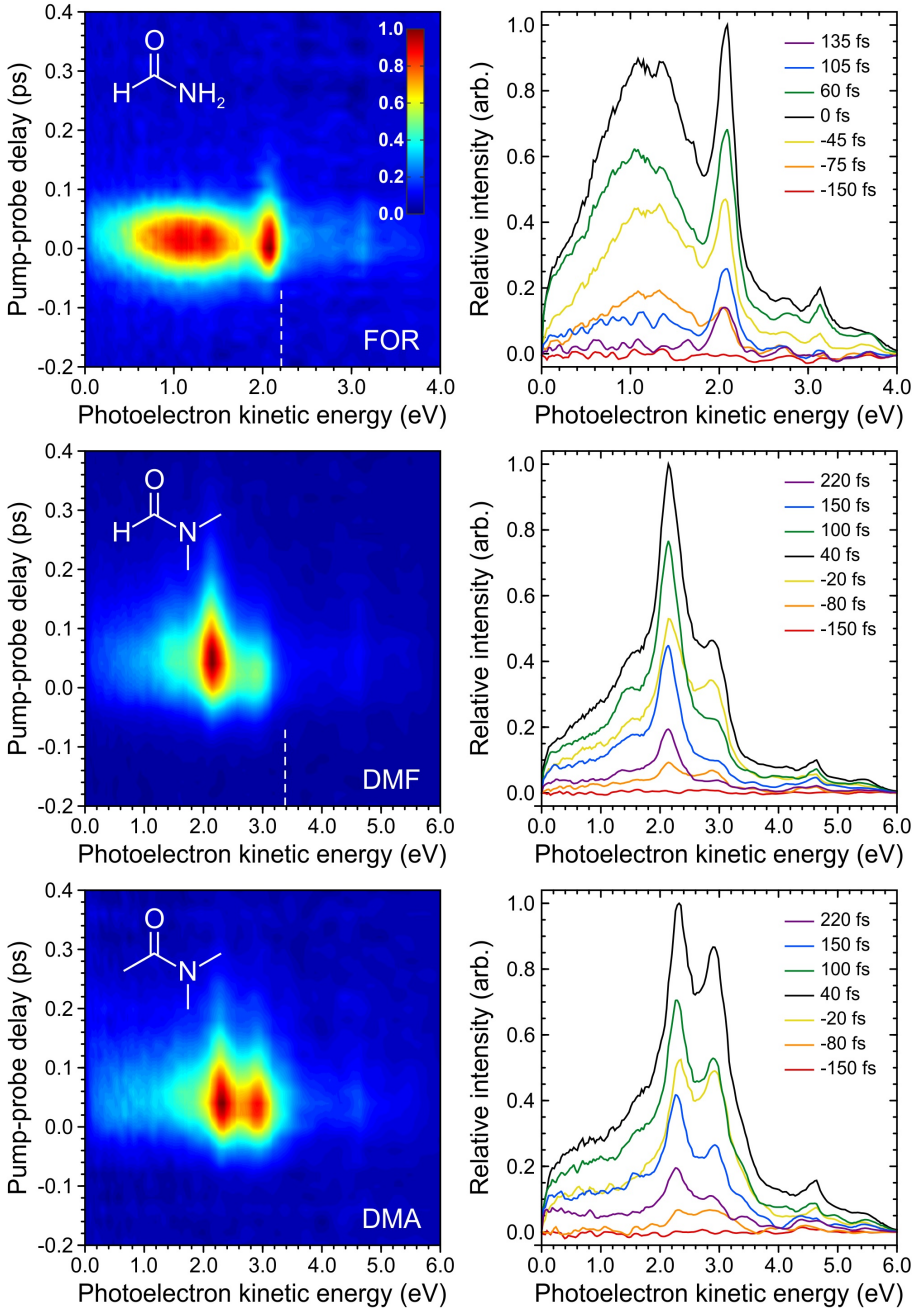

Figure 6.7: The time-dependent photoelectron spectra for all three amide systems using a 160 nm pump and 267 nm probe are shown on the left. The (1+1′) photoelectron kinetic energy cut-offs for FOR and DMF are indicated by the white vertical dashed lines. The right hand panels display slices through the photoelectron spectra at various pump-probe time-delays. This figure has been taken from reference [291].

transition that could energetically result in a signal at around 1.4 eV might be the π-3p$_y$ state, which is optically dark. Due to Koopmans' correlations this would again ionise to D_1, giving a matching kinetic energy of around 1.4 eV. However, it is worth noting that the computational results for this energy gap between the initially excited state and the dark π-3p$_y$ transition vary (Table 6.1).

In DMF and DMA assigning the states which are initially excited by the pump is more complex. The VUV absorption spectrum for DMF reported by Shastri *et al.* [308] suggests that one or several members of the 3d manifold will be prepared by a pump at around 160 nm. Using the decay associated spectra (DAS) it can be shown that the feature observed at 2.9 eV and including signal up to 3.3 eV may be the result of excitation to a 3d state in DMF. This signal from 2.9 eV up to the energetic cut-off corresponds to the population in that state that is vibrationally excited. This is discussed in more detail in Section 6.4.3 below. The π-3s state is predicted to lie 1.8 eV below the initial excitation. The lowest energy narrow feature observed at 1.5 eV in DMF is therefore likely to arise from an internal conversion process to this state. This is again based on the assumption that there is a strong propensity for $\Delta\nu = 0$ ionisation for Rydberg states. From the vertical ionisation energy provided by the absorption spectrum, and by again, making use of the Koopmans' correlations (n-3s is more likely to ionise to D_1 (n^{-1})), it can be concluded that the nearby n-3s state should result in a narrow Rydberg band at 1.4 eV. The *ab initio* calculations, however, predict a much larger gap of $\sim$ 0.8 eV (EOM-CCSD/aug-cc-pVTZ in Table 6.2) or at least >0.5 eV from the CASPT2 results [312]. Purely energetic based assignment is therefore to be made with caution. As already mentioned above it is not possible to assign the sharp feature at 2.9 eV to a specific band as there are a multitude of Rydberg states lying very close in energy in this region. The same is the case at 2.1 eV, where another narrow feature is observed. Using the *ab initio* calculations presented here, it is probable that the 2.1 eV feature arises due to a 3p Rydberg state being ionised. Whereas at 2.9 eV it could be a member of the 3p or 3d manifold which produces the observed signal.

For DMA, the initial excitation is observed as the shoulder at 3.3 eV in the photoelectron spectrum (seen more clearly in the time-slices in Figure 6.7). It is likely that this feature arises due to the ionisation of a 3d Rydberg state, as the states in DMA and DMF are found to be alike. The energetically lower-lying shoulder at 1.6 eV lines up with the π-3s state. Again, it is more complex to identify the nature of the signals at 2.9 eV and 2.3 eV, which cannot be assigned with confidence. As in DMF, however, it is probable that they arise from ionisation of members of the 3d or 3p Rydberg manifold.

6.4.2 Photoelectron Angular Distributions (PADs)

The β_2 and β_4 parameters for the angular distribution were fitted for the TRPEI data in all three systems (see Chapter 2 for details). The results for the time- as well as energy-dependence of both parameters are shown in Figure 6.8. Prior to the detailed discussion of the observations deduced from Fig 6.8, it is helpful to consider how the β parameters can be helpful in assigning state characters. As discussed in Chapter 1, the Rydberg states can be likened (with approximation) to atomic orbitals, as they are relatively far removed from the molecule which itself can then be analogous to the nucleus of the atom. Hence, the 3s Rydberg state can be expected to look like an atomic s orbital. The conservation of angular momentum ($\Delta l = \pm 1$) then dictates that for a state of s character, p photoelectron partial waves should be observed [14] (hence β_4 must be zero). For a 3p Rydbgerg state, both s and d partial waves should be produced, which would then be observable in the PADs as a non-zero β_4 parameter. Similarly, the ionisation of a 3d Rydberg state will give rise to both p and f photoelectron partial waves, which would also result in a non-zero β_4 parameter. However, contributions from f partial waves are expected to be small compared to that of the p wave. This is due to a notably larger centrifugal barrier which is to be overcome by the f waves [14]. Hence, close to the ionisation threshold, the β_4 contributions should be small for a 3d Rydberg state. The value of β_4 may be too small to be detected in some cases of 3d Rydberg ionisation, although the opposite has also been observed, for example, in the Rydberg ionisation of ammonia [321].

In the FOR data (Figure 6.8, top two panels), no strong features are observed for either β-parameter. The anisotropies for valence states have previously been reported to be low [22], which is in agreement with the results for FOR presented here. The β_2 parameter for the diffuse valence band observed below 1.8 eV is 0.6 and β_4 is 0.0. The narrow and distinct Rydberg feature at 2.1 eV yields β_2 and β_4 values of approximately 0.4 and 0.2, respectively. The low β_2 value is unexpected (compared to values for 3p states in amines [21, 22]) however, the non-zero β_4 parameter supports the hypothesis that the band centred at 2.1 eV arises due to ionisation from a 3p Rydberg state.

For DMF the anisotropy results show distinct features. Specifically, a strong band centred at 2.1 eV is observed for β_2, but a non-zero β_4 contribution is also visible at the same energy. The exact values of β_2 and β_4 extracted in this region are 0.9 and 0.2, respectively. This signature matches the sharp 3p/3d Rydberg band present in the time-resolved photoelectron spectrum. For the other two Rydberg peaks observed in the DMF photoelectron spectrum, at 1.5 eV (3s) and 2.9 eV (3d), the β_4 values are near zero and β_2 is discernible but much lower (~ 0.5) than at 2.1 eV. Considering the discussion on expected β observations for Rydberg states above, these results are consistent with the 3s and 3d assignment of these bands.

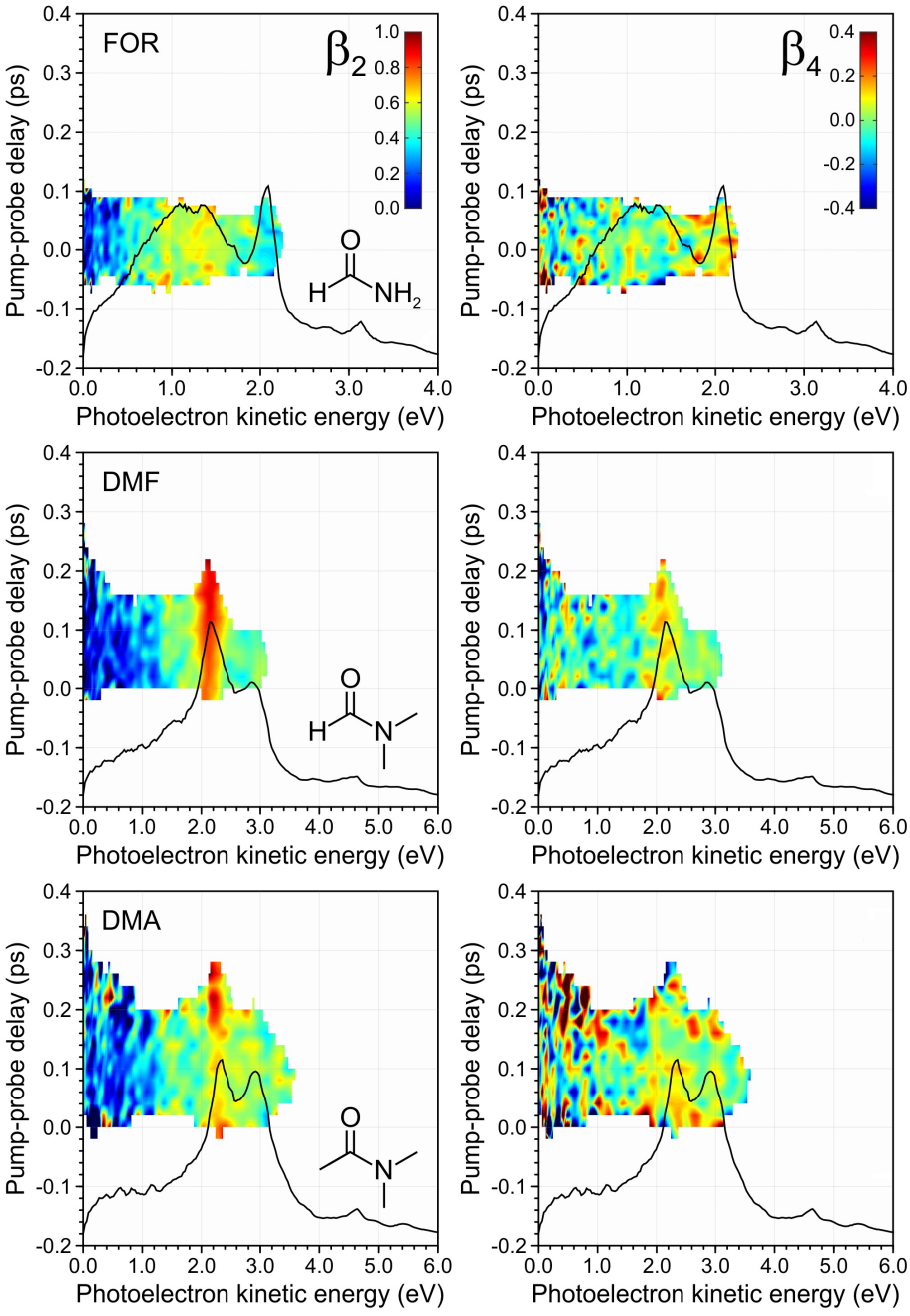

Figure 6.8: Plots of the anisotropy parameters β_2 and β_4 for FOR, DMF and DMA. Only regions of TRPEI data with $> 5\%$ of the maximum of the signal recorded. The black overlay shows the photoelectron spectra near $\Delta t = 0$ pump-probe delay. This figure has been taken from reference [291].

A distinct band for both β parameters is also observed in the DMA anisotropy plots presented in Figure 6.8. It is centred at 2.3 eV with β_2 and β_4 values of up to 1.0 and 0.3, respectively. Values of β_2 around 0.5 and β_4 of 0.0 are extracted for both of the high and low energy shoulders (3.3 eV and 1.6 eV) as well as the 2.9 eV band observed in the photoelectron spectrum of DMA. These again strengthen the assignment of the initially excited state as 3d Rydberg, and the lower energy shoulder as 3s Rydberg.

6.4.3 Decay Associated Spectra (DAS)

The decay associated spectra as well as the residuals of the fits for FOR, DMF and DMA are shown in Figure 6.9. Two exponential decays are required to globally fit the time evolution of each system (see Chapter 2 for details on the fitting routine). The residuals are the fit subtracted from the raw data and allow for the assessment of the goodness of the fits. No significant systematic errors are observed in these residuals. Two very fast lifetimes, 10-35 fs and 70-75 fs, are extracted for all three systems. These are short compared to cross-correlation (83-97 fs) but a fit using only one exponential decay does not describe the signal satisfactorily. Figure 6.10 shows transient profiles at two photoelectron kinetic energies along with the Gaussian cross-correlation to illustrate this.

In FOR, the short $\tau_1 = 10$ fs component dominates in describing the band below 2.1 eV, whereas both τ_1 and τ_2 are needed to an almost equal extent to describe the sharp feature centred at 2.1 eV. There is no negative DAS signal which implies that there is no significant internal conversion process taking place between the initially excited n-3p$_x$ Rydberg state and lower-lying Rydberg states of the 3p manifold. Therefore, it can be ruled out that the narrow features observed at 1.1 eV and 1.4 eV in the photoelectron spectrum (on top of the broader $\pi\pi^*$ valence band) are Rydberg states. They are instead likely to be vibrational structure.

In contrast to FOR, the DAS for DMF and DMA show, negative amplitude features in the τ_1 lifetime component. Sharp, narrow features are also present in these negative amplitudes. These indicate the presence of internal conversion processes between Rydberg states in the relaxation dynamics of both systems. The time-constant τ_1 is also about three times longer in DMF and DMA than in FOR, with τ_1 being 35 fs in DMF and 30 fs in DMA. Another feature of note is the fact that in all three systems, components of both lifetimes are required to fit the bands at high kinetic energies associated with initial excitation. This can be explained by the fact that there must be several possible decay pathways from the initially populated Rydberg state. It also implies that these pathways cannot be modelled using purely sequential or purely parallel fitting routines. Part of the initially prepared population appears to undergo internal conversion to a lower lying state (sequential model) but the DAS indicates that another mechanism which deactivates this pro-

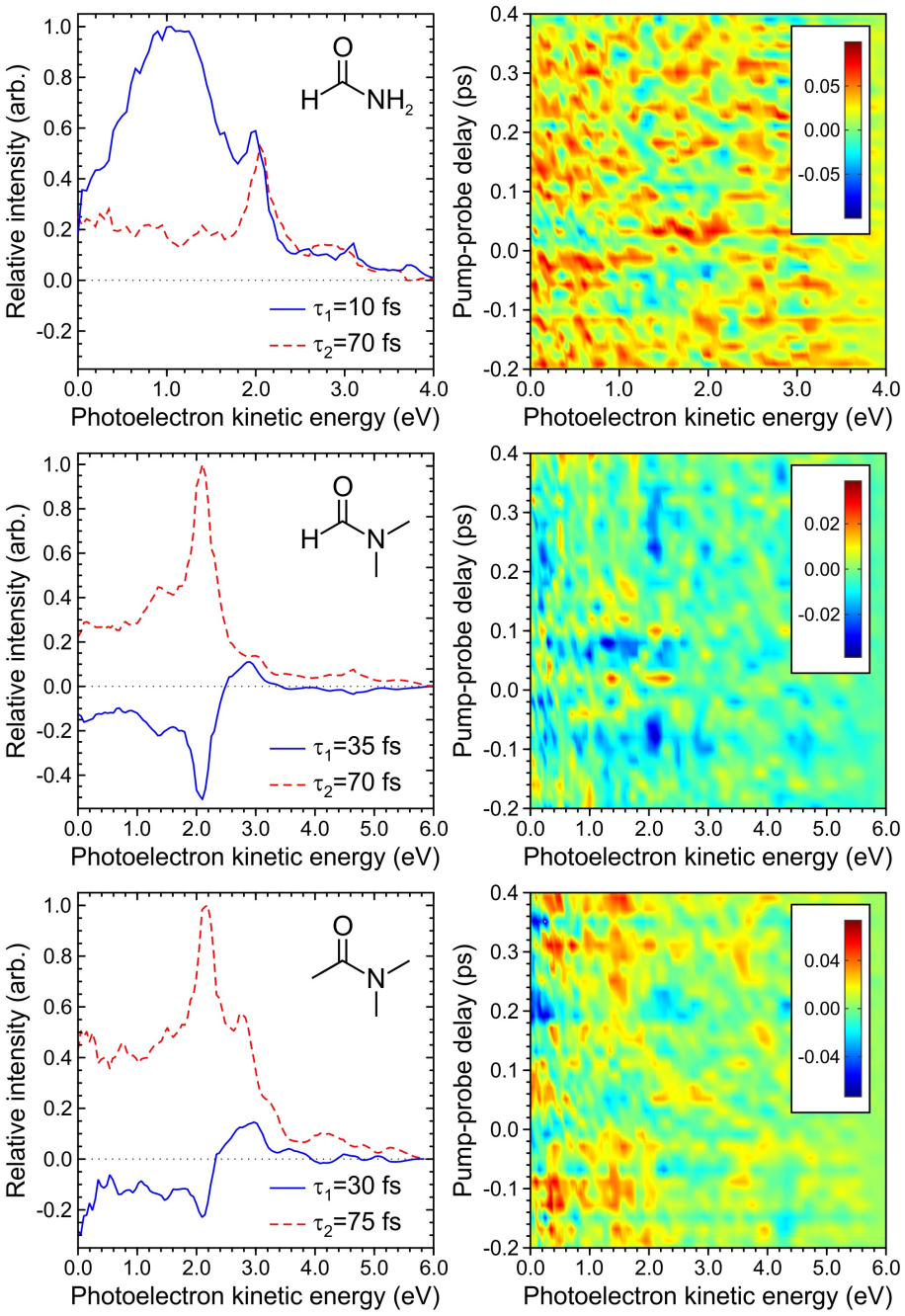

Figure 6.9: Decay associated spectra (DAS) for all three amides are shown on the left. The decay lifetimes indicated have uncertainties of ± 15% (1σ). The 2D residuals of the fits are shown on the right. This figure has been published in reference [291].

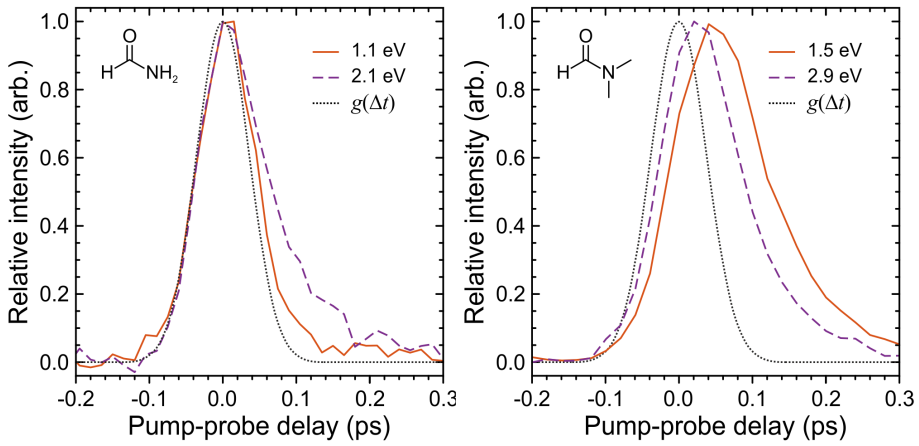

Figure 6.10: Intensity normalised transient profiles for both FOR (left) and DMF (right) at two photoelectron kinetic energies. The grey dotted line indicates the Gaussian cross-correlation with a FWHM of 85 fs and 90 fs for FOR and DMF respectively. These are the same values as used in the global fitting procedure. The data for DMA is very similar to DMF and is therefore omitted. This figure has been adapted from reference [291].

cess is also playing a role. These parallel processes support the suggestion that the state which is initially excited has a mixed Rydberg-valence character, as this mixed character may facilitate more than one relaxation pathway: one for each character of the state. Such pathways might be direct dissociation, a partial transfer of population to one or more lower-lying Rydberg states or intramolecular vibrational energy redistribution (IVR). Time-dependent bands in time-resolved photoelectron spectra can also be caused by large amplitude nuclear motions (on a single potential energy surface) as discussed in reference [110]. This can then, in a global 2D fitting routine, be erroneously interpreted as dynamics which evolve across several electronic states. This is not assumed to be the case here as a shift (sweep) towards lower energies is absent in any of the narrow bands presented here. If such a shift was present this would typically be an indicator for large amplitude motion [110, 322].

6.5 Discussion

When excited using a VUV pulse at 160 nm FOR, DMF and DMA exhibit narrow peaks superimposed on top of a broader background signal. The broad background signal is a consequence of the $\pi\pi^*$ valence state which is present in all three systems, whereas the narrow peaks are associated with states of Rydberg character. The observed features are in agreement with absorption spectra presented in previous studies (Section 6.1), as well as the predictions made by the *ab initio* calculations (summarised in Table 6.1 and 6.2). The photoelectron angular information (Figure 6.8) is crucial in supporting the assignment of the narrow spectral features to states with Rydberg character (Figure 6.7). High anisotropy, associated with Rydberg

states, is observed in the same energetic regions as the narrow spectral bands in DMF and DMA. The photoelectron angular information is not sufficient to assign the exact orbital character to all of the observed Rydberg states but the β-parameters found in spectral regions associated with 3s Rydberg character in DMF and DMA do support their assignment. The higher β_2 values in combination with β_4 values of zero match predictions made by the approximate atomic-like models of photoionisation (discussed in Chapter 1.). Furthermore, regions with β_4-parameters greater than zero are found to overlap with states that have been assigned 3p Rydberg character.

The decay associated spectra presented earlier in Figure 6.9 are key to identifying the mechanisms of the relaxation dynamics in the three amide systems under investigation. The negative amplitude features (τ_1) observed for DMF and DMA, indicate that sequential processes are taking place, which are likely due to internal conversion processes between excited singlet states. The narrow negative features superimposed on the broad background suggest that internal conversion takes place between states possessing Rydberg character, whereas the broad negative amplitude feature points to internal conversion between the initially excited state(s) (Rydberg) and lower-lying valence states. The swift depopulation of the initially excited state, as well as the existence of multiple relaxation pathways indicated by the DAS, reveal that parallel deactivation mechanisms must be active. The *ab initio* calculations presented earlier suggest that a single parallel pathway causes rapid fragmentation along the N-CO or N-CH_3 coordinates in DMF and DMA. The theoretical results shown in Figure 6.5 furthermore stipulate that the N-CO stretching coordinate is a crucial driving force for for all dissociation channels due to the strong mixing of the states observed along this stretch. Due to this mixing, population transfer between the 3p/3d Rydberg manifolds and the $\pi\pi^*$ valence state becomes possible at N-CO bond distances below 1.6 Å. As the $\pi\pi^*$ state appears to lower in energy upon even further elongation of the bond it is shown to provide access to a 3s Rydberg state and could also become degenerate with the nπ^* state at a point beyond 1.8 Å. An internal conversion mechanism to such lower-lying states might compete with dissociation along N-CO, but no evidence of a population of these lower-lying states is observed in the data shown here (for FOR) implying that dissociation is the major relaxation channel along this coordinate. As the DAS for FOR show no negative amplitude, internal conversion is an unlikely relaxation pathway. The initially populated n-3p$_x$ Rydberg state does, however, decay rapidly and is shown to be bound along both the N-H and N-CO coordinates in FOR (Figure 6.5). In order to account for the rapid relaxation observed it is proposed that internal conversion to a lower-lying Rydberg state or alternatively the $\pi\pi^*$ state, must still occur. It is possible that this process takes place at longer bond lengths, where the probe energy is insufficient to ionise the system efficiently, resulting in an apparent ultrafast decay of n-3p$_x$. This idea is discussed in more detail below.

No spectral features are observed to last beyond 300 fs for all three amides,

indicating that no long-lived bound states are involved in the relaxation. Instead, direct dissociation on a very short timescale is dominant. This would be expected when exciting with a high-energy pump as, after a decay process such as internal conversion or IVR, highly vibrational levels in the molecule will be populated, promoting rapid dissociation. A minor contribution from a (1+2′) ionisation process is observed in Figure 6.7. This also displays very short-lived features (lifetimes below 100 fs). Since, two photons are used to ionise in this scheme, more energy is available and therefore will project further into the ionisation continuum. This should reveal more information 'further along' the reaction coordinate. Since no long-lived signal arising from the lower-lying states, such as triplet states or the recovery of the ground state S_0, is evident the above suggested rapid fragmentation is confirmed. As shown by the potential energy cuts provided in Figure 6.5 (a) and (b), the 3s Rydberg states become dissociative along the N-H coordinate in FOR, implying that they facilitate H-atom elimination which aligns with the assignment of a very fast process. In the DAS however, there is no negative amplitude evident for narrow peaks below 1.8 eV implying that these 3s Rydberg states are not significantly populated. The absence of such signatures may again be due to an internal conversion process occurring at extended bond lengths. At such bond lengths the nature of the 3s Rydberg state will have evolved to valence character or the probe may have insufficient energy to ionise the system efficiently, both of which would result in the negative amplitude Rydberg signatures not being visible. This has been observed and discussed previously in reference [323].

The computed potential energy cuts along the N-CH_3 coordinate in DMF show an evolution of σ^* valence character by 3p Rydberg states. As DMF and DMA exhibit very similar properties and behaviour this model may be extended to DMA as well. This then suggests that the dissociation along this coordinate is facilitated by this 3p Rydberg to valence state evolution, whereas in FOR it is suggested that it is the 3s Rydberg to valence σ^* evolution that enables N-H bond dissociation. Prior to either scenario however, the population initially excited has to reach these 3p or 3s states through an interconversion mechanism between the members of the Rydberg manifold. The data presented here show that this is the case for DMF and DMA. Furthermore, due to the similar dynamical behaviour and extracted timescales for DMF and DMA, it can be concluded that large amplitude motion of the carbon atom with respect to the N-C-O plane (i.e. torsion) must be of small significance. The N-CO stretch coordinate itself is, however, likely to drive the relaxation dynamics.

6.6 Conclusion

This chapter discussed observations on the excited state dynamics in three small amide systems on excitation using a VUV pump pulse. The TRPEI data in combination with the extensive supporting *ab initio* calculations, indicate that excitation

of FOR, DMF and DMA at 160 nm results in rapid fragmentation of all three systems. The photofragment products cannot be detected directly using TRPEI but the extracted excited state lifetimes are all <100 fs, indicating that rapid nonradiative relaxation processes take place. The detailed and extensive *ab initio* calculations carried out by myself, reveal that the relaxation dynamics are facilitated by different Rydberg-to-valence evolution behaviour in the small primary and tertiary amide systems under investigation. In the primary amide FOR, the 3s Rydberg state evolves dissociative valence σ^* character, whereas in the tertiary systems DMF and DMA it is a member of the 3p Rydberg manifold that displays this evolution. In DMF and DMA there are internal conversion processes taking place as is evident from the TRPEI data presented. However, the ultrafast fragmentation process is dominant in both systems, complicating the comparison of the dynamics with those in FOR. A future investigation using slightly longer pump wavelengths, around 170 nm to 200 nm, to excite Rydberg states in DMF and DMA could help to provide a more detailed study of the internal conversion processes between these states. This could highlight differences in the dynamics of these two systems compared to FOR. Achieving tunable femtosecond pulses at these wavelengths often involves an optical parametric oscillator (OPO) and an extensive optical setup. However, a recent study employing hollow-core photonic crystal fibres has demonstrated that tunable light in the VUV region can be achieved with a much simpler optical setup [120]. This is discussed in more detail in Chapter 7, Section 7.2.

Chapter 7

Conclusions and Outlook

To conclude, this final chapter will firstly: provide a summary of the findings reported in this thesis and secondly: give an overview of several future directions which may build on the work presented in previous chapters.

7.1 Thesis Summary

Initially, the need for studying the ultrafast relaxation dynamics in biologically and environmentally relevant molecular systems was introduced in Chapter 1. This was followed by a discussion of the key concepts underlying time-resolved, photoionisation-based spectroscopy methods. The second chapter (Chapter 2) then provided a description of the experimental configurations used in the time-resolved photoelectron imaging studies carried out for this thesis. In addition, a summary of the underlying physical concepts was provided. Chapter 3 discussed the background theory for the quantum chemical *ab initio* calculations, which constituted a significant part of the studies presented in results Chapters 5 and 6.

The first experimental results were reported in Chapter 4 which was an investigation into the ultrafast relaxation dynamics of acetylacetone (AcAc) probed using pulses in the vacuum UV spectral region (160 nm). Acetylacetone is an environmental pollutant, it is also (in combination with UV light) being investigated for use in waste water treatment [209] and is a motif in chromophores that find use in sunscreens. The use of a short-wavelength probe expands the observation window along the reaction coordinate (as discussed in Chapter 1) by probing deeper into the ionisation continuum. This meant that the TRPEI study of AcAc presented here provides a quantitative link between several previous investigations, which sampled only smaller sub-sections of the overall reaction coordinate. The experimental results indicated that the population only very briefly resides in the initially excited $S_2(\pi\pi^*)$ state and is transferred to the lower lying $S_1(n\pi^*)$ state via an internal conversion process in less than 10 fs. A triple conical intersection between the $S_1(n\pi^*)$, $T_2(n\pi^*)$ and $T_1(\pi\pi^*)$ state, predicted by Squibb *et al.* [119], then provides a pathway for further relaxation, which was determined to proceed via ultrafast intersystem cross-

ing to $T_1(\pi\pi^*)$ within 1.6 ± 0.2 ps. The population then remains on the $T_1(\pi\pi^*)$ surface for some time (20 ± 4 ps), as it relaxes to the minimum geometry. A final, long lifetime of 330 ± 40 ps was extracted from the global fitting routine applied to the photoelectron spectrum. It was attributed to the decay of $T_1(\pi\pi^*)$, which may lead to the repopulation of the S_0 ground state.

The following chapter (Chapter 5) detailed an experimental investigation into the ultrafast relaxation dynamics of nitrobenzene and three of its methyl-substituted derivatives. Since a study of potential NO-donors by T. Suzuki *et al.* suggested a relationship between the nitro-group orientation and the NO release activity [18], understanding the effect of NO_2 group conformation on the excited state dynamics (ultimately resulting in the release of the desired NO), is of specific interest. The systems investigated using TRPEI with a pump of 267 nm and multiphoton probe using 400 nm were: nitrobenzene, 3,5-, 2,4- and 2,6-dimethylnitrobenzene (listed in order of increasing dihedral angle of NO_2 with respect to the carbon ring). No change in dihedral angle is observed when going from nitrobenzene to 3,5-dimethylnitrobenzene, however this system was used to determine the effect of ring-deformations which have been shown to be a key motion in the relaxation dynamics of phenol, aniline and other systems [94, 324]. A theoretical investigation of the molecular geometries found that the nitro-groups were 'locked' in place in their ground state (for the gas-phase TRPEI study). Potential energy curves of the first few excited states in NB and 2,6-DMNB were also produced using TDDFT and again confirmed significant barriers to free rotation of the nitro-group in the relevant excited states. The dynamics observed in all four systems were found to be very similar. An extremely rapid process (sub 30 fs) and two longer dynamical signatures ranging between 160-190 fs and 90-160 ps, respectively were observed. The fast sub 30 fs lifetime was assigned to the population leaving the Franck-Condon region, and relaxing to the minimum on the S_3 surface. The internal conversion from S_3 to the next lower-lying singlet state was determined to be complete within 200 fs, whereas the final relaxation step (90-160 ps) was attributed to the decay of the S_1 state. The nitro-group was identified as the dynamophore in the aromatic nitro-compounds studied, as the non-adiabatic dynamics are most likely facilitated by localised motions on the nitro-group.

In the final experimental chapter a TRPEI investigation into the excited state dynamics of small amide systems was presented. A pump pulse in the vacuum UV region (159.4 nm) was used to excite formamide (FOR), N,N-dimethylformamide (DMF) and N,N-dimethylacetamide (DMA), which were subsequently probed using 267 nm pulses. Small amides are of interest as they are found abundantly in nature as crucial motifs in peptides, neurotransmitters and DNA bases, to name a few examples. Furthermore, as they possess low-lying singlet states with mixed Rydberg-valence character, their study adds to understanding the role of such states in facilitating ultrafast radiationless transitions to the ground state (as observed

previously in various systems including those studied in references [20–23, 292]). Specifically, differences in the dynamics of aromatic and aliphatic, as well as primary, secondary and tertiary amine species have been observed (refer to Chapter 6 for the detailed discussion). By studying FOR (1°), DMF and DMA (both 3°), the influence on the dynamics, exerted by the proximity of the carbonyl group to either the NH_2 or $N(CH_3)_2$ groups could also be investigated. The experimental results show that rapid fragmentation takes place in all three systems when excited using 160 nm, as all excited state lifetimes recorded were below 100 fs. The detailed *ab initio* calculations were key in identifying the different Rydberg-to-valence evolution behaviour responsible for facilitating the relaxation dynamics in FOR (1°), DMF and DMA (3°). In the primary system the 3s Rydberg state is observed to evolve valence character, whereas in both tertiary systems 3p Ryberg states exhibit this evolution. Sequential processes revealed by negative features in the decay associated spectra (DAS) of DMF and DMA were assigned as signatures of these internal conversion processes to S_1. Prior to accessing these low-lying states, however, it is necessary for the population to undergo interconversion from the higher-lying members of the Rydberg manifold to states exhibiting mixed character. Again, this was indicated by sharp features found in the DAS, although several parallel pathways were found to be active, including fragmentation along the N-H and N-CH_3 coordinates. In FOR, no negative amplitude features were observed, but it was speculated that internal conversion to mixed Rydberg-valence states must still be taking place, due to the rapid relaxation observed.

In summary, the non-adiabatic relaxation dynamics of a collection of molecular systems were investigated using either high-energy pump or probe pulses. As a probe, vacuum UV pulses were employed to provide a quantitative, extended and near-complete picture of the excited state dynamics in acetylacetone. A multiphoton process employing two and/or three photons of 400 nm acted as a probe for the nitrobenzene systems, which revealed near-identical dynamical signatures for all four systems, despite the different steric-effects on the nitro-group. As a pump, vacuum UV wavelengths can be used to examine molecular systems which absorb at such short wavelengths. This was illustrated by the study on three amines: FOR, DMF and DMA, which are vastly common and relevant motifs in nature.

7.2 Future Directions: Photonic Crystal Fibre Sources for TRPEI

The advantages of using short-wavelength UV light (140-200 nm) in TRPEI experiments were discussed in the introduction of this thesis, and demonstrated in Chapter 4 as probe- and in Chapter 6 as pump-pulses. However, the method of producing VUV light via four-wave difference-frequency mixing in gas-filled cells still imposes

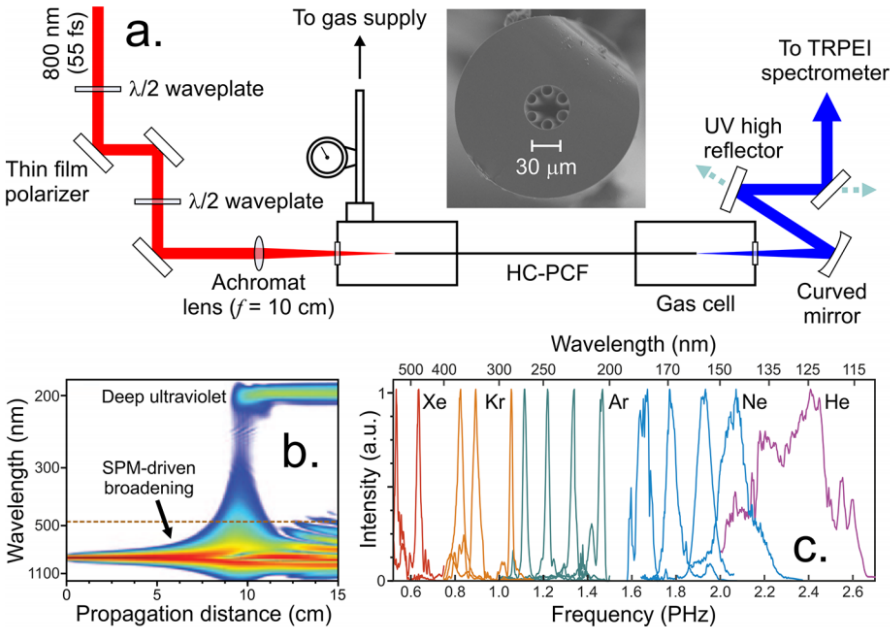

Figure 7.1: Subfigure (a) shows the optical setup used to produce the pump pulses, including an image of a cut-through of the HC-PCF. In (b) a plot of wavelength against propagation distance in the fibre highlights the production of deep-UV light from the input NIR pulse. Finally, (c) shows the wavelengths which can be produced using various noble gases in the HC-PCFs. This figure has been adapted from reference [120].

several limitations on the time-resolved experiments. The first is time-resolution: the cross-correlation of the 267 nm light produced using BBO crystals and the 160 nm light produced via four-wave mixing at Heriot-Watt University (HWU) (see Chapter 2, Section 2.3.2) is around 150 fs. Dynamical signatures below the cross-correlation value cannot be reliably distinguished and therefore it is preferential to employ shorter pulses. Due to the dispersion introduced when the VUV pulses pass through the exit window of the argon cell into the ultrahigh vacuum (UHV) chamber, pulses can be stretched and chirped. This is one restriction which makes it challenging to improve upon the time-resolution of the VUV pulses. The need for a window between the location of the VUV production and the UHV chambers can be avoided by producing the VUV light in hollow-core photonic crystal fibres (HC-PCFs).

The first demonstration of HC-PCFs as light sources for a TRPEI experiment has recently been carried out by N. Kotsina *et al.* in the Townsend group at HWU [120] in collaboration with the group of J. C. Travers (also at HWU). The experimental setup is shown in Figure 7.1 (a). The HC-PCF was shown to provide femtosecond output pulses tuneable between 242-258 nm which were used to excite styrene. The dynamics were then probed using a 267 nm probe pulse produced using a combination of BBO crystals (see reference [120]).

To produce UV using the HC-PCFs the setup shown in Figure 7.1 (a), was

employed. A NIR beam (800 nm, 55 fs) of a few microjoules energy is coupled into the fibre using a focusing lens. In the setup shown, both ends of the fibre are placed into Ar filled gas cells which will result in the hollow core of the HC-PCF being filled with the gas. The NIR pulse coupled into the fibre produces a varying refractive index in the noble gas which is dependent on the intensity of the pulse (a nonlinear effect which was introduced in Chapter 2). This results in the introduction of self-phase modulation (SPM) in the pulse. SPM causes the spectrum of the pulse to broaden, as the leading edge of the pulse is red-shifted and the back edge of the pulse is blue shifted (refer to Chapter 2 for a discussion of SPM). This effect can be seen in Figure 7.1 (b). The evacuated fibre itself introduces anomalous dispersion (negative group velocity dispersion - GVD), which counteracts the normal dispersion introduced by the gas filling the fibre. GVD and SPM both result in a chirped pulse, but GVD introduces a linear, relative frequency shift, whereas the frequency shift introduced by SPM is nonlinear and dependent on the temporal profile of the pulse. Generally, SPM produces an up-chirp in the pulse, so when the conditions are chosen such that GVD is negative, the two effects act together and the result is the formation of a soliton. Therefore, the tuning of the pressure in the fibre, by which the dispersion contribution of the gas can be adjusted, is vital to achieve the desired output. As SPM broadens the spectrum, and the positive chirp introduced by SPM is reduced due to the anomalous GVD, the pulse becomes compressed in time. The compression of the pulse results in more SPM occurring, which is again counteracted by the GVD etc.. This recurring cycle results in a continuous self-compression of the higher-order soliton. Eventually a point is reached at which phase-matching occurs between the self-compressed soliton (the spectrum of which can at this point have increased by more than one octave) and another frequency. The effect observed here is known as resonant dispersive wave (RDW) emission in which energy can couple between the two and the result is the production of another wavelength, for example in the deep-UV region as in the case shown in Figure 7.1 (b). The process typically has a conversion efficiency of over 10% [120].

The ultrafast UV output pulses can be as short as 3 fs [325] with a repetition rate that can reach the MHz range [326]. The polarisation of the input pulse is preserved for capillaries and also the fibre studied below [120], but may vary depending on the type of fibre. Being able to predict the polarisation of the output is crucial for TRPEI measurements, as the polarisation must be linear and parallel to the detector in the VMI setup. By adjusting the pressure and type of gas in the fibre, the frequency of the RDW emission can be tuned (Figure 7.1 (c)) [327–330]. For more details on the properties of the HC-PCFs and their use in ultrashort UV and VUV pulse production refer to [325, 327–329, 331, 332] and references therein.

The tunability of the ultrashort output pulses in the deep-UV and VUV regions of the spectrum provides flexible pump and probe pulses for a large variety of TR-PEI experiments. Although there is a trade-off between the spectral and temporal

resolution, the short pulses produced using HC-PCFs would be ideally suited for studying processes such as H-atom migration, which often play crucial roles in biological systems for example in large scale proteins [333]. As demonstrated in [120] the output of the HC-PCFs was stable for over four hours, thereby showing their suitability for TRPEI work. Ongoing work on this project aims to improve further on this demonstration.

The time-resolution of the UV pulses produced by the fibres could not be fully exploited in the study by Kotsina *et al.* since the probe pulse was generated using conventional methods, resulting in a longer pulse. Therefore, employing two HC-PCFs, one acting as a source of pump and the other as a source of probe pulses, is a critical next step for the improvement of the setup. Once this configuration is in place, the type of gas employed, its pressure and other types of HC-PCF can be used to shorten the wavelengths further and achieve VUV pulses. The ease with which the wavelengths can be tuned using the fibres is a great advantage in TRPEI experiments, as molecules often absorb in the deep-UV and VUV range, but each molecule will absorb at slightly different wavelengths. Therefore, this method provides a source ideally suited to excite large varieties of molecules. Conventionally, optical parametric amplifiers (OPAs) in combination with frequency doubling processes, can be used to produce tuneable UV light, however the process has very low efficiency (output of 0.1-0.5% with respect to the input NIR pulse) [120] and requires a significant amount of optical equipment and time-consuming alignment. All this can now be replaced by a single fibre.

As discussed earlier, the investigation into the excited state dynamics of small amides presented in Chapter 6, was complicated due to the rapid fragmentation observed in DMF and DMA. In order to better understand the internal conversion processes taking place between the various Rydberg states in DMF and DMA, access to a tunable light source in the VUV is crucial and could be provided by this HC-PCF setup. Wavelengths between 170 nm and 200 nm would be ideally suited to exciting the members of the Rydberg manifold that are of interest. A TRPEI experiment using these pump wavelengths would also allow for a better comparison of the ultrafast relaxation processes taking place in DMF and DMA, with respect to FOR. The tunability of the VUV light provided by the fibres described above furthermore provides an opportunity to study specific categories of molecules which absorb at slightly redder VUV wavelengths than the 160 nm produced using four-wave mixing. Numerous smaller systems such as alcohols and ethers absorb at wavelenghts between 180 nm - 200 nm. These can be easily achieved using the fibre by tuning the pressure of the noble gas. As already investigated for aliphatic and aromatic amines, alcohols and ethers would lend themselves to studies of trends in the relaxation dynamics between primary and secondary systems. Example systems would be ethanol, diethylether and tetrahydrofuran and further studies might consider molecular structures where oxygen is bound into a hexagonal structure of

carbon atoms.

7.3 Future Directions: VMI of Non-Volatile Systems

A recent project in the Townsend group developed a thermal desorption source which allows for non-volatile molecules to be studied in the gas phase [334].

Model chromophore systems such as uracil and thiouracil as well as the eumelanin subunit 5,6-dihydroxyindole have been prepared in the gas-phase using the thermal desorption source and were subsequently studied using time-resolved photoion-yield experiments [335, 336]. The thermal desorption source developed is outlined in [334, 335] and a schematic of the process is shown in Figure 7.2. The solid sample is deposited on a thin stainless steel foil, using minor amounts of methanol to affix it. The back of the foil is then irradiated by a continuous-wave desorption laser (445 nm) which is focused using a pair of lenses. The thermal heating of the back of the foil results in sample being carried into the gas-phase as a neutral plume. The configuration shown here additionally fitted the sample foil into a rotating mount, which could be controlled externally to replenish the sample by adjusting the area of the foil being irradiated [334].

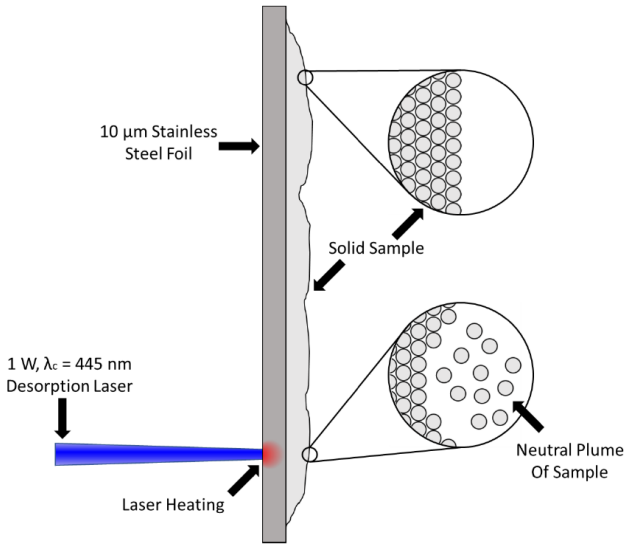

Figure 7.2: A schematic of the thermal desorption process and configuration employed at Heriot-Watt. This figure has been adapted from reference [334].

As mentioned above this technique was mostly used to record photoion-yield data, however a VMI electrode setup was included in the design of the experiment which would allow for time-resolved photoelectron imaging studies of non-volatile samples. Some preliminary electron velocity map images of several non-volatile systems, including guanine and 2-thiouracil, following one-colour ionisation were

obtained and presented in the thesis by S. W. Crane [334]. These VMI images are promising and the experiment can further be extended to include time-resolution through a pump-probe scheme. This kind of setup permits for the extension of the "bottom-up" approach by moving from the small model-chromophores to larger, more complex systems. Examples of non-volatile systems that would further our understanding of relaxation dynamics in biological systems include porphyrins which can be used in photodynamic therapy. The section below will outline how the use of this technology in combination with vacuum UV wavelengths will make the study of porphyrins accessible.

7.4 Future Directions: Systems for Photodynamic Therapy

Photodynamic therapy (PDT) is used in oncology to treat various forms of cancer including brain, lung, breast, prostate and skin cancer [337]. A photosensitive molecule (photosensitiser) is directed to the area which requires treatment and subsequently irradiated with light (typically in the visible range) [338]. The photosensitiser (PS) is excited to a singlet state which then decays to a lower lying triplet state via intersystem crossing. PTD is only possible when oxygen is present, as the photosensitiser, in its long-lived excited triplet state form, reacts with O_2. The electronic ground state of the O_2 molecule is also a triplet state and a collision between molecular oxygen and the photosensitiser results in $^1O_2$ and the PS in its electronic ground state [338]. This process is thought to be the most likely mechanism for photosensitisers used for the treatment of cancer, although it is also possible that a more complex electron-transfer process may be taking place simultaneously [339]. The reactive oxygen species (ROS) formed is harmful to biomolecules and will cause the death of undesirable cells (tumor) [338]. The first photosensitiser which is still used in the majority of PDT treatments today is 'haematoprphyrin derivative' (HDP) [340, 341]. These are organic heterocyclic compounds consisting of pyrrole subunits.

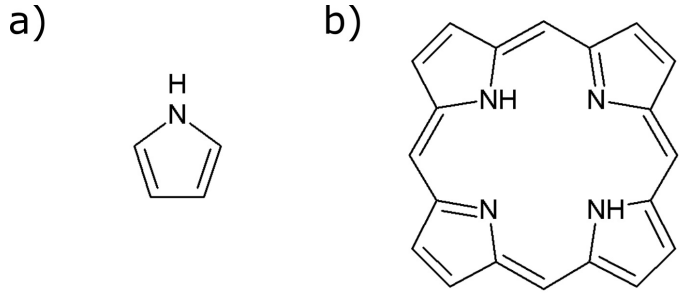

Figure 7.3: Pyrrole (a) and porphin (b), the simplest porphyrin. Metal ligands can bind to the nitrogen atoms in the centre of the macrocyle.

There has been great interest in understanding the dynamics of pyrrole as illus-

trated by references [342–348], and even dimers have been studied in the gas-phase [349]. Pyrrole is clearly an important motif and using the "bottom up" approach, the investigation of the dynamics can now be extended to porphyrins, the basic structure of which is shown in Figure 7.3. Such systems include the reactive centre in chlorophyll or haemoglobin, where magnesium or iron are bound to the nitrogen atoms in the centre of the porphyrin. There is a whole range of tetrapyrrole and porphyrin structures that have been suggested as photosensitisers [339] and understanding their dynamics could aid in predicting new structures in which long-lived triplet states can be accessed. Furthermore, the relaxation dynamics of such systems, especially chlorophyll which facilitates the first step in photosynthesis, are of great interest and provide opportunities to put the "bottom up" approach to the test by comparing the dynamics of the substructure pyrrole to those in larger systems. As it is triplet states that are of interest for photosensitisers, a high-energy probe is required to detect the dynamics in such lower-lying states. The use of HC-PCFs (as discussed in Section 7.2) will be crucial to produce short-wavelength probes that fulfil the energetic requirements for observing lower-lying states of different spin multiplicity in potential photosensitisers and porphyrin systems. Investigating the ultrafast dynamical processes of these systems in the gas-phase using time-resolved photoelectron spectroscopy techniques would therefore require a combination of the LIAD and HC-PCF experimental techniques described in the previous two sections. LIAD provides the capability of depositing these non-volatile systems into the gas-phase and the HC-PCF sources are required to produce sufficiently short and tunable probe wavelengths.

References

[1] R. Bersohn, Annual Review of Physical Chemistry **54**, 1 (2003).

[2] G. Wald, Science **162**, 230 (1968).

[3] R. R. Birge and L. M. Hubbard, Journal of the American Chemical Society **102**, 2195 (1980).

[4] R. Schoenlein, L. Peteanu, R. Mathies, and C. Shank, Science **254**, 412 (1991).

[5] A. Stolow, Faraday Discussions **163**, 9 (2013).

[6] C. E. Crespo-Hernández, B. Cohen, P. M. Hare, and B. Kohler, Chemical Reviews **104**, 1977 (2004).

[7] G. M. Roberts and V. G. Stavros, Chemical Science **5**, 1698 (2014).

[8] M. Staniforth and V. G. Stavros, Proceedings of the Royal Society A: Mathematical, Physical and Engineering Sciences **469**, 20130458 (2013).

[9] A. H. Zewail, Science **242**, 1645 (1988).

[10] M. J. Vrakking, Physics **9**, 112 (2016).

[11] T. Suzuki, Annual Review of Physical Chemistry **57**, 555 (2006).

[12] A. Stolow, International Reviews in Physical Chemistry **22**, 377 (2003).

[13] A. Stolow and J. G. Underwood, Advances in Chemical Physics **139**, 497 (2008).

[14] G. Wu, P. Hockett, and A. Stolow, Physical Chemistry Chemical Physics **13**, 18447 (2011).

[15] A. Stolow, A. E. Bragg, and D. M. Neumark, Chemical Reviews **104**, 1719 (2004).

[16] A. Stolow, Annual Review of Physical Chemistry **54**, 89 (2003).

[17] M. Miller and I. Megson, British Journal of Pharmacology **151**, 305 (2007).

[18] T. Suzuki, O. Nagae, Y. Kato, H. Nakagawa, K. Fukuhara, and N. Miyata, Journal of the American Chemical Society **127**, 11720 (2005).

[19] J.-P. Schermann, in *Spectroscopy and Modeling of Biomolecular Building Blocks*, edited by J.-P. Schermann (Elsevier, Amsterdam, 2008) pp. 251 – 296.

[20] M. N. R. Ashfold, G. A. King, D. Murdock, M. G. D. Nix, T. A. A. Oliver, and A. G. Sage, Physical Chemistry Chemical Physics **12**, 1218 (2010).

[21] J. O. F. Thompson, L. B. Klein, T. I. Sølling, M. J. Paterson, and D. Townsend, Chemical Science **7**, 1826 (2016).

[22] L. B. Klein, J. O. F. Thompson, S. W. Crane, L. Saalbach, T. I. Sølling, M. J. Paterson, and D. Townsend, Physical Chemistry Chemical Physics **18**, 25070 (2016).

[23] M. M. Zawadzki, M. Candelaresi, L. Saalbach, S. W. Crane, M. J. Paterson, and D. Townsend, Faraday Discussions **194**, 185 (2016).

[24] M. Born and R. Oppenheimer, Annalen der Physik **389**, 457 (1927).

[25] G. Herzberg and H. Longuet-Higgins, Discussions of the Faraday Society **35**, 77 (1963).

[26] M. A. Robb, M. Garavelli, M. Olivucci, and F. Bernardi, Reviews in Computational Chemistry **15**, 87 (2000).

[27] S. Matsika and P. Krause, Annual Review of Physical Chemistry **62**, 621 (2011).

[28] G. A. Worth and L. S. Cederbaum, Annual Review of Physical Chemistry **55**, 127 (2004).

[29] W. Domcke and G. Stock, Advances in Chemical Physics **100**, 1 (1997).

[30] D. R. Yarkony, The Journal of Physical Chemistry A **105**, 6277 (2001).

[31] B. G. Levine and T. J. Martínez, Annual Review of Physical Chemistry **58**, 613 (2007).

[32] S. Mahapatra, Accounts of Chemical Research **42**, 1004 (2009).

[33] W. Domcke and D. R. Yarkony, Annual Review of Physical Chemistry **63**, 325 (2012).

[34] J. Michl and V. Bonačić-Koutecký, *Electronic aspects of organic photochemistry* (Wiley, 1990).

[35] P. Suppan, *Chemistry and light* (Royal Society of Chemistry, 1994).

[36] C. E. Crespo-Hernández, G. Burdzinski, and R. Arce, The Journal of Physical Chemistry A **112**, 6313 (2008).

[37] D. S. N. Parker, R. S. Minns, T. J. Penfold, G. A. Worth, and H. H. Fielding, Chemical Physics Letters **469**, 43 (2009).

[38] R. S. Minns, D. S. N. Parker, T. J. Penfold, G. A. Worth, and H. H. Fielding, Physical Chemistry Chemical Physics **12**, 15607 (2010).

[39] T. J. Penfold, R. Spesyvtsev, O. M. Kirkby, R. S. Minns, D. S. N. Parker, H. H. Fielding, and G. A. Worth, The Journal of Chemical Physics **137**, 204310 (2012).

[40] L. Martínez-Fernández, I. Corral, G. Granucci, and M. Persico, Chemical Science **5**, 1336 (2014).

[41] O. Yushchenko, G. Licari, S. Mosquera-Vazquez, N. Sakai, S. Matile, and E. Vauthey, The Journal of Physical Chemistry Letters **6**, 2096 (2015).

[42] O. Schalk, M. S. Schuurman, G. Wu, P. Lang, M. Mucke, R. Feifel, and A. Stolow, The Journal of Physical Chemistry A **118**, 2279 (2014).

[43] A. Bhattacherjee, C. D. Pemmaraju, K. Schnorr, A. R. Attar, and S. R. Leone, Journal of the American Chemical Society **139**, 16576 (2017).

[44] M. El-Sayed, The Journal of Chemical Physics **38**, 2834 (1963).

[45] P. R. Stannard and W. M. Gelbart, The Journal of Physical Chemistry **85**, 3592 (1981).

[46] H. H. Jaffe and A. L. Miller, Journal of Chemical Education **43**, 469 (1966).

[47] P. M. Felker and A. H. Zewail, The Journal of Chemical Physics **82**, 2961 (1985).

[48] M. J. Frisch, G. W. Trucks, H. B. Schlegel, G. E. Scuseria, M. A. Robb, J. R. Cheeseman, G. Scalmani, V. Barone, G. A. Petersson, H. Nakatsuji, X. Li, M. Caricato, A. V. Marenich, J. Bloino, B. G. Janesko, R. Gomperts, B. Mennucci, H. P. Hratchian, J. V. Ortiz, A. F. Izmaylov, J. L. Sonnenberg, D. Williams-Young, F. Ding, F. Lipparini, F. Egidi, J. Goings, B. Peng, A. Petrone, T. Henderson, D. Ranasinghe, V. G. Zakrzewski, J. Gao, N. Rega, G. Zheng, W. Liang, M. Hada, M. Ehara, K. Toyota, R. Fukuda, J. Hasegawa, M. Ishida, T. Nakajima, Y. Honda, O. Kitao, H. Nakai, T. Vreven, K. Throssell, J. A. Montgomery, Jr., J. E. Peralta, F. Ogliaro, M. J. Bearpark, J. J. Heyd, E. N. Brothers, K. N. Kudin, V. N. Staroverov, T. A. Keith, R. Kobayashi, J. Normand, K. Raghavachari, A. P.

Rendell, J. C. Burant, S. S. Iyengar, J. Tomasi, M. Cossi, J. M. Millam, M. Klene, C. Adamo, R. Cammi, J. W. Ochterski, R. L. Martin, K. Morokuma, O. Farkas, J. B. Foresman, and D. J. Fox, "Gaussian 16 Revision A.03," (2016), Gaussian Inc. Wallingford CT.

[49] C. Sandorfy, *The role of Rydberg states in spectroscopy and photochemistry: low and high Rydberg states*, Vol. 20 (Springer Science & Business Media, 2002).

[50] A. L. Sobolewski, W. Domcke, C. Dedonder-Lardeux, and C. Jouvet, Physical Chemistry Chemical Physics **4**, 1093 (2002).

[51] A. L. Sobolewski and W. Domcke, Chemical Physics **259**, 181 (2000).

[52] S. W. Crane, O. Ghafur, L. Saalbach, M. J. Paterson, and D. Townsend, Chemical Physics Letters **738**, 136870 (2020).

[53] R. Polák, I. Paidarová, V. Sîpirko, and P. J. Kuntz, International Journal of Quantum Chemistry **57**, 429 (1996).

[54] G. C. G. Waschewsky, D. C. Kitchen, P. W. Browning, and L. J. Butler, The Journal of Physical Chemistry **99**, 2635 (1995).

[55] E. Kassab, J. Gleghorn, and E. Evleth, Journal of the American Chemical Society **105**, 1746 (1983).

[56] K. M. Dunn and K. Morokuma, The Journal of Physical Chemistry **100**, 123 (1996).

[57] C. Levi, G. Halász, Á. Vibók, I. Bar, Y. Zeiri, R. Kosloff, and M. Baer, The Journal of Chemical Physics **128**, 244302 (2008).

[58] E. Condon, American Journal of Physics **15**, 365 (1947).

[59] P. W. Atkins, *Molecular Quantum Mechanics*, second edition ed. (Oxford University Press, 1983).

[60] D. W. Turner and M. I. A. Jobory, Journal of Chemical Physics **37**, 3007 (1962).

[61] S. Hüfner, S. Schmidt, and F. Reinert, Nuclear Instruments and Methods in Physics Research Section A: Accelerators, Spectrometers, Detectors and Associated Equipment - Proceedings of the Workshop on Hard X-ray Photoelectron Spectroscopy **547**, 8 (2005).

[62] T. L. James, Journal of Chemical Education **48**, 712 (1971).

[63] K. Aron and P. M. Johnson, The Journal of Chemical Physics **67**, 5099 (1977).

[64] J. C. Miller, R. Compton, M. G. Payne, and W. Garrett, Physical Review Letters **45**, 114 (1980).

[65] E. J. Bieske and O. Dopfer, Chemical Reviews **100**, 3963 (2000).

[66] R. Haight, J. Bokor, J. Stark, R. Storz, R. Freeman, and P. Bucksbaum, Physical Review Letters **54**, 1302 (1985).

[67] V. Blanchet, M. Z. Zgierski, T. Seideman, and A. Stolow, Nature **401**, 52 (1999).

[68] M. Schmitt, S. Lochbrunner, J. Shaffer, J. Larsen, M. Zgierski, and A. Stolow, The Journal of Chemical Physics **114**, 1206 (2001).

[69] R. De Nalda and L. Bañares, *Ultrafast Phenomena in Molecular Sciences: Femtosecond Physics and Chemistry*, Vol. 107 (Springer International Publishing, DOI=10.1007/978-3-319-02051-8, 2013).

[70] J. Cooper and R. N. Zare, The Journal of Chemical Physics **48**, 942 (1968).

[71] K. L. Reid, Annual Review of Physical Chemistry **54**, 397 (2003).

[72] T. Seideman, Annual Review of Physical Chemistry **53**, 41 (2002).

[73] C. N. Yang, Physical Review **74**, 764 (1948).

[74] D. J. Leahy, K. L. Reid, and R. N. Zare, The Journal of Chemical Physics **95**, 1757 (1991).

[75] R. N. Zare, Annual Review of Analytical Chemistry **5**, 1 (2012).

[76] C. W. Wilkerson Jr, P. M. Goodwin, W. P. Ambrose, J. C. Martin, and R. A. Keller, Applied Physics Letters **62**, 2030 (1993).

[77] M. Ishikawa, K. Hirano, T. Hayakawa, S. Hosoi, and S. Brenner, Japanese Journal of Applied Physics **33**, 1571 (1994).

[78] R. Berera, R. van Grondelle, and J. T. Kennis, Photosynthesis Research **101**, 105 (2009).

[79] N. T. Hunt, Chemical Society Reviews **38**, 1837 (2009).

[80] S. Mukamel, Annual Review of Physical Chemistry **51**, 691 (2000).

[81] J. C. Williamson, J. Cao, H. Ihee, H. Frey, and A. H. Zewail, Nature **386**, 159 (1997).

[82] J. P. F. Nunes and M. Centurion, Advances in Atomic, Molecular, and Optical Physics **68**, 39 (2019).

[83] O. Zandi, K. J. Wilkin, Y. Xiong, and M. Centurion, Structural Dynamics **4**, 044022 (2017).

[84] D. W. Chandler and P. L. Houston, The Journal of Chemical Physics **87**, 1445 (1987).

[85] W. C. Wiley and I. H. McLaren, Review of Scientific Instruments **26**, 1150 (1955).

[86] A. T. J. B. Eppink and D. H. Parker, Review of Scientific Instruments **68**, 3477 (1997).

[87] D. W. Chandler, P. L. Houston, and D. H. Parker, The Journal of Chemical Physics **147**, 013601 (2017).

[88] D. Townsend, M. P. Minitti, and A. G. Suits, Review of Scientific Instruments **74**, 2530 (2003).

[89] R. N. Strickland and D. W. Chandler, Applied Optics **30**, 1811 (1991).

[90] M. J. Vrakking, Review of Scientific Instruments **72**, 4084 (2001).

[91] G. M. Roberts, J. L. Nixon, J. Lecointre, E. Wrede, and J. R. R. Verlet, Review of Scientific Instruments **80**, 053104 (2009).

[92] V. Dribinski, A. Ossadtchi, V. A. Mandelshtam, and H. Reisler, Review of Scientific Instruments **73**, 2634 (2002).

[93] G. A. Garcia, L. Nahon, and I. Powis, Review of Scientific Instruments **75**, 4989 (2004).

[94] R. A. Livingstone, J. O. F. Thompson, M. Iljina, R. J. Donaldson, B. J. Sussman, M. J. Paterson, and D. Townsend, The Journal of Chemical Physics **137**, 184304 (2012).

[95] R. A. Livingstone, *Ultrafast Molecular Dynamics of Model Biological Systems*, Ph.D. thesis, Heriot-Watt University (2012).

[96] B. J. Whitaker, *Imaging in molecular dynamics: technology and applications* (Cambridge University Press, 2003).

[97] A. Kantrowitz and J. Grey, Review of Scientific Instruments **22**, 328 (1951).

[98] G. Kistiakowsky and W. P. Slichter, Review of Scientific Instruments **22**, 333 (1951).

[99] S. Y. T. van de Meerakker, H. L. Bethlem, and G. Meijer, Nature Physics **4**, 595 (2008).

[100] D. H. Levy, Science , 263 (1981).

[101] W. Christen, K. Rademann, and U. Even, The Journal of Chemical Physics **125**, 174307 (2006).

[102] U. Even, J. Jortner, D. Noy, N. Lavie, and C. Cossart-Magos, The Journal of Chemical Physics **112**, 8068 (2000).

[103] J. B. Fenn, M. Mann, C. K. Meng, S. F. Wong, and C. M. Whitehouse, Science **246**, 64 (1989).

[104] J. Fenn, Journal of Biomolecular Techniques **13**, 101 (2002).

[105] D. D. Ebeling, M. S. Westphall, M. Scalf, and L. M. Smith, Analytical Chemistry **72**, 5158 (2000).

[106] K. K. Lehmann and G. Scoles, Science **279**, 2065 (1998).

[107] F. Vastola and A. Pirone, Advances in Mass Spectrometry **4**, 107 (1968).

[108] M. Karas, D. Bachmann, U. Bahr, and F. Hillenkamp, International Journal of Mass Spectrometry and Ion Processes **78**, 53 (1987).

[109] B. Lindner and U. Seydel, Analytical Chemistry **57**, 895 (1985).

[110] A. E. Boguslavskiy, O. Schalk, N. Gador, W. J. Glover, T. Mori, T. Schultz, M. S. Schuurman, T. J. Martínez, and A. Stolow, The Journal of Chemical Physics **148**, 164302 (2018).

[111] C. T. Chen, G. L. Wang, X. Y. Wang, and Z. Y. Xu, Applied Physics B **97**, 9 (2009).

[112] R. Iikubo, T. Sekikawa, Y. Harabuchi, and T. Taketsugu, Faraday Discussions **194**, 147 (2016).

[113] J. Nishitani, C. W. West, C. Higashimura, and T. Suzuki, Chemical Physics Letters **684**, 397 (2017).

[114] A. D. Smith, E. M. Warne, D. Bellshaw, D. A. Horke, M. Tudorovskya, E. Springate, A. J. H. Jones, C. Cacho, R. T. Chapman, A. Kirrander, and R. S. Minns, Physical Review Letters **120**, 183003 (2018).

[115] A. von Conta, A. Tehlar, A. Schletter, Y. Arasaki, K. Takatsuka, and H. J. Wörner, Nature Communications **9**, 3162 (2018).

[116] A. Ciavardini, M. Coreno, C. Callegari, C. Spezzani, G. De Ninno, B. Ressel, C. Grazioli, M. de Simone, A. Kivimaki, P. Miotti, F. Frassetto, L. Poletto, C. Puglia, S. Fornarini, M. Pezzella, E. Bodo, and S. Piccirillo, The Journal of Physical Chemistry A **123**, 1295 (2019).

[117] S. Adachi, T. Schatteburg, A. Humeniuk, R. Mitrić, and T. Suzuki, Physical Chemistry Chemical Physics (2019).

[118] S. Y. Liu, Y. Ogi, T. Fuji, K. Nishizawa, T. Horio, T. Mizuno, H. Kohguchi, M. Nagasono, T. Togashi, K. Tono, M. Yabashi, Y. Senba, H. Ohashi, H. Kimura, T. Ishikawa, and T. Suzuki, Physical Review A **81**, 031403 (2010).

[119] R. J. Squibb, M. Sapunar, A. Ponzi, R. Richter, A. Kivimäki, O. Plekan, P. Finetti, N. Sisourat, V. Zhaunerchyk, T. Marchenko, L. Journel, R. Guillemin, R. Cucini, M. Coreno, C. Grazioli, C. Di Fraia, C. Callegari, K. C. Prince, P. Decleva, M. Simon, J. H. D. Eland, N. Došlić, R. Feifel, and M. N. Piancastelli, Nature Communications **9**, 63 (2018).

[120] N. Kotsina, F. Belli, S. Gao, Y. Wang, P. Wang, J. C. Travers, and D. Townsend, The Journal of Physical Chemistry Letters **10**, 715 (2019).

[121] A. R. Bainbridge, J. Harrington, A. Kirrander, C. Cacho, E. Springate, W. A. Bryan, and R. S. Minns, New Journal of Physics **17**, 103013 (2015).

[122] J. Nishitani, C. W. West, C. Higashimura, and T. Suzuki, Chemical Physics Letters **684**, 397 (2017).

[123] J. Nishitani, Y. Yamamoto, C. W. West, S. Karashima, and T. Suzuki, Science Advances **5**, eaaw6896 (2019).

[124] T. Fuji, T. Horio, and T. Suzuki, Optics Letters **32**, 2481 (2007).

[125] T. Horio, R. Spesyvtsev, and T. Suzuki, Optics Express **21**, 22423 (2013).

[126] T. Horio, R. Spesyvtsev, and T. Suzuki, Optics Letters **39**, 6021 (2014).

[127] R. Uenishi, T. Horio, and T. Suzuki, The Journal of Physical Chemistry A **123**, 6848 (2019).

[128] R. Forbes, V. Makhija, K. Veyrinas, A. Stolow, J. W. L. Lee, M. Burt, M. Brouard, C. Vallance, I. Wilkinson, R. Lausten, and P. Hockett, The Journal of Chemical Physics **147**, 013911 (2017).

[129] M. R. Coates, M. A. B. Larsen, R. Forbes, S. P. Neville, A. E. Boguslavskiy, I. Wilkinson, T. I. Sølling, R. Lausten, A. Stolow, and M. S. Schuurman, The Journal of Chemical Physics **149**, 144311 (2018).

[130] M. Wollenhaupt, A. Assion, and T. Baumert, "Femtosecond Laser Pulses: Linear Properties, Manipulation, Generation and Measurement," in *Springer Handbook of Lasers and Optics, ISBN 978-0-387-95579-7. Springer-Verlag New York*, edited by F. Träger (2007).

[131] P. M. W. French, Reports on Progress in Physics **58**, 169 (1995).

[132] K. Wynne, G. D. Reid, and R. M. Hochstrasser, Optics Letters **19**, 895 (1994).

[133] P. G. Kryukov, Quantum Electronics **31**, 95 (2001).

[134] U. Keller, K. J. Weingarten, F. X. Kartner, D. Kopf, B. Braun, I. D. Jung, R. Fluck, C. Honninger, N. Matuschek, and J. A. Der Au, IEEE Journal of Selected Topics in Quantum Electronics **2**, 435 (1996).

[135] G. New, *Introduction to Nonlinear Optics* (Cambridge University Press, 2011).

[136] H. H. Li, Journal of Physical and Chemical Reference Data **9**, 161 (1980).

[137] R. L. Fork, O. E. Martinez, and J. P. Gordon, Opt. Lett. **9**, 150 (1984).

[138] D. Strickland and G. Mourou, Optics Communications **55**, 447 (1985).

[139] R. W. Boyd, *Nonlinear Optics* (Elsevier, 2003).

[140] G. Agrawal, in *Nonlinear Fiber Optics (Fifth Edition)*, Optics and Photonics, edited by G. Agrawal (Academic Press, Boston, 2013) pp. 397 – 456.

[141] P. A. Franken, A. E. Hill, C. W. Peters, and G. Weinreich, Physical Review Letters **7**, 118 (1961).

[142] D. A. Kleinman, A. Ashkin, and G. Boyd, Physical Review **145**, 338 (1966).

[143] T. Südmeyer, S. Marchese, S. Hashimoto, C. Baer, G. Gingras, B. Witzel, and U. Keller, Nature Photonics **2**, 599 (2008).

[144] M. Beutler, M. Ghotbi, F. Noack, and I. V. Hertel, Optics Letters **35**, 1491 (2010).

[145] M. Ghotbi, M. Beutler, and F. Noack, Optics Letters **35**, 3492 (2010).

[146] M. Ghotbi, P. Trabs, M. Beutler, and F. Noack, Optics Letters **38**, 486 (2013).

[147] M. Beutler, *Erzeugung abstimmbarer Femtosekunden Impulse im vakuum-ultravioletten Spektralgebiet*, Ph.D. thesis, Freie Universität Berlin (2012).

[148] M. M. Zawadzki, *Interrogating Nonadiabatic Molecular Dynamics Using Ultrafast Nonlinear Optics*, Ph.D. thesis, Heriot-Watt University (2017).

[149] R. Trebino, K. W. DeLong, D. N. Fittinghoff, J. N. Sweetser, M. A. Krumbügel, B. A. Richman, and D. J. Kane, Review of Scientific Instruments **68**, 3277 (1997).

[150] S. O. Williams and D. G. Imre, The Journal of Physical Chemistry **92**, 3363 (1988).

[151] G. Stock, R. Schneider, and W. Domcke, The Journal of Chemical Physics **90**, 7184 (1989).

[152] J. O. F. Thompson, L. Saalbach, S. W. Crane, M. J. Paterson, and D. Townsend, The Journal of Chemical Physics **142**, 03B612_1 (2015).

[153] J. O. F. Thompson, *Time-Resolved Photoelectron Imaging of Model Biological Chromophores*, Ph.D. thesis, Heriot-Watt University (2015).

[154] J. W. S. B. Rayleigh, *On the scattering of light by small particles* (1871).

[155] Y. Ogi, H. Kohguchi, D. Niu, K. Ohshimo, and T. Suzuki, The Journal of Physical Chemistry A **113**, 14536 (2009).

[156] Y. Cho and S.-J. Na, Measurement Science and Technology **16**, 878 (2005).

[157] K. Levenberg, Quarterly of Applied Mathematics **2**, 164 (1944).

[158] D. W. Marquardt, Journal of the Society for Industrial and Applied Mathematics **11**, 431 (1963).

[159] O. Schalk, A. E. Boguslavskiy, and A. Stolow, The Journal of Physical Chemistry A **114**, 4058 (2010).

[160] D. H. Parker and A. T. J. B. Eppink, in *Imaging in Molecular Dynamics: Technology and Applications* (Cambridge University Press, 2003).

[161] T. van Voorhis, T. Kowalczyk, B. Kaduk, L.-P. Wang, C.-L. Cheng, and Q. Wu, Annual Review of Physical Chemistry **61**, 149 (2010).

[162] F. Jensen, *Introduction to Computational Chemistry*, 2nd ed. (John Wiley and Sons Ltd, 2007).

[163] R. Ditchfield, W. J. Hehre, and J. A. Pople, The Journal of Chemical Physics **54**, 724 (1971).

[164] T. H. Dunning Jr, The Journal of Chemical Physics **90**, 1007 (1989).

[165] E. Papajak, J. Zheng, X. Xu, H. R. Leverentz, and D. G. Truhlar, Journal of Chemical Theory and Computation **7**, 3027 (2011).

[166] M. J. Frisch, J. A. Pople, and J. S. Binkley, The Journal of Chemical Physics **80**, 3265 (1984).

[167] E. R. Davidson and D. Feller, Chemical Reviews **86**, 681 (1986).

[168] F. Jensen, Wiley Interdisciplinary Reviews: Computational Molecular Science **3**, 273 (2013).

[169] D. R. Hartree, *The Calculation of Atomic Structures* (Wiley, 1957).

[170] J. C. Slater, Physical Review **34**, 1293 (1929).

[171] D. Hartree, in *Mathematical Proceedings of the Cambridge Philosophical Society*, Vol. 25 (Cambridge University Press, 1929) pp. 225–236.

[172] V. Fock, Zeitschrift für Physik **61**, 126 (1930).

[173] C. C. J. Roothaan, Reviews of Modern Physics **23**, 69 (1951).

[174] G. G. Hall, Proceedings of the Royal Society of London. Series A. Mathematical and Physical Sciences **205**, 541 (1951).

[175] C. Møller and M. S. Plesset, Physical Review **46**, 618 (1934).

[176] F. Coester and H. Kümmel, Nuclear Physics **17**, 477 (1960).

[177] F. Coester, Nuclear Physics **7**, 421 (1958).

[178] A. Szabo and N. S. Ostlund, *Introduction to Advanced Electronic Structure Theory* (Dover Publications, Inc., New York, 1996).

[179] M. Schmidt and K. Ruedenberg, The Journal of Chemical Physics **71**, 3951 (1979).

[180] R. J. Bartlett and M. Musial, Reviews of Modern Physics **79**, 291 (2007).

[181] W. Kohn, Reviews of Modern Physics **71**, 1253 (1999).

[182] P. Hohenberg and W. Kohn, Physical Review **136**, B864 (1964).

[183] W. Koch and M. C. Holthausen, *A chemist's guide to density functional theory* (John Wiley & Sons, 2015).

[184] W. Kohn and L. J. Sham, Physical Review **140**, A1133 (1965).

[185] A. D. Becke, Physical Review A **38**, 3098 (1988).

[186] J. P. Perdew and K. Schmidt, in *AIP Conference Proceedings*, Vol. 577 (AIP, 2001) pp. 1–20.

[187] A. D. Becke, The Journal of Chemical Physics **98**, 1372 (1993).

[188] A. D. Becke, The Journal of Chemical Physics **98** (1993).

[189] W. Koch and M. C. Holthausen, *A Chemist's Guide to Density Functional Theory*, 2nd ed., Vol. 3 (Wiley-VCH Verlag GmbH, 2001).

[190] H. Koch and P. Jørgensen, The Journal of Chemical Physics **93**, 3333 (1990).

[191] J. F. Stanton and R. J. Bartlett, Journal of Chemical Physics **98**, 7029 (1993).

[192] J. D. Watts, in *Radiation Induced Molecular Phenomena in Nucleic Acids: A Comprehensive Theoretical and Experimental Analysis*, edited by M. K. Shukla and J. Leszczynski (Springer Netherlands, Dordrecht, 2008) pp. 65–92.

[193] M. Caricato, G. W. Trucks, M. J. Frisch, and K. B. Wiberg, Journal of Chemical Theory and Computation **7**, 456 (2011).

[194] M. Schreiber, M. R. Silva-Junior, S. P. A. Sauer, and W. Thiel, The Journal of Chemical Physics **128**, 134110 (2008).

[195] D. Kánnár and P. G. Szalay, Journal of Chemical Theory and Computation **10**, 3757 (2014).

[196] A. Zangwill and P. Soven, Physical Review A **21**, 1561 (1980).

[197] E. Runge and E. K. U. Gross, Physical Review Letters **52**, 997 (1984).

[198] M. E. Casida, in *Recent Advances In Density Functional Methods: (Part I)* (World Scientific, 1995) pp. 155–192.

[199] M. R. Silva-Junior, M. Schreiber, S. P. Sauer, and W. Thiel, The Journal of Chemical Physics **129**, 104103 (2008).

[200] D. Jacquemin, V. Wathelet, E. A. Perpete, and C. Adamo, Journal of Chemical Theory and Computation **5**, 2420 (2009).

[201] D. Jacquemin, B. Mennucci, and C. Adamo, Physical Chemistry Chemical Physics **13**, 16987 (2011).

[202] M. J. Frisch, G. W. Trucks, H. B. Schlegel, G. E. Scuseria, M. A. Robb, J. R. Cheeseman, J. A. Montgomery, Jr., T. Vreven, K. N. Kudin, J. C. Burant, J. M. Millam, S. S. Iyengar, J. Tomasi, V. Barone, B. Mennucci, M. Cossi, G. Scalmani, N. Rega, G. A. Petersson, H. Nakatsuji, M. Hada, M. Ehara, K. Toyota, R. Fukuda, J. Hasegawa, M. Ishida, T. Nakajima, Y. Honda, O. Kitao, H. Nakai, M. Klene, X. Li, J. E. Knox, H. P. Hratchian, J. B. Cross, V. Bakken, C. Adamo, J. Jaramillo, R. Gomperts, R. E. Stratmann, O. Yazyev, A. J. Austin, R. Cammi, C. Pomelli, J. W. Ochterski, P. Y. Ayala, K. Morokuma, G. A. Voth, P. Salvador, J. J. Dannenberg, V. G. Zakrzewski, S. Dapprich, A. D. Daniels, M. C. Strain, O. Farkas, D. K. Malick, A. D. Rabuck, K. Raghavachari, J. B. Foresman, J. V. Ortiz, Q. Cui, A. G. Baboul, S. Clifford, J. Cioslowski, B. B. Stefanov, G. Liu, A. Liashenko, P. Piskorz, I. Komaromi, R. L. Martin, D. J. Fox, T. Keith, M. A. Al-Laham, C. Y. Peng, A. Nanayakkara, M. Challacombe, P. M. W. Gill, B. Johnson, W. Chen, M. W. Wong, C. Gonzalez, and J. A. Pople, "Gaussian 03, Revision D.01," (2004), Gaussian, Inc., Wallingford, CT.

[203] M. J. Frisch, G. W. Trucks, H. B. Schlegel, G. E. Scuseria, M. A. Robb, J. R. Cheeseman, G. Scalmani, V. Barone, B. Mennucci, G. A. Petersson, H. Nakatsuji, M. Caricato, X. Li, H. P. Hratchian, A. F. Izmaylov, J. Bloino, G. Zheng, J. L. Sonnenberg, M. Hada, M. Ehara, K. Toyota, R. Fukuda, J. Hasegawa, M. Ishida, T. Nakajima, Y. Honda, O. Kitao, H. Nakai, T. Vreven, J. A. Montgomery, Jr., J. E. Peralta, F. Ogliaro, M. Bearpark, J. J. Heyd, E. Brothers, K. N. Kudin, V. N. Staroverov, R. Kobayashi, J. Normand, K. Raghavachari, A. Rendell, J. C. Burant, S. S. Iyengar, J. Tomasi, M. Cossi, N. Rega, J. M. Millam, M. Klene, J. E. Knox, J. B. Cross, V. Bakken, C. Adamo, J. Jaramillo, R. Gomperts, R. E. Stratmann, O. Yazyev, A. J. Austin, R. Cammi, C. Pomelli, J. W. Ochterski, R. L. Martin, K. Morokuma, V. G. Zakrzewski, G. A. Voth, P. Salvador, J. J. Dannenberg, S. Dapprich, A. D. Daniels, . Farkas, J. B. Foresman, J. V. Ortiz, J. Cioslowski, and D. J. Fox, "Gaussian 09 Revision D.01," (2013), Gaussian Inc. Wallingford CT.

[204] R. Dennington, T. A. Keith, and J. M. Millam, "Gaussview Version 5," (2009), Semichem Inc. Shawnee Mission KS.

[205] J. B. Foresman and A. Frisch, *Exploring chemistry with electronic structure methods: a guide to using Gaussian* (Gaussian, 1996).

[206] R. L. Martin, The Journal of Chemical Physics **118**, 4775 (2003).

[207] E. R. Batista and R. L. Martin, Encyclopedia of Computational Chemistry (2002).

[208] S. Zhou, I. Barnes, T. Zhu, I. Bejan, M. Albu, and T. Benter, Environmental Science & Technology **42**, 7905 (2008).

[209] G. Zhang, B. Wu, and S. Zhang, Environmental Pollution **225**, 691 (2017).

[210] N. V. Belova, H. Oberhammer, N. H. Trang, and G. V. Girichev, The Journal of Organic Chemistry **79**, 5412 (2014).

[211] H. Nakanishi, H. Morita, and S. Nagakura, Bulletin of the Chemical Society of Japan **50**, 2255 (1977).

[212] M.-C. Yoon, Y. S. Choi, and S. K. Kim, Chemical Physics Letters **300**, 207 (1999).

[213] M.-C. Yoon, Y. S. Choi, and S. K. Kim, The Journal of Chemical Physics **110**, 11850 (1999).

[214] H. P. Upadhyaya, A. Kumar, and P. D. Naik, The Journal of Chemical Physics **118**, 2590 (2003).

[215] I. O. Antonov, K. Voronova, M.-W. Chen, B. Sztaray, P. Hemberger, A. Bodi, D. L. Osborn, and L. Sheps, The Journal of Physical Chemistry A **123**, 5472 (2019).

[216] S. Xu, S. T. Park, J. S. Feenstra, R. Srinivasan, and A. H. Zewail, The Journal of Physical Chemistry A **108**, 6650 (2004).

[217] X.-B. Chen, W.-H. Fang, and D. L. Phillips, The Journal of Physical Chemistry A **110**, 4434 (2006).

[218] L. Poisson, P. Roubin, S. Coussan, B. Soep, and J.-M. Mestdagh, Journal of the American Chemical Society **130**, 2974 (2008).

[219] P. K. Verma, F. Koch, A. Steinbacher, P. Nuernberger, and T. Brixner, Journal of the American Chemical Society **136**, 14981 (2014).

[220] B. Xie, G. Cui, and W.-H. Fang, Journal of Chemical Theory and Computation **13**, 2717 (2017).

[221] A. Bhattacherjee, C. D. Pemmaraju, K. Schnorr, A. R. Attar, and S. R. Leone, Journal of the American Chemical Society **139**, 16576 (2017).

[222] A. Bhattacherjee and S. R. Leone, Accounts of Chemical Research **51**, 3203 (2018).

[223] K. Watanabe, T. Nakayama, and J. Mottl, Journal of Quantitative Spectroscopy and Radiative Transfer **2**, 369 (1962).

[224] K. N. Houk, L. P. Davis, G. R. Newkome, R. E. Duke, and R. Nauman, Journal of the American Chemical Society **95**, 8364 (1973).

[225] H. Nakanishi, H. Morita, and S. Nagakura, Bulletin of the Chemical Society of Japan **51**, 1723 (1978).

[226] N. S. Hush, M. K. Livett, J. B. Peel, and G. D. Willett, Australian Journal of Chemistry **40**, 599 (1987).

[227] S. Evans, A. Hamnett, A. F. Orchard, and D. Lloyd, Faraday Discussions of the Chemical Society **54**, 227 (1972).

[228] C. Cauletti, C. Furlani, and G. Storto, Journal of Electron Spectroscopy and Related Phenomena **18**, 329 (1980).

[229] N. Kotsina and D. Townsend, Physical Chemistry Chemical Physics **19**, 29409 (2017).

[230] C. P. Schick and P. M. Weber, The Journal of Physical Chemistry A **105**, 3725 (2001).

[231] W. Cheng, C. L. Evans, N. Kuthirummal, and P. M. Weber, Chemical Physics Letters **349**, 405 (2001).

[232] R. Montero, F. Castano, R. Martinez, and A. Longarte, The Journal of Physical Chemistry A **113**, 952 (2009).

[233] O. Schalk, A. E. Boguslavskiy, and A. Stolow, The Journal of Physical Chemistry Letters **5**, 560 (2014).

[234] Q. Hao, J. Long, X. Deng, Y. Tang, B. Abulimiti, and B. Zhang, The Journal of Physical Chemistry A **121**, 3858 (2017).

[235] T. Chwee, G. Lim, Z. Wong, M. Sullivan, and W. Fan, Physical Chemistry Chemical Physics **18**, 7404 (2016).

[236] R. Forbes, V. Makhija, K. Veyrinas, A. Stolow, J. W. L. Lee, M. Burt, M. Brouard, C. Vallance, I. Wilkinson, R. Lausten, and P. Hockett, The Journal of Chemical Physics **147**, 013911 (2017).

[237] A. R. Butler and D. L. H. Williams, Chemical Society Reviews **22**, 233 (1993).

[238] P. G. Wang, M. Xian, X. Tang, X. Wu, Z. Wen, T. Cai, and A. J. Janczuk, Chemical Reviews **102**, 1091 (2002).

[239] R. A. Vogt, C. Reichardt, and C. E. Crespo-Hernández, The Journal of Physical Chemistry A **117**, 6580 (2013).

[240] D. B. Galloway, J. A. Bartz, L. G. Huey, and F. F. Crim, The Journal of Chemical Physics **98**, 2107 (1993).

[241] M. Takezaki, N. Hirota, and M. Terazima, The Journal of Physical Chemistry A **101**, 3443 (1997).

[242] M. Takezaki, N. Hirota, and M. Terazima, The Journal of Chemical Physics **108**, 4685 (1998).

[243] Y. He, A. Gahlmann, J. S. Feenstra, S. T. Park, and A. H. Zewail, Chemistry–An Asian Journal **1**, 56 (2006).

[244] Y.-M. Li, J.-L. Sun, H.-M. Yin, K.-L. Han, and G.-Z. He, The Journal of Chemical Physics **118**, 6244 (2003).

[245] C. Kosmidis, K. W. D. Ledingham, H. S. Kilic, T. McCanny, R. P. Singhal, A. J. Langley, and W. Shaikh, The Journal of Physical Chemistry A **101**, 2264 (1997).

[246] M.-F. Lin, Y. T. Lee, C.-K. Ni, S. Xu, and M. C. Lin, The Journal of Chemical Physics **126**, 064310 (2007).

[247] M. L. Hause, N. Herath, R. Zhu, M. C. Lin, and A. G. Suits, Nature Chemistry **3**, 932 (2011).

[248] O. Schalk, D. Townsend, T. J. A. Wolf, D. M. P. Holland, A. E. Boguslavskiy, M. Szöri, and A. Stolow, Chemical Physics Letters **691**, 379 (2018).

[249] A. Giussani and G. A. Worth, Journal of Chemical Theory and Computation **13**, 2777 (2017).

[250] J.-M. Mewes, V. Jovanović, C. M. Marian, and A. Dreuw, Physical Chemistry Chemical Physics **16**, 12393 (2014).

[251] J. Quenneville, M. Greenfield, D. S. Moore, S. D. McGrane, and R. J. Scharff, The Journal of Physical Chemistry A **115**, 12286 (2011).

[252] T. Glenewinkel-Meyer and F. F. Crim, Journal of Molecular Structure: THEOCHEM **337**, 209 (1995).

[253] Y. Liu, Y. Yan, W. Yin, B. Liu, T. Gerber, and G. Knopp, Laser Physics Letters **16**, 035301 (2019).

[254] A. Marshall, A. Clark, R. Jennings, K. W. D. Ledingham, and R. P. Singhal, International Journal of Mass Spectrometry and Ion Processes **112**, 273 (1992).

[255] M. L. Hause, N. Herath, R. Zhu, M. C. Lin, and A. G. Suits, Nature Chemistry **3**, 932 (2011).

[256] M. Takezaki, N. Hirota, M. Terazima, H. Sato, T. Nakajima, and S. Kato, The Journal of Physical Chemistry A **101**, 5190 (1997).

[257] C. Kosmidis, K. Ledingham, A. Clark, A. Marshall, R. Jennings, J. Sander, and R. Singhal, International Journal of Mass Spectrometry and Ion Processes **135**, 229 (1994).

[258] C. Kosmidis, A. Clark, R. Deas, K. Ledingham, A. Marshall, and R. Singhal, *UV laser induced photochemistry of nitrobenzene and nitrotoluene isomers*, Tech. Rep. (1995).

[259] C. Reichardt, R. A. Vogt, and C. E. Crespo-Hernández, The Journal of Chemical Physics **131**, 224518 (2009).

[260] J. S. Zugazagoitia, C. X. Almora-Díaz, and J. Peon, The Journal of Physical Chemistry A **112**, 358 (2008).

[261] J. O. F. Thompson, L. Saalbach, S. W. Crane, M. J. Paterson, and D. Townsend, The Journal of Chemical Physics **142**, 114309 (2015).

[262] G. Scoles, D. Bassi, U. Buck, and D. Laine, *Atomic and Molecular Beam Methods*, Vol. 1,2 (Oxford University Press New York, 1988).

[263] D. Irimia, R. Kortekaas, and M. H. Janssen, Physical Chemistry Chemical Physics **11**, 3958 (2009).

[264] M. Van Beek and J. Ter Meulen, Chemical Physics Letters **337**, 237 (2001).

[265] B. Yan, P. F. H. Claus, B. G. M. van Oorschot, L. Gerritsen, A. T. J. B. Eppink, S. Y. T. van de Meerakker, and D. H. Parker, Review of Scientific Instruments **84**, 023102 (2013).

[266] A. R. McKay, M. E. Sanz, C. R. S. Mooney, R. S. Minns, E. M. Gill, and H. H. Fielding, Review of Scientific Instruments **81**, 123101 (2010).

[267] M. Xie, Z. Zhou, Z. Wang, D. Chen, and F. Qi, International Journal of Mass Spectrometry **303**, 137 (2011).

[268] M. Staikova and I. G. Csizmadia, Journal of Molecular Structure: THEOCHEM **467**, 181 (1999).

[269] P. C. Chen and Y. C. Chieh, Journal of Molecular Structure: THEOCHEM **583**, 173 (2002).

[270] K. B. Borisenko and I. Hargittai, Journal of Molecular Structure **382**, 171 (1996).

[271] A. Domenicano, G. Schultz, I. Hargittai, M. Colapietro, G. Portalone, P. George, and C. W. Bock, Structural Chemistry **1**, 107 (1990).

[272] T. Correll, N. W. Larsen, and T. Pedersen, Journal of Molecular Structure **65**, 43 (1980).

[273] L. A. Carreira and T. G. Towns, Journal of Molecular Structure **41**, 1 (1977).

[274] J. C. Sancho-Garcıa and A. J. Pérez-Jiménez, The Journal of Chemical Physics **119**, 5121 (2003).

[275] S. H. Hastings and F. A. Matsen, Journal of the American Chemical Society **70**, 3514 (1948).

[276] J. E. Abbott, X. Peng, and W. Kong, The Journal of Chemical Physics **117**, 8670 (2002).

[277] S. Nagakura, M. Kojima, and Y. Maruyama, Journal of Molecular Spectroscopy **13**, 174 (1964).

[278] S. Krishnakumar, A. K. Das, P. J. Singh, A. Shastri, and B. Rajasekhar, Journal of Quantitative Spectroscopy and Radiative Transfer **184**, 89 (2016).

[279] A. Dreuw, J. L. Weisman, and M. Head-Gordon, The Journal of Chemical Physics **119**, 2943 (2003).

[280] R. A. W. Johnstone and F. A. Mellon, Journal of the Chemical Society, Faraday Transactions 2: Molecular and Chemical Physics **68**, 1209 (1972).

[281] T. Kobayashi and S. Nagakura, Bulletin of the Chemical Society of Japan **47**, 2563 (1974).

[282] T. Kobayashi and S. Nagakura, Chemistry Letters **1**, 903 (1972).

[283] V. Butcher, M. L. Costa, J. M. Dyke, A. R. Ellis, and A. Morris, Chemical Physics **115**, 261 (1987).

[284] M. J. Dewar and D. E. David, Journal of the American Chemical Society **102**, 7387 (1980).

[285] K. S. Haber, J. W. Zwanziger, F. X. Campos, R. T. Wiedmann, and E. R. Grant, Chemical Physics Letters **144**, 58 (1988).

[286] G. Reiser, W. Habenicht, K. Müller-Dethlefs, and E. W. Schlag, Chemical Physics Letters **152**, 119 (1988).

[287] K.-P. Huber and G. Herzberg, *Molecular Spectra and Molecular Structure: IV. Constants of Diatomic Molecules* (Van Nostrand Reinhold Co., 1979).

[288] D. B. Galloway, T. Glenewinkel-Meyer, J. A. Bartz, L. G. Huey, and F. F. Crim, The Journal of Chemical Physics **100**, 1946 (1994).

[289] S. C. Xu and M. C. Lin, Journal of Physical Chemistry B **109**, 8367 (2005).

[290] O. Schalk, A. E. Boguslavskiy, A. Stolow, and M. S. Schuurman, Journal of the American Chemical Society **133**, 16451 (2011).

[291] M. A. B. Larsen, T. I. Sølling, R. Forbes, A. E. Boguslavskiy, V. Makhija, K. Veyrinas, R. Lausten, A. Stolow, M. M. Zawadzki, L. Saalbach, N. Kotsina, M. J. Paterson, and D. Townsend, The Journal of Chemical Physics **150**, 054301 (2019).

[292] G. M. Roberts and V. G. Stavros, Chemical Science **5**, 1698 (2014).

[293] L. B. Klein, T. J. Morsing, R. A. Livingstone, D. Townsend, and T. I. Sølling, Physical Chemistry Chemical Physics **18**, 9715 (2016).

[294] L. Saalbach, *Excited State Molecular Properties - MPhys Research Project*, Master's thesis, Heriot-Watt University (2016).

[295] R. J. MacDonell, O. Schalk, T. Geng, R. D. Thomas, R. Feifel, T. Hansson, and M. S. Schuurman, The Journal of Chemical Physics **145**, 114306 (2016).

[296] H. Hunt and W. Simpson, Journal of the American Chemical Society **75**, 4540 (1953).

[297] K. Kaya and S. Nagakura, Theoretica Chimica Acta **7**, 117 (1967).

[298] H. Basch, M. Robin, and N. Kuebler, The Journal of Chemical Physics **49**, 5007 (1968).

[299] D. Ter Steege, C. Lagrost, W. Buma, D. Leigh, and F. Zerbetto, The Journal of Chemical Physics **117**, 8270 (2002).

[300] J. Gingell, N. Mason, H. Zhao, I. Walker, and M. Siggel, Chemical Physics **220**, 191 (1997).

[301] D. P. Chong, Journal of Electron Spectroscopy and Related Phenomena **184**, 164 (2011).

[302] I. Antol, M. Barbatti, M. Eckert-Maksić, and H. Lischka, Monatshefte für Chemie - Chemical Monthly **139**, 319 (2008).

[303] I. Antol, M. Eckert-Maksić, M. Barbatti, and H. Lischka, The Journal of Chemical Physics **127**, 234303 (2007).

[304] I. Antol, M. Eckert-Maksic, and H. Lischka, The Journal of Physical Chemistry A **108**, 10317 (2004).

[305] P. G. Szalay and G. Fogarasi, Chemical Physics Letters **270**, 406 (1997).

[306] L. Serrano-Andrés and M. P. Fülscher, Journal of the American Chemical Society **118**, 12190 (1996).

[307] J. D. Hirst, D. M. Hirst, and C. L. Brooks, The Journal of Physical Chemistry **100**, 13487 (1996).

[308] A. Shastri, A. K. Das, S. Krishnakumar, P. J. Singh, and B. Raja Sekhar, The Journal of Chemical Physics **147**, 224305 (2017).

[309] G. Fogarasi, Journal of Molecular Structure **978**, 257 (2010).

[310] P. J. Stephens, F. Devlin, C. Chabalowski, and M. J. Frisch, The Journal of Physical Chemistry **98**, 11623 (1994).

[311] T. Yanai, D. P. Tew, and N. C. Handy, Chemical Physics Letters **393**, 51 (2004).

[312] M. L. Lipciuc, S. H. Gardiner, T. N. Karsili, J. W. Lee, D. Heathcote, M. N. Ashfold, and C. Vallance, The Journal of Chemical Physics **147**, 013941 (2017).

[313] S. Leach, N. Champion, H.-W. Jochims, and H. Baumgärtel, Chemical Physics **376**, 10 (2010).

[314] D. Sweigart and D. Turner, Journal of the American Chemical Society **94**, 5592 (1972).

[315] T. L. L. Henriksen, R. Isaksson and J. Sandström, Acta Chemica Scandinavica B **B35**, 489 (1981).

[316] C. Brundle, D. Turner, M. Robin, and H. Basch, Chemical Physics Letters **3**, 292 (1969).

[317] G. Bieri, L. Asbrink, and W. v. Niessen, Journal of Electron Spectroscopy and Related Phenomena **27**, 129 (1982).

[318] M. Baldwin, A. Loudon, K. Webb, and P. Cardnell, Organic Mass Spectrometry **12**, 279 (1977).

[319] H. Siegbarn, L. Asplund, P. Kelfve, K. Hamrin, L. Karlsson, and K. Siegbahn, Journal of Electron Spectroscopy and Related Phenomena **5**, 1059 (1974).

[320] S. Pratt, Reports on Progress in Physics **58**, 821 (1995).

[321] P. Hockett, M. Staniforth, K. L. Reid, and D. Townsend, Physical Review Letters **102**, 253002 (2009).

[322] S. P. Neville, Y. Wang, A. E. Boguslavskiy, A. Stolow, and M. S. Schuurman, The Journal of Chemical Physics **144**, 014305 (2016).

[323] M. M. Zawadzki, J. O. F. Thompson, E. A. Burgess, M. J. Paterson, and D. Townsend, Physical Chemistry Chemical Physics **17**, 26659 (2015).

[324] J. O. F. Thompson, L. Saalbach, S. W. Crane, M. J. Paterson, and D. Townsend, The Journal of Chemical Physics **142**, 114309 (2015).

[325] C. Brahms, D. R. Austin, F. Tani, A. S. Johnson, D. Garratt, J. C. Travers, J. W. Tisch, P. St. J. Russell, and J. P. Marangos, Optics letters **44**, 731 (2019).

[326] F. Köttig, F. Tani, C. M. Biersach, J. C. Travers, and P. St. J. Russell, Optica **4**, 1272 (2017).

[327] J. C. Travers, W. Chang, J. Nold, N. Y. Joly, and P. St. J. Russell, Jorunal of the Optical Society of America B **28**, A11 (2011).

[328] A. Ermolov, K. F. Mak, M. H. Frosz, J. C. Travers, and P. St. J. Russell, Physical Review A **92**, 033821 (2015).

[329] K. F. Mak, J. C. Travers, P. Hölzer, N. Y. Joly, and P. St. J. Russell, Optics Express **21**, 10942 (2013).

[330] F. Belli, A. Abdolvand, W. Chang, J. C. Travers, and P. St. J. Russell, Optica **2**, 292 (2015).

[331] N. Y. Joly, J. Nold, W. Chang, P. Hölzer, A. Nazarkin, G. Wong, F. Biancalana, and P. St. J. Russell, Physical Review Letters **106**, 203901 (2011).

[332] P. St. J. Russell, P. Hölzer, W. Chang, A. Abdolvand, and J. C. Travers, Nature Photonics **8**, 278 (2014).

[333] J. Zhao, T. Song, M. Xu, Q. Quan, K. W. M. Siu, A. C. Hopkinson, and I. K. Chu, Physical Chemistry Chemical Physics **14**, 8723 (2012).

[334] S. W. Crane, *Time-Resolved Spectroscopy of Non-Volatile Biomolecule Analogues*, Ph.D. thesis, Heriot-Watt University (2018).

[335] O. Ghafur, S. W. Crane, M. Ryszka, J. Bockova, A. Rebelo, L. Saalbach, S. De Camillis, J. B. Greenwood, S. Eden, and D. Townsend, The Journal of Chemical Physics **149**, 034301 (2018).

[336] S. W. Crane, O. Ghafur, T. Y. Cowie, A. G. Lindsay, J. O. F. Thompson, J. B. Greenwood, M. W. P. Bebbington, and D. Townsend, Physical Chemistry Chemical Physics **21**, 8152 (2019).

[337] D. E. Dolmans, D. Fukumura, and R. K. Jain, Nature Reviews Cancer **3**, 380 (2003).

[338] P. Agostinis, K. Berg, K. A. Cengel, T. H. Foster, A. W. Girotti, S. O. Gollnick, S. M. Hahn, M. R. Hamblin, A. Juzeniene, D. Kessel, M. Korbelik, J. Moan, P. Mroz, D. Nowis, J. Piette, B. C. Wilson, and J. Golab, CA: A Cancer Journal for Clinicians **61**, 250 (2011).

[339] H. Abrahamse and M. R. Hamblin, Biochemical Journal **473**, 347 (2016).

[340] S. Schwartz, K. Absolon, and H. Vermund, Univ. Minn. Medical Bulletin **27**, 7 (1955).

[341] T. J. Dougherty, G. B. Grindey, R. Fiel, K. R. Weishaupt, and D. G. Boyle, Journal of the National Cancer Institute **55**, 115 (1975).

[342] B. Cronin, M. G. D. Nix, R. H. Qadiri, and M. N. R. Ashfold, Physical Chemistry Chemical Physics **6**, 5031 (2004).

[343] G. M. Roberts, C. A. Williams, H. Yu, A. S. Chatterley, J. D. Young, S. Ullrich, and V. G. Stavros, Faraday Discussions **163**, 95 (2013).

[344] T. N. V. Karsili, B. Marchetti, R. Moca, and M. N. R. Ashfold, The Journal of Physical Chemistry A **117**, 12067 (2013).

[345] R. Montero, V. Ovejas, M. Fernández-Fernández, Á. Peralta Conde, and A. Longarte, The Journal of Chemical Physics **141**, 014303 (2014).

[346] S. W. Crane, M. M. Zawadzki, J. O. F. Thompson, N. Kotsina, O. Ghafur, and D. Townsend, The Journal of Chemical Physics **145**, 234304 (2016).

[347] O. M. Kirkby, M. A. Parkes, S. P. Neville, G. A. Worth, and H. H. Fielding, Chemical Physics Letters **683**, 179 (2017).

[348] I. Lamas, A. Longarte, A. Peralta Conde, G. Muga, D. Townsend, and R. Montero, The Journal of Physical Chemistry A **123**, 8982 (2019).

[349] S. P. Neville, O. M. Kirkby, N. Kaltsoyannis, G. A. Worth, and H. H. Fielding, Nature Communications **7**, 11357 (2016).